Development of Materials and Coating Technology for Pyrochemical Reprocessing Plant Applications

By

A. Ravi Shankar

Enrolment No: ENGG 02200704012

Indira Gandhi Centre for Atomic Research, Kalpakkam

A thesis submitted to the
Board of Studies in Engineering Sciences
In partial fulfillment of requirement
For the Degree of

DOCTOR OF PHILOSOPHY

of

HOMI BHABHA NATIONAL INSTITUTE

August, 2013

Homi Bhabha National Institute

Recommendations of the Viva Voce Board

As members of the Viva Voce Board, we certify that we have read the dissertation prepared by **Mr. A. Ravi Shankar** entitled *"Development of Materials and Coating Technology for Pyrochemical Reprocessing Plant Applications"* and recommend that it may be accepted as fulfilling the dissertation requirement for the Degree of Doctor of Philosophy.

_____ 22 Sept, 2014 **Date:**
Chair Person – Prof. T. Jayakumar

_____ 22/9/04 **Date:**
Supervisor-Convener - Prof. U. Kamachi Mudali
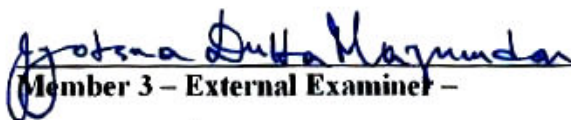
_____ **Date:** 22/8/14.
Member 1 – Prof. K. Nagarajan

_____ 22/9/2014 **Date:**
Member 2 – Prof. A.K. Tyagi

_____ **Date:** 22.9.2014
Member 3 – External Examiner –

Final approval and acceptance of this dissertation is contingent upon the candidate's submission of the final copies of the dissertation to HBNI.

I hereby certify that I have read this dissertation prepared under my direction and recommend that it may be accepted as fulfilling the dissertation requirement.

Date: 22/9/14

(Prof.Dr.U. Kamachi Mudali)
(Research Supervisor & Convener)
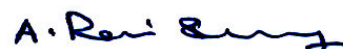
Place: Kalpakkam

STATEMENT BY AUTHOR

This dissertation has been submitted in partial fulfilment of requirements for an advanced degree at Homi Bhabha National Institute (HBNI) and is deposited in the library to be made available to borrowers under rules of the HBNI.

Brief quotations from this dissertation are allowable without special permission, provided that accurate acknowledgement of source is made. Requests for permission for extended quotation from or reproduction of this manuscript in whole or in part may be granted by the Competent Authority of HBNI when in his or her judgment the proposed use of the material is in the interests of scholarship. In all other instances, permission must be obtained from the author.

A. Ravi Shankar

DECLARATION

I, hereby declare that the thesis entitled "**Development of Materials and Coating Technology for Pyrochemical Reprocessing Plant Applications**" submitted to Homi Bhabha National Institute (HBNI), Mumbai, India, for the award of **Doctor of Philosophy** in **Engineering Science** is the record of work carried out by me under the guidance of **Prof. Dr.U. Kamachi Mudali**, Associate Director, Corrosion Science and Technology Group, Indira Gandhi Centre of Atomic Research (IGCAR). The work is original and has not been submitted earlier as a whole or in part for a degree, diploma, associateship, fellowship at this or any other Institution/University of higher learning.

A. Ravi Shankar
A. Ravi Shankar

I dedicate this thesis to

my Mother A. Ananda Leela

& my Sister A. Amrutha Valli

A C K N O W L E D G E M E N T S

C O N T E N T S

| SYNOPSIS

Metallic fuelled Fast Breeder Reactors (FBR) with co-located pyrochemical reprocessing plants have been proposed as the best option to increase the breeding gain, reduce the doubling time of the fuel and reprocess short cooled and high burnup fuel [1-7]. Pyrometallurgical nuclear fuel recycle process, called pyroprocess, has originally been developed by Argonne National Laboratory (ANL) [8-13]. The Russian RIAR (Research Institute of Atomic Reactors) process was also related to the pyroelectrochemical processes for recycling of irradiated fast reactor oxide fuels [14]. Pyroprocessing is the optimal means of treating spent metallic fuels from fast breeder reactors and is included in Global Nuclear Energy Partnership (GNEP) program in order to meet the requirements of the next generation fuel cycle [15]. Pyrochemical reprocessing involves salt purification, electrorefining, consolidation of electrodeposited uranium, plutonium and minor actinides (MA) in a cathode processor into an ingot form and casting of the fuel into slugs in an injection casting furnace. The heart of the pyroprocess is the 'electrorefiner', where fuel is dissolved electrolytically from the anode baskets and electro-transported to one of two types of cathodes involving solid steel or liquid cadmium [16]. In the early 1980s, the studies on the electro-deposition of uranium at solid cathodes have been conducted at ANL towards the integral fast reactor (IFR) fuel processing program [13]. The electrorefining process was carried out in an electrorefiner containing molten chloride salt (LiCl–KCl) floating on liquid cadmium, operating at $500^{o}C$ under an argon atmosphere [12,13]. The chopped spent fuel charged into an anode basket of the electrorefiner was refined in the molten salt while uranium was recovered at

a solid cathode and U-Pu-MA was collected at a liquid cadmium cathode [8]. The major part in implementation of the pyrochemical reprocessing technology involves identification, development, testing and qualification of reliable corrosion resistant materials/coatings for service in corrosive molten LiCl–KCl eutectic salt operating at 500 to 600°C for salt purification and electrorefining operations. Selection of reliable materials and coatings for fabrication of equipment in pyrochemical reprocessing is of major importance as these processes are carried out remotely under intense radiation and maintenance and repair are not feasible. Limited literature exists on corrosion of alloys, ceramics and coatings in molten LiCl–KCl eutectic salt under air, Cl$_2$ and ultra high purity argon environments typically encountered in a pyrochemical reprocessing plant. Therefore, selection and testing of candidate materials in molten LiCl–KCl salt at 500 to 600°C are vital for identification and development of corrosion resistant materials/coatings for salt purification and electrorefining operations in pyrochemical reprocessing plant. Nickel and its alloys are the candidate materials for salt purification system where structural materials are exposed to molten LiCl–KCl eutectic salt under Cl$_2$ bubbling. Cr-Mo steels are the candidate materials for electrorefiner system where structural materials are exposed to molten LiCl–KCl eutectic salt under ultra high purity argon atmosphere. Since metallic materials exhibit poor performance in molten salt environment at high temperatures, corrosion protection coatings such as plasma sprayed partially stabilized zirconia (PSZ) has been proposed. In the present study corrosion testing and characterization of candidate materials in molten LiCl–KCl salt under air, Cl$_2$ and ultra high purity argon environments has been carried out. In order to improve the performance of the coatings optimization of plasma spray process parameters through co-

injection of bond coat and ceramic coat powders using single torch has been carried out. Post surface treatment such as laser remelting of PSZ coating has also been attempted.

In summary the study evaluated the corrosion behaviour of candidate materials in molten LiCl–KCl eutectic salt under Cl_2, air and ultra high purity argon environments. Weight loss results indicated that the corrosion resistance of the materials increased in the following order 2.25Cr-1Mo < 9Cr-1 Mo < Inconel 600 ~ Inconel 690 ~ Inconel 625 < YSZ coating < Pyrolytic graphite in molten salt under ultra high purity argon environment. Inconel 600 and Inconel 690 offered better corrosion resistance in molten salt under air environment compared to Inconel 625, while Inconel 690 offered better corrosion resistance in molten salt under Cl_2 environment. Characterisation of corroded surfaces and scales by XRD, SEM and EDX aided in identifying the morphology, composition and phases of corrosion products and understand the degradation behaviour. The study revealed intergranular corrosion, corrosion along twin boundaries and preferential dissolution of precipitates within the grain, for Inconel 600 and Inconel 625 exposed to molten salt under Cl_2 bubbling while welds revealed interdendritic dissolution. The mechanism of corrosion of Cr-Mo steels, 316L SS & Ni base alloys was found to be due to selective dissolution of Cr with eventual formation of voids and formation of chromium rich compound at the surface and subsequent spallation. PSZ coating in molten LiCl–KCl eutectic salt exhibited excellent corrosion resistance and attempts were made to improve the durability of coating by achieving graded coating. Graded coating exhibited marginally higher adhesion strength (9.6 ± 2.3 MPa) compared to duplex coating (7.6 ± 2.3 MPa). Laser remelting of PSZ coatings resulted in dense, smooth and hard surface (1230 VHN) with beneficial non-transformable t' phase.

This thesis comprises of six chapters. A brief overview of the individual chapters is presented below.

CHAPTER I

INTRODUCTION & LITERATURE REVIEW

A brief description about pyrochemical reprocessing of spent nuclear metallic fuel, advantages and unit processes are described. This chapter also provides a brief introduction on molten salt corrosion, mechanism of molten salt corrosion such as active oxidation, selective attack, thermal mass transfer and effect of moisture etc. Literature review on corrosion of materials and coatings for various equipment in pyrochemical reprocessing plant is highlighted. It also focuses on the aim and objective of the present thesis.

CHAPTER II

EXPERIMENTAL DETAILS

This chapter describes various experimental techniques used for the investigation, which comprises material of investigation, molten salt corrosion, plasma spray coating etc. Characterisation techniques like optical microscopy, XRD, SEM, EDX, LRS and microhardness have been used in the present study.

CHAPTER III - Results and Discussion

CORROSION OF MATERIALS IN MOLTEN LiCl-KCl SALT UNDER Cl_2, AIR AND UHP ARGON

In the present study corrosion investigations were carried out on candidate materials in molten LiCl–KCl eutectic salt under air, Cl_2 and ultra high purity argon environments for application in pyrochemical reprocessing plant. This chapter describes

the corrosion of candidate Ni base alloys and their welds in molten LiCl–KCl salt under Cl$_2$ environment for salt purification system. Characterisation techniques like Optical microscopy, SEM, EDX and XRD were utilised to examine surface morphology and understand the mechanism of corrosion.

In order to study the effect of accidental ingression of oxygen and moisture, corrosion investigations were carried out in molten LiCl–KCl eutectic salt in the presence of air. Characterisation of scales and corroded surfaces were carried out by SEM, EDX and XRD. Based on morphology of attack, composition and phases of corrosion products, the mechanism of corrosion of candidate materials were deduced.

This chapter also describes the corrosion behaviour of materials in molten LiCl–KCl eutectic salt under UHP argon atmosphere. Characterisation techniques like XRD, SEM and EDX were utilised to understand the mechanism of corrosion under UHP argon atmosphere.

CHAPTER IV- Results and Discussion

PREPARATION AND CHARACTERISATION OF THERMAL BARRIER PSZ COATINGS (DUPLEX AND GRADED)

Since metallic materials undergo accelerated corrosion under severe corrosive environment and high temperatures, the vessels and crucibles need to be coated with corrosion resistant ceramic material. Ceramic oxide coatings increase inertness, corrosion resistance and durability of materials in aggressive molten LiCl–KCl salt. Plasma sprayed partially stabilized zirconia (PSZ) coating on candidate materials has been proposed and corrosion tests were carried out in molten LiCl–KCl salt at 600°C up to 2000 h under

UHP Ar atmosphere. The corrosion tested surfaces and cross section samples examined using optical microscope and scanning electron microscope was also presented.

This chapter also focuses on functionally graded PSZ coatings as they are capable of improving the durability of coatings and adhesion strength by reducing the thermal expansion mismatch stresses. Graded PSZ coatings were produced by air plasma spray technique by co-injection of premixed powders of different proportions of zirconia and NiCrAlY powders through single plasma torch. Characterisation of the graded coating was carried out to show the absence of reaction between metallic bond coat and ceramic top coat and formation of graded layer. Corrosion, adhesion and thermal cycling studies were conducted on duplex and graded PSZ coatings and the results were presented.

CHAPTER V- Results and Discussion

LASER REMELTING OF PLASMA SPRAYED PSZ COATING

Laser remelting of plasma sprayed PSZ coating and their characterization are discussed in Chapter V. PSZ coating by plasma spray process usually contains ~10% porosity and microcracks due to splat type of melting and solidification. These pores and micro-cracks may cause corrosion of the substrate as molten LiCl–KCl salt may penetrate through these pores on prolonged exposure. Laser remelting of plasma sprayed PSZ coating has been attempted and the resultant microstructures, hardness and phases formed were discussed. Characterisation of laser remelted surfaces was carried out by optical microscope, SEM, EDX and XRD. An attempt was made to decrease the segmented cracks by depositing ZrO_2, $ZrO_2 + SiO_2$, SiO_2 and laser re-melting and the results obtained were presented.

CHAPTER VI

SUMMARY, CONCLUSIONS AND SCOPE FOR FUTURE WORK

Summary and conclusions of the work performed for the development of materials and coating technology for pyrochemical reprocessing plant applications is provided. This chapter also includes the scope for extending this study for pyrochemical reprocessing plant applications.

▎ L I S T   O F   F I G U R E S

15

19

❚ L I S T   O F   T A B L E S

IV LIST OF ABBREVIATION

FBR: Fast Breeder Reactors

IFR: Integral Fast Reactor

ANL: Argonne National Laboratory

RIAR: Research Institute of Atomic Reactors

IGCAR: Indira Gandhi Centre for Atomic Research

KAERI: Korean Atomic Energy Research Institute

PUREX: Plutonium Uranium Reduction Extraction

PDF: Powder Diffraction File

JCPDS: Joint Committee on Powder Diffraction Standards

MA: Minor Actinide

FP: Fission Product

EF: Electroformed

TBC: Thermal Barrier Coating

YSZ: Yttria Stabilised Zirconia

PSZ: Partially Stabilised Zirconia

FGM: Functionally Graded Material

HAZ: Heat Affected Zone

UHP: Ultra High Purity

GIXRD: Glancing Incidence X-ray Diffraction

CW: Contineous Wave

SEM: Scanning Electron Microscopy

EDX: Energy Dispersive analysis of X-Rays

Inconel, Nimonic: Trade name of Special Metals Corporation

Hastelloy, Haynes: Trade name of Haynes International, Inc

V LIST OF PUBLICATIONS

1. JOURNALS

1. **A. Ravi Shankar** and U. Kamachi Mudali, Corrosion of 316L Stainless Steel in Molten LiCl–KCl Salt, Materials and Corrosion, 2008, 59 (11) pp 878- 882.

2. **A. Ravi Shankar** and U. Kamachi Mudali, Laser Surface Modification of Plasma Sprayed Yttria Stabilized Zirconia Coatings on Type 316L Stainless Steel, Surface Engineering, 2009, 25 (3) pp 241-248.

3. **A. Ravi Shankar**, S. Mathiya, K. Thyagarajan and U. Kamachi Mudali, Corrosion and Microstructure Correlation on Materials in Molten LiCl–KCl Medium, Metallurgical and Materials Transactions-A, 2010, 47 (7) pp 1815-1825.

4. **A. Ravi Shankar**, A. Kanagasundar and U. Kamachi Mudali, Corrosion of Nickel Containing Alloys in Molten LiCl–KCl Medium, Corrosion, 2013, 69 (1) pp 48-57.

5. **A. Ravi Shankar**, K. Thyagarajan and U. Kamachi Mudali, Corrosion Behaviour of Candidate Materials in Molten LiCl–KCl Salt Under Argon Atmosphere, Corrosion 2013, 69 (7) pp. 655-665.

2. CONFERENCES

1. **A. Ravi Shankar** and U. Kamachi Mudali, Corrosion resistant zirconia thermal barrier coating over 316L SS for molten chloride environments, *Poster Presentation for10th International conference on advanced materials, October 8-13, 2007, Bangalore.*

2. **A. Ravi Shankar** and U. Kamachi Mudali, Laser Consolidation of Plasma Sprayed Yttria Zirconia Coatings on Type 316L Stainless Steels, *Poster Presentation for*

The Indian Institute of Metals, NMD-ATM 2007, 61th Annual Technical Meeting, 13-16 Nov, 2007, Mumbai.

3. **A. Ravi Shankar**, S. Mathiya and U. Kamachi Mudali, Corrosion of Materials in Molten LiCl–KCl Medium, *Proceedings for Fourteenth National Congress on Corrosion Control, September 18-20, 2008, Hyderabad.*

4. **A. Ravi Shankar**, A. Kanagasundar and U. Kamachi Mudali, Corrosion of Nickel base alloys in Molten LiCl–KCl Medium, *Poster Presentation for The Indian Institute of Metals, NMD-ATM 2009, 63rd Annual Technical Meeting, November 14-17, 2009, Kolkata. (**Best poster**).*

5. U. Kamachi Mudali, **A. Ravi Shankar** and S. Ningshen, "Plasma Sprayed Thermal Barrier Coatings for Molten Chloride Environment", Proc. SMT-25, Sweden, 20-22 Jun 2011.

3. REPORTS

1. U. Kamachi Mudali, **A. Ravi Shankar**, C. Mallika, K. Thyagarajan, S. Ningshen, B.P. Reddy and K. Nagarajan, "Materials and Coating Technologies for Pyrochemical Reprocessing of Spent Metallic Fuel from Fast Breeder Reactors" Technical Report submitted to Director IGCAR, September 2011.

CHAPTER 1

INTRODUCTION AND LITERATURE REVIEW

In India the total energy demand in 2050 is envisaged to be about 1000 GWe [1] and nuclear energy is the most promising option to meet India's huge energy demand and decrease CO_2 emissions. In a nuclear reactor, power is produced by the fission of fissile isotopes like ^{235}U. Nuclear reactors can be classified into converters and breeders, based on the fuel utilization. In converter reactors, fissile nuclear fuel will be consumed whereas in breeder reactors more fissile fuel is produced than the fuel that is consumed. Natural uranium contains 0.7% fissile ^{235}U and balance ^{238}U is a fertile isotope and can become fissile isotope (^{239}Pu) by neutron absorption. Similarly neutron absorption by fertile ^{232}Th isotope produces ^{233}U fissile isotope. India has an abundant resource of thorium, hence for energy security, a nuclear power programme based on ^{232}Th - ^{233}U fuel cycle is advantageous. In fast breeder reactor, ^{233}U is produced by breeding ^{232}Th blankets. Hence fast breeder reactors (FBR) are very important for the Indian Nuclear Programme. FBRs usually use mixed uranium oxide-plutonium oxide as fuel. A sodium cooled prototype fast breeder reactor of 500 MWe with mixed oxide fuel is under construction in India and FBRs with metallic fuel has been chosen as the best option for future fast reactors [2-4] with pyrochemical reprocessing to close the nuclear fuel cycle [5-7]. Metallic fuels have several advantages compared to ceramic fuels, like oxides, carbides and nitrides. In India, research reactors, Dhruva, APSARA and KAMINI have been using uranium metal and U-Al alloy as fuel for a long time. However certain problems were encountered with metallic fuels such as (i) low solidus temperature of

metallic fuels and (ii) excessive swelling of metallic fuels on irradiation. The limitation of low solidus temperature of U-Pu alloy was overcome by addition of Zr and the swelling problem had been solved using bond sodium [8]. Metallic fuel swells when irradiated because of the release of fission gases. The thermal bond provided by introducing liquid sodium inside the cladding has good compatibility with metallic fuel and the gas plenum provided in the cladding accommodates the released fission gas [8]. As metallic fuelled FBR's provide high breeding ratio, low doubling time and inherent safety features, it has been decided that FBRs in India will use metallic fuel beyond 2020 [1,4].

Fast breeder reactors (FBRs) require lot of Pu to start, so higher breeding ratios and shorter doubling times are required to deploy more FBRs. This is achieved by using metallic fuel in the FBRs. Apart from this metallic fuelled FBRs possesses several advantages such as inherent safety and minor actinide (MA) burning capabilities which are summarised as follows:

1) FBRs with metallic fuel can allow much higher burnup of nearly 200 GWd/t. EBR-II reactor at ANL achieved a burnup of 19.9% [8,9].

2) Highest breeding ratios are possible such as 1.36 with U-Pu-6%Zr as fuel and 1.47 with U-Pu as fuel with Zircaloy liner.

3) Shorter doubling times of ~10 years, enable production & recycle of more U-Pu-MA and help in commissioning more FBR's in less time.

4) Along with U and Pu, minor actinides are fissionable in fast spectrum thus significantly reducing the volume and radiotoxicity of long lived minor actinides in waste.

5) The high thermal conductivity and low fuel temperature of metallic fuel provides inherent safety to the metallic fuelled FBRs and also metallic fuel has good compatibility with molten sodium coolant.

6) In case of raise in temperature, the core diameter increases causing neutron leakage thus reducing the reactivity and subsequently reducing the reactor power, which is an inherent safety feature.

7) Fabrication of metallic fuel is easier compared to oxide or carbide fuels.

In nuclear reactor, the fission process yields a wide range of fission products and heavy elements like Pu, Np, Am etc. The fissile material uranium and plutonium that is produced via neutron absorption can be used as fuel after separation from the fission products. Therefore, it is necessary to recycle the nuclear fuel after a specified level of burn up in the reactor. The separation of fission products and recovery of uranium and plutonium is done by reprocessing of irradiated fuel (spent fuel). The spent nuclear fuel (metallic fuel) from fast breeder reactor contains uranium, plutonium, fission products and long lived radioactive minor actinides (MA) which need to be reprocessed to separate fission products (FP) and recover U-Pu-MA to fabricate fresh fuel. PUREX process is an aqueous reprocessing method, which is a well established method and is currently being used world wide for the recovery of uranium and plutonium from spent oxide and carbide nuclear fuels. For reprocessing of spent metallic fuels, electrorefining method [8] which is pyrochemical process and fuel fabrication by injection casting method [8], has been chosen as the promising fuel cycle concept. A brief description of the pyrochemical reprocessing envisaged for reprocessing of spent metallic fuel from future FBRs is as follows.

1.1. PYROCHEMICAL REPROCESSING

Pyrometallurgical nuclear fuel recycle process, called pyroprocess, has originally been developed by Argonne National Laboratory (ANL), USA for reprocessing of U-Pu-Zr metallic fuel of the Integral Fast Reactor (IFR) [10-12]. The integral fast reactor is a concept where reprocessing of irradiated fuel, fabrication of fuel and waste disposal facilities are co-located at the reactor site itself. In early 1980s, the studies on the eletro-deposition of uranium at solid cathodes by electrorefining of U-Pu-Zr spent fuel have been conducted at ANL towards the integral fast reactor fuel processing program [13]. The Russian RIAR (Research Institute of Atomic Reactors) process was also related to recycling of irradiated fast reactor oxide fuel by electrowinning method which is similar to pyroelectrochemical processes [14]. Pyroprocessing is being developed world wide to recover minor actinide (MA) along with U & Pu and burning of them in fast reactors [15]. Apart from USA, Japan (Central Research Institute of Electric Power Institute-CRIEPI) and South Korea (Korea Atomic Energy Research Institute-KAERI) are actively pursuing research on pyrochemical reprocessing.

Pyrochemical reprocessing methods employ molten LiCl–KCl salt to separate fission products from spent fuel and recover U and Pu [16]. In pyrochemical reprocessing the fuel is maintained in the metallic state throughout the process. Pyrochemical reprocessing is a molten salt electrorefining process, which is ideally suited for reprocessing metallic fuels because of high actinide recovery, co-deposition of U-Pu (non-proliferation), good separation of U-Pu-MA from spent fuel etc. Pyro chemical reprocessing offers several advantages over aqueous reprocessing (Purex process) [4-6,17].

The advantages of pyrochemical reprocessing are detailed as follows:

1) High plutonium containing and high burn up (highly irradiated) fuels with short cooling time are difficult to reprocess by purex process because of radiolytic degradation of solvent at high levels of radiation and complex formation. No such problems in reprocessing high plutonium containing short cooled fuels by pyrochemical reprocessing.

2) In Purex process only uranium and plutonium are recovered from the spent fuel and fission products and minor actinides are disposed as waste. The radiotoxicity of minor actinides in waste remains for hundreds of thousands of years. In pyrochemical reprocessing minor actinides are separated and recycled thus reducing the radiotoxicity to few hundreds of years.

3) In pyrochemical reprocessing criticality problems are less compared to aqueous process, due to option of low atomic number neutron moderating element.

4) In pyrochemical reprocessing, process steps are less and hence compact plant can be co-located with reactor.

5) The process can be adopted for reprocessing spent metallic fuel (U-Pu-Zr alloy) as well as mixed oxide fuel.

6) There is no liquid waste in pyrochemical reprocessing and only small amount of solid waste is generated. The process volumes are low and hence volume of waste generated is low.

7) Pyrochemical reprocessing is proliferation resistant as U & Pu are co-deposited and activity of recovered fuel is high.

Pyrochemical reprocessing poses the following challenges for effective implementation of the technology.

1) High processing temperatures of around 500°C to 1200°C with molten salts, fission products, molten uranium and plutonium under intense radiation causes degradation of structural materials and corrosion resistant container materials are required.

2) Operation and maintenance of high purity argon atmosphere and remote handling are difficult.

3) Process involves handling molten chloride salts and highly corrosive and toxic chlorine gas at 500°C which demands corrosion resistant materials.

4) The process exhibits low separation factors of 10^2-10^3.

5) The decontamination factors achievable are 10^3 to 10^4 times less than those attainable by purex process.

A typical process flow chart of pyrochemical reprocessing of spent metallic fuel from fast breeder reactors is shown in Fig 1.1.

Pyrochemical reprocessing involves four important basic operations:

(i)   Dismantling of the spent fuel pin from fuel assembly and shearing of the fuel pins with a pin chopper (chopping).

(ii)   Removal of bonded sodium by vacuum distillation.

(iii)   Electrorefining to recover U, Pu and MA from the chopped fuel pins in an electrorefiner and

(iv)   Consolidation of the electrodeposited U, Pu and minor actinides and separation of the occluded salt and Cd in a cathode processor.
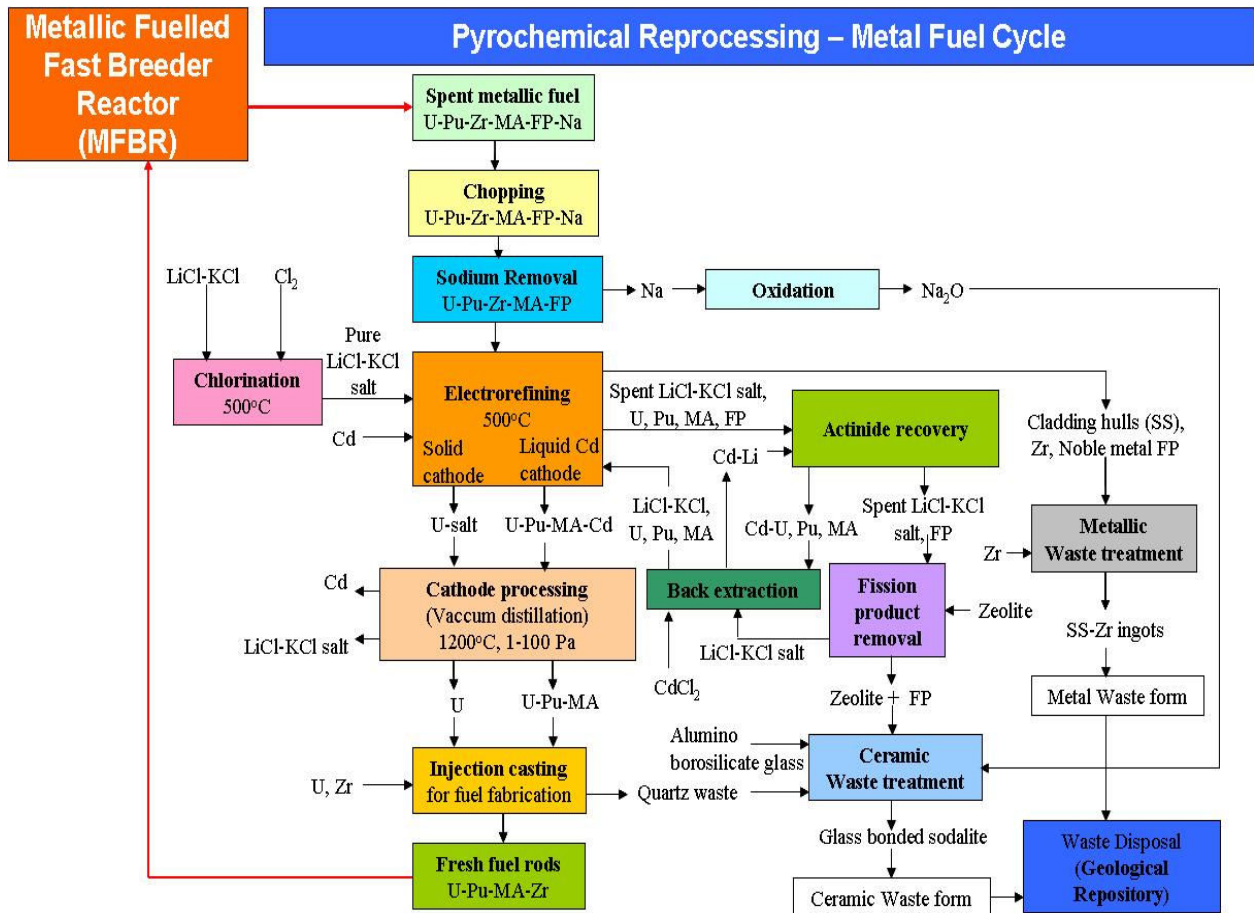
Figure 1.1. Process flow chart of pyrochemical reprocessing of spent metal fuel cycle from fast breeder reactors.

In addition to the above mentioned operations spent electrolyte salt is periodically treated for removal of fission product elements. During the electrorefining process of spent fuel, alkaline earth and rare earth fission products present in the fuel would accumulate in the molten electrolyte salt. To get better decontamination factors, these fission products are to be removed periodically by passing through the zeolite column. Prior to the ion exchange treatment in the zeolite column the actinides in the salt have to be recovered by reductive extraction using cadmium-lithium alloy as shown in Fig 1.1. After the removal of actinides from the electrolyte salt, the salt left with alkali, alkaline

earth and lanthanide chlorides will be passed through lithium/potassium tagged zeolite columns, wherein the fission products will be ion exchanged/occluded by the zeolite and LiCl–KCl electrolyte will be regenerated which can be recycled to the electrorefiner. The radioactive waste (metallic and ceramic radioactive waste) generated has to be treated and disposed in geological repository. The major equipments in pyrochemical reprocessing plant are electro-refiner, cathode processor and injection casting system. The equipments like electrorefiner, cathode processor and injection casting system of pyrochemical reprocessing plant are operated remotely under intense radioactive environment and maintenance free operation should be aimed or preferred. A brief description of each of these processes, are described below. The aim/objective of the present study is then presented.

1.1.1. Salt Purification

Molten LiCl–KCl eutectic salt is used as electrolyte in molten salt electrorefining process of pyrochemical reprocessing. The purity of salt is important in electrorefining process. As LiCl salt is highly hygroscopic in nature salt purification process need to be carried out. The impure LiCl–KCl salt containing moisture is removed by vacuum drying at 150°C and then followed by bubbling chlorine gas in molten salt at 500°C. Corrosion is an important issue during salt purification as the high temperature molten salt containing moisture and chlorine gas is highly corrosive. Also the purity of salt depends on the usage of corrosion resistant materials. Material selection is therefore vital for the purity of the salt and for the successful operation of salt purification system. Therefore materials testing and selection for manufacturing of vessels and components for salt purification

system are of paramount importance. A brief literature survey on materials for molten chloride application under Cl_2 gas are presented in section 1.3.

1.1.2. Electrorefining

Molten salt electrorefining is the key step in pyrochemical reprocessing for separating U-Pu-MA and fission products from spent metallic fuel. Molten salt electrorefining process for processing U-Pu-Zr metallic fuel was developed by Argonne National Laboratory (ANL) [13,18]. The molten LiCl–KCl salt acts as an electrolyte in this process. The melting point of LiCl is 610^oC and that of KCl is 772^oC. However LiCl–KCl eutectic mixture exhibits a low melting point of 351^oC. Therefore purified (chlorinated) eutectic salt mixture of LiCl (58.5 mol%) – KCl (41.5 mol%) is used in this process. Apart from low melting point, LiCl–KCl salt has high thermodynamic stability having wide electrical window and is resistant to radiation damage. Molten LiCl–KCl salt also facilitates electro-transport of U & Pu, and has high solubility for U, Pu & FP chlorides. The schematic diagram of the electrorefining process proposed by ANL is shown in Fig. 1.2. The chopped spent nuclear fuel pins are placed in perforated anode basket of the electrorefiner which acts as anode. The uranium is recovered by depositing on solid cathode as dendrities while U-Pu-MA is recovered in liquid cadmium cathode as shown in the figure.

The process depends on the thermodynamic stabilities of the chlorides of U, Pu and fission products to separate them [19]. Table 1.1 presents the Gibbs free energy of formation of chlorides of the elements of fuel, fission products and cladding materials at 500^oC, which are classified according to their thermodynamic stability.
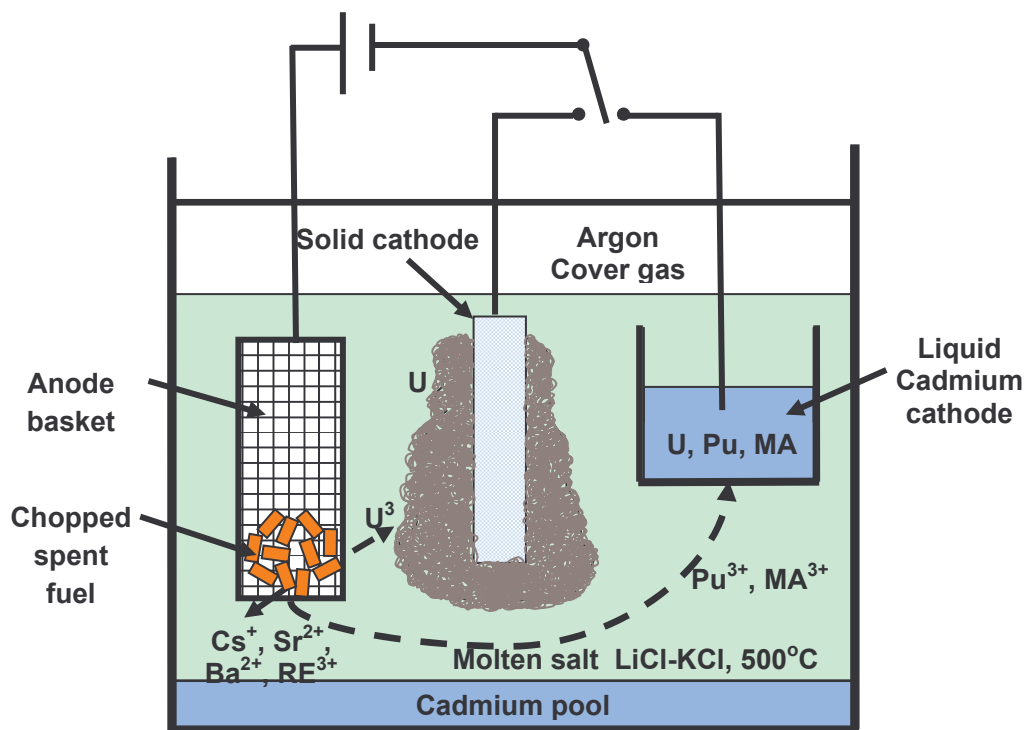
Figure 1.2. The schematic diagram of electrorefining process.

The low stability chlorides shown on the right side of the table are relatively less stable and therefore these elements remain in the metallic state. Thus the noble metal fission product elements present in the spent fuel remain in anode basket in metallic state. The chlorides shown in the middle of the table are intermediate stablility between them and are electro-transportable depending on the redox conditions. Thus U, Pu, minor actinides (Am, Np, Cm) are transported from anode to cathode by applying potential. When $CdCl_2$ is added to the melt, the U, Pu, minor actinides and some rare earth elements present in metallic form in the spent fuel will get oxidized and dissolved in the melt as follows:

$$2\,U \;+\; 3\,CdCl_2 \;\rightarrow\; 2\,UCl_3 \;+\; 3\,Cd \qquad\qquad\qquad ….Eq.\ (1.1)$$

$$2\,Pu \;+\; 3\,CdCl_2 \;\rightarrow\; 2\,PuCl_3 \;+\; 3\,Cd \qquad\qquad\qquad ….Eq.\ (1.2)$$

$$2\,Ce \;+\; 3\,CdCl_2 \;\rightarrow\; 2\,CeCl_3 \;+\; 3\,Cd \qquad\qquad\qquad ….Eq.\ (1.3)$$

Table 1.1 Gibbs free energy of formation of chlorides at 500°C (-ΔG°f kcal/g-mole equiv. of Chlorine [19].

Very stable chlorides (Elements that remain in salt)		Elements that are Electro-transportable		Relatively less stable chlorides (Elements that retain in metal phase)	
Compound	-ΔG°f	Compound	-ΔG°f	Compound	-ΔG°f
$BaCl_2$	87.9	$CmCl_3$*	64.0	$CdCl_2$	32.2
CsCl	87.8	$PuCl_3$	62.4	$FeCl_2$	29.2
RbCl	87.0	$AmCl_3$*	62.1	$NbCl_5$	26.7
KCl	86.7	$NpCl_3$	58.1	$MoCl_4$	16.8
$SrCl_2$	84.7	UCl_3	55.2	$TcCl_4$	11.0
LiCl	82.5	$ZrCl_4$	46.6	$RhCl_3$	10.0
NaCl	81.2			$PdCl_2$	9.0
$CaCl_2$	80.7			$RuCl_4$	6.0
$LaCl_3$	70.2				
$PrCl_3$	69.0				
$CeCl_3$	68.6				
$NdCl_3$	67.9				
YCl_3	65.1				

estimated value

A layer of liquid cadmium is thus formed in the electrorefiner. The electrorefining process is thus carried out in molten LiCl–KCl salt floating on liquid cadmium operating at 500°C under argon atmosphere.

The liquid cadmium is useful in serving the following purposes [20,21]:

Cadmium can be contained in low carbon steels and limits the corrosion of electrorefiner vessel because cadmium will be oxidised before steel ($CdCl_2$ is stable than $FeCl_2$). Cadmium aids in recovery of U metal deposited on the cathode as dendrites that tend to detach from the cathode and fall. Cadmium allows co-deposition of U, Pu and MA by compensating the differences in the thermodynamic stabilities of the chlorides. Cadmium

has high solubility of U & Pu at 500°C & retains fission products. The boiling point of Cd is 767°C at 1 atm pressure thus allowing separation of the recovered U-Pu-MA from Cd by distillation. Cadmium also aids in raising the criticality limit.

Since $PuCl_3$ is more stable than UCl_3, uranium will be deposited (reduction) on solid cathode as follows.

UCl_3 + Pu → U + $PuCl_3$ ....Eq. (1.4)

UCl_3 + Np → U + $NpCl_3$ ....Eq. (1.5)

UCl_3 + Am → U + $AmCl_3$ ....Eq. (1.6)
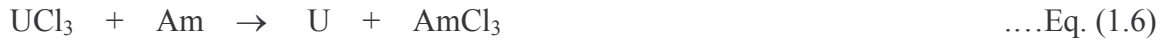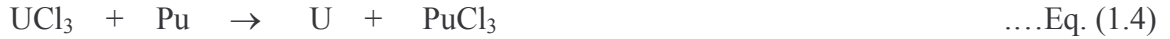
Thus uranium is electro-transported to a solid cathode, where it deposits as metallic dendrite. In order to recover plutonium and minor actinides, a liquid cadmium cathode is used as shown in Fig 1.2. The relatively lower activity coefficients (10^{-4}) of Pu and other MA compared to that of uranium (88.4) in liquid cadmium compensate for the differences in the thermodynamic stabilities of the chlorides which allow Pu and MA in the electrolyte to be recovered along with uranium [2]. Zirconium behaves as noble metal in the presence of Cd. Thus U, U-Pu-MA are recovered and deposited on solid cathode and liquid cadmium cathode respectively. As more and more batches of fuel are reprocessed, the amounts of the alkali metal, alkaline earth, and rare-earth fission products in the salt continue to increase. When the amount of fission products in the salt becomes very large, the rare earth decontamination factor i.e. the ratio of the amount of rare earth in the feed to that in the deposit becomes too low. At that point, the salt must be treated to recover the actinides and separate the fission products. After the removal of actinides and fission products, the salt is recycled. The material used for fabricating the electrorefiner should be resistant to high temperature molten LiCl–KCl salt and molten

Cd. A brief literature survey on materials for electrorefiner application is presented in section 1.3.

1.1.3. Cathode Processor

The cathode deposit from liquid cadmium cathode of electrorefiner contains U, Pu and MA along with cadmium and small amounts of LiCl–KCl salt. The cadmium and small amount of salt present in the cathode deposit has to be separated. Similarly the cathode deposit (Uranium) from solid cathode of electrorefiner contains entrapped (occluded) LiCl–KCl salt and small amounts of Cd which need to be separated. The separation of occluded LiCl–KCl salt and/or Cd is accomplished in cathode processor [22-24]. The low boiling points and high vapour pressure of LiCl–KCl salt and Cd allows distillation process to separate them from U and/or U-Pu-MA cathode deposit. Distillation process is therefore essential for the separation of occluded salt and Cd from uranium and consolidation of uranium which is carried out in a cathode processor as shown in Fig 1.3. The cathode deposit from electrorefiner containing occluded salt and/or cadmium is placed in a ceramic coated graphite crucible which is loaded in the cathode processor. The crucible containing cathode deposit is inductively heated using passively cooled induction coil. The cathode deposit is heated to 700–900°C at pressures ranging from less than 10 to 100 Pa to distill off the salt and cadmium from the deposit [24]. The melting point of uranium is around 1132°C and therefore consolidation of uranium in to ingot is done by heating up to 1200°C. The consolidated uranium ingot is released from the crucible by ingot dumping. All these operations of the cathode processor are performed remotely by overhead cranes and manipulators [25]. For efficient and uninterrupted operation of the cathode processor for uranium melting reliable inert
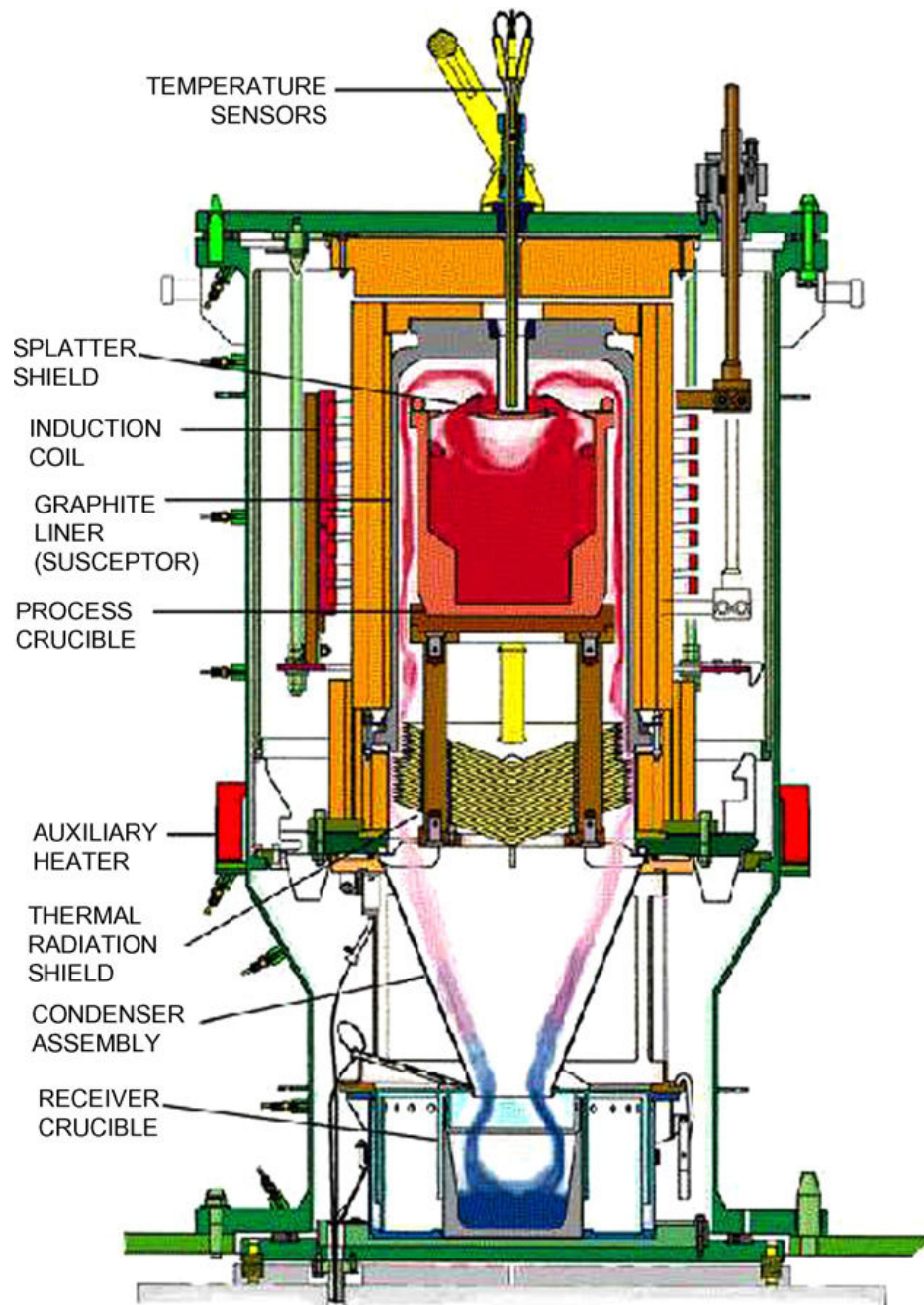
Figure 1.3. The schematic diagram of cathode processor [24].

ceramic coated crucibles are of paramount importance. The material used for the fabrication of crucible should with stand reaction from molten salt, molten Cd and molten uranium, at such high temperatures.

Graphite crucibles are used as process crucible as they can be easily fabricated and has the ability to withstand high temperature (good thermal shock and thermal cycling resistance). However, slight contact between the molten uranium with graphite causes an interaction that leads to the ingot being firmly stuck in the crucible and destruction of crucible is required to recover the ingot [22]. In addition, graphite reacts with nuclear materials to form carbides and contaminates the uranium ingot. Therefore due to the chemical reactivity of uranium and most alloying elements with graphite, a protective coating is generally applied to the crucible [22,26].

Zirconia coated crucibles have been used for cathode processing due to their ability to withstand high temperatures, release consolidated products, and react minimally with the process charge [23]. Zirconia wash coat applied on graphite crucibles were used to protect graphite from contact with the uranium which gave good mould release but after melting, crucible has to be cleaned to remove the excess zirconia via wire brush and coating must be re-applied [22,23]. The cumbersome cleaning and re-coating operation span several days and the removed coating consists of significant amounts of uranium [22,23]. Therefore plasma sprayed HfN coating on niobium crucible has been developed and tested by Idaho National Laboratory, USA, to verify the crucible's compatibility with salt and uranium [22]. Their tests (five times) in cathode processor indicated no degradation to the niobium crucible or its HfN coating and the uranium ingot released successfully. Vasconcelos et al. [27] reported that no reaction was observed between titanium nitride and uranium even at $1427^{o}C$. Therefore magnetron sputter deposited nitride coatings were prepared [28,29] and evaluated for uranium melting applications

[28]. Recently it is reported that ceramic lined crucibles eliminated cleaning and coating operations although minor process losses and crucible degradation was observed [25].

1.1.4. Injection Casting

The fuel ingots from the cathode processor are melted and fabricated into fresh fuel rods in injection casting system as shown in Fig 1.4. The ingot from cathode processor is melted with additional zirconium, uranium and/or plutonium to get desired composition in ceramic coated graphite crucible [8]. Injection casting is carried out at about 1250–1350°C. High silica glass tube moulds with very high softening temperatures were used for casting fuel rods [30]. The quartz tube moulds need to be coated to prevent reaction and facilitate easy removal of fuel rod with good surface finish. The coated crucible and quartz tube moulds are placed in injection casting furnace. By applying vacuum and pressurization (by applying inert gas pressure) of melting chamber of the furnace, the molten metal from the crucible is raised in to coated quartz tube moulds [30]. The solidified fuel rod is separated from quartz tube moulds by crushing the quartz tubes. After demoulding the shrinkage voids present in the fuel rod will be removed and finished to desired dimensions [8]. All the operations need to be carried out remotely due to handling of radioactive materials. It is reported that the broken glass contains 1 to 9 g of alloy as fine particles [30]. In order to avoid loss of fuel in broken quartz tube moulds and avoid generation of active waste, it is essential to develop reusable moulds. Chen et al. [31] investigated several types of coatings made of borides, nitrides carbides, sulfides, and oxides in contact with uranium and heated to 1600°C and their study revealed that only NbC, TiN, VC and Y_2O_3 coatings exhibited 90° contact angle and thus were not wet by U-10%Zr [31]. The authors concluded that yttria (Y_2O_3) coatings offer best chemical

39

compatibility with uranium because of yttria's nonreactivity and nonwettability with uranium [31]. Nagaraj et al. [32] showed that plasma sprayed yttria coating on tantalum crucible exhibited excellent corrosion resistance against liquid uranium tested at 1300°C up to 80 h in vacuum. Cho et al. [33] reported that plasma sprayed YSZ coating on graphite showed good adhesion and no reaction of the YSZ coated layer was reported after testing for 1 h at 1300°C with uranium. It is of paramount importance to use reliable materials and coatings to avoid uninterrupted operation.
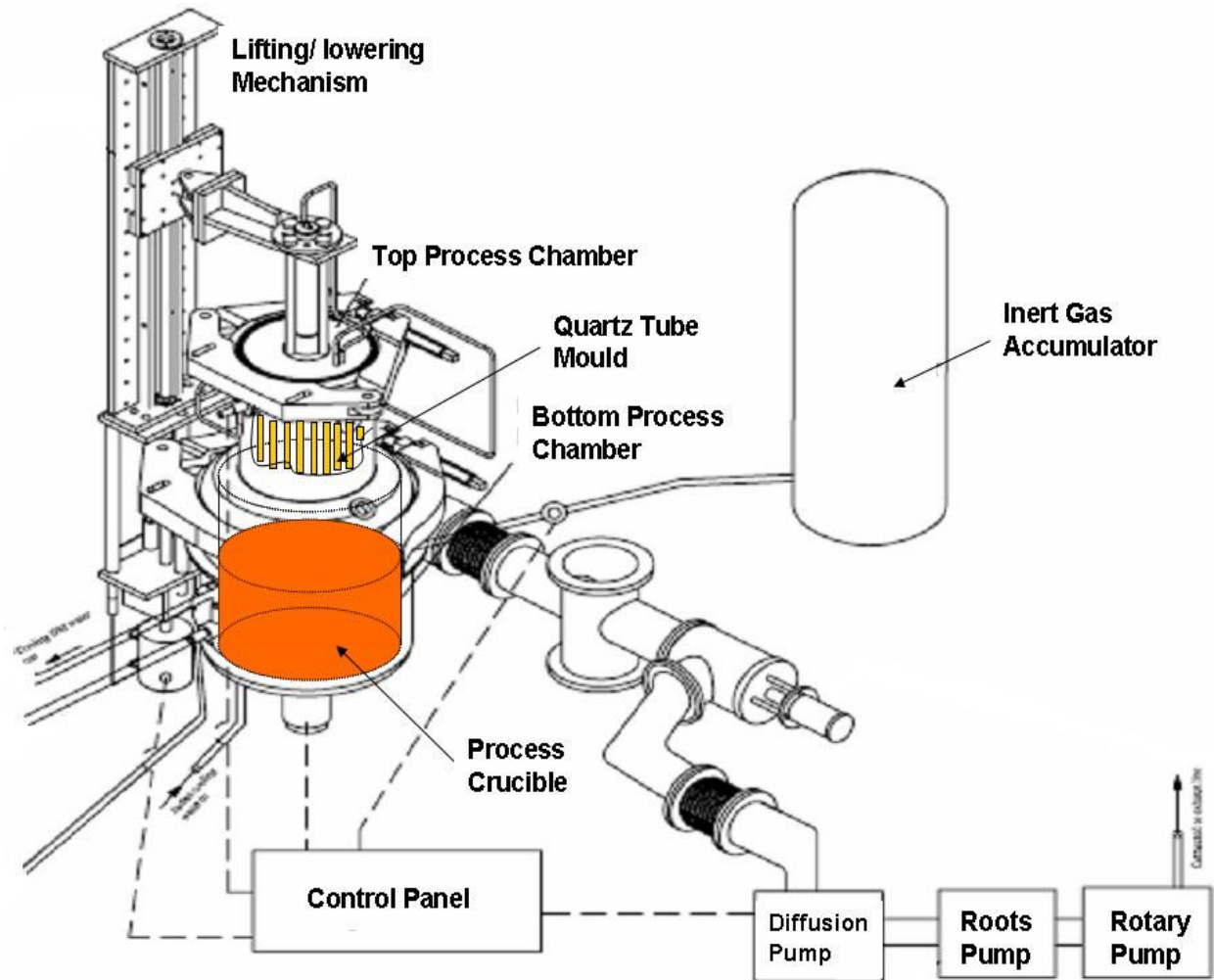
Figure 1.4. The schematic diagram of injection casting system.

1.1.5. Aim of the Study

Material selection is the key to successful operation of pyrochemical reprocessing plant as the operations are carried out remotely under intense radioactive environment. For selection of reliable materials and coating technology for such high temperature corrosive environment, it is essential to understand the corrosion behaviour of candidate materials. The literature survey on molten salt corrosion and materials and coatings for various unit operations (salt purification & electrorefiner) in pyrochemical reprocessing are presented in section 1.3.

The aim of the present study is:

1) To determine the corrosion behaviour of candidate materials in molten LiCl–KCl salt under Cl_2 bubbling to simulate the salt purification environment.

2) To determine the corrosion behaviour of candidate materials in molten LiCl–KCl salt under ultra high purity argon atmosphere to simulate the electrorefiner environment.

3) The mechanism of corrosion of candidate materials in molten LiCl–KCl environment are better understood under severe corrosive conditions. Therefore corrosion behaviour of materials was studied under air environment to simulate the severe corrosive conditions and/or accidental ingression of oxygen in molten salt environment conditions.

4) The study also consists of selection of corrosion resistant coating material and coating technology for improving the corrosion resistance.

5) To determine the corrosion behaviour of corrosion resistant coating in molten LiCl–KCl salt under ultra high purity argon atmosphere.

6) Improving the durability of the coating by optimization of coating parameters to achieve graded coatings.

7) Laser remelting for consolidation of coating is also attempted.

1.2. CORROSION IN MOLTEN CHLORIDE SALT

1.2.1. Introduction

Molten chloride salts are widely used for electrowinning of metals and alloys, for annealing and normalizing of steels, in high-temperature batteries, fuel cells, etc [34]. Molten salts are used as a heat transfer medium in nuclear reactors, however, compatibility of structural materials and corrosion is an inevitable serious problem. Molten salts have been widely employed in nuclear and chemical industry because of its physical and chemical characteristics like high electrical conductivity, high processing rate and high diffusion rate. Since pyrochemical reprocessing utilizes molten chlorides (LiCl–KCl), at high temperature, high corrosion resistance materials are required for the practical application. The corrosion of metals and alloys in molten chlorides has been attributed mostly to the presence of trace impurities like moisture, water and oxygen present in the salt [35,36]. Even in the absence of oxygen, metals and alloys can corrode owing to a trace of water or moisture present in molten chloride salt [36].

1.2.2. Comparison between Molten Salt Corrosion and Aqueous Corrosion

The differences in molten salt and aqueous solution are in temperature and electrical conductivity [36]. Most of the electrochemical principles applicable to aqueous corrosion, such as anodic reactions leading to metal dissolution and cathodic reduction of the oxidant, are also applicable to molten salt corrosion [37]. Even though the electrochemical principles are similar, there are major differences between aqueous and molten salt corrosion. Table 1.2 summarises the differences between molten salt corrosion and aqueous corrosion.

43

Table 1.2 Differences between molten salt corrosion and aqueous corrosion [36,38].

AQUEOUS	MOLTEN SALT
Simple anodic and cathodic reactions	Complex situation with several oxidants (O_2, H^+, H_2O, OH^-)
Passive state can be easily maintained (e.g. SS, Ti)	Passive state maintenance is less promising due to salt
Pourbaix diagram can be used to understand M-H_2O corrosion (Potential – pH)	Basicity diagrams can be used to understand M-Salt corrosion (Potential – pO^{2-})
Anodic reaction involves dissolution of metal and formation of metal oxides	Anodic reaction involves dissolution of metal and formation of salt films (metal chlorides/metal oxides)
Cathodic reaction involves reduction of species	Cathodic reaction is complicated and depends on oxidants and trace impurities
Hydrogen ions are displaced to form hydrogen or other solute such as dissolved O_2 is reduced.	Either one of the metal cations is displaced to produce metal or with some dissolved Cl_2 or O_2 or ions such as nitrate or ferric are reduced.
Predominately molecular and containing very low activities of H^+ and OH^-	Molten salts are predominately ionic
They operate at relatively low temperature	Molten salt system operates at higher temperatures than aqueous system which leads to different types of corrosion

1.2.3. Mechanism of Molten Salt Corrosion

Thermodynamic stabilities can predict whether a metal in contact with molten salt will react or not. For example consider the displacement reaction between nickel and molten sodium chloride salt. The reaction can be written as

$Ni + 2NaCl \rightarrow NiCl_2 + 2Na$ $\Delta G° = 486.47$ kJ/mol (at $600°C$)   ….Eq. (1.7)

If the free energy change is negative, i.e. the potential difference is positive, corrosion proceeds spontaneously. Since the free energy change is positive, nickel cannot displace sodium from a sodium chloride melt and hence nickel will not corrode in molten sodium chloride unless some other reducible impurity is present [38]. Distillation of the displaced metal out of the melt is one of the factors which can prevent equilibrium being reached, and under such conditions corrosion can continue indefinitely [38]. In molten salt corrosion, the relative nobilities of the molten salt and the metal are important [37,38]. A noble metal in contact with a pure molten salt or a base-metal cation can react only to a very limited extent provided the anion is not reducible [38]. In molten salt corrosion dissolution of the less noble element is the most probable mechanism and even occurs when the element is present at low concentration [37]. Therefore, it is usual to choose a container metal for molten salts sufficiently noble for the displacement reaction to be negligible [38].

There are two general mechanisms in molten salt corrosion [34,37,38]

1. Metal dissolution based on the solubility of metal in the molten salt.

2. Oxidation of metal ions similar to that in aqueous corrosion

The direct metal dissolution mechanism is similar to the dissolution in molten metal and is not common [37]. The most common mechanism is by oxidation of metal to

ions. For this reason, molten salt corrosion has been identified as an intermediate between liquid metal corrosion and aqueous corrosion [37].

Uniform corrosion is a common form of molten salt corrosion, however other forms of corrosion such as selective attack, Intergranular corrosion, thermal mass transfer, galvanic corrosion, stress corrosion cracking, erosion corrosion are also observed in molten salts [37].

1.2.3.1   *Selective attack*

Molten salt corrosion often exhibits selective attack and internal oxidation [37]. Molten salt corrosion is complicated due to diffusion at high temperature, particularly where alloy components have different affinities for the environment [34,38]. Selective outward diffusion of the less noble component occurs, and vacancies move inwards. The vacancies segregate to form visible voids (Kirkendall effect) particularly at grain boundaries [34,38]. Selective attack of Inconel 600 alloy was observed in molten chloride melts [37]. This type of corrosion is not desirable because the porosity present inside leads to failure even though the outside surface appears sound [38].

1.2.3.2   *Active oxidation*

The corrosion in oxidising atmosphere was more severe with molten chloride salt than without molten chloride salt, because of active oxidation process [39]. A schematic illustration of circulation of chlorine in active oxidation process is shown in Fig 1.5. Corrosion initially starts with dissolution of metal and formation of metal chloride as the Gibbs free energy of formation of metal chloride is negative. In oxidising atmosphere metal oxides are stable, therefore metal chlorides oxidise to form metal oxides. Due to low oxygen partial pressure at the metal/oxide interface, metal chlorides can form at the
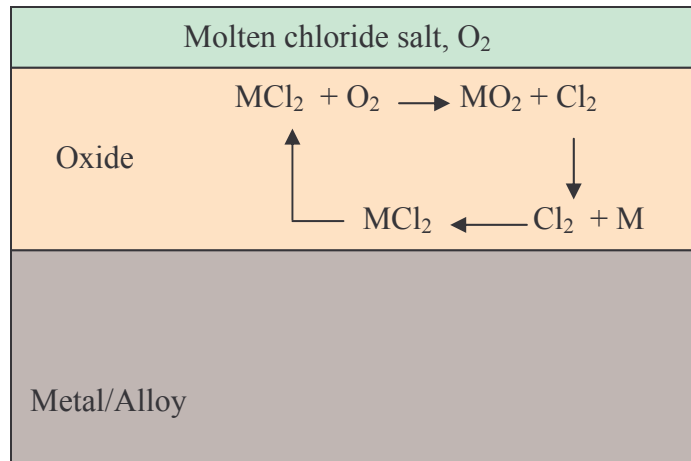
Figure 1.5. Schematic illustration of circulation of chlorine in active oxidation process.

interface [39]. The oxide scales become porous due to the precipitation of metal oxide in the existing oxide scale leading to massive growth stresses and results in cracks in the oxide scale [40]. Thus the porous, brittle oxide scale with cracks allow easy transport of chlorides/chlorine. The melting point of most of the chlorides are low compared to that of oxides, and if partial pressure of metal chlorides are significant, the metal chloride can diffuse outward [40] through pores and cracks in the scale [39] and oxidise to form metal oxides. The chlorine thus released diffuses back to the substrate and results in new metal chloride formation [39,40]. Thus the process is catalysed by chlorine [40] and the active oxidation process continues as shown in the figure.

1.2.3.3 *Intergranular corrosion*

Intergranular corrosion is the major corrosion morphology by molten chloride salts [41]. Alloy 600 exposed to molten KCl salt at 870^oC for 6 months under thermal cycling showed severe intergranular corrosion [37,41]. It is also reported that cold work may significantly increase intergranular corrosion [41].

1.2.3.4   Thermal mass transfer

When a temperature gradient exists in a molten salt system containing metal in contact with molten salt, thermal potentials are set up, which results in removal of metal from high-temperature regions and deposition of metal at low temperature regions. Thus thermal gradients in molten salt system can cause dissolution of metal at hot spots and metal deposition at cold spots [37]. Since dissolution and deposition reactions are electrolytic in molten salt corrosion, an electrical path is necessary between the hot and cold regions of the metal. As this type of mass transfer requires an electrolytic current, Edeleanu and Gibson [42] suggested that this type of mass transfer be called "faradic mass transfer". These mass transfer deposits can lead to blockages in non-isothermal circulating systems as in the case of liquid metal corrosion [34,38]. However, unlike liquid metal corrosion mass transfer which occurs by temperature-solubility effect, molten salt mass transfer requires electrical path [34,38].

1.2.3.5   Aggressiveness of molten salt towards metal

The redox potential of molten salt is a measure of its aggressiveness towards metal in contact with molten salt [34,38], which is calculated from the free energies of formation of appropriate oxides and chlorides. The higher the oxidizing power of the molten salt, the more will be the metal corrosion giving metal ions, before the equilibrium is reached [38]. The aggressiveness of the salts towards metals is dependent on the nature of the cation [34].

The aggressiveness of chloride melts in contact with air is in the order [34,38]:

$$LiCl \sim MgCl_2 \sim CaCl_2 >> NaCl > KCl$$

1.2.3.6 Effect of impurities in the melt

From thermodynamic stabilities, it is clear that molten chloride does not react with metals and alloys and corrosion of metals and alloys in molten chloride salt is due to the trace impurities [36]. Water and oxygen are the main contaminants in molten chloride salt and complete removal of impurities is necessary to prevent corrosion [36]. Moisture in LiCl–KCl eutectic had a significant effect on corrosion of 316L stainless steel [43]. Nishikata et al. [44] confirmed from the electrochemical studies that Fe, Ni and their alloys corrode in molten chloride only in the presence water, oxygen or other oxidants and water has great influence than dissolved oxygen. Impurities such as water have a great influence on oxygen reduction in molten chloride [44]. Kinoshita et al. [43] concluded that LiCl–KCl eutectic most likely forms LiOH when moisture is introduced in the system and the reaction is

$$LiCl + H_2O \rightarrow LiOH + HCl \qquad\qquad ....Eq. (1.8)$$

Moisture causes more corrosion, due to the conversion of LiCl into LiOH and HCl.

1.2.4 Corrosion in Molten LiCl–KCl Eutectic Salt

Feng and Melendres [45] studied the anodic polarisation of Fe, Co, Ni, Cu and Mo in molten LiCl–KCl eutectic melt containing lithium oxide at 375 and 450°C. They found that the anodic corrosion rates decreased in the order Fe > Ni > Co > Cu > Mo and a 75°C lowering in temperature from 450 to 375°C resulted in a decrease in the corrosion rate by roughly 2-3 times. They also reported that the reduction of oxide films on Fe, Co, and Cu was reversible, quasi-reversible for nickel and irreversible for Mo. Colom and Bodalo [46] studied the electrochemical behaviour of iron in molten LiCl–KCl eutectic at

$400–600^{0}C$ and concluded that ferric ions are the oxidising species controlling the corrosion process. Raleigh et al. [47] studied the anodic dissolution characteristics of Ni, Mo, and 304 stainless steel in LiCl–KCl eutectic melt and observed that Mo and Ni followed Tafel-type dissolution kinetics in pure eutectic melts and Ni formed non-passivating layer in Li_2O saturated melt.

Tada and Ito [48] studied the passive oxide film growth and pitting corrosion of Ni in LiCl–KCl eutectic melt containing oxide ion. They observed the formation of a dense and adherent film at more negative potentials than that of the conventional passivation. They arrived at the conclusion that this oxide film formation occurs by the interdiffusion of adsorbed oxygen atoms formed by the discharge of oxide ions at the nickel surface and named this new type of passivation behaviour of nickel as under-potential passivation [48]. They also investigated the electrochemical behaviour of pitting corrosion of nickel and estimated critical pitting potential at $500^{0}C$.

Anodic behaviour of iridium in molten LiCl–KCl eutectic melt at 400 and $600^{0}C$ was studied by Colom and Plaza [49]. At $400^{0}C$ no metal attack was detected and at high positive potentials chlorine evolution was observed by them. Passivation was attributed to the precipitation of supersaturated alkali iridium chlorides, although the formation of porous IrO_2 layer was also observed [49].

Electrochemical corrosion behaviour of Ni_3Al-based intermetallic compounds in molten 58 LiCl– 42 KCl (mol%) salt was studied at $450^{0}C$ [50]. These authors reported that flade potential could not be observed and electrochemical passivation did not occur in pure molten LiCl–KCl salt. However, they found that Ni_3Al-based intermetallic compounds showed passivation behaviour and their anodic current densities were

lowered in the presence of Li_2CO_3 indicating Li_2CO_3 as an effective inhibitor. On the contrary, the anodic current densities were higher in the molten LiCl–KCl salt in the presence of metallic oxides such as MgO, ZnO and MnO_2. It was reported that Ti-8Al-1Mo-1V alloy undergoes stress corrosion cracking in molten LiCl–KCl melt [51]. Materials undergoing localized corrosion and forming non protective films are not desirable for fabrication of critical components in pyrochemical reprocessing plant.

1.3   Literature Review on Corrosion and Compatibility of Materials

Various studies have been done on corrosion of structure materials in molten chlorides, focusing on potentiodynamic polarization and electrochemical impedance spectroscopy on the corrosion under inert atmosphere or in the presence of oxide ions as discussed in the above section. However for practical applications, immersion studies exposing the samples, simulating the actual service conditions is the best method to determine the corrosion resistance of materials, coating/surface modified material. Accelerated immersion tests for measuring uniform corrosion from coupon weight loss are fundamental in corrosion engineering which produce results in a reasonable testing time.

Indacochea et al. [35] carried out corrosion studies on eleven specimens along with welds such as type 316L stainless steel (SS), type 422 SS, type 430 SS, 2.25 Cr-1 Mo steel, and Ta in annealed and welded conditions, in molten LiCl salt with 3.5 wt% Li_2O, 1 wt% Li_3N saturated with lithium metal at 725°C for 30 days under argon atmosphere. Their study showed negligible weight loss and thickness reductions for type 316L stainless steel (SS), type 422 SS, type 430 SS, 2.25 Cr-1 Mo steel, and Ta in annealed and welded conditions as shown in Table 1.3 [35].

Table 1.3. Weight change of materials exposed to LiCl molten salt with 3.5 wt%

Li_2O, 1 wt% Li_3N at 725°C for 30 days [35].

S.No	Material	Percent weight loss	Thickness reduction, mm
1	316L SS (annealed)	NA	0.00
2	316L SS (as welded)	0.18	0.03
3	316L SS (welded and aluminized)	0.28	0.03
4	2.25Cr-1Mo (annealed)	0.04	0.00
5	2.25Cr-1Mo (as welded)	0.04	0.06
6	422 SS (annealed)	0.04	0.02
7	422 SS (as welded)	0.04	0.00
8	430 SS (annealed)	0.02	0.05
9	430 SS (as welded)	0.02	0.02
10	Ta (annealed)	1.17	0.04
11	Ta as welded)	1.13	0.06

Pyrolytic graphite has been used for RIAR oxide pyro process which utilizes molten salt with O_2 and Cl_2 gases at high temperatures. Asou et al. [52] studied thermodynamic evaluation of candidate materials and weight loss experiments in molten salt with O_2 and Cl_2 gases. The ΔG^o values of chemical reactions between candidate materials and Cl_2 gas as reported is shown in Fig 1.6 [52]. As shown in Fig 1.6, BeO, $ZrSiO_4$, SiO_2 and ZrO_2 exhibit stability. Similarly thermodynamic evaluation of candidate materials with chlorine, oxygen and UO_2Cl_2 at 650°C as reported is shown in Table 1.4 [53]. From the table it is clear that ZrO_2 and $ZrSiO_4$ are stable with chlorine, oxygen and UO_2Cl_2 at 650°C. As can be seen from the table nitrides and carbides are not stable with chlorine, oxygen and UO_2Cl_2 [53].
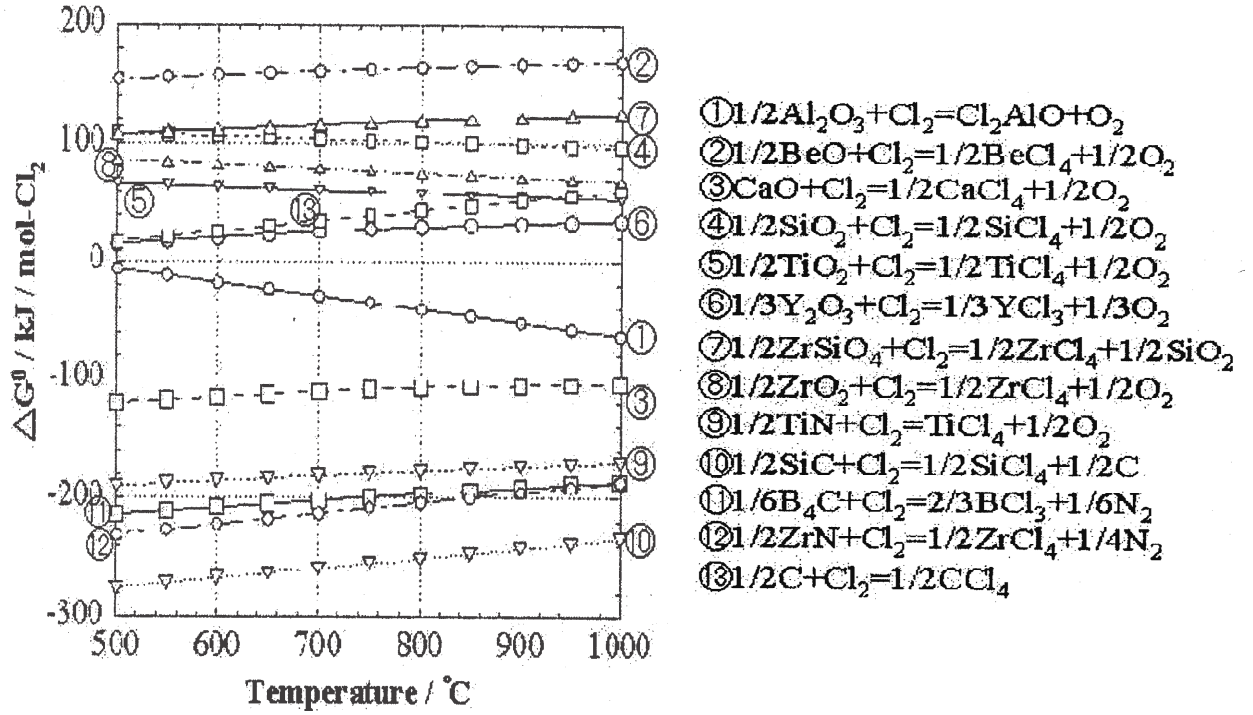
Figure 1.6. Free energy change of chemical reactions between candidate materials

and Cl₂ gas [52].

The legend entries shown in the figure:

① $1/2Al_2O_3 + Cl_2 = Cl_2AlO + O_2$
② $1/2BeO + Cl_2 = 1/2BeCl_4 + 1/2O_2$
③ $CaO + Cl_2 = 1/2CaCl_4 + 1/2O_2$
④ $1/2SiO_2 + Cl_2 = 1/2SiCl_4 + 1/2O_2$
⑤ $1/2TiO_2 + Cl_2 = 1/2TiCl_4 + 1/2O_2$
⑥ $1/3Y_2O_3 + Cl_2 = 1/3YCl_3 + 1/3O_2$
⑦ $1/2ZrSiO_4 + Cl_2 = 1/2ZrCl_4 + 1/2SiO_2$
⑧ $1/2ZrO_2 + Cl_2 = 1/2ZrCl_4 + 1/2O_2$
⑨ $1/2TiN + Cl_2 = TiCl_4 + 1/2O_2$
⑩ $1/2SiC + Cl_2 = 1/2SiCl_4 + 1/2C$
⑪ $1/6B_4C + Cl_2 = 2/3BCl_3 + 1/6N_2$
⑫ $1/2ZrN + Cl_2 = 1/2ZrCl_4 + 1/4N_2$
⑬ $1/2C + Cl_2 = 1/2CCl_4$

Beryllia is reported to exhibit excellent corrosion resistance in molten salt and uranium [20] and was used as crucible [17,20], and scrapper [21] in electrorefiner. However the toxicity and scarcity of the beryllia makes it unsuitable. Asou et al. [52] carried out weight loss studies on candidate materials in molten NaCl–KCl–CsCl–UO₂Cl₂ melt for 6 h at 600-650°C under Cl₂ and O₂ gas. Their study revealed that ZrSiO₄ has good corrosion resistance than pyrolytic graphite. Takeuchi et al. [53] carried out weight loss studies on candidate ceramic materials in molten NaCl–KCl salt under Cl₂ bubbling at 750°C for 24 h. Their study revealed that alumina, beryllia, silicon nitride (Si₃N₄), mullite (Al₆Si₂O₁₃) and cordierite (Mg₂Al₃(AlSi₅O₁₈) showed good corrosion resistance than pyrolytic graphite. Similar corrosion studies in molten salt in the presence of fission product chlorides under Cl₂ and O₂ gas also revealed that silicon nitride, mullite and cordierite showed good corrosion resistance than pyrolytic graphite [53].

Table 1.4. Thermodynamic evaluation of candidate materials with chlorine, oxygen and UO$_2$Cl$_2$ at 650°C [52,53].

Materials		Cl$_2$(g)	O$_2$(g)	UO$_2$Cl$_2$(l) +Cl$_2$(g)	Evaluation
Oxides	Al$_2$O$_3$	X	O	X	X
	SiO$_2$	O	O	O	©
	TiO$_2$	O	O	X	X
	ZrO$_2$	**O**	**O**	**Δ**	**O**
	ZrSiO$_4$	**O**	**O**	**Δ**	**O**
	Y$_2$O$_3$	O	O	X	X
	BeO	O	O	O	©
	MgO	X	O	X	X
	CaO	X	O	X	X
Nitrides	Si$_3$N$_4$	X	X	X	X
	CrN	X	X	X	X
	ZrN	X	X	X	X
	TiN	X	X	X	X
	BN	X	X	X	X
Carbides	SiC	X	X	X	X
	B$_4$C	X	X	X	X
Others	C	O	X	X	X
	W	X	X	X	X

ΔGo > 0: No corrosion reaction occurs, indicated by the symbol "**O**"
ΔGo ~ 0: Some corrosion reactions occur, indicated by the symbol "**Δ** "
ΔGo < 0: Corrosion reactions occur, indicated by the symbol "**X**"
 © Compatible material but not suitable due to other problems like fragility,
     non availability, toxicity etc.,

Table 1.5 summarizes the literature survey on materials for salt purification

system and electrorefiner in pyrochemical reprocessing plant. There is not much literature

on LiCl–KCl melts and limited literature exists on corrosion studies in LiCl–Li$_2$O melts.

It is clear from the table that most of the immersion corrosion studies were conducted on

LiCl–Li$_2$O melts and limited literature exists on corrosion in LiCl–KCl melts. Therefore

immersion corrosion studies were conducted in the present study in molten LiCl–KCl

melts for pyrochemical reprocessing application. In our present study Cr-Mo steels, 316L

stainless steel, Ni, Ni base alloys (Inconel 600, Inconel 625, Inconel 690) were

considered along with ceramic coatings for corrosion studies in molten LiCl–KCl salt.

Table 1.5. Literature survey on materials for salt purification system and electrorefiner in pyrochemical reprocessing plant.

Reference	Materials	Test conditions in molten salt	Results/conclusions
Indacochea et al. [35]	Ferrous alloys (316L SS, 2.25Cr-1Mo steel, 422 SS, 430 SS) and tantalum samples in annealed and as welded condition	Tested in molten LiCl–3.5 wt% Li_2O and 1 wt% Li_3N salt saturated with Li metal at 725°C for 30 days in argon atmosphere.	1. Tantalum and ferrous alloys did not experience corrosion in molten salt at 725°C for 30 days under reducing conditions.
Indacochea et al. [54]	First set: Tantalum, 316L stainless steel, 422 stainless steel, 430 stainless steel, and 2.25Cr–1 Mo steel Second set: 304 stainless steel, 316L stainless steel, Inconel 600, and Inconel 625	Tested in molten LiCl with 3.5 wt.% Li_2O and 1 wt.% Li_3N salt, first set at 750°C for 30 days and second set at 650°C for 6 days under Ar and Ar–10% O_2 atmosphere.	1. None of these materials corroded when tested with pure argon as the cover gas and when a cover gas of Ar + 10% O_2 was used corrosion was found to be extreme even though the test temperature was reduced to 650°C and exposure time was decreased to 6 days. 2. During corrosion oxygen present as gas plays a critical role rather than as oxide. 3. 316L and 304 stainless-steel exhibited similar corrosion resistance 4. 316L SS welded specimen undergone severe corrosion with intergranular attack in the heat-affected zone even though the carbon content in the stainless steel was low. 5. The effect of aluminium coating on 316L SS studied was inconclusive probably due to coating peel off.
Hosoya et al. [55]	Ni-based Superalloy Hastelloy-X and Refractory metals (Ta and W)	Tested in molten $NdCl_3$–NaCl–KCl salt at 500°C–800°C for 60 min.	1. Refractory metals Ta and W exhibited no evidence of attack and revealed glossy surfaces even after immersion test. 2. Tantalum, tungsten and Hastelloy-X exhibited corrosion-resistance in the absence of moisture and oxygen in molten chloride salt.

Reference	Alloys	Test conditions	Findings
Cho et al. [56]	Inconel 713LC, Nimonic 80A and Nimonic 90	Tested in molten LiCl–Li$_2$O salt under Ar–10%O$_2$ atmosphere at 675°C for 72–216 h.	1. Inconel 713LC alloy exhibited the highest corrosion resistance among the alloys tested and the corrosion rate was in the order: Inconel 713LC < Nimonic 80A < Nimonic 90. 2. Nimonic 80A and Nimonic 90 exhibited uniform corrosion behaviour while Inconel 713LC exhibited localised corrosion behaviour. 3. Excess Cr resulted in deleterious effect on corrosion resistance, while Al and Ti enhanced corrosion resistance by forming protective oxide layers.
Cho et al. [57]	Inconel 713LC, Inconel MA 754, Haynes 214 and Haynes HR-160	Tested in molten LiCl–Li$_2$O salt under Ar–10%O$_2$ at 675°C for 72–216 h.	1. Inconel 713LC alloy exhibited the best corrosion resistance among the alloys tested and the corrosion rate was in the order: Inconel 713LC < Inconel MA 754 < Haynes214 < Haynes HR-160. 2. Inconel MA 754 and Haynes 214 exhibited uniform corrosion behaviour while Inconel 713LC exhibited localized corrosion behaviour. Haynes HR-160, exhibited intergranular corrosion.
Cho et al. [58]	Haynes 263, Inconel 718, Nimonic 80A and Incoloy 800H	Tested in molten LiCl–Li$_2$O salt under Ar–10%O$_2$ atmosphere at 650°C for 72 to 216 h.	1. Haynes 263 alloy exhibited the best corrosion resistance among the examined alloys and the corrosion rate was in the order: Haynes 263 < Nimonic 80A < Inconel 718 < Incoloy 800H. 2. Inconel 718, Nimonic 80A and Incoloy 800H exhibited uniform corrosion behaviour while Haynes 263 exhibited localized corrosion behaviour.

Reference	Materials	Test Conditions	Observations
Cho et al. [59]	Haynes 263, Haynes 75, Inconel 718 and Inconel X-750	Tested in molten LiCl–Li$_2$O salt under Ar–10%O$_2$ atmosphere at 650°C for 72 to 216 h.	1. Haynes 263 alloy exhibited the highest corrosion resistance among the examined alloys and the corrosion rate was in the order: Haynes 263 < Haynes 75 < Inconel X-750 < Inconel 718. 2. Inconel 718 and Inconel X-750 exhibited uniform corrosion behaviour while Haynes 263 exhibited localized corrosion behaviour. 3. Corrosion was observed to be delayed due to accumulation of Ni around the inner oxides. 4. Excess Fe resulted in deleterious effect on corrosion resistance.
Burris et al. [20]	Low carbon and Chrome steel	Electro-refiner with LiCl–KCl salt and Cadmium.	1. Low carbon steels are resistant to attack by molten chloride salts and are attractive materials for containers, stirrers, thermowells of electrorefiner. 2. Low carbon steel vessels effectively contained molten salt–cadmium electrolyte and electrode system for electrorefining. 3. The solubility of iron in liquid cadmium at 480°C was 2.8×10^{-4} wt%. 4. Iron cathode used in electro-refining at 550°C with LiCl-KCl-PuCl$_3$ electrolyte resulted in the formation of Pu-Fe eutectic alloy and subsequently dripped from the iron cathode into a tantalum crucible as the eutectic alloy was liquid at the operating temperature.
Takeuchi et al.[53]	SiC, Si$_3$N$_4$, BN, AlN, ZrB$_2$, ZrO$_2$, BeO, Al$_2$O$_3$, Y$_2$O$_3$, Al$_6$Si$_2$O$_{13}$, Mg$_2$Al$_3$(AlSi$_5$O$_{18}$), Pyrographite .	Tested in 2CsCl–NaCl molten salt and vapour phase at 650°C. Total flow rate was 150 ml/min under Cl$_2$+O$_2$ gas.	1. For severe corrosive environment encountered in RIAR process, silicon nitride (Si$_3$N$_4$), mullite (Al$_6$Si$_2$O$_{13}$), and cordierite (Mg$_2$Al$_3$(AlSi$_5$O$_{18}$)) were found to be the promising materials. 2. The corrosion rate of these materials was less than 0.01 mm/y and no cracks were observed after 480 h corrosion test under Cl$_2$+O$_2$ atmosphere.

Reference	Material/Method	Test conditions	Findings
			3. Pyrographite showed high corrosion rate of >0.5 mm/y and revealed severe damage due to the effect of oxygen. 4. The corrosion resistance of Si_3N_4 was reported to be excellent in molten salt with Cl_2, O_2 and fission product chlorides.
Asou et al. [52]	ZrO_2 and ZrO_2–SiO_2 on graphite by plasma spray process. Pyrolytic graphite on high density graphite by CVI for oxide pyroprocess.	Tested in NaCl–KCl–CsCl–UO_2Cl_2 (5 wt% U) for 6 h at 600 and 650°C under $Cl_2 + O_2$ gas.	1. Based on thermodynamic calculations SiO_2, ZrO_2, BeO and ZrO_2–SiO_2 were found to be the promising candidate materials. 2. ZrO_2–SiO_2 was found to be the most promising candidate material compared to pyrolytic graphite. The lifetime of ZrO_2–SiO_2 was found to be three times longer than that of ZrO_2 and pyrolytic graphite. 3. The life time of ZrO_2 was found to be shortest compared to ZrO_2–SiO_2 and pyrolytic graphite.
Cho et al. [60]	Fe–Ni–Cr alloys	Tested in molten LiCl–25 wt% Li_2O at 650°C–850°C for 25 h.	1. Corrosion rate of Fe–Ni–Cr alloys accelerated with addition of Li_2O in the salt and with increasing Cr content in the alloys
Liu et al. [61]	Nickel	Tested in molten LiCl–10 wt% Li_2O at 750°C for 5 to 50 h.	1. Nickel corroded fast by forming porous layer of NiO which is converted to $Li_2Ni_8O_{10}$ and then $LiNiO_2$.
Liu et al. [62]	NiAl–28Cr–5.8Mo-0.2Hf	Tested in molten LiCl–10 wt% Li_2O at 750°C for 10 to 25 h.	1. Cr(Mo) phase in the alloy corroded severely than Ni(Al) β phase.
Periasamy et al. [63]	ZrN and HfN	Tested in 28.5% LiCl–36.3% KCl–29.4% NaCl–5.8% UCl_3 at 525–900°C for 4–485 h.	1. ZrN and HfN experienced weight loss under all experimental conditions due to formation of volatile products and electrochemical dissolution. 2. Formation of Zr–Cl and Hf–Cl volatile products was believed to occur due to reaction of the nitrides with $Cl_2(g)$ or Cl^-, generated due to reaction of UCl_3 species present in the salt with oxygen.

1.4 Status of development of thermal barrier coating

Thermal-barrier coatings (TBCs) are widely used for gas-turbine engines in aerospace industry and power generation industry. Yttria stabilized zirconia (YSZ) coatings ($ZrO_2 - 7-8$ wt% Y_2O_3) with high thermal expansion coefficient and low thermal conductivity is widely used as thermal barrier coating. The stability of YSZ up to 1200^oC was attributed to the metastable tetragonal prime (t') phase present, while higher toughness offered by YSZ was attributed to transformation toughening or ferroelastic domain switching events. TBCs are deposited by air plasma-spraying (APS) or by electron beam physical vapor deposition (EBPVD) [64]. The performance of TBCs depends on the microstructure which varies depending on the coating technique. Conventional APS thermal barrier coating exhibits a layered structure parallel to the coating surface, built up from solidification of individual splats consisting of inter-splat pores and cracks, while EB-PVD coatings exhibit columnar structure with elongated grains perpendicular to the coating surface. Development of advanced TBCs have been focusssed on extending the durability of the coating by adopting novel approaches. The development of dense vertically cracked (DVC) microstructures produced by advanced APS technique, and feathery microstructures with vertical separations produced by EBPVD technique offers excellent coating compliance to thermal cycling thus exhibiting enhanced durability [64]. With the advancement of novel suspension plasma spraying (SPS) enhanced durability compared to conventional APS coatings could be achieved by producing nanostructured coatings [64]. Development of functionally graded material (FGM) is another approach for improving durability by avoiding sharp interface between ceramic top caot and metallic bond coat. The compositionally and/or microstructurally

graded interfaces, in FGM can be more resistant to crack initiation and propagation and are also useful in lowering peak stresses and eliminating stress singularities at certain crack sensitive locations as thermal expansion coefficient and Young's modulus changes gradually in the graded region [65].

1.5 Hot corrosion behaviour of thermal barrier coating

Hot corrosion is an accelerated corrosion resulting from the presence of molten salt deposits and other contaminants on the surface which degrades the protective film. Hot corrosion of TBCs in gas turbine engines are caused by either alkaline sulfate-vanadate mixtures (from environment and fuel) or by silica deposits (from environment - sand, volcanic ash).

Gas turbines operated under saline environment with fuels contaminated with sulphur and vanadium molten salt deposits mainly consisting of alkaline sulfate-vanadate mixtures (Na_2SO_4 and $NaVO_3$) may condense on the TBCs [66]. The stabilisers used in TBCs such as yttria, magnesia and calcia react with sulfur, sodium and vanadium contaminants in gas turbine engines operating under sea atmosphere [67]. The reaction of molten salts especially alkaline sulfate-vanadate mixtures, with TBC could result in de-stabilization of the non-transformable tetragonal phase (t') in YSZ. In YSZ TBC the destabilisation products usually consists of YVO_4 and monoclinic-ZrO_2. The formation of monoclinic-ZrO_2 is detrimental to the durability of the TBC.

The degradation of YSZ TBCs due to molten silicate deposits (fine sand and volcanic ash particulates from the environment) is commonly referred to as CMAS (calcium-magnesium-alumino-silicate) attack as the major component is the silicate glass [68]. The mechanism of attack is by infiltration, dissolution and, upon saturation, re-

precipitation of one or more crystalline phases formed due to interaction between molten silicate glass and YSZ [69]. The approach adopted to mitigate CMAS related damage was by deposition of rare-earth zirconates, such as $Gd_2Zr_2O_7$ (GZO) as the top coat over YSZ [69].

In the present thesis application of TBC to hot corrosion environment encountered in pyrochemical reprocessing of metallic fuel is proposed. The hot corrosion studies of air plasma sprayed YSZ-TBC in molten LiCl-KCl salt towards their potential application was pursued in the present study. An attempt was also made in the present study towards preparation of FGM by plasma spray process in order to improve the durability of the coating.

CHAPTER 2

EXPERIMENTAL DETAILS

2.1 Introduction

The present chapter discusses the experimental details on corrosion testing of candidate materials in molten LiCl–KCl eutectic salt under Cl_2, air and ultra high purity argon atmosphere. This chapter also describes the preparation and characterization of duplex and graded partially stabilized zirconia (PSZ) coating for molten chloride application. Laser remelting of PSZ coating and characterization is then described.

2.2 Materials and Sample Preparation

The nominal chemical composition of the alloys in wt% used in the present study is tabulated in Table 2.1. Inconel samples have been received as long sheet. The electroformed nickel (EF Ni) and EF Ni with Ni-W coating (EF Ni-W) used in the present study was obtained from Central Electrochemical Research Institute (CECRI), Karaikudi. The dimensions of electroformed Ni plate with and without Ni-W coating obtained were 264 × 79 × 3 mm and 262 × 98 × 3 mm, respectively. Similarly Cr-Mo steels and stainless steel plate were obtained from which defect free samples of desired dimensions were cut for corrosion studies in molten LiCl–KCl salt.

2.3 Salt Preparation

The salt used for the corrosion studies was a eutectic salt composed of 44.4 wt% of LiCl and 55.52 wt% of KCl. The LiCl–KCl salt was highly hygroscopic in nature and easily absorbs oxygen and moisture from the atmosphere. In order to remove oxygen and

Table 2.1. Nominal chemical composition of alloys used in the present study in wt%.

Alloy	Ni	Cr	Fe	Mn	Si	Mo	Ti	Ta+Nb
2.25Cr-1Mo	-	2.18	Bal	-	0.18	0.93	-	-
9Cr-1Mo	-	9.27	Bal	0.63	0.75	1.05	-	-
304L SS	10.5	18.5	Bal	1.64	0.8	-	-	-
316L SS	12.1	17.9	Bal	1.76	0.98	2.45	-	-
Inconel 600	72	17	10	1	-	-	-	-
Inconel 625	62	21.5	4.25	-	-	9	-	3.15
Inconel 690	60	29.58	9.05	0.21	0.25	-	0.2	0.02

moisture present in the as-received salt, the salt was purified by chlorination and all the operations with salt were carried out in an inert argon atmosphere glove box. The salt mixture was prepared by mixing and vacuum drying in the oven. The vacuum dried salt was then put in the salt purification chamber and heated above the eutectic temperature ($\sim$350°C). Argon gas was continuously purged through the inlet chamber of salt purification vessel. The argon gas purging process was followed by chlorination process. For chlorination, high purity chlorine gas was purged into the molten salt through the chlorine inlet chamber. The process of chlorination was carried out for about 30 min. The chlorinated salt mixture is then cooled under argon gas. The purified salt was then transferred in to inert argon atmosphere glove box.

2.4   Molten Salt Corrosion Experiments and Characterization

2.4.1 Molten salt corrosion experiment under Cl$_2$ bubbling and characterisation

2.4.1.1 Sample preparation

Ni base alloys are candidate materials for salt purification applications because of the aggressive molten chloride salt and chlorine gas environment. Inconel 600, Inconel 625 and Inconel 690 samples of size 50 × 12 × 5 mm were cut from the plate stock and polished upto 1200 grit emery paper for corrosion testing. Autogenous weld samples of Inconel 600, Inconel 625 and Inconel 690 samples were prepared and subjected to radiography. Radiographic examination (BALTOGRAPH) was carried out for all the welded joints as per ASME SEC III DIV I. Weld samples for corrosion testing were prepared from defect free regions of Inconel autogenous weld pads. Defect free samples from the weldment of size 50 × 12 × 5 mm similar to the base metal were cut from the welded plate and polished for corrosion studies. The samples were cleaned with acetone and dried before corrosion test.

2.4.1.2 Molten salt corrosion experiment

For conducting molten salt corrosion experiment under Cl$_2$ bubbling, chlorination cell was used. The schematic diagram of quartz chlorination cell used for corrosion testing in molten LiCl–KCl salt under Cl$_2$ bubbling is shown in Fig.2.1. Inconel 600 plate sample (base metal) and Inconel 600 weldment sample was fixed to the alumina sleeve sample holder. Vacuum dried LiCl–KCl eutectic salt transferred in to alumina crucible was placed inside the chlorination cell as shown in Figure 2.1. Around 100 g of salt was loaded for each experiment into the cell along with samples and sealed. The sealed cell
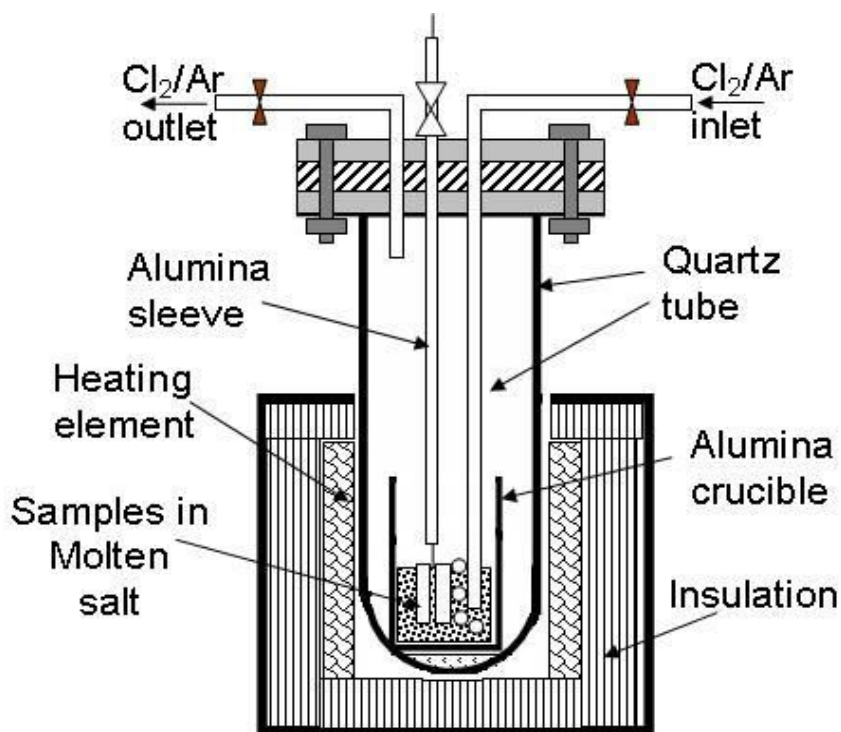
Figure 2.1 Schematic diagram of chlorination cell used for corrosion testing in molten LiCl–KCl salt under Cl₂ bubbling.

was placed in the furnace and heated under argon atmosphere upto 600°C. The complete setup used for conducting molten salt corrosion experiment under Cl_2 bubbling along with chlorination cell is shown in Figure 2.2.

The experimental set up consisting of argon and chlorine gas lines connected to the gas inlet and out let ports of chlorination cell is shown. The argon gas was passed through H_2SO_4 to absorb residual oxygen present in the gas and then chlorine gas was bubbled through molten salt and was passed out through NaOH solution as shown schematically (Fig 2.2). After the desired temperature was reached, the samples were submerged in the molten salt. The samples were lifted/withdrawn from the molten salt after 30 minutes of Cl_2 bubbling at ~500°C. Temperature was monitored during the experiment and the heating and cooling cycles recorded were shown in Figure 2.3.
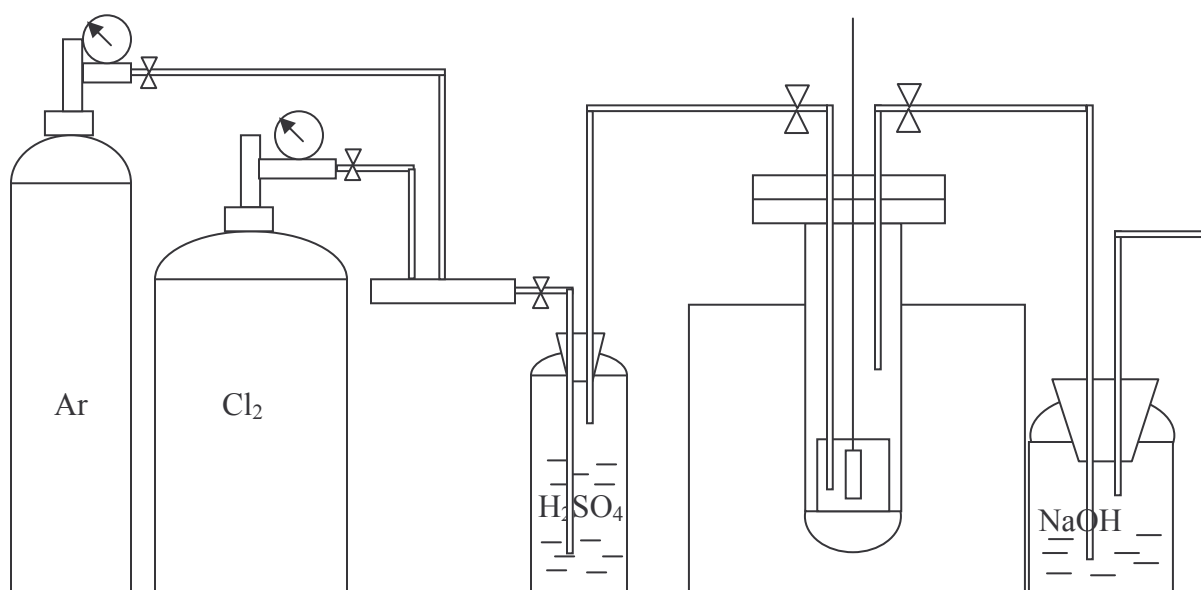
Figure 2.2. Schematic experimental set up for corrosion testing in molten LiCl–KCl salt under Cl₂ bubbling.
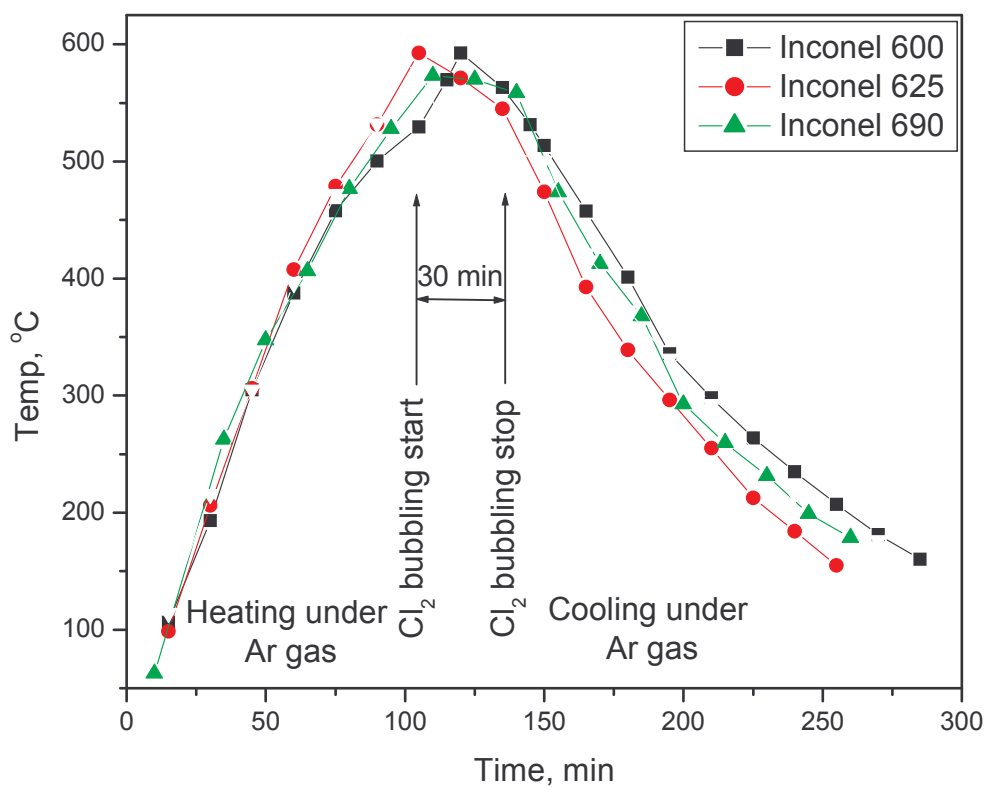
Figure 2.3. Temperature vs time graph of chlorination cycle used for corrosion testing in molten salts under Cl₂ bubbling.

Similarly corrosion experiments were carried out on Inconel 625 and its weld, Inconel 690 and its weld, in molten LiCl–KCl salt under Cl_2 bubbling for 30 minutes. After the corrosion test, samples were removed and cleaned with distilled water and then ultrasonically cleaned with acetone and dried. The weight losses of the samples were noted before and after the corrosion test. The corrosion rates of the exposed samples were then calculated as shown in Equation (1) [70]

Corrosion rate (mm/year) = $(8.76 \times 10^4 \times W) / (A \times D \times t)$ ....Eq. (2.1)

Where:

 t = time of exposure, h,

 A = total surface area, cm^2,

 W = weight loss, g, and

 D = density of the sample, g/cm^3

These experiments under highly toxic and corrosive Cl_2 environment simulate the salt purification process and provide valuable information for material selection and associated corrosion mechanisms involved.

2.4.1.3 Characterisation of samples

The as-received Inconel alloys and their weldments were metallographically prepared and etched to understand the microstructure. The samples were polished up to diamond finish and electrolytically etched with HF-5 ml, glycerol-10 ml, ethanol-20 ml, distilled water-65 ml. The electrolytic etching was done at 11 V for 2 sec. The surface morphology and compositional analysis of corroded surfaces were carried out using ESEM Philips XL-30 scanning electron microscopy (SEM) attached with EDX. GIXRD (Glancing Incidence X-ray Diffraction) was carried out with 2θ step size of 0.1 degree

and with time per step as 7 sec, using STOE diffractometer on the corroded surfaces. Powder Diffraction File-2 was used for the phase analysis of the XRD patterns and PDF-2 codes [71] of the phases observed were provided in square brackets.

2.4.2 Molten salt corrosion experiment under air and characterisation

Corrosion experiments under air environment were carried out to simulate the severe corrosive conditions and/or accidental ingression of oxygen in molten salt environment. Moreover, the mechanism of corrosion of materials in molten LiCl–KCl environment is better understood by exposing the samples to severe corrosive conditions. Therefore EF Ni, EF Ni coated with Ni-W (EF Ni-W), 316L SS and Ni base alloys (Inconel 600, 625 and 690) were tested in molten chloride salt under air environment. The samples of size $25 \times 25 \times 3$ mm were cut and polished on all the faces up to 1200 grit emery paper and then with diamond paste to get a mirror like finish for corrosion testing. Molten salt corrosion test was done for electroformed nickel (EF Ni), 316L SS, Ni base alloys (Inconel 600, Inconel 690, Inconel 625) in polished condition and for EF Ni-W molten salt corrosion test was done in as coated condition without any prior sample preparation on the coated surface. The samples were cleaned with water and acetone before corrosion testing. Around 1.62 g of LiCl–KCl salt was placed on coated surface of the sample, kept in the molten salt furnace and heated to the desired temperature. The schematic diagram of the molten salt furnace used is shown in Figure 2.4. Molten salt corrosion testing was carried out at 400, 500 and 600^{0}C for 2 h in air. During corrosion test, the salt melt can spread and cover the whole surface of the sample forming salt films. After the corrosion test, samples were removed and cleaned with water and then ultrasonically cleaned with acetone, such that the entire loose corrosion product was
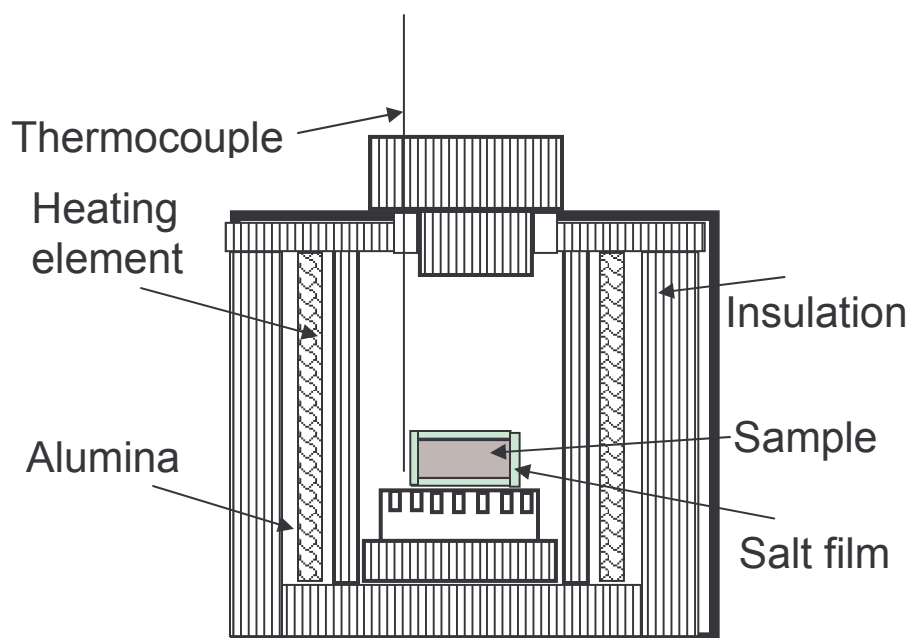
Figure. 2.4. Schematic diagram of the molten salt furnace.

removed. The weight of the samples was noted before and after the corrosion test. Percentage weight loss of the samples was then calculated. The salt films formed over the corroded surfaces were carefully preserved for further characterization. Corrosion tests on Ni base alloys were repeated to check the reproducibility.

The surface morphology and compositional analysis was carried on as received and 600^0C corrosion tested surfaces and salt film surfaces using ESEM Philips XL-30 attached with EDX. Cross section micrographs of the corroded samples and cross section X-ray elemental maps of salt films formed on the samples were also observed in SEM.

GIXRD was carried out with 2θ step size of 0.1 degree and with time per step as 5 sec, using STOE diffractometer for as received and on 600^oC corrosion tested surfaces of 316L SS, Ni base alloys, EF Ni and EF Ni-W and also from their corrosion products (salt film). XRD patterns were obtained from both salt exposed and detached surfaces i.e, top

and bottom surfaces of the salt films. Powder Diffraction File-2 was used for the phase analysis of the XRD patterns and PDF-2 codes [71] of the compounds observed were provided in square brackets.

Surface analysis of salt films formed on EF Ni, 316L SS and Inconel 625 tested at 600°C was carried out by HR 800 (Jobin Yvon) laser Raman spectrometer equipped with 1800 grooves/mm holographic grating. He-Ne laser of 633 nm has been used as an excitation source with approximately 5 μm spot size, and spectral resolution of 4 cm^{-1}. An Ar^{+} laser of 488 nm was used as an excitation source for surface analysis of salt films formed on Inconel 600, Inconel 625 and Inconel 690 tested at 600°C.

2.4.3 Molten salt corrosion experiment under UHP Argon and characterization

In order to carry out molten salt corrosion experiment under UHP argon it is essential to use glove box. The inert argon atmosphere glove box allows storing and handling of LiCl–KCl salt at less than 10 ppm of oxygen and moisture. Figure 2.5 shows the schematic of the complete setup consisting of double modular glove box and molten salt test assembly. The set up consists of a double modular glove box for storage of salt and loading of salt and samples in the cell under Ar atmosphere. Purified (chlorinated) LiCl–KCl eutectic salt as described in section 2.3 was stored under Ar atmosphere in the glove box as the salt is highly hygroscopic in nature. The purified eutectic LiCl (44.48 wt%) and KCl (55.52 wt%) salt was loaded in the alumina crucible along with sample and thermocouple and sealed in a stainless steel cell inside the glove box. Around 500 g of salt is loaded into the cell along with samples and the cell is sealed. The amount of salt loaded is such that samples are covered by a height of 30 mm of molten eutectic LiCl–

KCl salt. The sealed cell is transferred to the molten salt test assembly (MOSTA) and heated under UHP Ar to 600°C. The tests were carried out in a molten salt test assembly, for corrosion testing of samples in molten LiCl–KCl salt with continuous argon purging through out the experiment. The schematic diagram of the furnace used for the corrosion studies is shown in Fig 2.6. The samples are lifted/withdrawn from the molten salt after 25, 100, 250, 500, 1000 and 2000 hrs of exposure. 2.25Cr-1Mo steel, 9Cr-1Mo steel, 316L SS, Inconel 600, Inconel 625, and Inconel 690 samples were tested under similar conditions for various durations. After the corrosion test, samples were removed and cleaned with distilled water and then ultrasonically cleaned with acetone and dried. The weight and dimensions of the samples were noted before and after the corrosion test. The percentage weight loss of the exposed samples was then determined to assess the extent of corrosion. The tested samples were observed by ESEM Philips XL-30 scanning electron microscope (SEM) to observe the changes in surface morphology of the samples. Cross section examination of the samples was carried out by SEM and optical microscope. EDX analysis and x-ray elemental mapping was also carried out at different regions on the corroded sample. GIXRD was carried out on corrosion tested samples with 2θ step size of 0.1 degree and with time per step as 5 sec, using STOE diffractometer. Powder Diffraction File-2 was used for the phase analysis of the XRD patterns and PDF-2 codes [71] of the compounds observed were provided in square brackets.
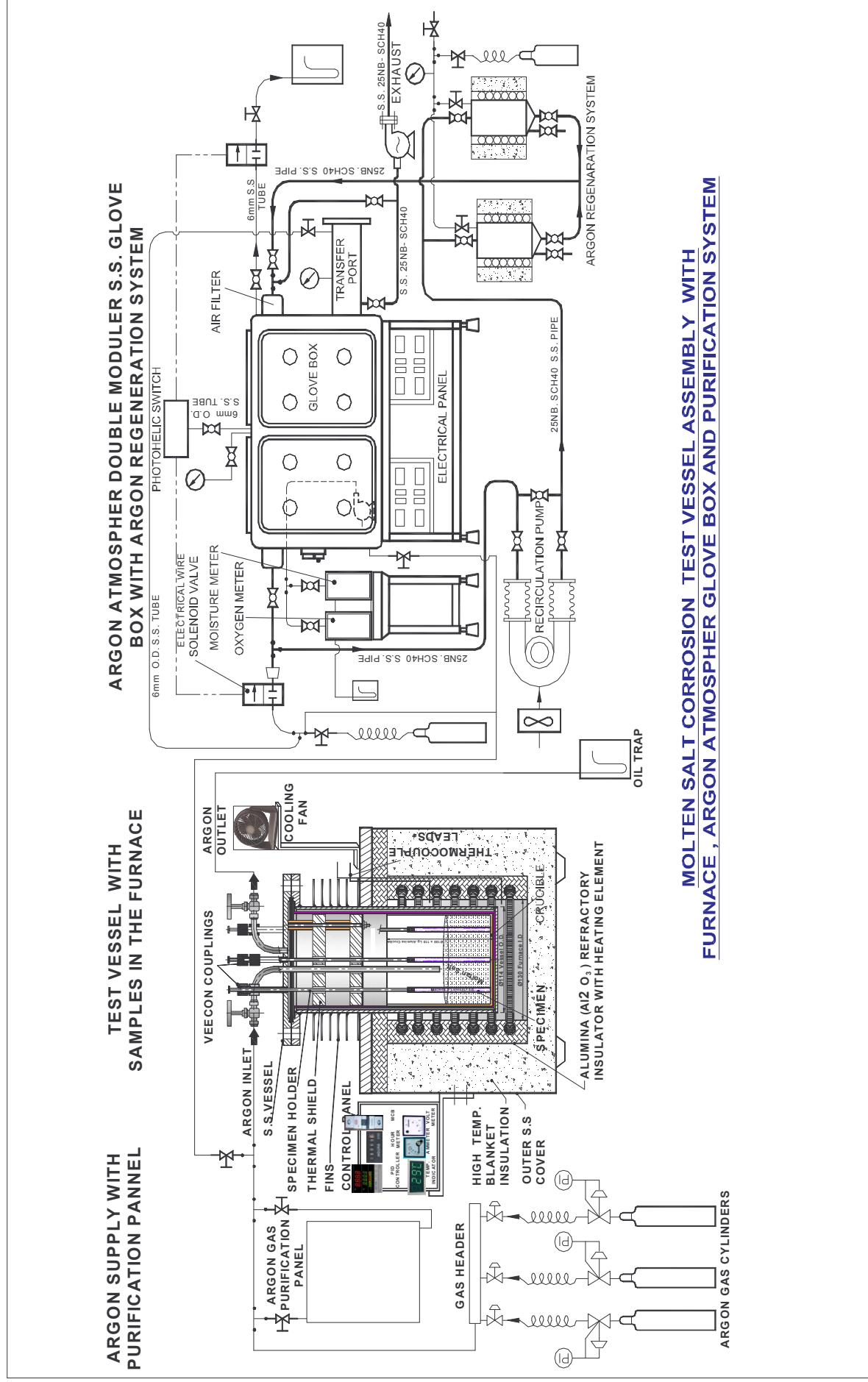
Figure 2.5. Schematic of the complete setup consisting of double modular glove box and molten salt test assembly.

72
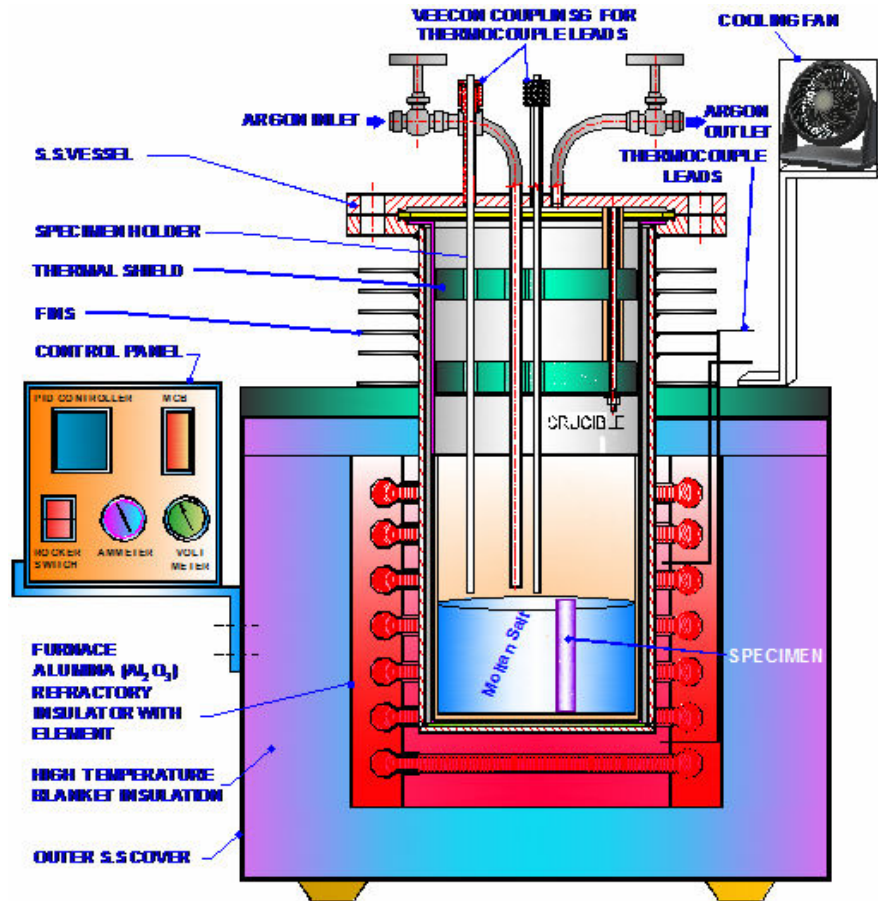
Figure 2.6. Schematic of the corrosion cell in the furnace.

2.5 Preparation of Plasma Spray Coatings (Duplex and Graded)

In plasma spray process molten ceramic or metallic droplets impact the substrate to be coated at high velocities and the deposit solidifies rapidly on impact. The heating is caused by the plasma generated by initiating an electric arc between tungsten cathode and a water-cooled copper anode. The arc ionizes the argon + hydrogen/nitrogen gas, thereby producing plasma and increasing the gas temperature to around 15,000°C. The increase in gas temperature results in an increase in volume and thus a high pressure plasma gas jet exits from the nozzle. The ceramic/metallic powder introduced infront of the nozzle is

73

heated to the molten state and accelerated towards the substrate at high velocities by the high pressure plasma gas jet.

Plasma spray process was used to coat partially stabilised zirconia (ZrO_2 – 8 wt% Y_2O_3) coating with an intermediate bond coat of NiCrAlY on rod samples of 6 mm in diameter $\times$ 100 mm in length. The bond coat applied prior to the top ceramic coat was 50 μm thick whilst the top coat (PSZ) was around 250 μm thick. The intermediate bond coat and partially stabilised zirconia (PSZ) top coat was deposited on 316L SS, 9Cr-1Mo steel and Inconel 625 rod samples. The coated layers were produced by M/s Plasma Spray Processors, Mumbai by using a METCO 9MB type plasma gun. The composition of the ceramic powder used was Y_2O_3 (7-9%) – SiO_2 (1%) – TiO_2 (0.2%) – Al_2O_3 (0.2%) – Fe_2O_3 (0.2%) – ZrO_2 (balance). The particle sizes of bond coat and ceramic coat powders were between 250 $\pm$ 50 μm and 80 $\pm$ 20 μm, respectively. The plasma spray process parameters employed are tabulated in Table 2.2.

2.5.1 Molten salt corrosion testing of PSZ coated samples under UHP Argon and characterisation

Corrosion tests were carried out on PSZ coated samples (2.2Cr-1Mo, 9Cr-1Mo, 304L SS, 316L SS) in molten LiCl–KCl eutectic salt in molten salt test assembly (MOSTA) as described in section 2.4.3. The tests were carried out at a temperature of 600°C for 100 h, 250 h, 500 h, 1000 and 2000 h with continuous argon purging through out the experiment. Percentage weight loss of the exposed samples was then determined to assess the extent of corrosion. The tested samples were examined by ESEM Philips XL-30 scanning electron microscope (SEM) to observe the changes in surface

morphology of the samples. Cross section examination of the samples was carried out by SEM and optical microscope to observe the penetration of salt and coating integrity.

2.5.2 Optimisation of coating parameters and characterization

Conventional duplex coating consists of 250 μm thick PSZ top ceramic coat with an intermediate NiCrAlY metallic bond coat (BC) of 50 μm thick, as described in section 2.5, with a sharp interface. Graded coating on the other hand comprises of gradation in PSZ top ceramic coat and NiCrAlY metallic bond coat with gradual variation. In order to prepare graded coatings Inconel 625 samples of size $20 \times 20 \times 6$ mm polished up to 600 grit emery paper were used. Commercially available PSZ powder, CoNiCrAlY powder and NiCrAlY powder were used as starting powders. For graded coating, the commercial powders (PSZ:CoNiCrAlY/ NiCrAlY) in the ratio of 25:75, 50:50 and 75:25 by weight were blended for 30 min. Inconel 625 samples were grit blasted prior to plasma spraying. The plasma spray was carried out using a 40 kW Metco 9MB plasma gun. Atmospheric plasma spraying (APS) using CoNiCrAlY/NiCrAlY powder, premixed powders and yttria stabilized (8 mol% Y_2O_3) zirconia (PSZ) powder was carried out on the substrates. The parameters employed for depositing duplex and three different functionally graded coatings (FGM1, FGM2 & FGM3) are tabulated in Table 2.2. For FGM1 & FGM2 coating CoNiCrAlY was used as bond coat while for FGM3 coating NiCrAlY was used. The cross section samples for optical and SEM examinations were prepared by mounting the coated samples and polishing up to diamond finish. The metallographic preparation of plasma sprayed samples was carried out as per ASTM standard E 1920-03 [72] to avoid pull out of particles. Cross section microstructures of the coated samples were examined using optical microscope (Leica make, model DMILM, Germany) and scanning electron

microscope (ESEM, Philip XL – 30 & FE-SEM, FEI Quanta 200F) attached with EDX. Microhardness tester (SHIMADZU make, model HMV-2) was used to determine the hardness of the phases observed. X-ray diffraction (XRD) studies were carried out using a Philips X'pert MPD system (40 kV, 30 mA, Cu Kα_1 radiation at 1.54056 Å) to identify the phases present. A 2θ scanning rate of 0.05º s^{-1} was used to determine the peak positions of the phases in the range of 20º<2θ<80º.

Molten salt corrosion tests were carried out on duplex and graded (FGM3) PSZ coating over Inconel 625 in molten LiCl-KCl eutectic salt under UHP argon atmosphere in molten salt test assembly (MOSTA) as described in section 2.4.3. The corrosion tests were carried out at 600°C for 100 h, 250 h, 500 h, 1000 and 2000 h. In order to determine the adhesion strength of duplex and graded (FGM3) coating, samples of size 25.4 mm dia × 38.1 mm long were prepared as per ASTM C 633–01 [73]. Adhesion testing was done on three sets of samples and average adhesion strength was determined. Thermal cycling studies was conducted on two sets of samples up to 250 cycles on duplex and graded (FGM3) coating at 750°C, holding for 10 min followed by forced air cooling to ambient temperature for 10 min. Weight loss of the samples was measured after every 10 cycles and average percentage weight loss was determined.

Table 2.2. Plasma spray parameters employed for duplex and graded PSZ coating on Inconel 625.

Coating	Composition, wt%	Thickness, μm	Voltage, V	Current, A	Powder feed rate, g/min	carrier gas flow rate, l/min	Hydrogen flow rate, l/min	Spray distance, mm
PSZ	100% PSZ	300	50-60	450	35-40	37-40	10-15	75-100
FGM1	100% BC	50	42-43	450	35-40	37	5-7	100
	75% BC + 25% PSZ	75	42-43	450	35-40	37	10-15	100
	50% BC + 50% PSZ	75	42-43	450	35-40	37	10-15	100
	25% BC + 75% PSZ	75	42-43	450	35-40	37	10-15	100
	100% PSZ	75	50-60	450	35-40	37	10-15	100
FGM2	100% BC	50	42-43	450	50	37	5	100
	75% BC + 25% PSZ	75	42-43	450	30	40	7	120
	50% BC + 50% PSZ	75	42-43	450	30	40	7	120
	25% BC + 75% PSZ	75	42-43	450	30	40	7	120
	100% PSZ	75	50-60	450	30	40	10-15	100
FGM3	100% BC	50	42-43	450	50	37	5	100
	75% BC + 25% PSZ	75	42-43	450	30	40	5	120
	50% BC + 50% PSZ	75	42-43	450	40	40	7	120
	25% BC + 75% PSZ	75	42-43	450	40	40	10	120
	100% PSZ	75	42-43	450	40	37	10-15	100

2.6 Laser Remelting of Plasma Spray Coatings and Characterisation

2.6.1 Laser re-melting

Lasers have been used for the modification of materials surface. Lasers can deliver high energy density to a localized surface area without significantly heating up the substrate. Plasma sprayed PSZ coatings of 250 μm thick were coated with an intermediate NiCrAlY bond coat of 50 μm thick over AISI type 316L SS samples of size 25 × 15 × 5 mm. The coated layers were produced using a METCO 3MB type plasma gun with optimized spray parameters. Laser surface modification of PSZ coatings were carried out using a continuous wave (CW) CO_2 laser. The schematic diagram of 500 W multi beam CW CO_2 laser system used in the present study is shown in Fig. 2.7. The laser system characteristics and processing parameters employed are tabulated in Table 2.3. The plasma sprayed samples were re-melted with different scan speeds of 1, 2.5 and 5 mm/s, at 50 W power, scanned over an area of 10 mm × 15 mm.

2.6.2 Sealing and laser remelting

Some of the as-sprayed PSZ coatings were given an overlay of ZrO_2, $ZrO_2 + SiO_2$ and then laser treated in order to alter the surface composition and crack density. Laser re-melting was done on the overlay samples with a scan speed of 5 mm/s and 50W power. The laser treated PSZ coatings with segmented cracks was also given an overlay of ZrO_2 and then heat treated at $800^{o}C$ for 12 hours in order to seal the segmented cracks.

78
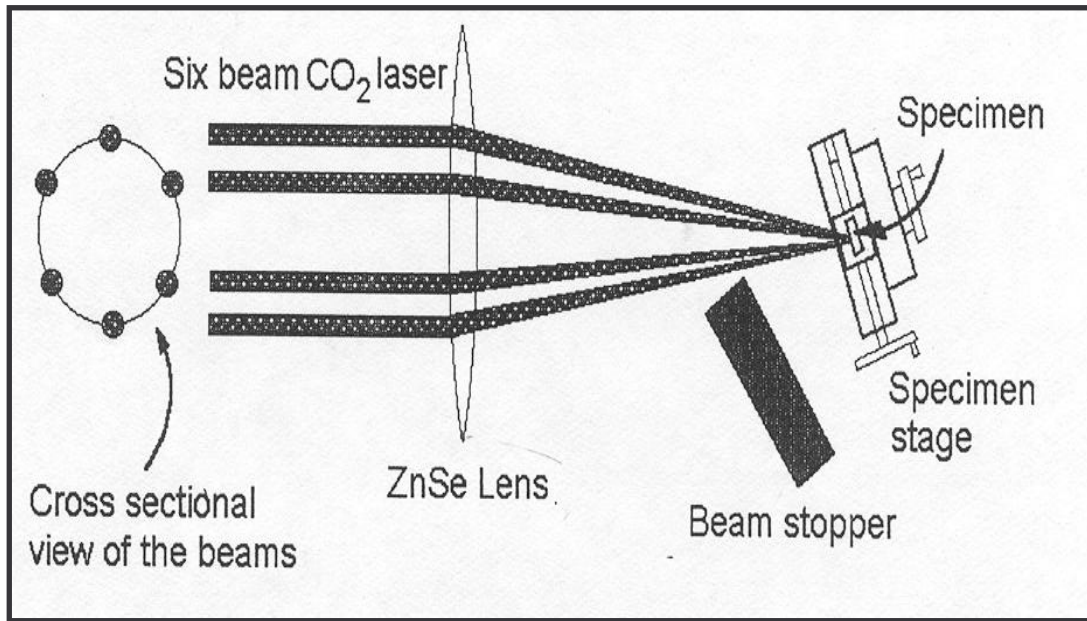
Figure 2.7. Schematic diagram of 500 W multi beam CW CO$_2$ laser system.

Table 2.3 Laser system characteristics and processing parameters.

Laser Parameters	
Power (W)	500
Energy density (Wcm^{-2})	10^4 - 10^5
Focal length (mm)	210
Wave type	Continuous
TEM mode	00
Processing parameters	
Power (W)	50
Beam diameter (mm)	1.5
Scan speed (mm/sec)	1, 2.5, 5
Interaction time (sec)	1.5, 0.6, 0.3
Track shift (mm)	0.5
Shield gas	Argon

2.6.3 Silica deposition

Silica was deposited over as-sprayed PSZ coating using CO_2 laser to achieve dense coatings. The schematic diagram of 3.5 kW CO_2 laser at RRCAT, Indore used for laser deposition is shown in Fig. 2.8. Silica powder was applied on the surface of the specimen with polyvenyl alcohol as binder and subsequenly dried and then melted with CO_2 laser. The laser is operated in pulse modulated mode for silica deposition process. The laser parameters employed are peak power- 700 W, base power- 350 W, frequency- 300 Hz, scan rate-1500 mm/min, width of laser glazed track- 3 – 3.5 mm, and shift between two successive laser tracks- 1.5 mm.
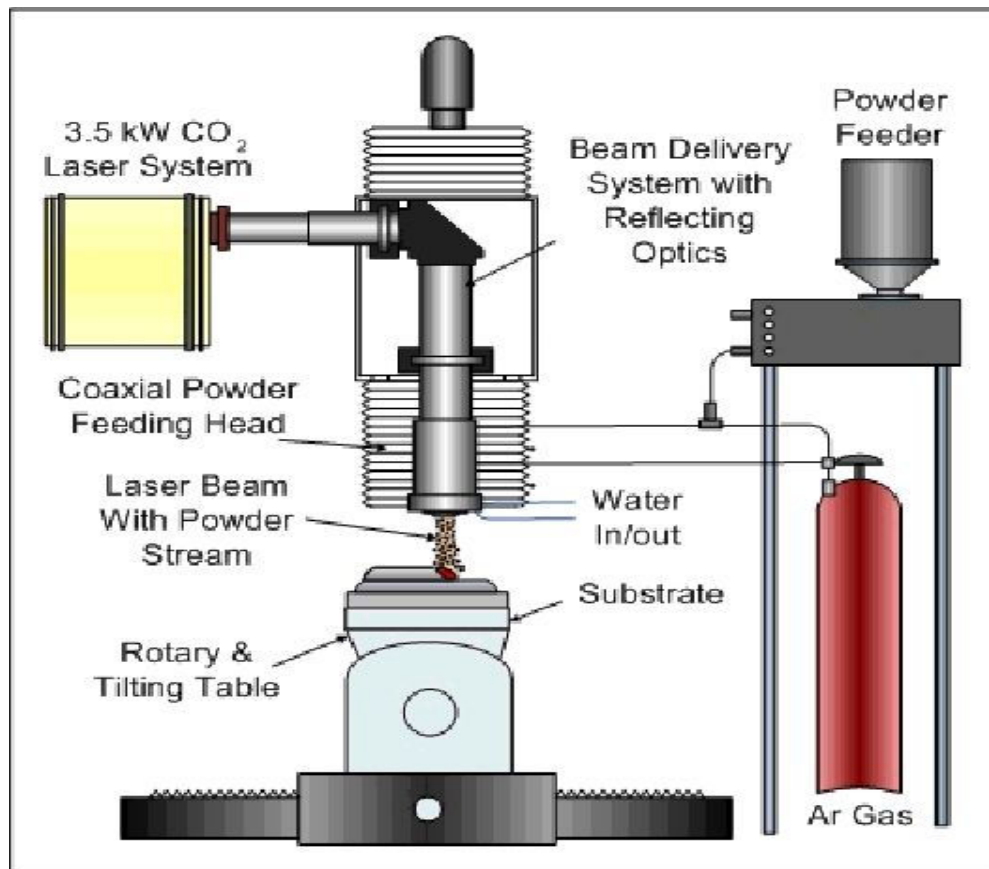
Figure 2.8. Schematic diagram of 3.5 kW CO_2 laser system.

2.6.4 Coating characterization

The surface morphologies of the laser re-melted samples were examined by optical and Scanning Electron Microscopy (SEM) (ESEM Philips XL-30), to observe changes in surface morphology. The samples for cross section studies were mounted using a cold curing resin material such as araldite and hardener at room temperature. The mounted samples were cut using a diamond saw in an oil medium. The samples were polished following metallographic techniques as per ASTM standard E 1920-03 [72]. After polishing the surfaces were cleaned with acetone and then the samples were examined using optical microscopy.

X-ray diffraction (XRD) studies were carried out using a Philips X'pert MPD system (40 kV, 30 mA, Cu Kα_1 radiation at 154.056 pm) to examine the phases present before and after laser re-melting. A 2θ scanning rate of $0.05°$ s^{-1} was used to determine the peak positions of the phases in the range of $20°<2\theta<80°$. Micro-hardness tester (SHIMADZU make, model HMV-2) was used to analyze the micro-hardness in the as-coated and laser re-melted regions. The micro-hardness measurements were made along the cross section and on re-melted surface using 100 g load.

CHAPTER 3

CORROSION OF MATERIALS IN MOLTEN LiCl-KCl SALT IN Cl₂, AIR and UHP ARGON ATMOSPHERE

3.1 CORROSION IN MOLTEN SALT UNDER Cl₂

As discussed earlier in section 1.1.1, salt purification process involves highly corrosive molten LiCl–KCl eutectic salt under chlorine gas environment. Materials for salt purification system used should have good corrosion resistance, such that it will form a nonsoluble film in the melt to avoid contamination of the salt. It has been widely accepted that Ni-rich alloys suffer from less attack in chlorine-containing environments than carbon steels and stainless steel [74]. It has been postulated that nickel base alloys are more resistant than steels because partial pressure of nickel chloride is significantly lower than partial pressure of iron chlorides and the Gibbs free energy change of $NiCl_2$ formation is less negative than that of $FeCl_2$ formation [39]. Corrosion studies carried out on various ceramic materials in molten $NaCl–KCl–CsCl–UO_2Cl_2$ salt at 600^oC and 700^oC under O_2 and Cl_2 gases showed that the corrosion rate of $ZrO_2–SiO_2$ is less than that of pyrolytic graphite [52]. Similarly Takeuchi et al. [53] showed that Si_3N_4, $Al_6Si_2O_{13}$ and $Mg_2A_{l3}(AlSi_5O_{18})$ exhibit good corrosion resistance than pyro graphite in molten NaCl-KCl salt under Cl_2 bubbling at 750^oC for 24 h. Limited literature exists on corrosion of alloys, ceramics and graphite in molten chloride salt under Cl_2 bubbling. For the engineering scale salt purification system at Radio Chemistry Lab, IGCAR, Inconel 600 was used for the fabrication of outer vessel with high density graphite as an inner liner. Therefore candidate materials Ni base alloys like Inconel 600, Inconel 625 and Inconel

690 and its welds were evaluated in molten LiCl–KCl eutectic salt at ~500°C under Cl_2 bubbling.

3.1.1 Optical microstructure

The optical microstructures of Inconel 600 base metal and its weld are shown in Figures 3.1a-d respectively. The microstructure of Inconel 600 base metal showed well delineated grain boundaries with equiaxed grains (Figure 3.1a) and carbide precipitation along the grain boundaries. The fusion line microstructure of Inconel 600 weld is shown in Figure 3.1b. The weld microstructure clearly shows columnar grains growing towards the centre of the weld. The coarse grained heat affected zone (HAZ) adjacent to the weld region is clearly depicted in Figure 3.1c. The magnified view of the weld microstructure containing columnar grains growing towards the centre of the weld is shown in Figure 3.1d revealing cellular dendritic structure.
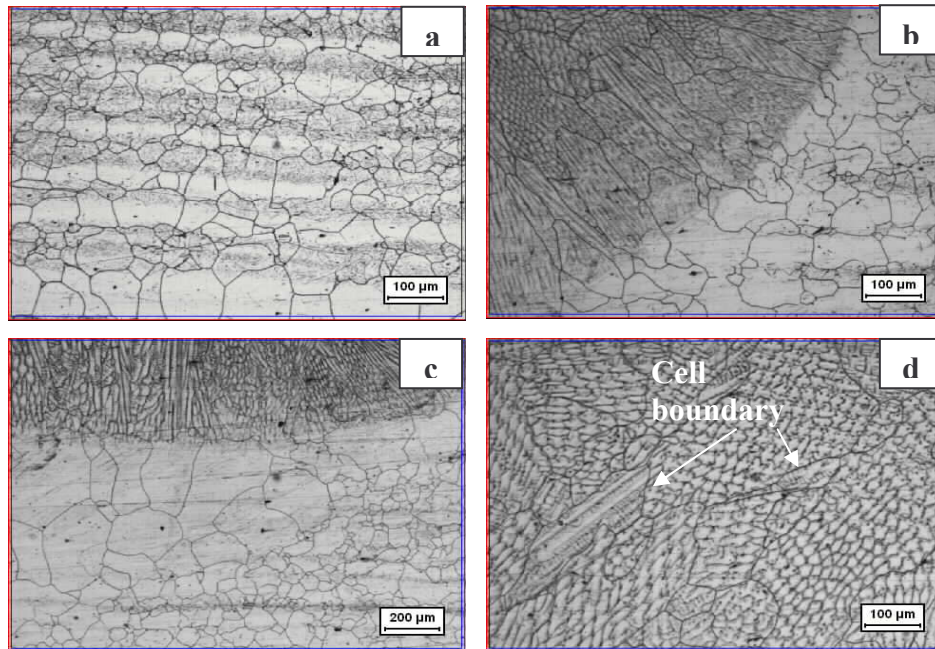
Figure 3.1. Optical microstructures of Inconel 600 (a) base metal (b) fusion line (c) HAZ and (d) weld region.

The optical microstructures of Inconel 625 base metal and its weld are shown in Figures 3.2a-d respectively. The presence of twins was more predominant in Inconel 625 (Figure 3.2a). The base metal region adjacent to the weld has undergone coarsening as shown in Figure 3.2b. The fusion line microstructure and weld region microstructure, consisting of dendritic structure as shown in Figure 3.2c and 3.2d respectively. Dendritic structure with primary axis in the solidification direction is clearly shown in Figure 3.2d.

The optical microstructures of Inconel 690 base metal and its weld are shown in Figures 3.3a-c respectively. Inconel 690 base metal has exhibited a fine grain structure compared to Inconel 600 and Inconel 625. The microstructure of Inconel 690 also
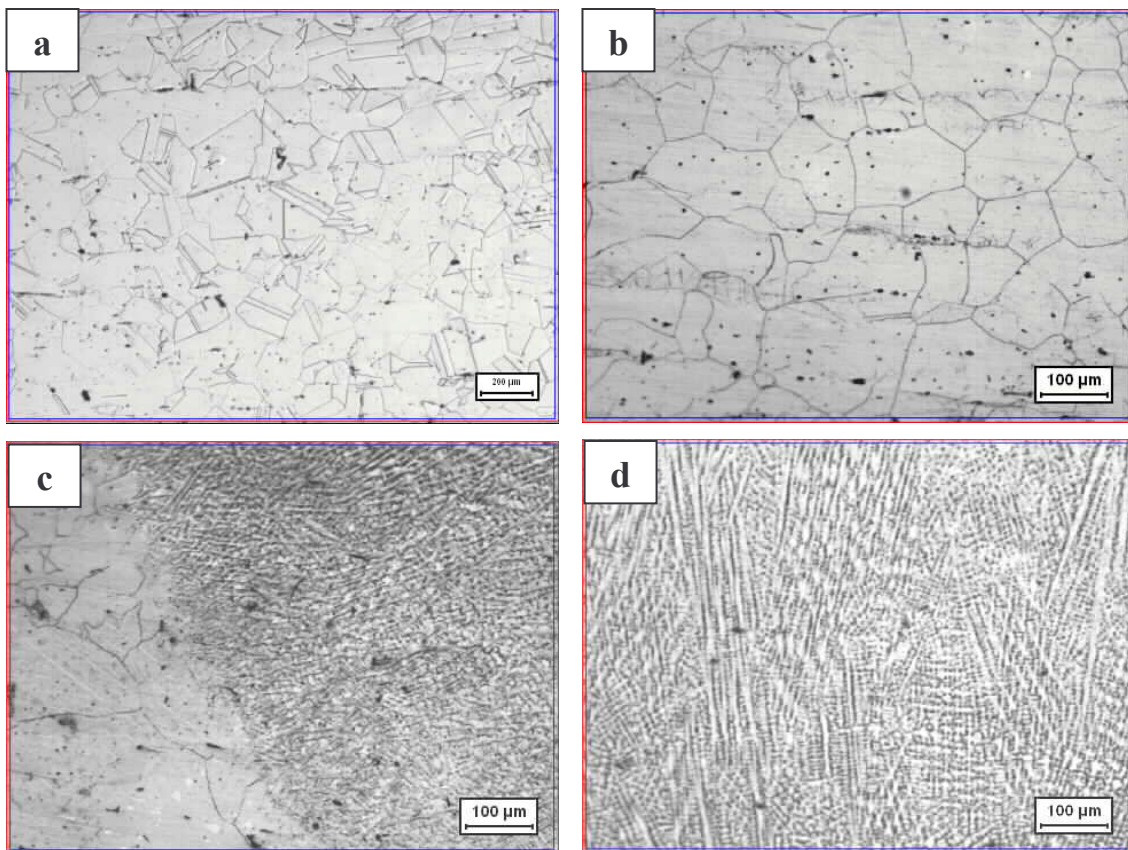
Figure 3.2. Optical microstructures of Inconel 625 (a) base metal (b) adjacent to base metal (c) fusion line and (d) weld region.

showed well delineated grain boundaries with equiaxed grains. The high magnification

SEM micrograph of Inconel 690 base metal (Fig 3.3b) revealed Ti rich precipitates and

fine chromium rich precipitates (carbides) along grain boundaries. The HAZ adjacent to

the weld region consisting of coarse grains is clearly shown in Figure 3.3b. The weld

region of Inconel 690 exhibited cellular dendritic structure with cell boundaries in wavy

form which could be due to presence of fine precipitates along grain boundaries

hindering the growth.
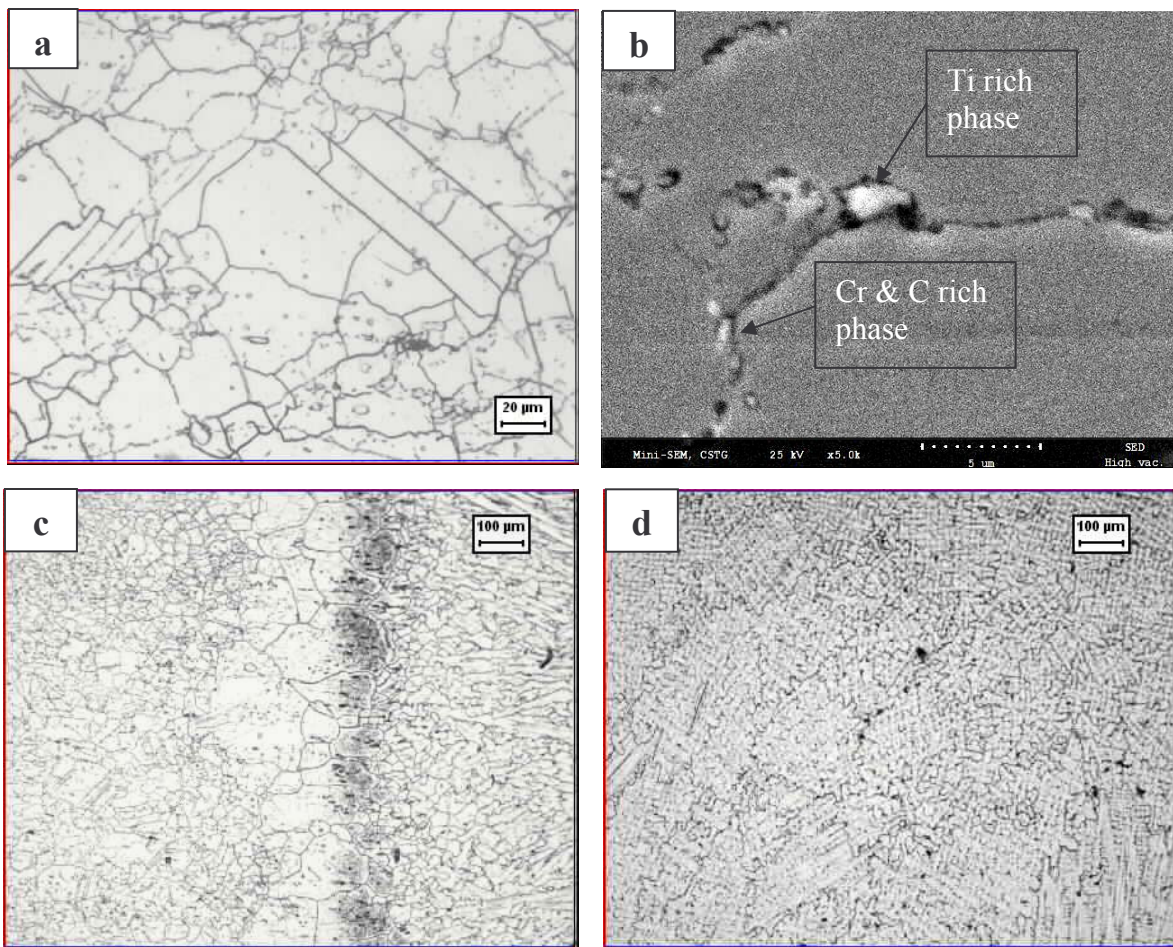
Figure 3.3. Optical microstructures of Inconel 690 (a) base metal, (c) HAZ, (d) weld

region, (b) high magnification SEM micrograph of Inconel 690 base metal.

3.1.2 Corrosion of Inconel 600, 625, 690 and its welds

3.1.2.1 Corrosion rate

The corrosion rate of Inconel 600, Inconel 625 and Inconel 690 and its welds exposed to molten LiCl–KCl salt at 500^oC for 30 min under Cl_2 bubbling is shown in Figure 3.4. The corrosion rate results indicated that Inconel 690 is better than Inconel 600 and Inconel 625. Corrosion rate of Inconel 600, 625 and 690 samples were found to be 1.32, 2.54, 0.99 mm yr^{-1} respectively while Inconel 600, 625 and 690 welds exhibited corrosion rates of 1.36, 2.90, 0.90 mm yr^{-1} respectively. Inconel 625 showed the highest corrosion rate compared to Inconel 600 and Inconel 690. Inconel 625 weldment exhibited marginally higher corrosion rate compared to base metal. Indacochea et al. [54] reported that Inconel 625 performed poorly and had a serious reduction in mass, one-half of its original weight, and a significant decrease in thickness when tested in LiCl–3.5 wt% Li_2O at 650^oC in argon + 10% oxygen atmosphere. The poor performance of Inconel 625 was attributed by Indacochea et al. [54] as a consequence of molybdenum and chromium present. The catastrophic attack induced by molybdenum in Fe and Ni base alloys during hot corrosion has been reported [75]. In another study nickel molybdate (or tungstate) was identified in the scale and this induced formation of a highly friable and porous scale which was reported to be responsible for the enhancement in attack [76]. The mechanism postulated for this type of attack consists of the formation of a layer of MoO_2 at the scale-alloy interface, which is oxidized to liquid MoO_3 with subsequent cracking of the scale [75]. The accelerated attack of Inconel 625 in molten LiCl–KCl salt in the presence of Cl_2 observed in the present study could also be attributed to the presence of Mo.
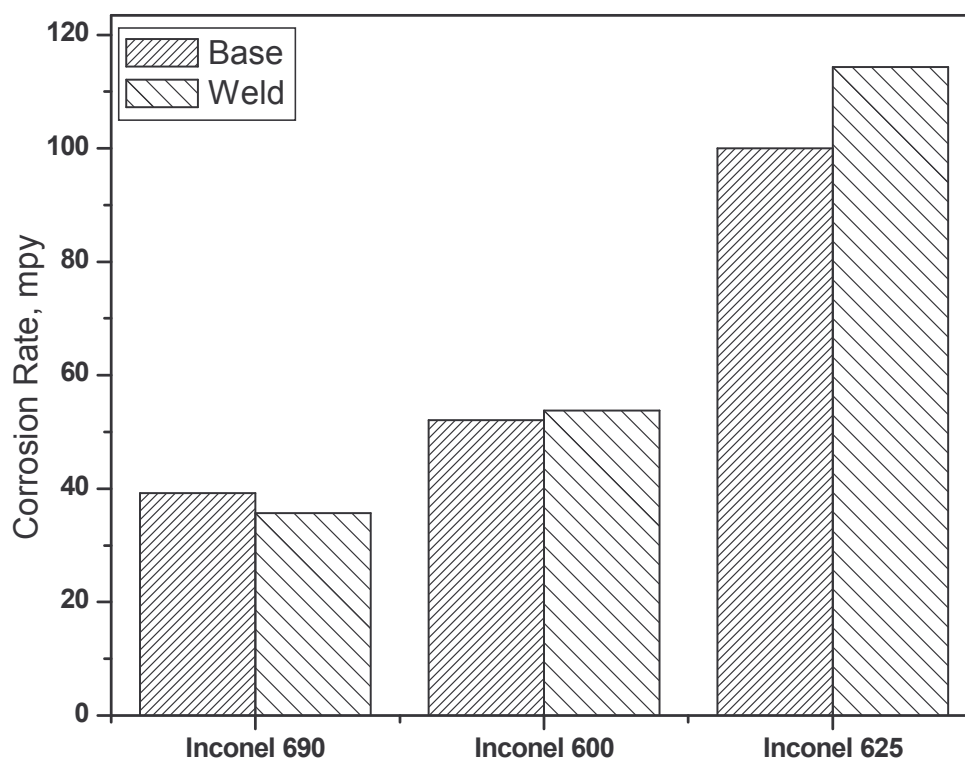
Figure 3.4. Corrosion rate of various grades of Inconel alloys and its welds exposed to molten LiCl–KCl salt at 500°C for 30 min under Cl$_2$ bubbling.

3.1.2.2 Surface morphology and cross section studies of corroded surfaces

The surface morphology of Inconel 600, Inconel 625 and Inconel 690 samples exposed to molten LiCl–KCl salt under Cl$_2$ bubbling are shown in Figures 3.5a-c respectively. The surface morphology of Inconel 600 and Inconel 625 exhibited dense and porous regions while the surface morphology of Inconel 690 exhibited more or less uniform attack. EDX measurements were made from the regions indicated in the micrographs and the results were tabulated in Table 3.1. As shown in the table the chemical composition of Inconel 600 from regions A and B of fig 3.5a were similar. Similarly Inconel 690 also did not indicate marked difference in regions A and B of fig 3.5c. The composition of Inconel 600 and Inconel 690 were not much different from the

base metal composition. Inconel 625 also exhibited similar chemical composition in regions A, B and C of fig 3.5b. However a slight enrichment of Mo was observed on the corroded regions as compared to the base metal composition. From these results it was evident that there was no marked difference in the chemical composition at various regions for the samples exposed to molten LiCl-KCl salt under Cl_2 bubbling. This indicates that there is no thick scale formation and preferential enrichment or depletion of elements on the surface. This is contrary to the corrosion behaviour of 316L stainless steel and Ni base alloys tested in molten LiCl–KCl salt in air and argon environment which are discussed in section 3.2.3, 3.2.4, 3.2.5, 3.3.2 & 3.3.3, where distinct scales on the surface were observed with enrichment of Cr on the surface.
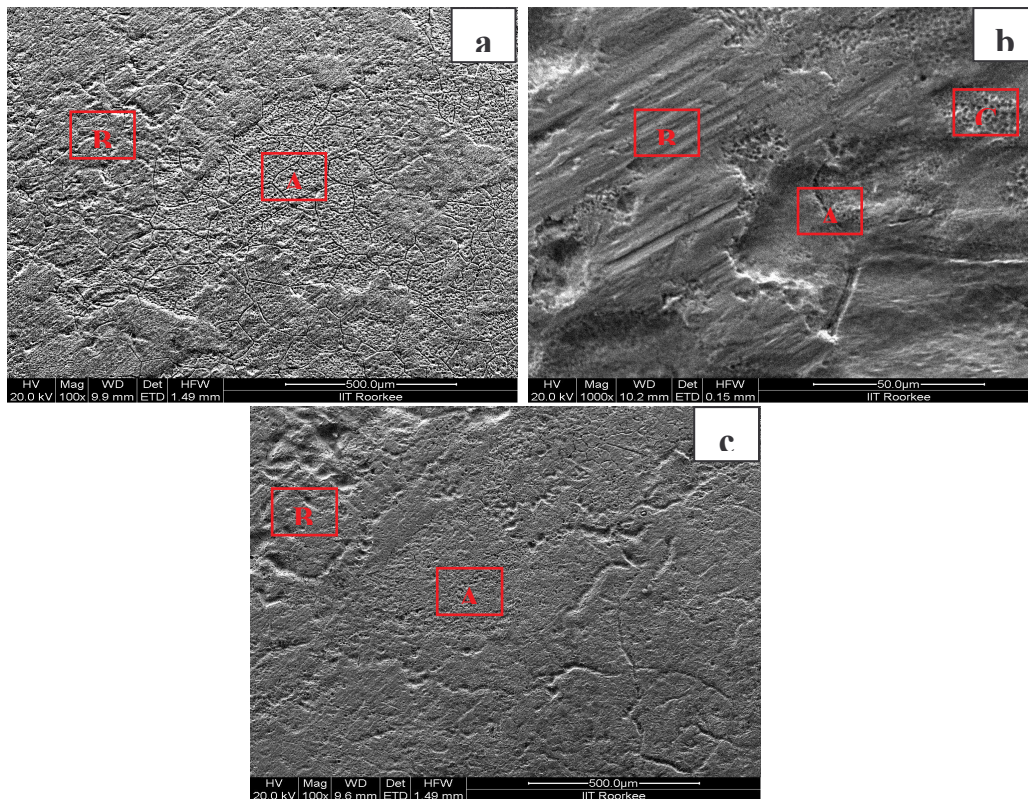
Figure 3.5. Surface morphology of (a) Inconel 600 (b) Inconel 625 and (c) Inconel 690 exposed to molten LiCl–KCl salt at 500°C for 30 min under Cl_2 bubbling.

Table 3.1. Chemical composition (in wt% by EDX) from regions shown in Fig 3.5 of various grades of Inconel alloys after corrosion test.

Material		Ni	Cr	Fe	Mn	Si	Al	Mo	Ta	O	Cl
Inconel 600	A	70.97	15.43	08.77	0.25	1.35	-	-	-	3.22	-
	B	70.22	15.98	08.37	0.53	1.03	-	-	-	3.87	-
Inconel 625	A	52.98	18.49	04.16	0.79	0.88	00.71	12.59	04.81	4.01	0.59
	B	51.33	18.41	03.68	0.52	1.17	00.78	14.22	03.72	4.42	1.76
	C	55.98	19.56	04.29	1.07	-	-	9.82	05.69	3.31	0.29
Inconel 690	A	61.24	28.34	02.67	-	0.14	03.53	-	-	4.07	-
	B	58.55	26.43	04.87	0.98	0.65	03.98	-	-	4.29	-

These results suggest that the mechanism of degradation of Ni base alloys in molten LiCl–KCl salt under chlorine gas is different from that in air and argon environment. The films formed on the surface of Ni base alloys are soluble in molten salt under Cl_2 bubbling which resulted in much accelerated corrosion.

High temperature corrosion in molten salts results in selective attack with dissolution and internal oxidation leading to scale formation. Local corrosion behaviour was reported for Inconel 713LC and Nimonic 80A, Nimonic 90 was reported to exhibit uniform corrosion behaviour in molten LiCl–Li_2O salt [56]. Selective attack of Inconel 600 was observed in molten chloride melts and it is reported that the resulting attacked region consisted of layers of porous, sponge like morphology with disconnected pores located along grain boundaries [77]. The high resolution SEM micrographs of Inconel 600, Inconel 625 and Inconel 690 exposed to molten LiCl–KCl salt under Cl_2 bubbling are shown in Figures 3.6a-f respectively. The surface morphology of corroded Inconel

600 surface (Figure 3.6a and 3.6b) clearly revealed intergranular corrosion and preferential dissolution of precipitates with in the grain. Similarly the surface morphology of corroded Inconel 625 surface also exhibited intergranular corrosion (Figure 3.6c and 3.6d). The surface morphology of Inconel 690 (Figure 3.6e and 3.6f) on the other hand did not show any such localized attack. The surface morphology of Inconel 600 shown in Figure 3.6a revealed selective dissolution of twin boundaries and predominant attack on twin boundaries was observed on Inconel 625 as shown in Figure 3.6d apart from intergranular corrosion. Inconel 690 exhibited a porous morphology in contrast to other Ni base alloys as shown in Figure 3.6e and 3.6f. The localized intergranular attack and attack along twin boundaries could be attributed to the presence of Cr depleted regions around the carbide precipitates formed along these boundaries which make these regions more anodic compared to the matrix. The preferential dissolution of precipitates also indicates that the depleted regions around these precipitates act as anodic sites compared to the matrix and undergoes preferential dissolution. The preferential dissolution of precipitates observed could also be due to preferentially attack of precipitates/carbides leading to the formation of volatile species.

A schematic illustration of mechanism of attack at high temperatures in oxidizing/chloridizing environments as reported is shown in Fig 3.7 [78]. As shown in the figure the carbides at grain boundaries may get preferentially attacked leading to the formation of volatile metal chlorides and gaseous CO_2 [78]. It is reported that intergranular attack of alloys in molten salt occurred along grain boundaries and lowering carbon content and decreasing grain size resulted in improvement [41]. Inconel 690 with lesser carbon content compared to Inconel 600 and Inconel 625 (Table 2.1) has lesser
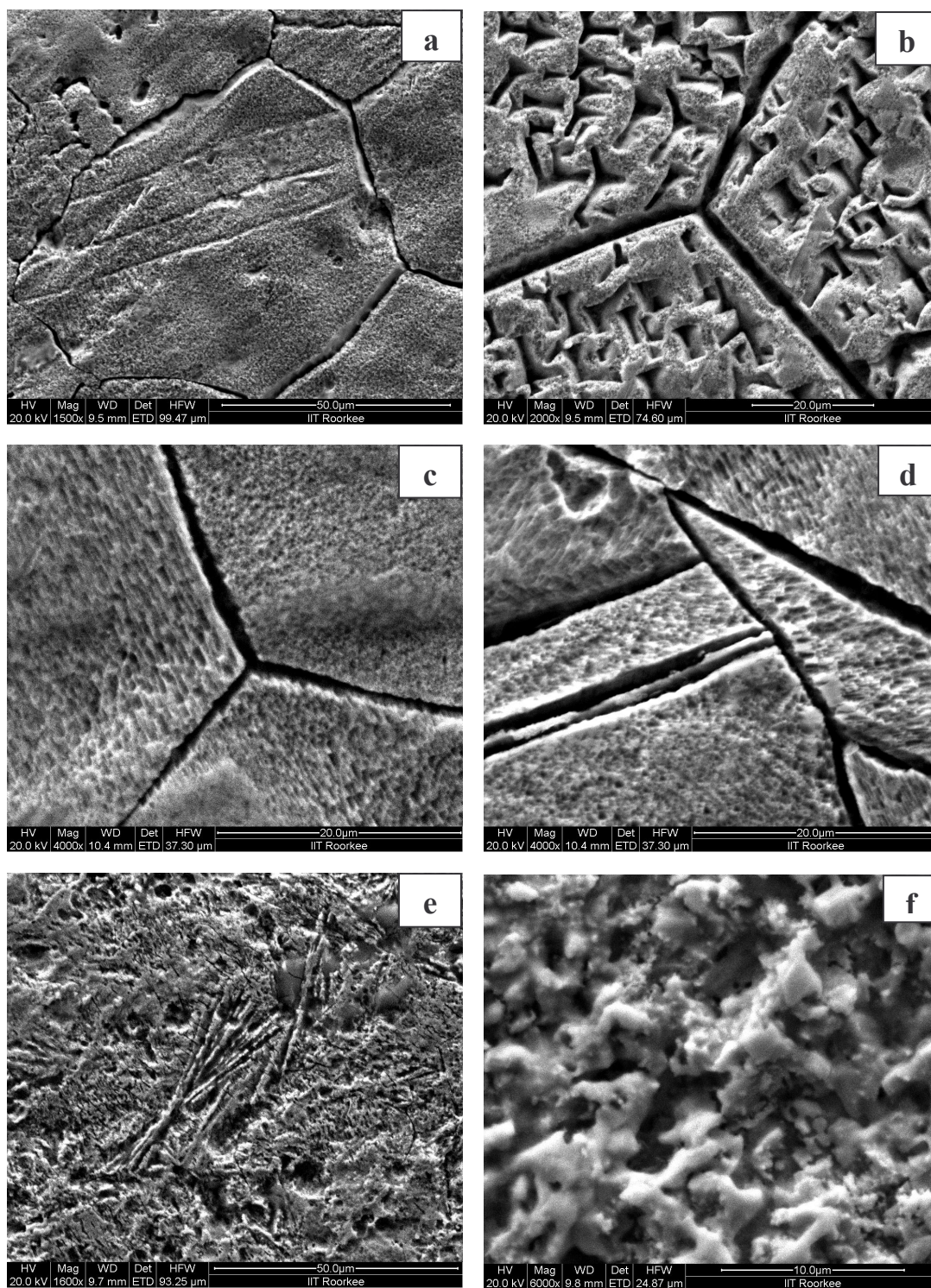
Figure 3.6. Surface morphology of (a & b) Inconel 600 (c & d) Inconel 625 and (e & f) Inconel 690 exposed to molten LiCl–KCl salt under Cl₂ bubbling.

carbide precipitation and thus lesser localized corrosion along grain boundaries and twin boundaries. From the carbides at grain boundaries $CrCl_2$ could be formed and this volatile $CrCl_2$ would be oxidized and results in the precipitation of Cr_2O_3 under Cl_2 and O_2 atmosphere [78]. In case of high Mo containing alloys, the formation of oxychlorides is particularly detrimental in oxidizing-chloridizing atmospheres [79]. Bender and Schutze [78] suggested that in order to keep corrosion rates low where formation of volatile metal chlorides takes place, the vapor pressure of the chlorides in the environments should not exceed a critical value of 10^{-4} bar. Therefore Ni base alloy with lesser carbon content and molybdenum content are preferable for molten LiCl–KCl salt medium in the presence of Cl_2.

The surface morphology of weldments of Inconel 600, Inconel 625 and Inconel 690 exposed to molten LiCl–KCl salt in the presence of Cl_2 are shown in Figures 3.8a-f respectively. The fusion line microstructure of Inconel 600 (Figure 3.8a) and Inconel 625 (Figure 3.8c) is clearly revealed while for Inconel 690 (Figure 3.8e) no such distinction could be made. The fusion line boundary was sharp and well delineated for Inconel 600.
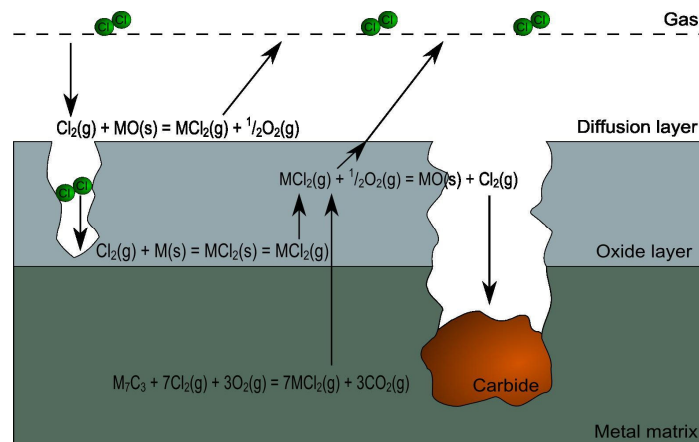
Figure 3.7 Schematic mechanism of attack in oxidizing/chloridizing environments [78].

The intergranular attack on the base metal of Inconel 600 and 625 are also evident in the weldment sample. The surface morphology of Inconel 600 (Figure 3.8b) and Inconel 625 (Figure 3.8d) samples in the weld region revealed the dendritic structure present in the weld region. This indicates that cell boundaries and interdendritic boundaries undergone selective dissolution in the weld region for Inconel 600 and 625 respectively. As discussed earlier in section 3.1.1, Inconel 600 sample exhibited cellular dendritic structure as shown in Figure 3.1d. After corrosion the cell boundaries in Inconel 600 sample also undergone selective attack compared to the dendritic structure present with in the cell (Figure 3.8b). These results clearly indicated that Inconel 600 and 625 exhibited localized attack while Inconel 690 (Figure 3.8f) exhibited uniform dissolution. It is reported that the portion of the welded 316L SS coupon was also found to have corroded extensively in addition to significant intergranular corrosion attack observed in the heat affected zone and the base metal, when tested in LiCl with 3.5 wt% Li_2O for 6 days at $650^{\circ}C$ in argon with 10% oxygen atmosphere [54]. These results suggest that weldments are prone to corrosion and fabrication techniques with optimized welding procedure are preferable for manufacturing of crucibles and techniques like seamless manufacturing are required.

The cross section micrographs of corroded samples are presented in Figures 3.9a-c respectively. These micrographs do not exhibit corrosion products, enriched and/or depleted layers. These results also indicate that the corrosion products formed are soluble and therefore dissolved in to the molten salt.
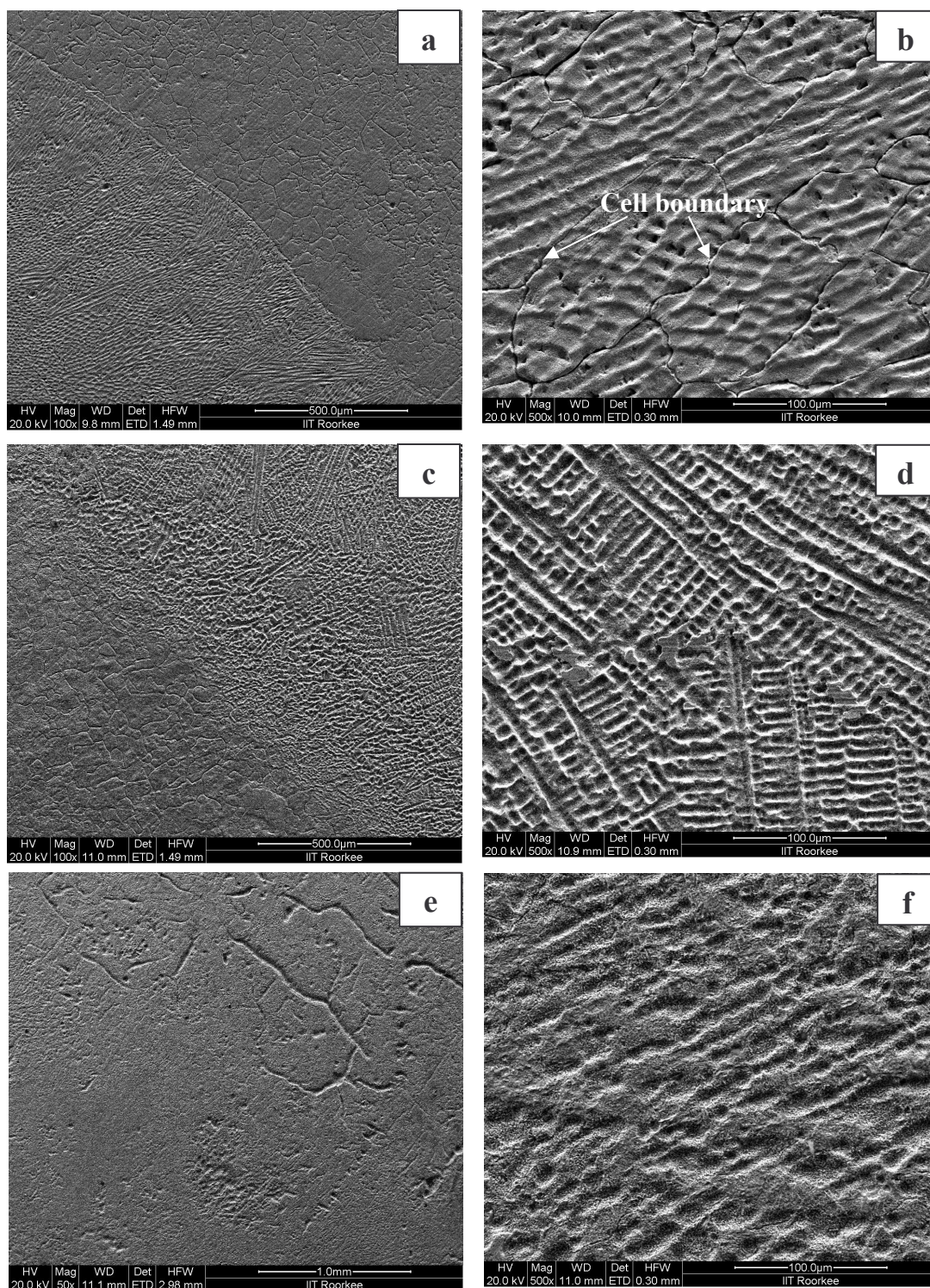
Figure 3.8. Surface morphology of welds of (a & b) Inconel 600 (c & d) Inconel 625 and (e & f) Inconel 690 exposed to molten LiCl–KCl salt under Cl₂ bubbling.
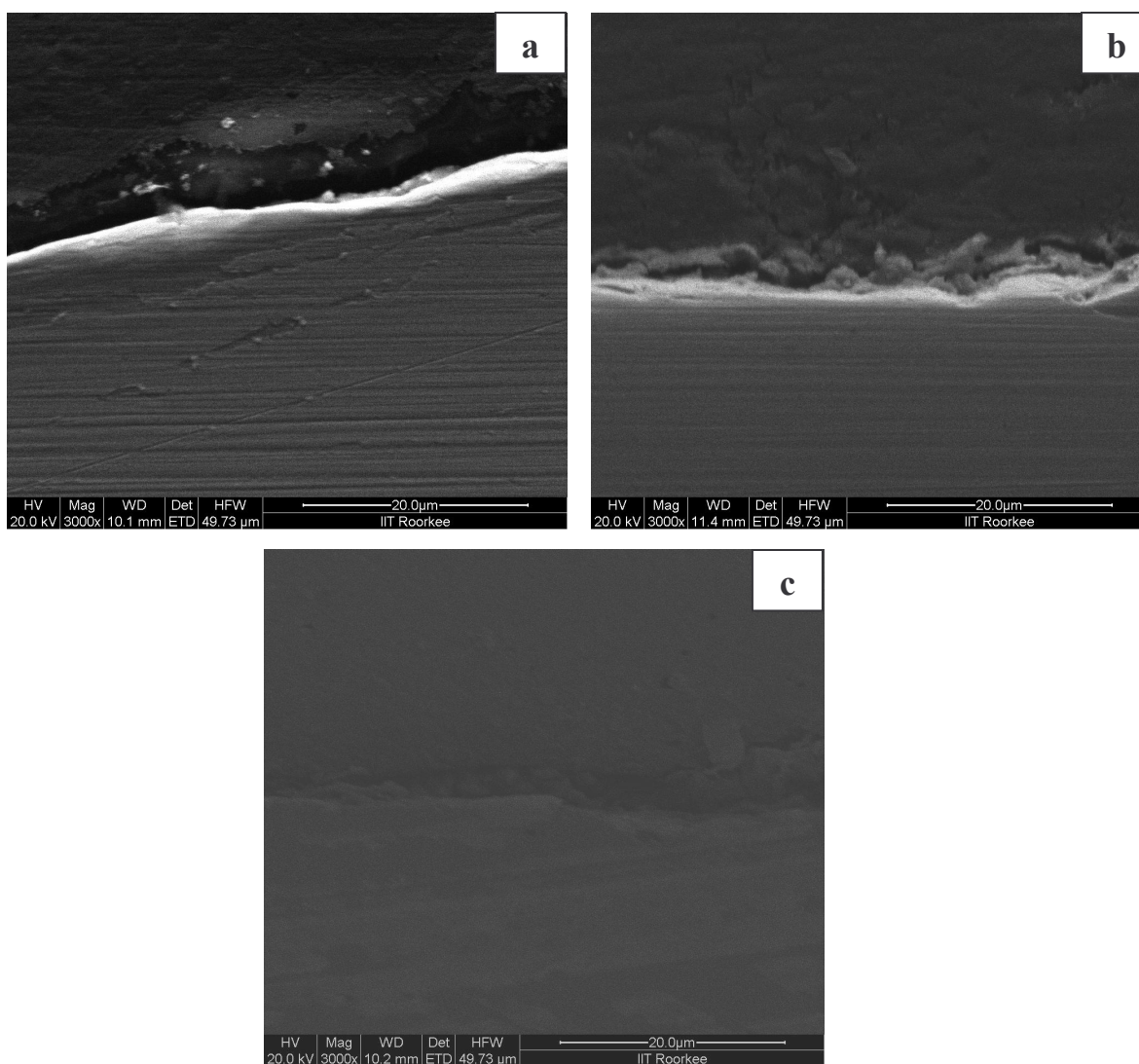
Figure 3.9. Cross section SEM of (a) Inconel 600 (b) Inconel 625 and (c) Inconel 690 exposed to molten LiCl–KCl salt under Cl₂ bubbling.

The short time tests carried out in the present study simulates the aggressive attack due to the presence of moisture, oxygen and chlorine present in molten salt during lab scale salt purification process. However, considering the practical difficulties in handling high temperature molten salt under highly toxic and lethal chlorine gas, long term corrosion studies are required to simulate engineering scale salt purification conditions.

3.1.2.3 Characterisation of exposed surfaces by GIXRD

The GIXRD pattern of corroded surface of Inconel alloys after corrosion test is shown in Figure 3.10. As shown in Figure 3.10, the major reflections correspond to austenite ($Fe_{0.7}Cr_{0.19}Ni_{0.11}$) [33-0397] phase on Inconel 690 and 625. The major Ni [04-0850] phase observed on Inconel 600 indicates that selective leaching/dealloying has occurred on the surface leaving a Ni rich layer. However EDX elemental composition did not reveal Ni enriched region on Inconel 600 surface. Molten salt corrosion in chlorine environment also did not result in the formation of loosely adherent scales. Thus from the results of SEM-EDX, cross section SEM and GIXRD, it is clear that corrosion products formed are soluble in molten LiCl–KCl under Cl_2 bubbling and resulted in severe corrosion. This necessitates the use of graphite liner or ceramic coatings for corrosion protection.
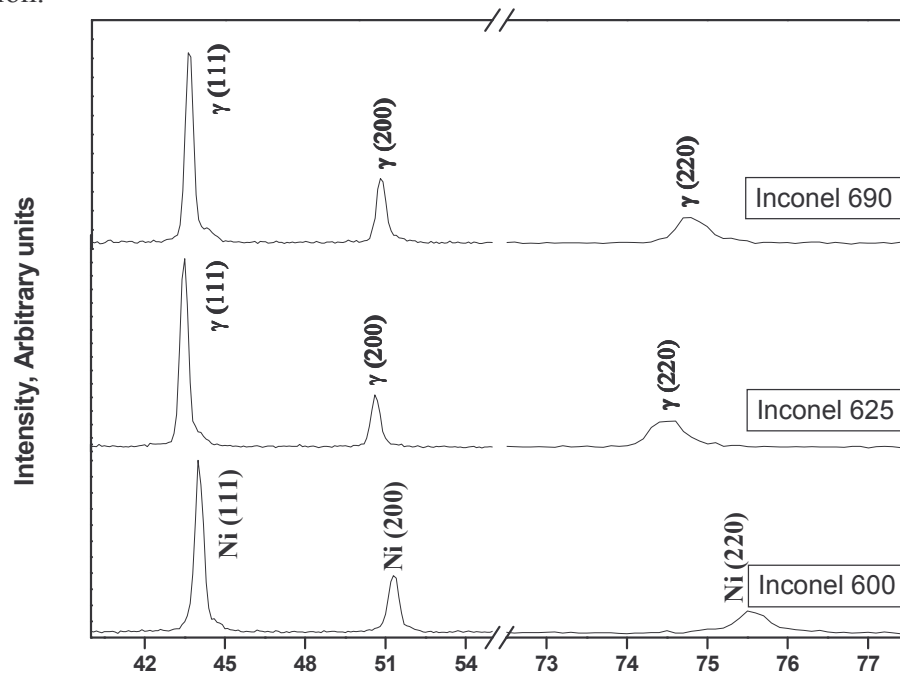
Figure 3.10. GIXRD pattern of Inconel 600, Inconel 625, and Inconel 690 exposed to molten LiCl–KCl salt under Cl_2 bubbling.

3.1.3 Summary

1. Corrosion tests performed on Inconel 600, Inconel 625, and Inconel 690 in molten LiCl–KCl salt under Cl_2 bubbling indicated that Inconel 690 showed better corrosion resistance compared to Inconel 600 and Inconel 625. The higher corrosion rate of Inconel 625 is attributed to the development of Mo rich layers, catastrophic oxidation and breakaway.

2. The surface morphology of corroded Inconel 600 and Inconel 625 surface clearly revealed intergranular corrosion, corrosion along twin boundaries and preferential dissolution of precipitates with in the grain. The surface morphology of Inconel 690 on the other hand did not show any such localized attack.

3. The surface morphology of weldments of Inconel 600 and Inconel 625 revealed cell boundary dissolution and interdendritic dissolution in the weld region respectively while uniform corrosion was observed on Inconel 690 weldment. The intergranular and interdendritic dissolution was attributed due to Cr depleted regions around carbide precipitates which led to preferential dissolution along these boundaries.

4. GIXRD analysis indicated austenite phase on Inconel 690 and 625 while major Ni phase was observed on Inconel 600 indicating that selective leaching/dealloying has occurred. No oxide scales/corrosion products were observed unlike those formed in molten LiCl–KCl salt under air and UHP argon environment.

5. The results indicated that Inconel 690 with uniform dissolution is preferable for corrosion resistance in molten LiCl–KCl salt at high temperature under chlorine bubbling in comparison to Inconel 600 and 625 where localized dissolution was observed.

3.2 CORROSION IN MOLTEN SALT UNDER AIR

The unit operations like salt preparation and electro refining involve the presence of molten LiCl–KCl eutectic salt from 500 to 600°C. Accidental ingressions of moisture and oxygen will aggravate the corrosion of structural materials used and hence the materials selected should withstand such aggressive environment. Moreover the mechanism of corrosion of materials are better understood by exposing materials to molten salt environment under severe corrosive conditions. Therefore corrosion behaviour of candidate materials was studied in molten LiCl–KCl eutectic salt under air environment. Ni based alloys exhibit better corrosion resistance than carbon steels and stainless steel in chlorine-containing environments [74]. Hosoya et al. [55] made a study on the compatibility of structural materials with molten chloride mixture at high temperature and showed that nickel based super alloy i.e, Hastelloy–X is exceedingly resistive against oxidation owing to its adherent oxide scale. Several authors have suggested that molybdenum may be deleterious in hot corrosion. In the present study candidate materials like electroformed Ni, with and without Ni-W coating, 316L stainless steel and Ni base alloys were studied. The investigation also aims in determining the corrosion behaviour of Mo containing nickel-base alloy in molten salt compared to nickel-base alloys without Mo. In the present study nickel base alloy Inconel 600 without Mo and less Cr, Inconel 625 with Mo and high Cr and Inconel 690 without Mo and high Cr were chosen and tested in molten LiCl–KCl salt in the presence of air, in order to evaluate their corrosion resistance.

3.2.1 Corrosion of Electroformed Ni

Electroforming (EF) is an effective and economical alternative for fabricating precision parts that are difficult to make by conventional manufacturing means [74]. Electroforming is a useful technique where welding needs to be avoided since some of the welded regions in some materials are more prone to corrosion attack. EF Ni shows excellent strength, toughness, and ductility and is extremely resistant to corrosion in wide range of environments [81]. Nickel also shows high corrosion resistance in molten chloride as well as in molten fluoride [48] and is regularly employed at elevated temperature [82] as the NiO saturated film developed was not expected to dissolve and provide good corrosion resistance [83]. Arons et al. [84] reported that tungsten is the only material known to be capable of withstanding the corrosive attack of wide range of liquid metals. Electrodeposition of nickel–tungsten (Ni–W) alloys has been utilized for various applications due to their unique combination of tribological, magnetic, electrical and electro-erosion properties. They also exhibit good mechanical properties (e.g., high tensile strength and hardness, as well as superior abrasion resistance), good resistance to strong oxidizing acids, and high temperature corrosion [85].

Molten salt corrosion has been studied mainly by gravimetric method and surface observation of corroded samples. Figure 3.11 shows the percentage weight loss of the EF Ni, EF Ni-W, 316L SS and Inconel 625 exposed to molten LiCl–KCl salt at 400, 500 and $600^{\circ}C$ for 2 h in air. The corrosion rate of metallic materials is strongly influenced by molten salt temperature. The corrosion rates increases with increase in temperature as the diffusion rates increase with increase in temperature. It can be inferred from the weight loss measurements that EF Ni shows highest corrosion attack, when compared with EF

Ni-W at a particular temperature. For instance, at 600°C the percentage weight loss for EF Ni is 15.6 % while the weight loss for EF Ni-W at the same temperature is only 7.0 %. EF Ni shows a percentage weight loss of 1.0 % at 400°C, which was increased to 3.3 % at 500°C and further, increased to 15.6 % at 600°C. It is reported that the presence of moisture in the molten salt will enhance the corrosion to a greater extent than in dried melts [86]. The increased corrosion rate for EF Ni could be attributed to the nature of films formed on the surface apart from the presence of moisture and increase in diffusion rate of corrosive ions with increase in temperature.
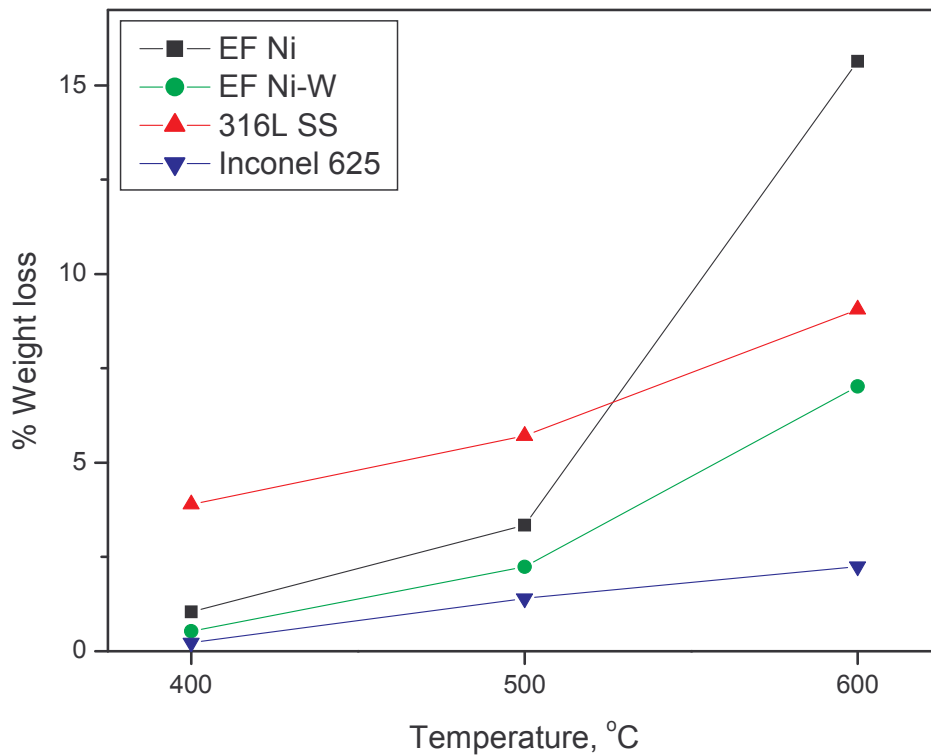
Figure. 3.11. Percentage weight loss of EF Ni, EF Ni-W, 316L SS, and Inconel 625 at various temperatures in molten LiCl-KCl salt for 2 hours in air.

Figure 3.12a and b shows the SEM image for electroformed nickel in untreated and in tested condition respectively. The as received EF Ni deposits exhibited a banded or lamellar structure. These banded features (Figure 3.12 (a)) disappear on dissolution resulting in smooth and porous surface as shown in Figure 3.12(b). After the corrosion test, salt film formed on EF Ni was highly brittle and light green in color and got detached from the sample, from all sides. This indicates that the molten salt has spread all over the sample and the metal has undergone uniform corrosion. The surface morphology of the salt film and their EDX spectrum from exposed top surface and from detached bottom surface of the salt film was smooth and porous. The EDX analysis clearly showed differences in the quantities of Ni, K and Cl in top and bottom surfaces of the salt film, the top surface being rich in K and Cl while the bottom surface being rich in Ni. The concentration of elements in wt % from exposed top surface were- Ni-17.56, K-41.90, and Cl-40.54, while from the detached bottom surface were- Ni-93.80, K-2.71, and Cl-3.49. The cross section of the light green colored salt film formed on electroformed Ni was mounted and observed in SEM (Figure 3.13(a)). The surface morphology of the cross section of the salt film revealed loosely bound particles. The back scattered electron image (Figure 3.13(a)) of the cross section of the salt film (thickness-1086 μm) clearly revealed two distinct layers within the salt film. Figure 3.13(b) shows that the salt film has Ni rich (bright region-615 μm) and Ni depleted layers (dark region-471 μm). The corresponding elemental X-ray maps of Ni, K, Cl from the cross section of the same salt film are also shown. The salt film also has fine distribution of KCl and also few large agglomerates of KCl distributed.
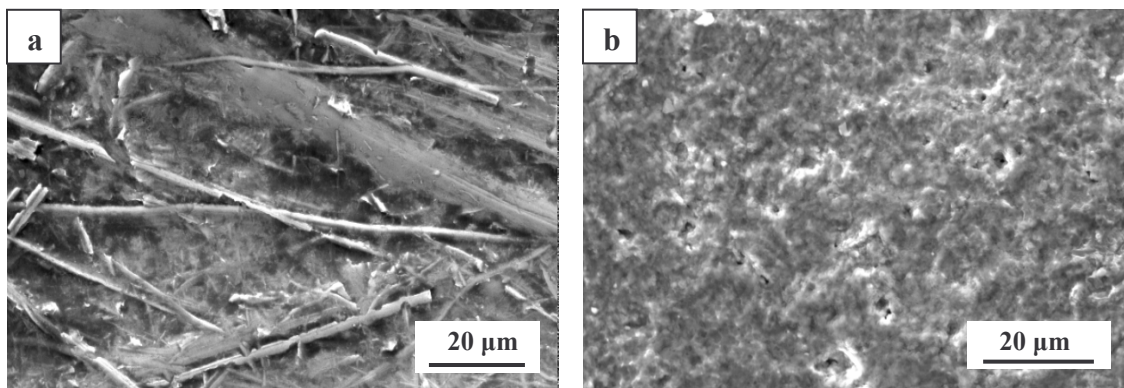
Figure. 3.12. SEM Micrograph of EF Ni (a) untreated and, (b) tested in molten LiCl–KCl salt.
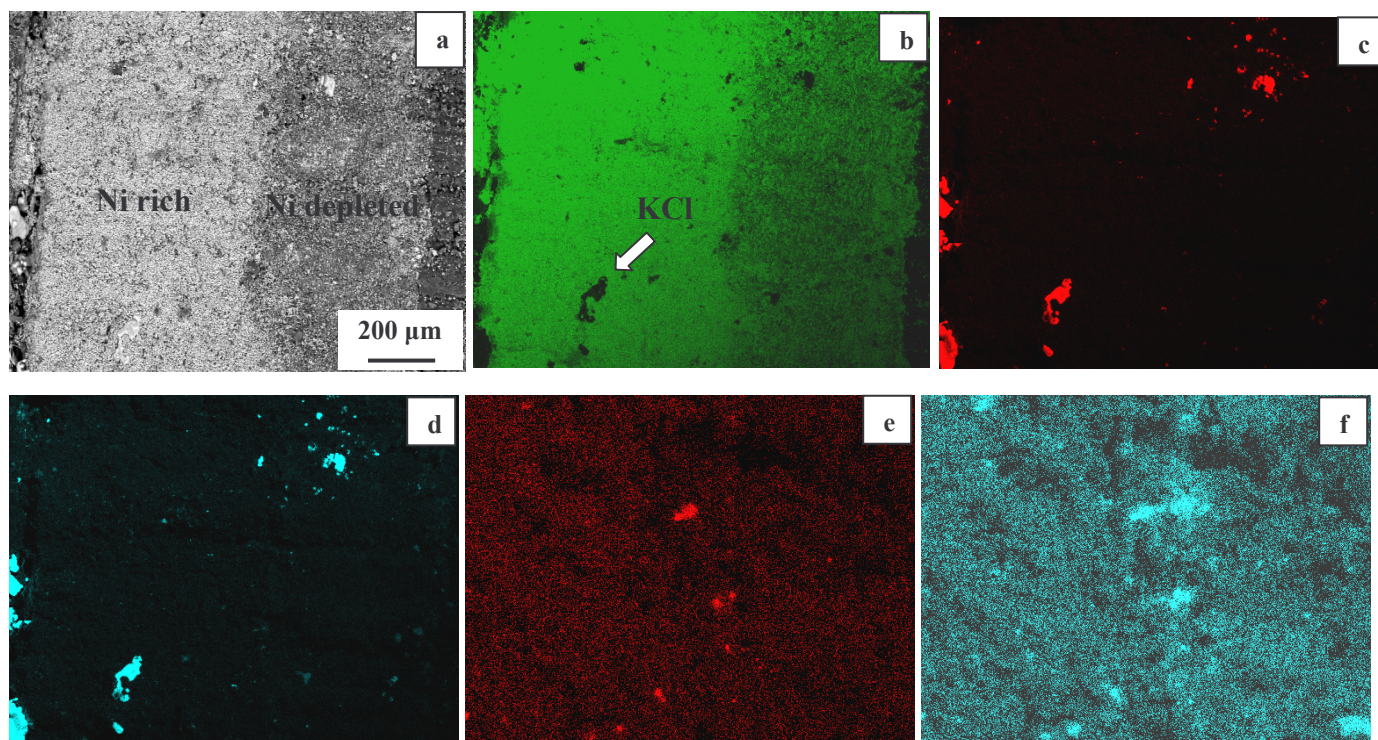
Figure. 3.13 (a) Back scattered SEM image of the cross section of the salt film, (b-d) elemental X-ray maps of Ni, K, Cl respectively, (e & f) elemental X-ray maps of K, Cl respectively at high magnification.

The XRD reflections from EF Ni as-received unpolished, EF Ni as-received polished, and tested EF Ni is shown in Figure 3.14(a). The XRD peaks from as-received EF Ni sample matches with 111, 200 and 220 standard FCC reflections of Ni [04-0850]. The XRD pattern from molten salt treated EF Ni, obtained after the salt film got detached shows no deviation from that of the pattern obtained for as-received EF nickel, except with a change in the intensity of the 200 and 111 reflections. Figure 3.14(b) shows the XRD pattern obtained from the exposed top surface, detached top surface, and detached bottom surface of the salt film. The exposed top surface is rich in KCl [41-1476] along with the trace of NiO [47-1049]. This is because LiCl–KCl molten salt was placed on the exposed surface of the EF Ni. The detached top surface contains only nickel oxide with the absence of KCl. But the detached bottom surface contains both NiO and KCl. This shows that KCl salt has penetrated through the porous NiO layer and Ni is migrating towards the top surface to form NiO rich layer. This is in close agreement with the EDX results.

Laser Raman spectra from the surface of the salt film formed on the electroformed nickel is shown in Figure 3.14(c). The Raman spectrum exhibited a strong, broad peak at 501 cm^{-1} indicating the presence of NiO. Thus it was confirmed from XRD and laser Raman spectroscopy that the corrosion product was mainly NiO. Tada et al. [48] has put forward a mechanism for the formation of very thin nickel oxide during the electrochemical measurement and surface analysis of nickel in molten LiCl–KCl eutectic melt containing oxide ions at 450°C.
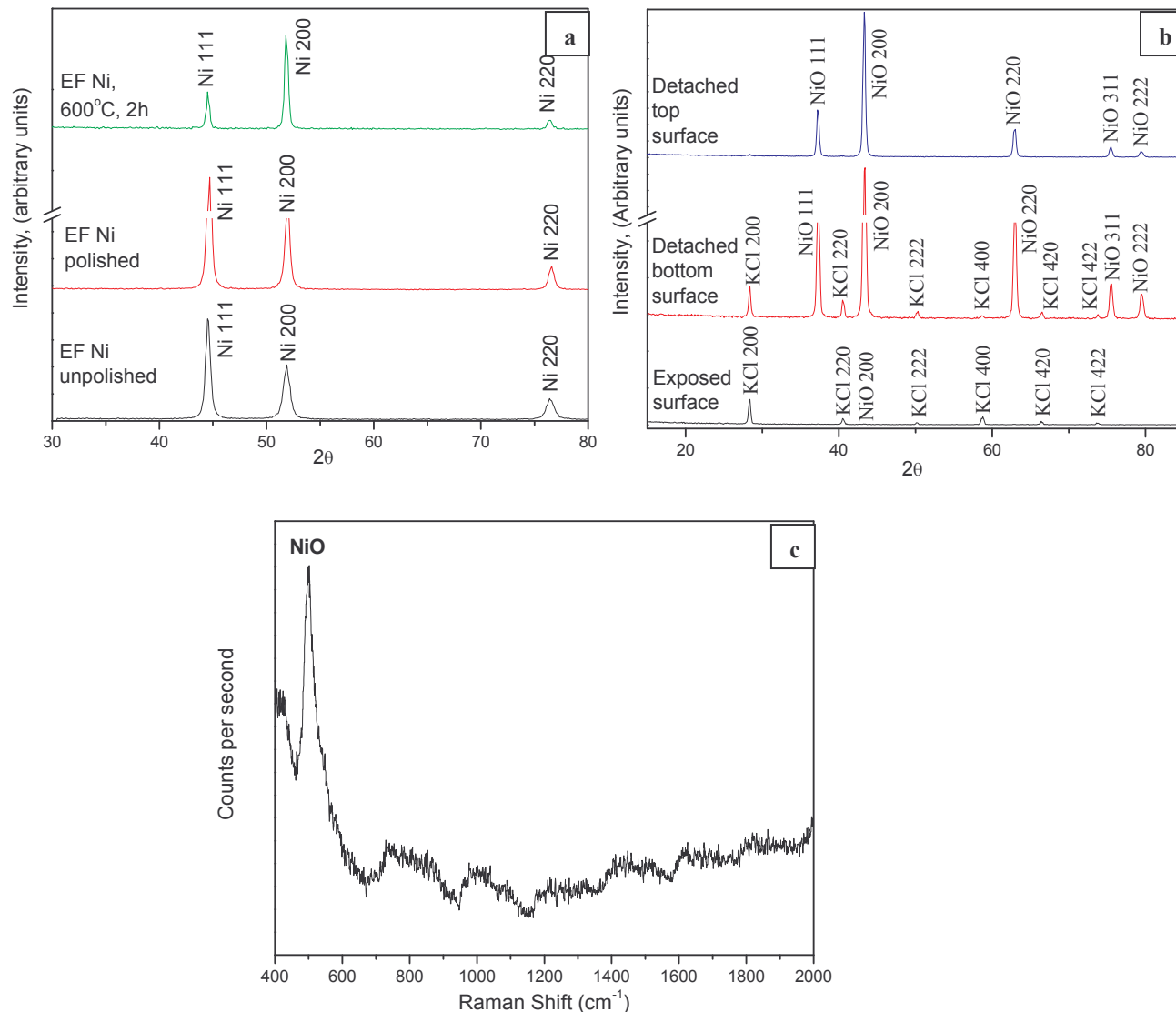
Figure. 3.14. XRD pattern (a) from EF Ni surface (b) from salt film surface and (c) Laser Raman spectra of the salt film.

Based on the observations from the present study a schematic diagram of the mechanism of corrosion of Ni in molten LiCl–KCl eutectic salt under air environment is shown in Fig 3.15. The mechanism involves outward diffusion of Ni, and inward diffusion of (Li,K)Cl through the porous and brittle NiO salt film. The brittle and porous thick salt film gets easily detached from the surface exposing fresh Ni surface, resulting in accelerated corrosion.
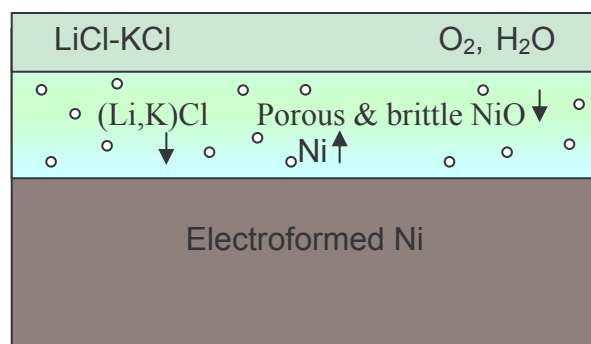
Figure. 3.15. Mechanism of corrosion of Ni exposed to molten LiCl–KCl salt.

3.2.2 Corrosion of Electroformed Ni-W

As discussed earlier the corrosion of EF Ni with Ni-20 wt% W coating on only one face (i.e exposed surface), resulted in less percentage weight loss than that of EF Ni without coating. The EF Ni-W would have performed better than or equal to Inconel 625 if the coating was applied all over the sample. No salt film was observed on the Ni-W coated surface, while the salt film similar to that formed on EF Ni was formed on the uncoated sides. This shows that Ni-20 wt % W coating increases the corrosion resistance in molten LiCl–KCl salt. Figure 3.16(a-c), shows the SEM surface morphology of the EF Ni-W before and after testing. The SEM image shows the presence of deep cracks on the surface. This is typical microstructure for stressed deposits, as cracking occurs in highly stressed deposits. Figure 3.16(a) shows the SEM image of the as-received EF Ni-W surface containing cracks which is similar to the Ni-W alloy observed by Eliaz et al. [85] that contains 35 at% W. These cracks are detrimental from corrosion point of view. Figure 3.16(b) and (c) clearly shows that the material has undergone preferential attack in those cracked regions. The EDX analysis from the tested surface in wt% is Ni-68.98, W-31.02, while from the crack region is Ni-49.32, W-48.64, Cl-2.04. This shows

enrichment of W on the tested surface and in the cracked region. Figure 3.17(a) shows the cross sectional view of the as-received EF Ni-W. It is clear from this figure that there is a sharp interface between EF Ni and the Ni-W coating which is intact. The thickness of the Ni-W coating was found to be uniform and is around 50 μm. The SEM image also shows few vertical cracks present in the Ni-W coating, through which penetration of the molten LiCl–KCl salt has occurred. The composition of the EF Ni-W coating was found to be Ni-69.50, W-20.50 (wt %) from the EDX analysis while from the substrate it is Ni-100.00. Figure 3.17(b) and (c) shows the opening up of a crack in the Ni-W coating, which has occurred due to the stresses present in the coating and due to the penetration of the molten salt. Also it is evident that the coating thickness has reduced to about 25 μm and the arrows in Figure 3.17(b) and (c) shows subsequent coating disintegration by opening up of crack.

The results of Ni-W coating in molten LiCl–KCl salt in air indicated that the coating has exhibited good corrosion resistance; however cracks need to be avoided. The present study clearly indicates the importance in fabrication of crack-free coating which is vital for improving the corrosion resistance. The average microhardness value from the cross section of EF Ni-W, on the coating and on the substrate were 665 and 328 VHN, respectively. From the microhardness measurements, it is clear that the hardness value on the Ni-W coating was much higher than that on the substrate.
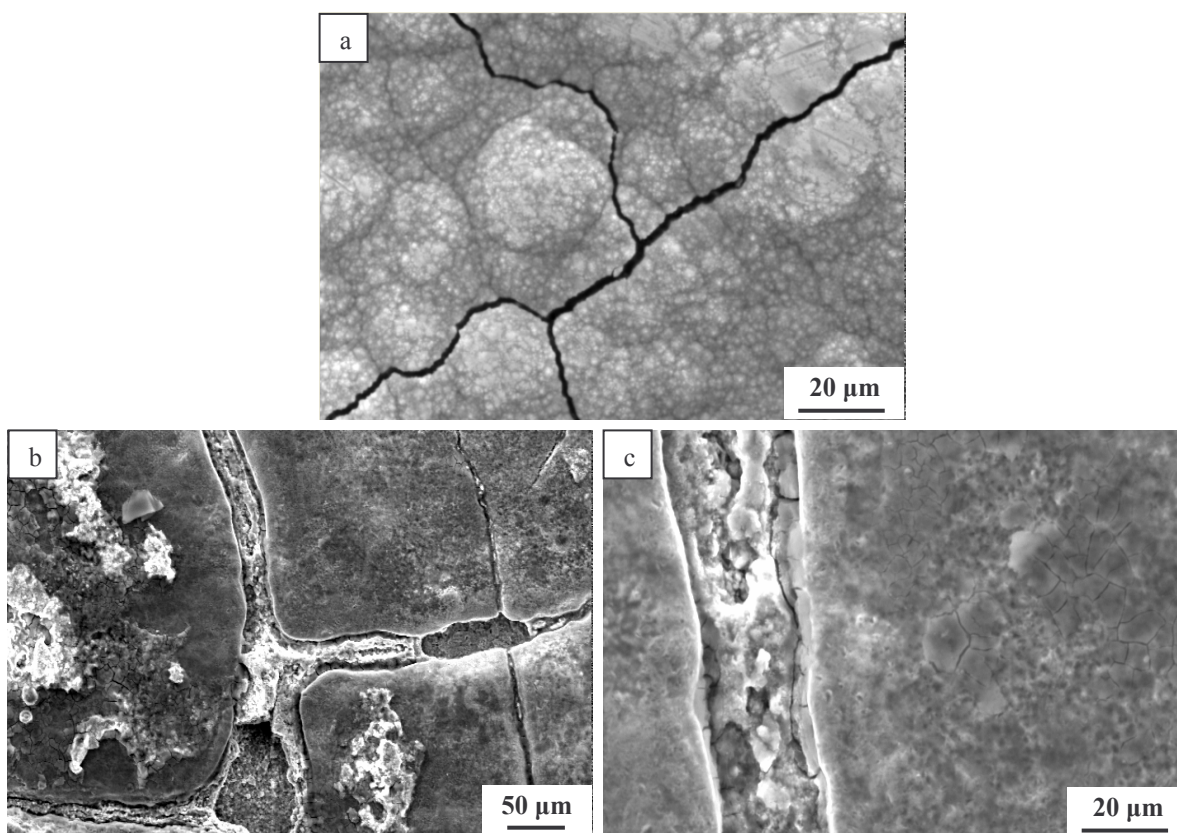
Figure. 3.16. SEM micrograph of EF Ni-W surface (a) before corrosion test, and (b & c) after corrosion testing in molten LiCl–KCl salt.
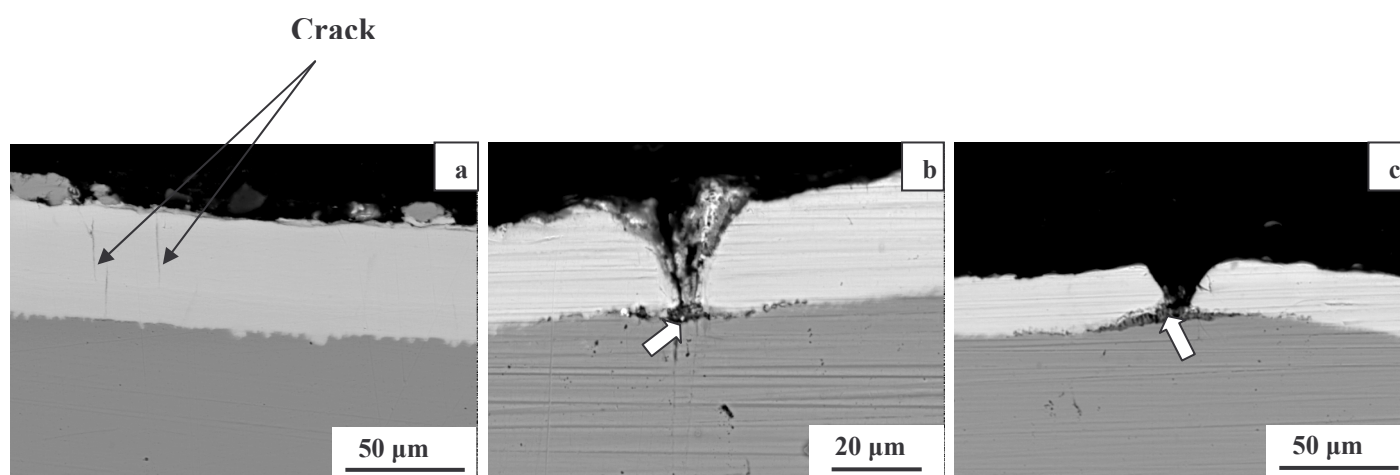
Figure. 3.17. SEM micrograph of the cross section of EF Ni-W (a) before corrosion test, (b & c) after corrosion test showing the opening up of cracks and disintegration of the tungsten coating.

Figure 3.18 shows the XRD pattern of EF Ni-W uncoated side, Ni-W coated side and tested EF Ni-W. The XRD pattern in all cases consists of 111, 200 and 220 FCC reflections corresponding to Ni [04-0850]. The XRD reflections on the coated side shifted to smaller values compared to the uncoated side, indicating the expansion of the lattice of Ni due to the presence of W in the coated side. This shows that tungsten is in the solid solution form. Tungsten forms single- phase solid solution alloy with nickel, at tungsten addition up to about 35 wt% tungsten. With increasing tungsten addition above this concentration a second phase, the intermetallic compound, WNi_4, will form in the matrix; and at a tungsten content of 44 wt% the matrix is principally WNi_4 [82].
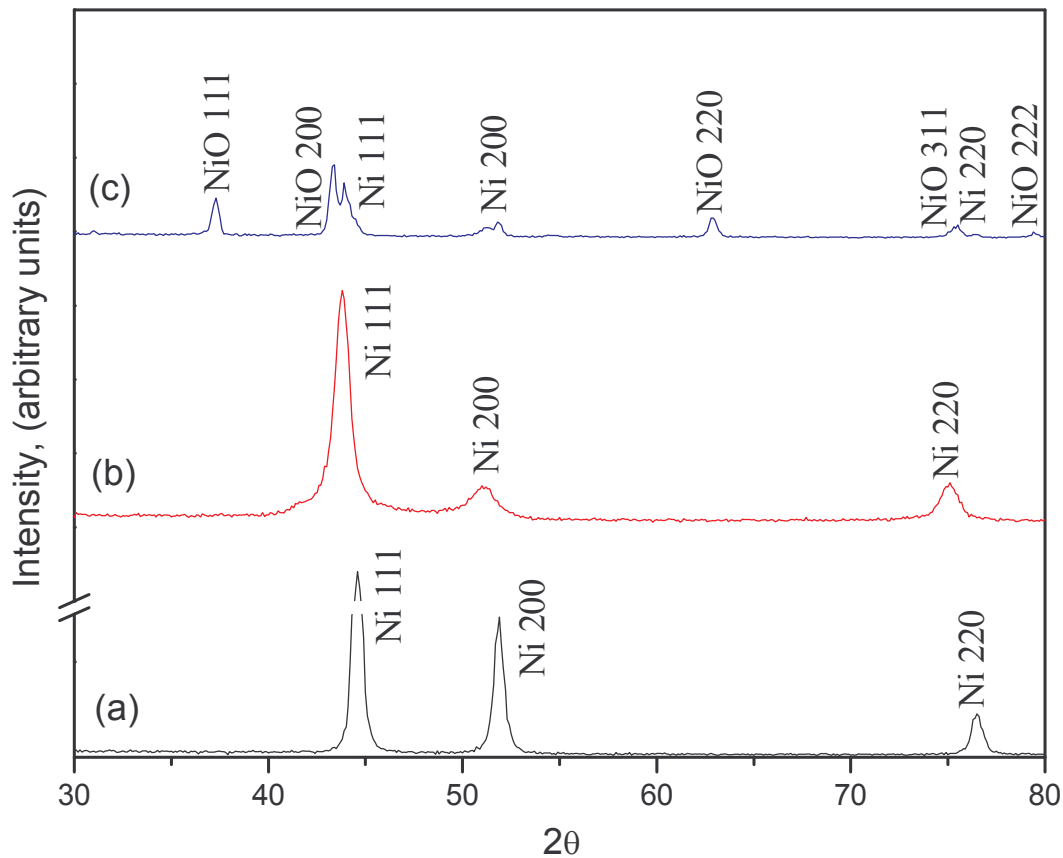
Figure. 3.18. XRD pattern of EF Ni-W (a) uncoated side (b) coated side and (c) coated side treated with molten LiCl–KCl salt.

The XRD pattern of the tested EF Ni-W sample consists of major reflections of protective NiO film along with FCC Ni-W solid solution. The broadening of the reflections in the coated side and tested surface of EF Ni-W sample indicates the presence of nano crystalline/stresses in the coating/film.

Based on the observations a schematic diagram of the mechanism of corrosion of Ni-W coating in molten LiCl–KCl is shown in Fig 3.19. The mechanism involves outward diffusion of Ni-W, and inward diffusion of KCl through NiO salt film. The enrichment of W in the outer layer results in formation of tungsten rich film which is protective. The EDX and XRD results in the present study also revealed the formation of W rich NiO film on the surface suggesting that the improved corrosion resistance of EF Ni-W over EF Ni could be due to tungsten enrichment. Sriraman et al. [87] studied the corrosion behaviour of nanocrystalline Ni–W and Ni–Fe–W alloys in 3.5wt% NaCl and 1N sulphuric acid solution. They concluded that the superior corrosion resistance of Ni–W alloy films was due to the preferential dissolution of nickel and formation of tungsten rich film on the surface, which inhibited further corrosion.
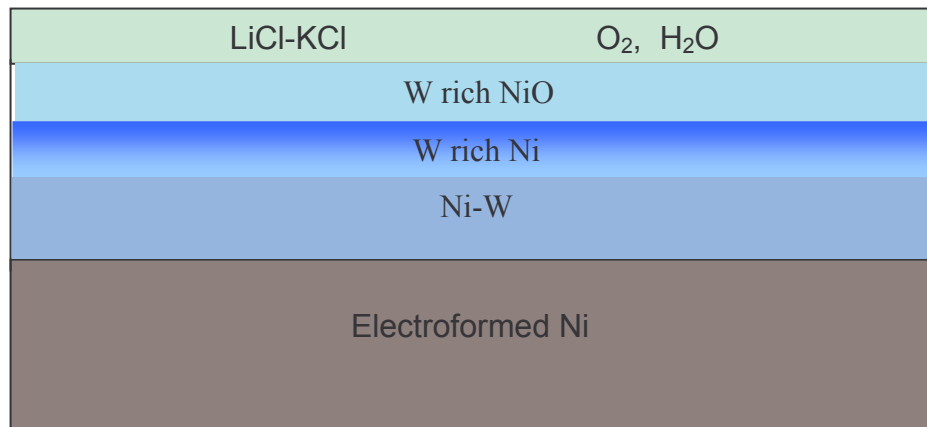
Figure. 3.19. Mechanism of corrosion of Ni-W coating over EF Ni exposed to molten LiCl–KCl salt.

3.2.3 Corrosion of type 316LSS

Type 316L stainless steel has suffered highest percentage weight loss when compared to EF Ni, EF Ni-W and Inconel 625. The surface morphology of tested 316L SS is shown in Figure 3.20. The surface morphology indicates accelerated corrosion and at high magnification a porous surface is revealed. The chemical composition of the tested surface (after removing corrosion product) from EDX analysis in wt % is as follows: Fe-68.30, Cr-17.25, Ni-11.74, Mo-2.71 which is similar to the base composition. The salt film formed on 316L SS is also porous and brittle in nature which got completely detached. The surface morphology of the salt film from top surface and from bottom surface is shown in Figure 3.21. Unlike the smooth surface morphology of salt film formed on EF Ni surface, the salt film on 316L SS top surface is rough and growth of corrosion product as needles was observed (Figure 3.21(a)), while the detached bottom surface (Figure 3.21(b)) was smooth. The chemical composition of the salt film from EDX analysis, in wt % is as follows: Fe-32.89, Cr-34.22, Ni-13.17, Mo-2.39, Cl-14.64, K-2.70. This indicates that there is an enrichment of Cr and Ni in the salt film. This shows that the mechanism of corrosion is selective diffusion of Cr and Ni to the surface with the formation of porous layer below and formation of chromium compounds at the surface. The presence of chlorine peak indicates that there is some salt left in the corrosion product.

Figure. 3.20. SEM image for 316L SS treated with molten LiCl–KCl salt at (a) 500x and, (b) 1000x.
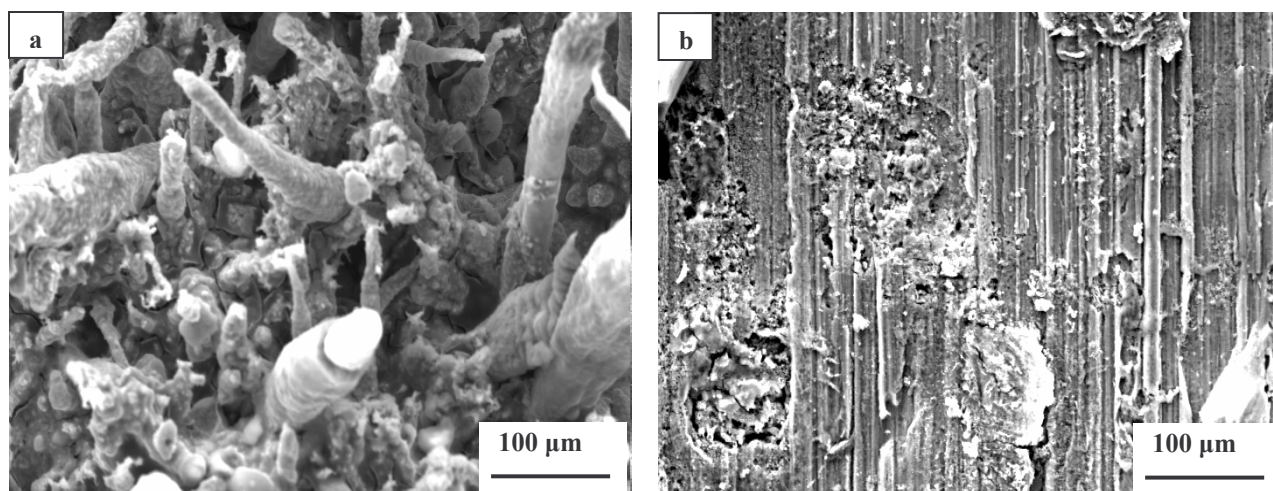
Figure. 3.21. Surface morphology of the salt film from 316L SS surface exposed to LiCl–KCl salt (a) from salt exposed surface and, (b) from detached surface.

Figure 3.22(a) shows the XRD pattern of 316L SS tested surface and salt film formed over it. The austenitic crystal structure reflections Fe0.7Cr0.19Ni0.11 [33-0397] were matched exactly with the tested surface and no surface oxide film was observed, while the salt film consisted of Cr_2O_3 [38-1479], NiO [44-1159], $NiCr_2O_4$ [88-0108] and

KCl [04-0664]. The presence of Mo in the salt film is evident from the EDX which is not manifested in the XRD pattern. Raman spectra of the salt film formed on 316L SS is shown in Figure 3.22(b). The set of Raman peaks at 225 cm^{-1}, 292 cm^{-1}, 405 cm^{-1}, and 606 cm^{-1} are assigned to α-Fe_2O_3 (hematite). The Raman peak at 647 cm^{-1} could correspond to Fe-Ni-Cr spinel oxide, as the variation in spinel composition and structure (for example, replacing Ni^{2+} for Fe^{2+} or Fe^{3+} for Cr^{3+} in the oxide) is also known to have an influence on the spinel band [88]. The salt film formed on 316L SS and on EF Ni were porous in nature, which allowed penetration of salt, moisture and oxygen through the film and this porous, brittle and non adherent film exposes fresh surface and accelerates the corrosion processes.

The EDX, XRD and laser Raman spectroscopy results confirm that the corrosion product consists of Cr_2O_3, NiO and $NiCr_2O_4$. Based on the results obtained the mechanism of corrosion of 316L SS exposed to molten LiCl–KCl salt under air environment is depicted in Fig 3.23. The mechanism involves outward diffusion of Cr, and formation of Cr rich outer layer (Cr_2O_3) and Ni rich inner layer (NiO). The solid state reaction between the two layers results in the formation of spinels ($NiCr_2O_4$) which causes cracks at the interface as shown in the figure. Thus the porous and brittle film gets easily detached from the surface, resulting in accelerated corrosion. This mechanism of formation of Cr rich outer layer and Ni rich inner layer with eventual formation of voids underneath due to selective out ward diffusion of Cr as shown in Fig 3.23 is clearly evident during molten salt corrosion of 316L SS under argon atmosphere as discussed in section 3.3.2.
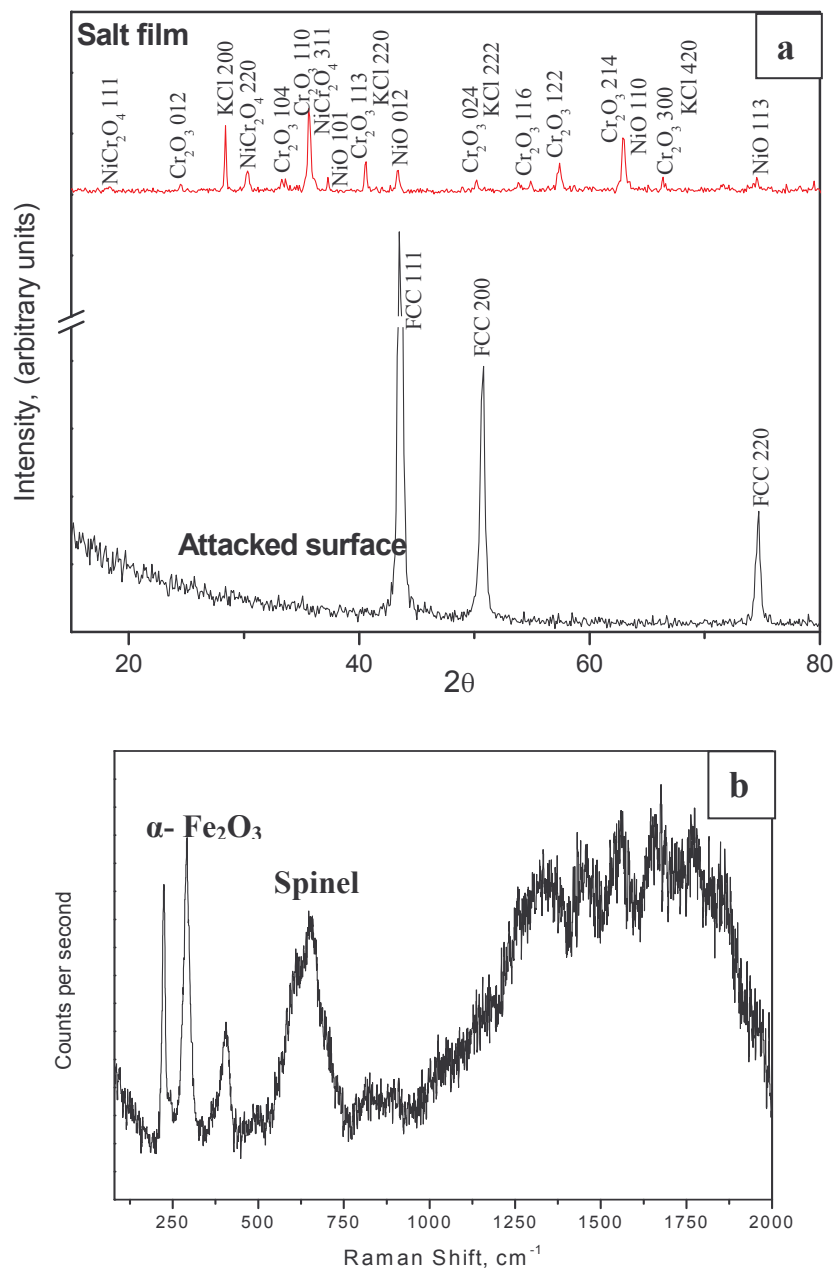
Figure. 3.22 (a) XRD pattern of 316L SS treated surface and salt film, (b) Laser Raman spectra of the salt film.
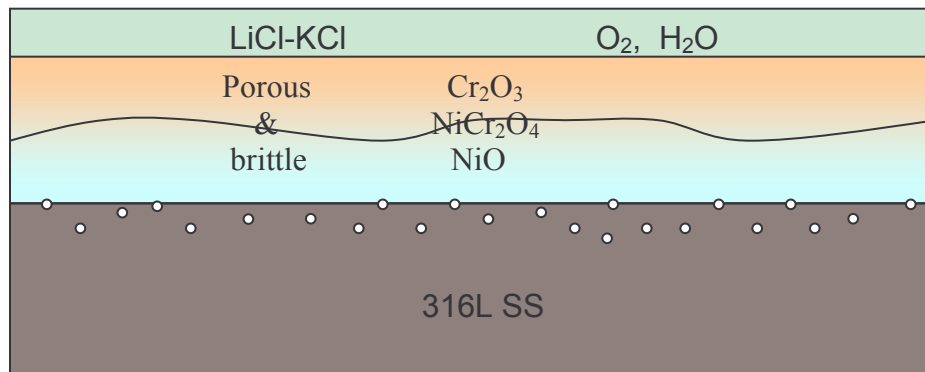
Figure. 3.23. Mechanism of corrosion of 316L SS exposed to molten LiCl–KCl salt under air environment.

3.2.4 Corrosion of Inconel 625

As shown in Figure 3.11, Inconel 625 exhibited superior corrosion resistance when compared to 316L SS, EF Ni and EF Ni-W. The amount of corrosion product formed on the surface was also less when compared to 316L SS. The superior corrosion resistance of Inconel 625 is also evident from the SEM microstructures shown in Figure 3.24. Figure 3.24(a) shows porous nature of the surface, and at high magnification selective dissolution of grain boundaries and precipitates is evident (Figure 3.24(b)). The EDX analysis from the matrix in wt % is Ni-87.67, Cr-2.25, Mo-9.54, Fe-0.54, while from the tested region in wt % is Ni-65.34, Cr-18.96, Mo-12.05, Fe-3.65. This shows that there is an enrichment of Cr and Mo on the tested region. The surface morphology of the salt film from top surface and from bottom surface collected from tested Inconel 625 is shown in Figure 3.25. Like 316L SS the salt film on Inconel 625 top surface is also rough and growth of corrosion product as layers is observed (Figure 3.25(a)), while the bottom surface (Figure 3.25(b)) is smooth. The EDX analysis from the salt film in wt % is as follows: Ni-3.96, Cr-47.61, Mo-14.91, Fe-6.49, Cl-24.38, K-2.65. This clearly indicates

114

that there is significant enrichment of Cr and Mo in the salt film. This large enrichment of Cr and lack of Ni in the salt film indicates that the surface underneath the salt film is enriched with Ni which might have protected the material from further corrosion. Enrichment of Ni in an outer corrosion layer was identified by Cho et al. [56,57] and thus Ni was considered as a useful element for enhancement of the corrosion resistance in a hot molten salt under an oxidizing atmosphere. It is also reported that Nickel inhibits the internal diffusion of oxygen ion by its accumulation on the interface of oxide/oxide or beneath of the oxide layers [56,57].
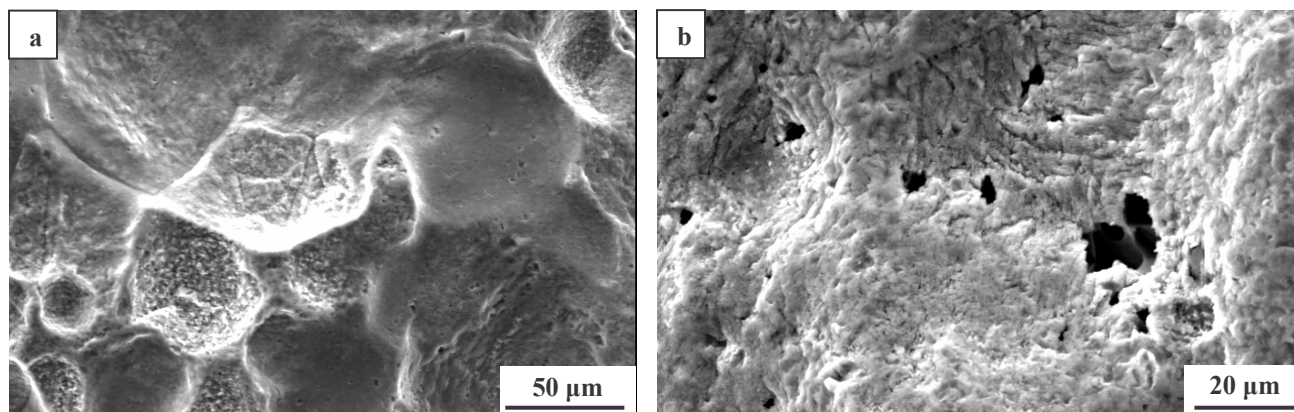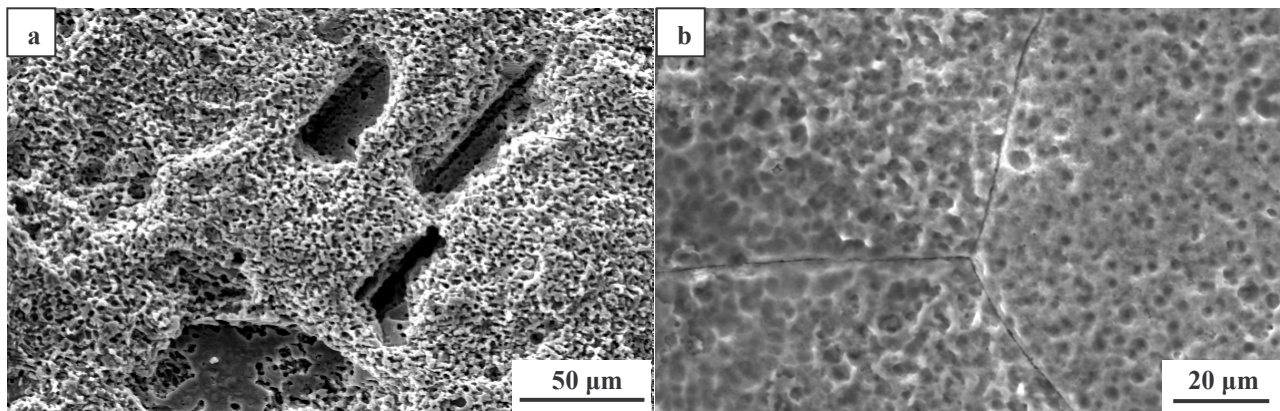

Figure. 3.24. SEM image for Inconel 625 treated with molten LiCl–KCl salt at (a) 500x and (b) 1000x.
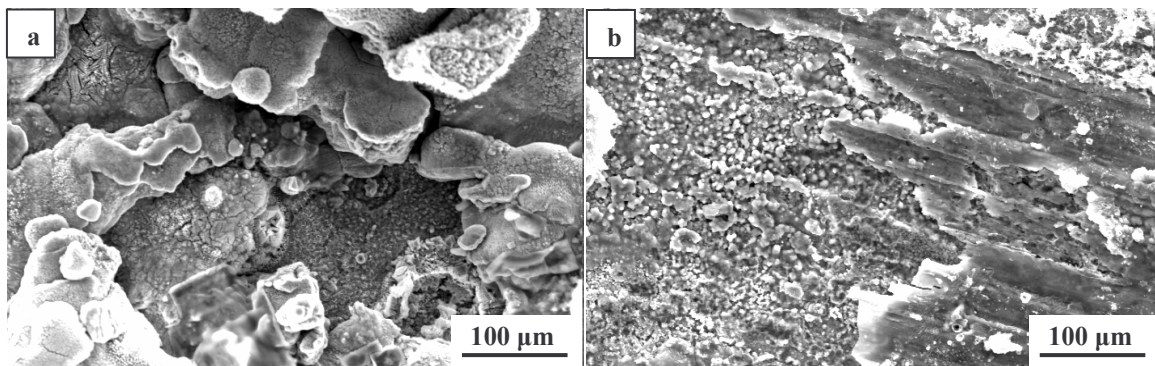
Figure. 3.25. Surface morphology of the salt film from Inconel 625 surface exposed to LiCl–KCl salt (a) from salt exposed surface and (b) from detached surface.

Figure 3.26(a) shows the XRD pattern of Inconel 625 tested surface and salt film formed over it. The tested surface consisted of FCC crystal structure reflections along with NiO. The improved corrosion resistance of Inconel 625 can be attributed to the presence of this adherent and protective NiO present on the tested surface which is evident from the XRD pattern on the tested surface. The XRD pattern from the salt film revealed the presence of Cr_2O_3 and NiO. Cho et al. [57] has reported that Inconel 713LC alloy showed the highest corrosion resistance among the alloys tested in molten LiCl-Li_2O salt and the corrosion products of Inconel 713LC were Cr_2O_3, $NiCr_2O_4$ and NiO. It is reported that a solid state reaction between NiO and Cr_2O_3 might caused the formation of the $NiCr_2O_4$ spinel oxides [56]. EDX analysis of the salt film formed on 316L SS and Inconel 625 indicated the presence of Mo which could be in the form of spinel oxides. Raman spectra of the salt film formed on Inconel 625 is shown in Figure 3.26(b). The spinel peak at 679 cm^{-1} has appeared as a stronger peak and the peak at 554 cm^{-1} correspond to Cr_2O_3. The Raman intensity ratio of the 549 cm^{-1} band (Cr_2O_3) to the 680 cm^{-1} band (spinel) was suggested as an indication of the extent of corrosion of alloy HT-9 based on chromia formation [88]. In our present study the intensity of the spinel peak increased relative to that of the Cr_2O_3 peak. The mechanism of corrosion of Inconel 625 appears to be same as that of 316L SS, i.e, the outward diffusion of chromium followed by formation of chromium rich compound and spallation. However, lesser amount of deleterious element Cr in the alloy and the enrichment of nickel below the salt film with protective NiO film might have enhanced the corrosion resistance of Inconel 625. However in order to understand the mechanism and effect of Mo and Cr in Ni base alloys

116

further detailed investigation was carried out on Ni base alloys in molten LiCl–KCl salt as discussed in forthcoming section.
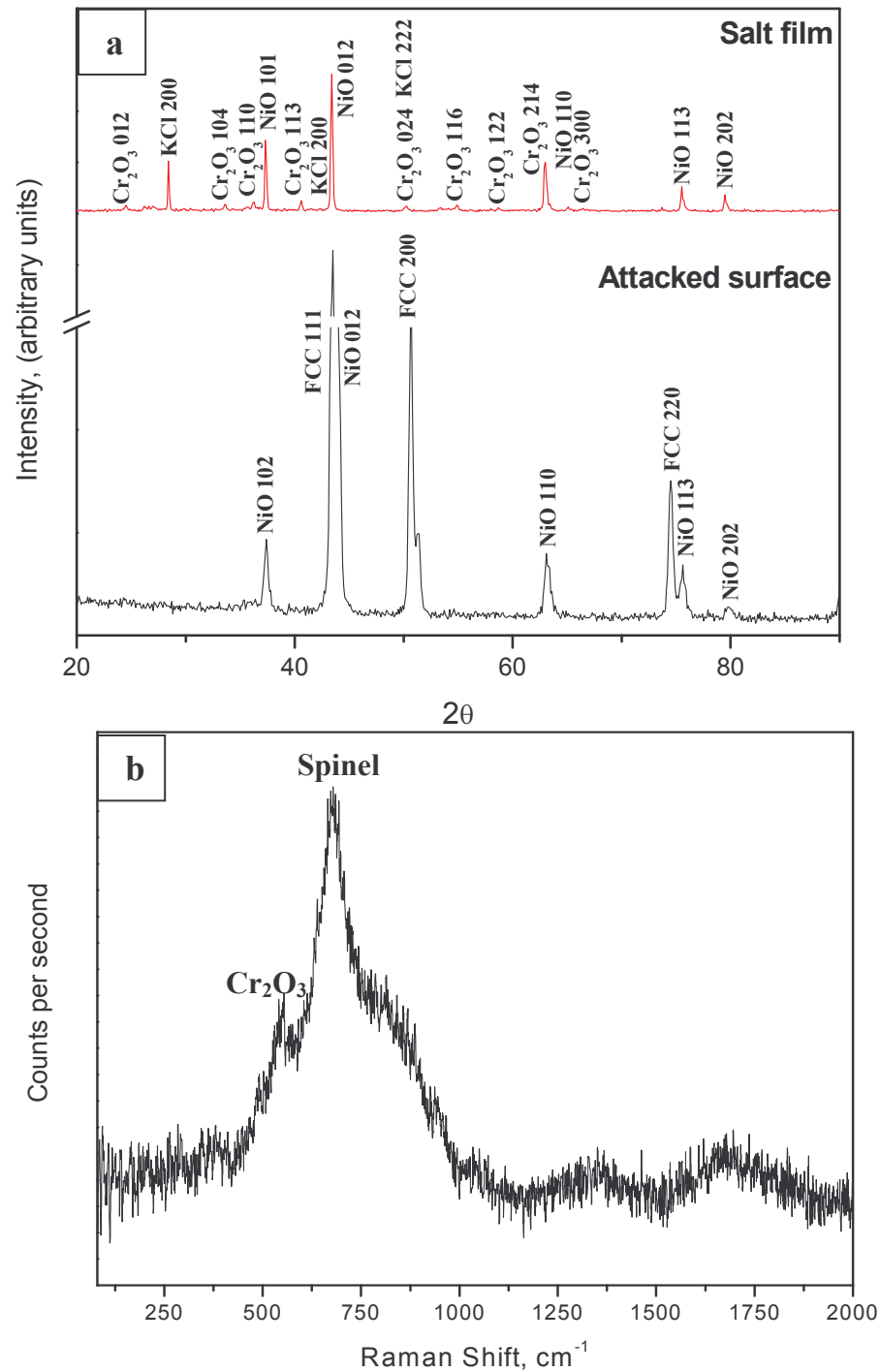
Figure. 3.26 (a) XRD pattern of Inconel 625 treated surface and salt film, (b) Laser Raman spectra of the salt film.

117

3.2.5 Corrosion of Inconel 600, 625, 690 Alloys

3.2.5.1 Corrosion rate

The average corrosion rate of Inconel 600, Inconel 625 and Inconel 690 studied at 400°C, 500°C and 600°C are shown in Figure 3.27. The average variation in corrosion rate data was determined to be ±10.01 mm/yr. It can be inferred from the corrosion rate measurements that Inconel 600 and Inconel 690 suffered less attack at 600°C compared to Inconel 625. The corrosion rate increased significantly with increase in temperature. Inconel 690 showed lower corrosion rate at all temperatures. It is generally accepted that increasing the chromium content in nickel-base alloys increases the resistance to hot corrosion [76]. However, Cho et al. [60] concluded that higher the Cr content in an alloy, the faster the corrosion rate of the alloy in molten LiCl–Li$_2$O salt and therefore, a high Cr content in the alloy would not improve the corrosion resistance. Moreover it is generally realized that Cr is not an effective element for improving corrosion resistance of Fe-base and Ni-base alloys due to chloride salt attack [74]. This suggests that high Cr content in nickel base alloys might not improve the corrosion resistance in molten LiCl–KCl salt. It is reported that oxygen active elements Al and Ti preferentially oxidised and formed corrosion layer [89].

Inconel 625 containing Mo has exhibited higher corrosion rate compared to Inconel alloys without Mo. Indacochea et al. [54] also observed similar result for Inconel 625 tested in LiCl with 3.5 wt% Li$_2$O for 6 days at 650°C in argon with 10% oxygen atmosphere. This suggests that the presence of Mo in Inconel 625 is not beneficial to improve corrosion resistance in molten LiCl–KCl salt in air. The catastrophic attack induced by molybdenum in Fe and Ni base alloys during hot corrosion have been

reported [75] and the characteristic features of the hot corrosion of molybdenum-containing alloys is catastrophic breakaway [76]. Catastrophic oxidation is the term referred to a situation in which liquid phase is formed in the oxidation process [77]. It is reported that the melting point of $MoCl_5$ is 194°C [77] and that of mixed oxides of MoO_2-MoO_3, MoO_2-MoO_3-Cr_2O_3 and MoO_2-MoO_3-NiO were 778, 772 and 764°C respectively [90]. The formation of Cr_2O_3 and NiO oxides results in enrichment of Mo, subsequent formation of low melting phases results in breakaway of film, resulting in accelerated corrosion. It is also reported that the development of a molybdenum-rich layer in the oxide adjacent to the metal appears to be the common factor [76].
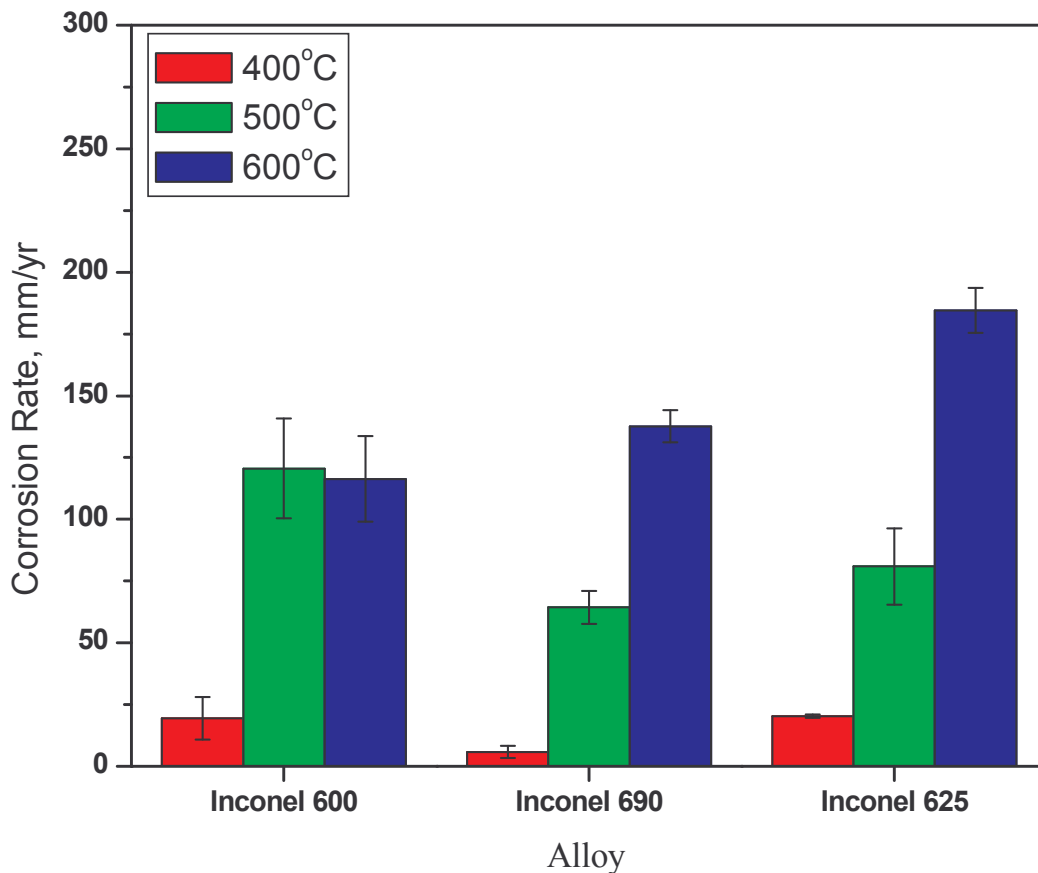
Figure 3.27. Average corrosion rate of Inconel alloys at different temperatures in molten LiCl–KCl salt for 2 h.

3.2.5.2 Surface morphology of corroded surfaces

Figures 3.28a-c, shows the SEM images of tested alloys after corrosion test. SEM images of all the attacked surfaces showed porous morphology due to the dissolution of alloying elements from the samples. The chemical composition from these attacked surfaces (AS) are analysed by EDX and are tabulated in Table 3.2. The EDX analysis clearly shows enrichment of Ni and depletion of Cr and Fe content on all the surfaces compared to the base metal composition. This clearly indicates preferential outward diffusion of elements during molten salt corrosion. The EDX analysis from Inconel 625 attacked surface shows enrichment of Mo on the surface. The enrichment of Mo on Inconel 625 attacked surface indicates development of Mo rich layer which could cause breakaway as discussed earlier.
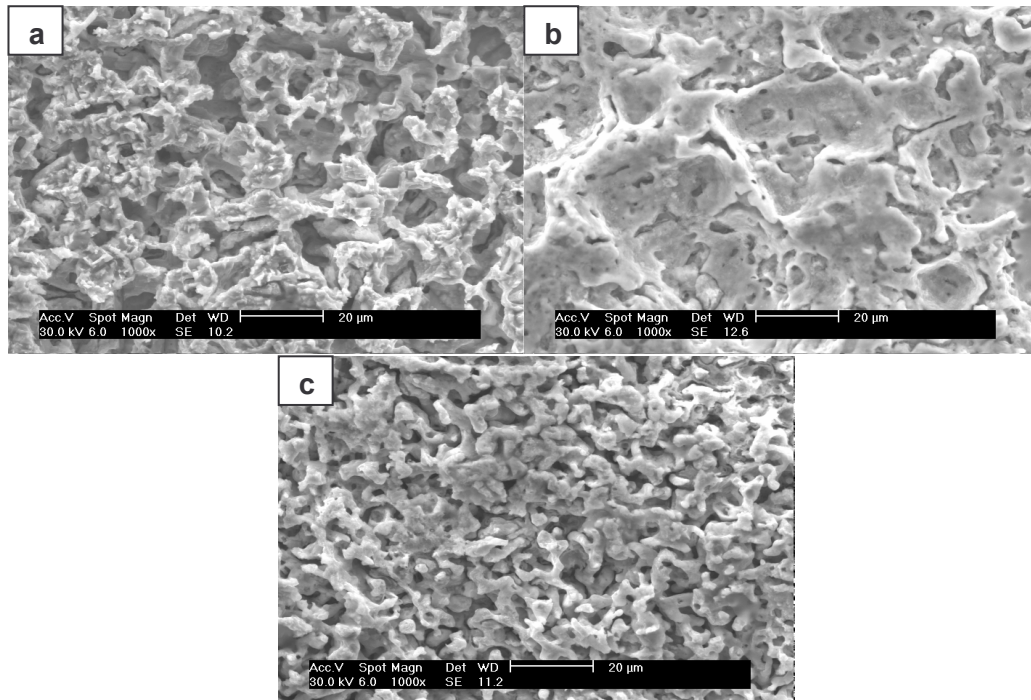
Figure 3.28. SEM images of 600°C/2 h attacked surface of (a) Inconel 600 (b) Inconel 625 and (c) Inconel 690 after corrosion test.

During corrosion test, the salt melt spreads and covers the whole surface of the sample causing a hot corrosion process [74]. The scales formed after corrosion test were brownish black in color and got detached from the sample, from all sides. This indicates that the molten salt has spread all over the sample and the alloy has undergone corrosion uniformly. Li et al. [91] studied the degradation of Ni, NiAl and FeAl alloys induced by $ZnCl_2$–KCl melt at 400^oC. They also observed that although only one big surface of each sample was initially coated with salt, all the surface of the corroded samples were covered with corrosion products, due to the flow of molten salt during the process. Figure 3.29a-c, shows the surface morphology of the detached scales formed on Inconel alloys after corrosion test.
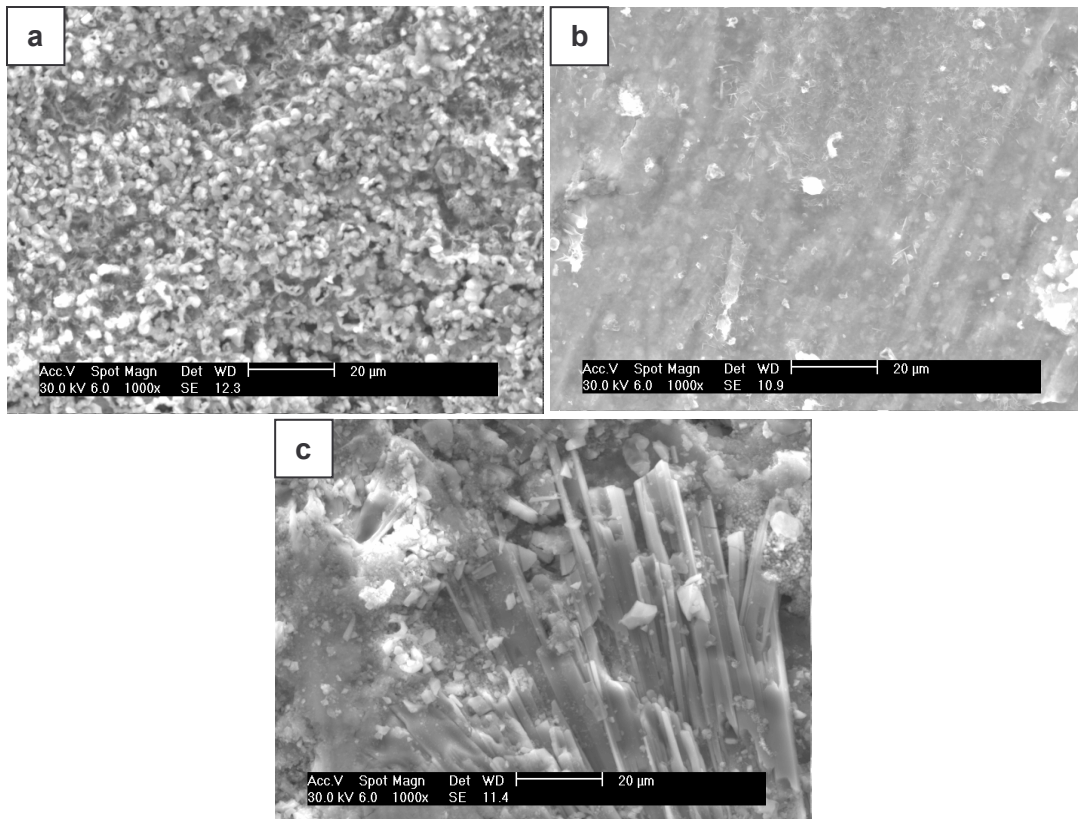
Figure 3.29. Surface morphology of the scale formed at 600^oC/2 h on (a) Inconel 600 (b) Inconel 625 and (c) Inconel 690 after corrosion test.

The surface morphology of Inconel 600 scale is porous in nature while for Inconel 625 and 690 smooth and dense surfaces were observed. Inconel 625 and Inconel 690 exhibited growth of corrosion product as layers (Figure 3.29b and 3.29c). Cho et al. [60] also showed that the scales on the alloys 800H and KSA-5 are porous and consisted of two phases: a dark matrix and light islands. The chemical composition from scales (S) as analysed by EDX are tabulated in Table 3.2. As seen from the table all the scales showed depletion of Ni. The EDX analysis of Inconel 600 scale showed enrichment of Cr and Fe, while Inconel 625 showed enrichment of Cr and Mo.

Table 3.2. Chemical composition of alloys in wt%; A-As received, AS- EDX analysis from attacked surface, S- EDX analysis from scales formed.

Material		Ni	Cr	Fe	Mn	Si	Al	Mo	Ti	Ta+Nb	K	Cl
Inconel 600	A	72	17	10	1	-	-	-	-	-	-	-
	AS	91.54	5.05	3.41	-	-	-	-	-	-	-	-
	S	4.01	75.60	12.45	-	1.72	1.58	-	1.17	-	0.98	2.48
Inconel 625	A	64.18	18.01	4.25	-	-	-	11.01	-	-	-	-
	AS	74.89	6.24	1.76	-	-	-	16.05	-	-	0.21	0.85
	S	4.56	17.43	0.90	-	0.60	1.07	15.52	0.92	26.67	9.33	23.02
Inconel 690	A	60	29.58	9.05	0.21	0.25	-	-	0.2	0.02	-	-
	AS	96.08	3.21	0.71	-	-	-	-	-	-	-	-
	S	4.70	36.34	4.38	-	-	7.98	-	0.93	8.88	13.98	22.8

Inconel 690 scale also shows enrichment of Cr. The enrichment of Ni and depletion of Cr on the attacked surfaces and enrichment of Cr and depletion of Ni in the scale clearly indicates preferential outward diffusion of Cr occurring from Inconel alloy surfaces to the scale during corrosion. Thus selective outward diffusion of Cr could be one of the common phenomena during molten salt corrosion. This will be discussed in detail in next section.

3.2.5.3 Cross section studies of corroded samples and scales

Figure 3.30 shows the EDX elemental X-ray maps from the cross section of Inconel alloys after corrosion test. As shown in Figure 3.30a, Inconel 600 top layer is enriched with Cr, and the layer beneath is enriched with Ni and depleted with Cr and Fe. As Cr has higher affinity towards oxygen, an outer Cr enriched layer and Ni rich layer beneath was observed as shown clearly for Inconel 600. It can be clearly seen from Figure 3.30a that the Cr enriched top layer on Inconel 600 is getting spalled off from Ni enriched layer beneath. Inconel 625 top layer is enriched with Si and depleted with Cr, Ni, Fe and Mn (Figure 3.30b). This shows that the Cr and Ni enriched layers on Inconel 625 got spalled off. Inconel 690 top layer is enriched with Ni and depleted with Cr and Mn (Figure 3.30c). It can be concluded from the X-ray maps (Figure 3.30) that Ni rich layer is adherent to the Inconel 600 and 690 substrates. Therefore the adherence of Ni rich layer could be responsible for improved corrosion resistance of Inconel 600 and 690. The top Cr rich layer spalled off and the intermediate Ni rich layer adherent is thus revealed on Inconel 690.
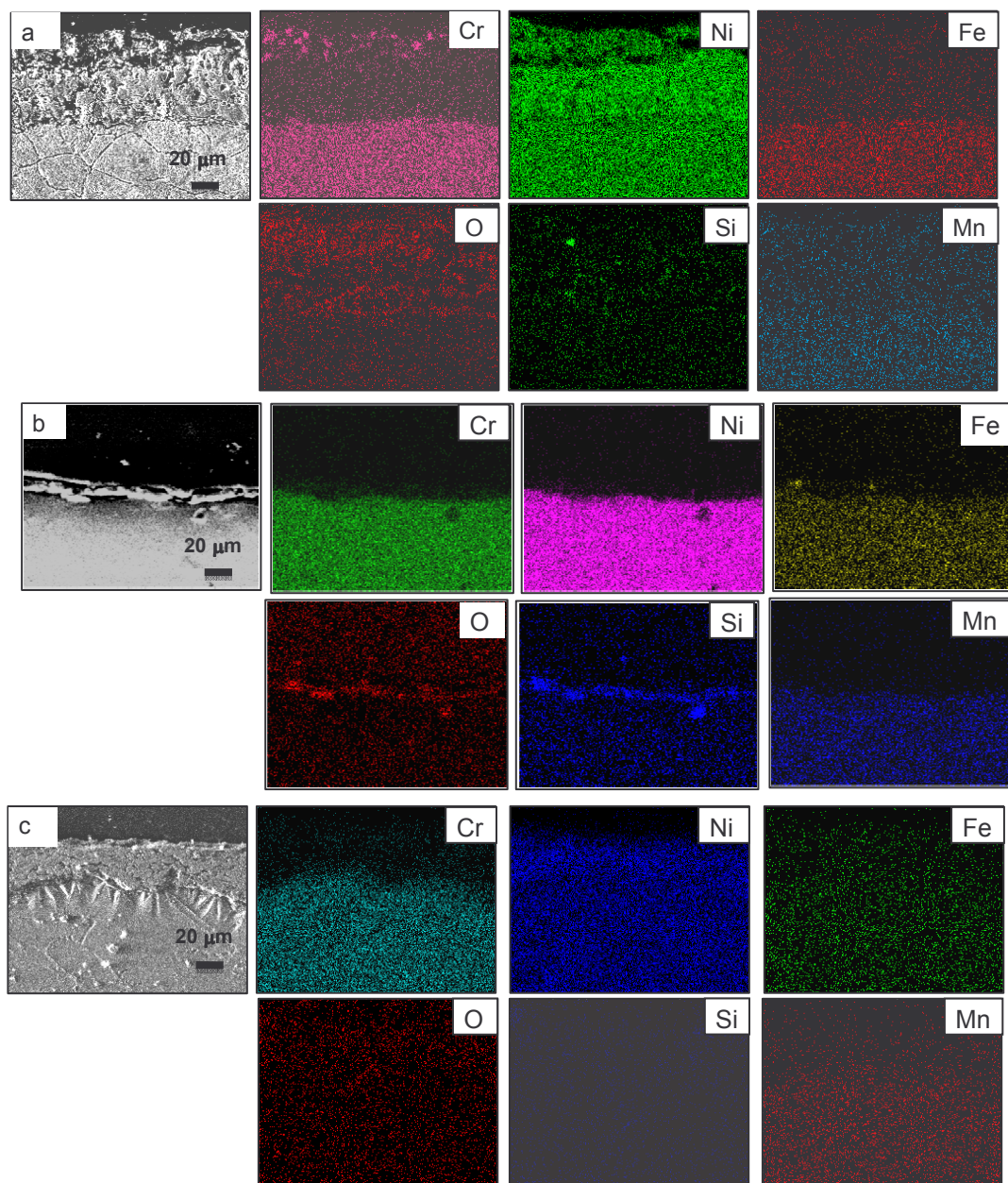
Figure 3.30. EDX X-ray maps from the cross section of (a) Inconel 600 (b) Inconel 625 and (c) Inconel 690 after corrosion test at 600°C/2 h.

This indicates that the growth and spallation of Cr and Ni rich layers occurs repeatedly. These results are in good agreement with the EDX analysis carried out on the attacked surfaces and scales. Oxygen is present in all the top layers indicating that these layers comprise predominantly oxides.

Figure 3.31 shows the cross section SEM micrograph with corresponding EDX line profile from the scales formed on Inconel alloys. As seen from the micrograph, the scales formed on Inconel 600 and 690 are thin (60 and 160 μm) compared to that on Inconel 625 (350 μm). In Inconel 600, 625 and 690, Cr and Ni enriched layers are evident within the scales. In comparison to Inconel 600, Inconel 625 exhibited a distinct separation of Cr rich and Ni rich layers (Figure 3.31b). Inconel 690 also showed the formation of separate Cr rich and Ni rich layers with an additional intermediate layer in the scale. Even though the cross section result of the exposed sample for Inconel 690 (Figure 3.30c) showed only Ni enriched layer, the cross section result of the scale for Inconel 690 (Figure 3.31c) showed Cr and Ni enriched layers. The cracks present along these separate layers are also visible in Figure 3.31c. Thus the EDX elemental maps of attacked surfaces and line profiles of scales reveal the formation of Cr and Ni rich layer. The evidence for Cr rich outer layer and Ni rich layer beneath as observed for 316L SS and Inconel 600 could not be seen for Inconel 690, because the rate of diffusion of Cr and Ni in these alloys would be different and therefore the time required for the formation and spallation of these well delineated Cr and Ni rich layers will be different. Exposures of these alloys for different times would more clearly show the formation and spallation of these layers. However, the Cr and Ni enriched layers shown in the cross section result of either scale (Figure 3.31 b&c) or exposed sample (Figure 3.30b&c), also indicates the

125

formation of Cr and Ni enriched layers. Thus the absence of Cr rich surface in Figures 3.30b&c indicates that the Cr rich layer could have spalled off. The interface region between the Cr rich layer and Ni rich layer could be the probable region for spallation to occur where spinel oxide could form.
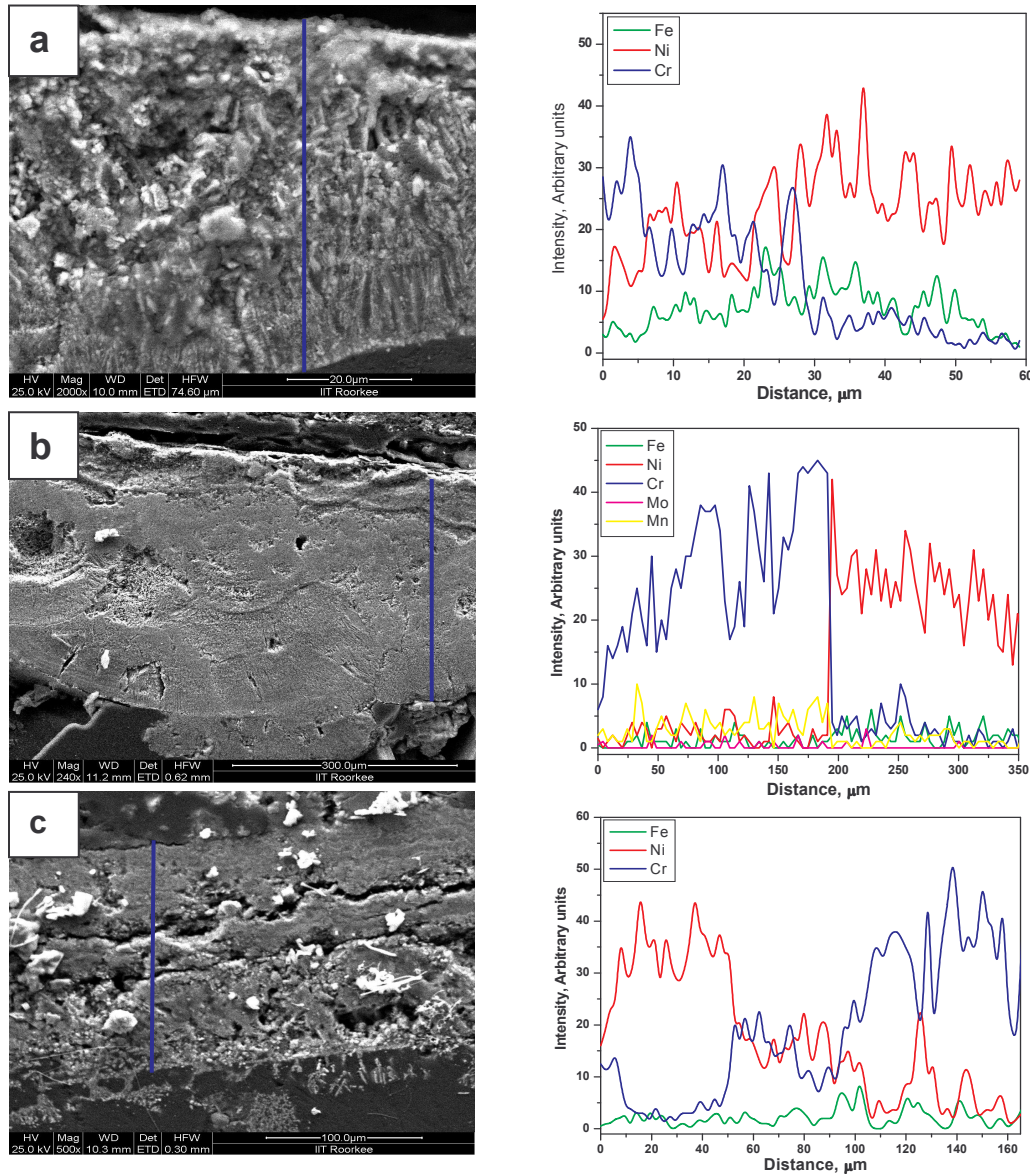
Figure 3.31. Cross section SEM micrograph with corresponding EDX line profile from the scale formed at 600°C/2 h on (a) Inconel 600 (b) Inconel 625 and (c) Inconel 690.

126

Thus it is evident that the cycle of growth of Cr and Ni enriched layers and spallation repeats as corrosion occurs. The present results also suggest that the mechanism of degradation of Ni-base alloys in molten LiCl–KCl is by selective outward diffusion of Cr and Ni, forming enriched layers and subsequent spallation. Thus from the results of the present study it is clear that Mo do not improve the corrosion resistance of Ni-base alloys in molten LiCl–KCl salt environment in air and Cr, Ni selectively diffuses outwards forming enriched layers and subsequently spalls. Cho et al. [56,57] and Kim et al. [92] found that Inconel 713LC showed the best performance among super alloys tested under LiCl–Li$_2$O molten salt [56,57,92]. The new alloy developed by Kim et al. [58] has similar composition with that of Inconel 713LC, but with reduced Si and Mo contents exhibited a much better corrosion resistance.

3.2.5.4 XRD analysis

GIXRD pattern of attacked surface of Inconel alloys after corrosion test is shown in Figure 3.32. As shown in Figure 3.32, the major reflections correspond to austenite (Fe$_{0.7}$Cr$_{0.19}$Ni$_{0.11}$) [33-0397] and Ni [04-0850] with a minor NiO [44-1159] phase. Except Inconel 625 all the alloys exhibited Ni phase, and Inconel 625 has shown a major austenite reflection indicating the presence of Fe and Cr rich layer on the surface. The major Ni phase in all the alloys also clearly indicated that selective leaching/dealloying has occurred on the surface leaving a Ni rich layer.

Figure 3.33 shows the XRD pattern of scales formed on Inconel alloys after corrosion test. The XRD pattern indicate that Cr$_2$O$_3$ [38-1479], NiO [44-1159], and KCl [41-1476] are the phases present in various proportions in all the scales. Spinel oxide
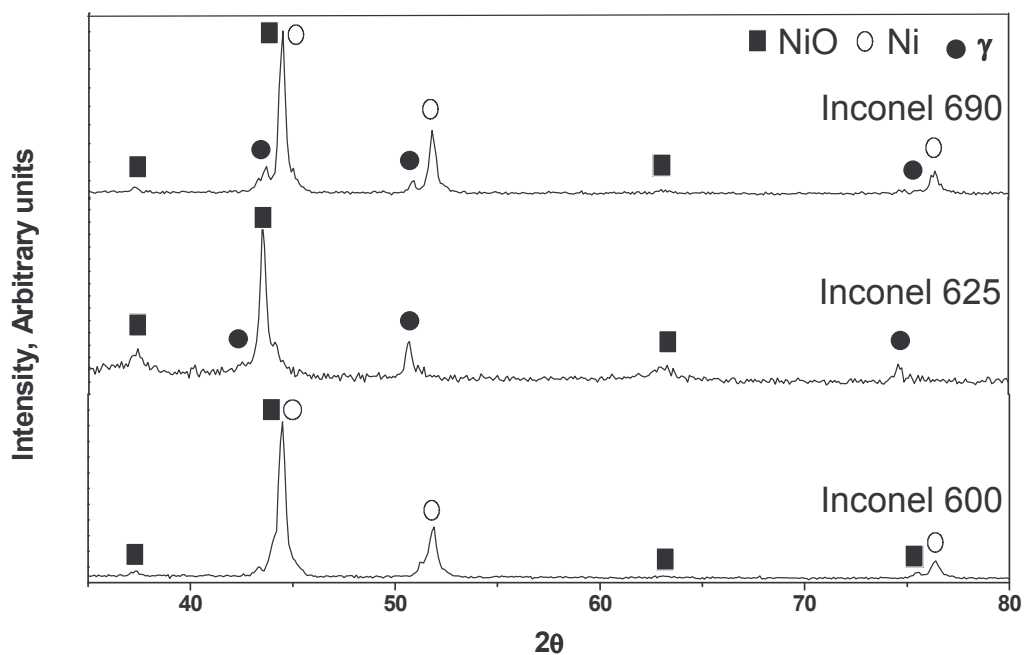
Figure 3.32. GIXRD pattern of attacked surface of Inconel alloys after corrosion test at 600°C/2 h.
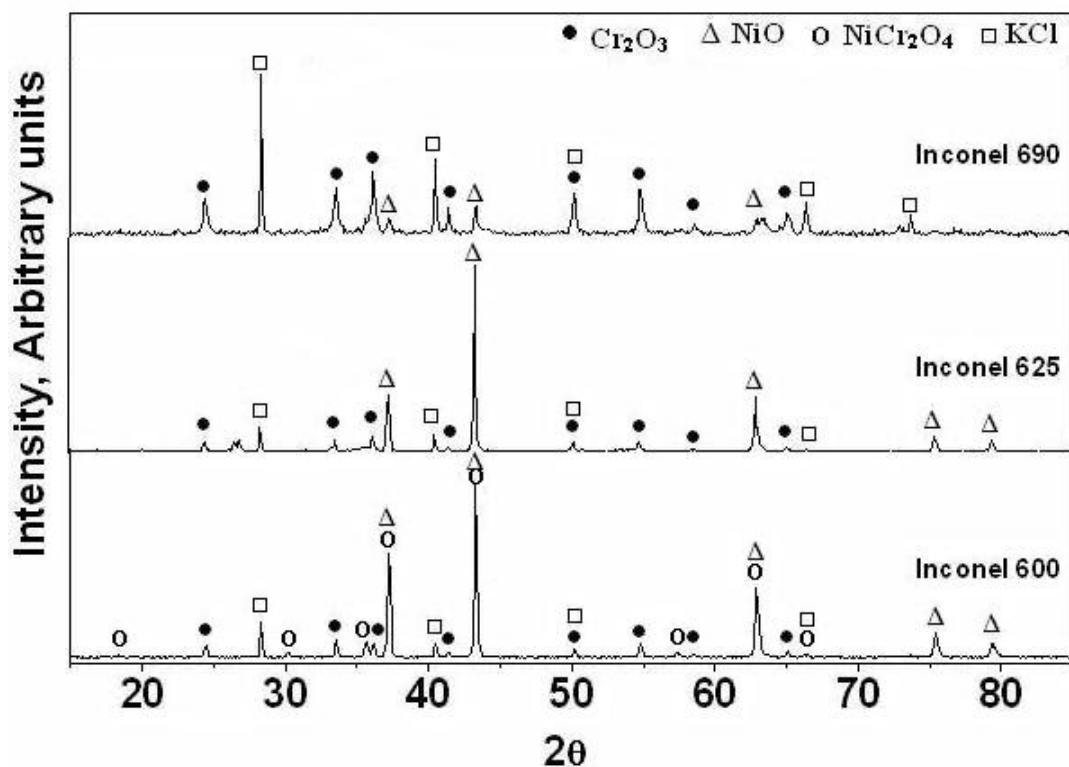
Figure 3.33. XRD pattern of scales formed at 600°C/2 h on Inconel alloys after corrosion test.

NiCr$_2$O$_4$ [88-0108] was observed in the scale of Inconel 600. Apart from oxides and spinel phases, the scales consisted of substantial amounts of KCl.

From a thermodynamic point of view, Cr$_2$O$_3$ is the most stable oxide in Ni-Cr-Fe based alloys [56,58]. In the present study Cr$_2$O$_3$ is formed on all the alloys tested as obviously Cr$_2$O$_3$ is the most stable oxide. The Ni and Fe based oxides are formed by the external diffusion of the Fe and Ni ion through the initially formed Cr based oxide layer [59]. Concurrently, NiFe$_2$O$_4$, a spinel oxide forms by a solid-state reaction with the surface generated Fe$_2$O$_3$ and NiO [58]. It is reported that a solid state reaction between NiO and Cr$_2$O$_3$ might cause the formation of the NiCr$_2$O$_4$ spinel oxides [56,57,93]. In the present study the formation of NiCr$_2$O$_4$ spinel oxide was found apart from Cr$_2$O$_3$ and KCl. The results of Park et al. [94] indicates that a new mixed metal oxide such as NiFe$_2$O$_4$ is formed during the corrosion process, as confirmed by the X-ray diffraction study. In the present and earlier studies, Fe and Mo were detected by EDX in the corrosion products after the corrosion tests, however, Fe and Mo rich corrosion products were not detected in XRD. It is reported that Fe in the alloys is dissolved into the molten mixture by some unknown mechanisms [60]. Phases such as potassium chromate and other Li containing oxides were not observed in the present study. These phases could form on long exposure times and some of these oxides could be present in the form of spinels. The test duration in the present study was confined to 2 h as the weight loss and attack was significant due to severe corrosive environment. The fraction of alloying additions like Al and Si present in Inconel alloys could also play a vital role in the corrosion process, and therefore all the changes could not be explained.

3.2.5.5 LRS analysis

The Raman spectra of the scales formed on Inconel alloys is shown in Figure 3.34. The Raman peaks at 549 cm^{-1} and 690 cm^{-1} correspond to Cr_2O_3 and spinel oxides respectively. The broad peak at 824 cm^{-1} could be attributed to the Cr(VI) oxide possibly Fe-Ni-Cr spinel oxide. Thus it was evident from XRD and laser Raman spectroscopy that the corrosion product was mainly oxides and spinel phases.

From the EDX, XRD and laser Raman spectroscopy results it is evident that the corrosion product consists of Cr_2O_3, NiO and $NiCr_2O_4$. Thus based on the results obtained the mechanism of corrosion of Ni base alloys (Inconel 600, Inconel 690, Inconel 625) exposed to molten LiCl–KCl salt under air environment is shown in Fig 3.35. The mechanism is similar to that of 316L SS exposed exposed to molten LiCl–KCl salt under air environment. The mechanism involves selective outward diffusion of Cr, and formation of Cr_2O_3 layer and NiO inner layer.
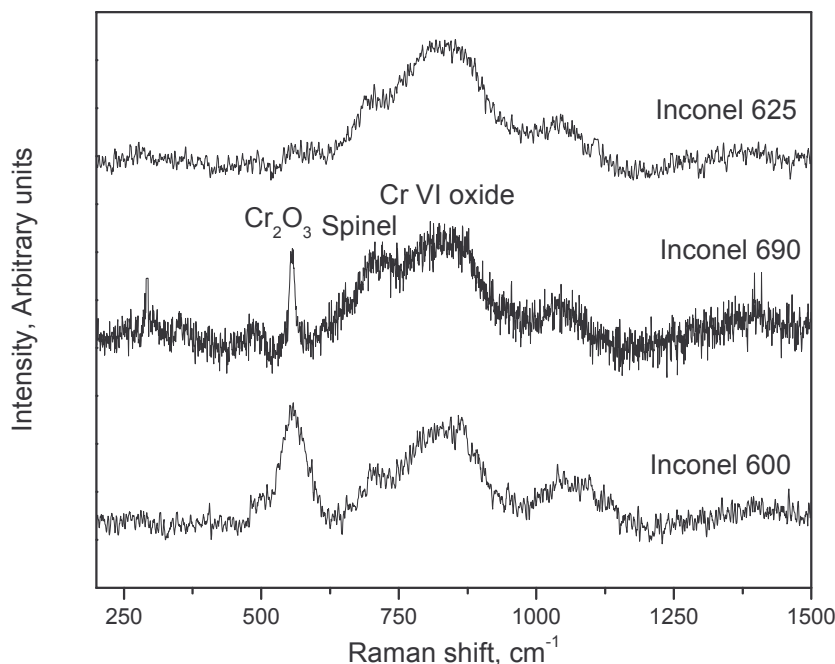
Figure 3.34. Laser Raman spectra of scales formed at 600°C/2 h on Inconel alloys.
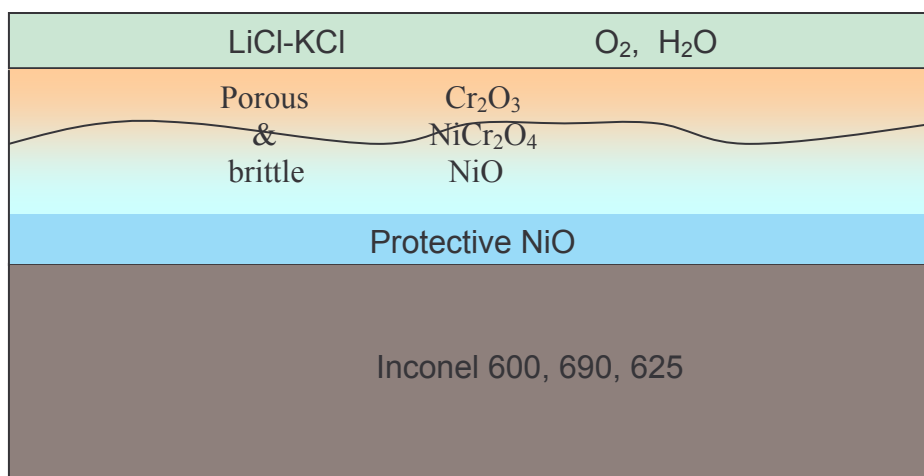
Figure. 3.35. Mechanism of corrosion of Ni base alloys exposed to molten LiCl–KCl salt under air environment.

The solid state reaction between the two layers results in the formation of spinels ($NiCr_2O_4$) which causes cracks at the interface. However, the dense and adherent NiO layer underneath the porous & brittle salt film decreases the rate of formation of layers and hence shows relatively less corrosion. The presence of NiO is evident from the GIXRD patterns from the attacked surfaces of Ni base alloys (Inconel 600, Inconel 690, Inconel 625) shown in Fig 3.26a and Fig 3.32.

3.2.6 Summary

1. Corrosion tests performed on EF Ni and EF Ni-W in molten LiCl–KCl salt in air showed that the percentage weight loss for EF Ni with Ni-20 wt% tungsten coating showed improved corrosion resistance than EF Ni alone.

2. Characterisation of salt films formed on EF Ni by XRD, SEM and EDX showed the presence of two distinct layers Ni rich and Ni depleted. The salt film comprises of mainly thick, porous and brittle NiO, with KCl penetrating in to the salt film and

accelerating the corrosion. XRD and Laser Raman spectroscopy analysis also confirmed the presence of NiO in the salt film.

3. The presence of cracks in EF Ni-W due to stresses are found to be detrimental from the corrosion resistance point of view, however, the presence of protective tungsten rich NiO films on the surface might have resulted in improved corrosion resistance.

4. Type 316L stainless steel exhibited highest percentage weight loss when compared to EF Ni, EF Ni-W and Ni base alloys. Characterisation of salt films formed on 316L SS by XRD, SEM and EDX revealed the selective diffusion of Cr and Ni to the surface with the formation of Cr_2O_3, NiO and $NiCr_2O_4$ and subsequent spallation.

5. Corrosion tests performed on Inconel 600, Inconel 625 and Inconel 690 in molten LiCl–KCl salt in the presence of air indicated that Inconel 600 and Inconel 690 showed better corrosion resistance compared to Inconel 625. The results indicated that Mo containing Inconel 625 do not improve the corrosion resistance in molten LiCl–KCl salt at high temperature in the presence of air.

6. EDX analysis of Ni base alloy corroded surfaces and scales indicated preferential outward diffusion of elements during molten salt corrosion. Cross section SEM and EDX analysis of scales and exposed samples also indicated that the mechanism of corrosion is due to selective outward diffusion of Cr and Ni, and formation of Cr and Ni rich layers and subsequent spallation.

7. XRD and LRS analysis of Ni base alloy scales revealed the presence of Cr_2O_3, NiO and spinel oxides apart from KCl.

3.3 CORROSION IN MOLTEN SALT UNDER UHP ARGON

Electrorefining is the foremost important step in pyrochemical reprocessing and the process involves use of molten LiCl–KCl eutectic salt as electrolyte floating on a liquid cadmium with temperatures around 500°C under an argon atmosphere [13,18]. Understanding the degradation of candidate materials in the presence of molten salt and liquid cadmium is essential for the design of various critical components and also for the successful operation of pyrochemical reprocessing plant as the process is carried out remotely under intense radioactive environment. It is essential to choose a container material for electrorefining which is noble and displacement reaction with molten salt and liquid cadmium is negligible [38]. It is reported that molten Cd leaches Ni and therefore the container material should be made with Ni free material [21]. Low carbon and Cr-Mo steels can be conveniently used as container material as molten Cd present in the electrorefiner protects the steel container since CdCl$_2$ is more stable than FeCl$_2$ [20]. The solubility of iron in molten Cd at 480°C is reported as 2.8 × 10^{-4} wt% and low carbon steels were also reported resistant to attack by molten chlorides [20]. Cr-Mo steels are used widely in process industries because they offer high strength at elevated temperatures combined with adequate toughness and corrosion resistance. 2.25Cr-1Mo steel was used for electrorefining process vessel for EBR II Fuel Conditioning Facility at Argonne National Laboratory, USA [95]. Based on international experience 2.25Cr-1Mo steel was chosen as the initial candidate material for the fabrication of electrorefiner vessel. 9Cr-1Mo steel is preferred over 2.25Cr-1Mo steel because of its good high temperature properties and good corrosion resistance properties in chloride environment. Because 9Cr-1Mo steel has good high temperature corrosion resistance properties, it is

considered as an alternative candidate material for the fabrication of electrorefiner vessel in pyrochemical reprocessing plant.

Nickel possesses high corrosion resistance in molten chloride as well as in molten fluoride [48] and is employed for applications at elevated temperature [82]. Therefore Ni base alloys were considered as candidate materials for the fabrication of transfer lines of salt purification system where Cd free molten LiCl–KCl salt is exposed.

Thus Cr-Mo steels, Ni-base alloys and high density graphite will be utilized in the high temperature molten chloride salt under ultra high purity argon environment for undertaking various unit operations like salt preparation and electrorefining. The aim of the present study is to determine the corrosion behaviour of candidate materials like 2.25Cr-1Mo, 9Cr-1Mo, Inconel 600, Inconel 625 and Inconel 690 in molten LiCl–KCl eutectic salt under ultra high purity argon atmosphere exposed for various durations and understand the degradation behaviour.

3.3.1 Corrosion of Cr-Mo steels

3.3.1.1   *Weight loss studies*

Figure 3.36 shows the percentage weight loss of candidate materials exposed to molten LiCl–KCl salt at 600°C for different time of exposure. From the percentage weight loss values of 2.25Cr-1Mo and 9Cr-1Mo it can be inferred that 2.25Cr-1Mo suffers more corrosion attack when compared to 9Cr-1Mo. For instance, at 600°C the percentage weight loss for 9Cr-1Mo is 0.31% while the percentage weight loss for 2.25Cr-1Mo steel is 0.88% for 100 h of exposure. The percentage weight loss of high density graphite samples exposed to molten LiCl–KCl salt at 600°C were also plotted for comparison purpose.
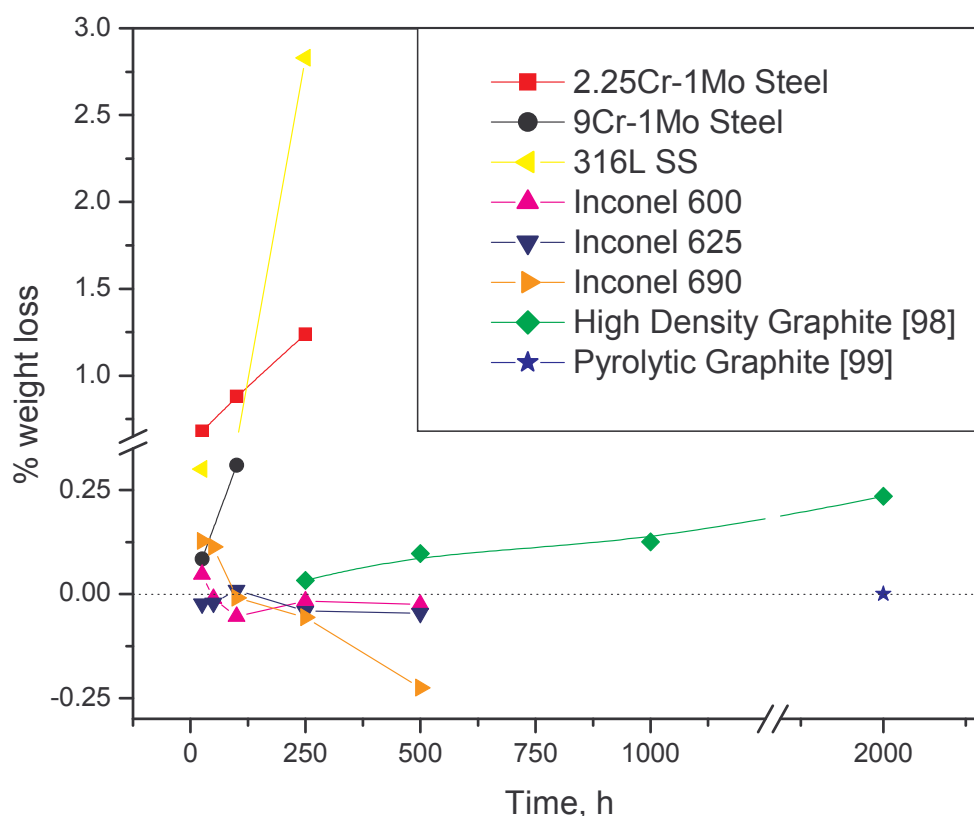
Figure 3.36. Percentage weight loss of candidate materials exposed to molten LiCl–KCl salt at 600°C.

High density graphite tested up to 2000 h suffers minor attack compared to both 2.25Cr-1Mo and 9Cr-1Mo steel as shown in the figure.

3.3.1.2 Surface morphology of exposed Cr-Mo steel surfaces

The SEM micrographs from corrosion product region, from matrix adjacent to the corrosion product (attacked region) and vapour exposed region of 2.25Cr-1Mo steel samples tested in molten LiCl–KCl salt at 600°C for 25, 100 and 250 h are shown in Figure 3.37. The corrosion product region exhibited faceted grains while the attacked region exhibited porous morphology. The increase of molten salt attack on attacked region with increase in exposure time can be clearly seen from the SEM micrographs of

135

	25 h	**100 h**	**250 h**

Corrosion product region

Attacked region

Vapour exposed region
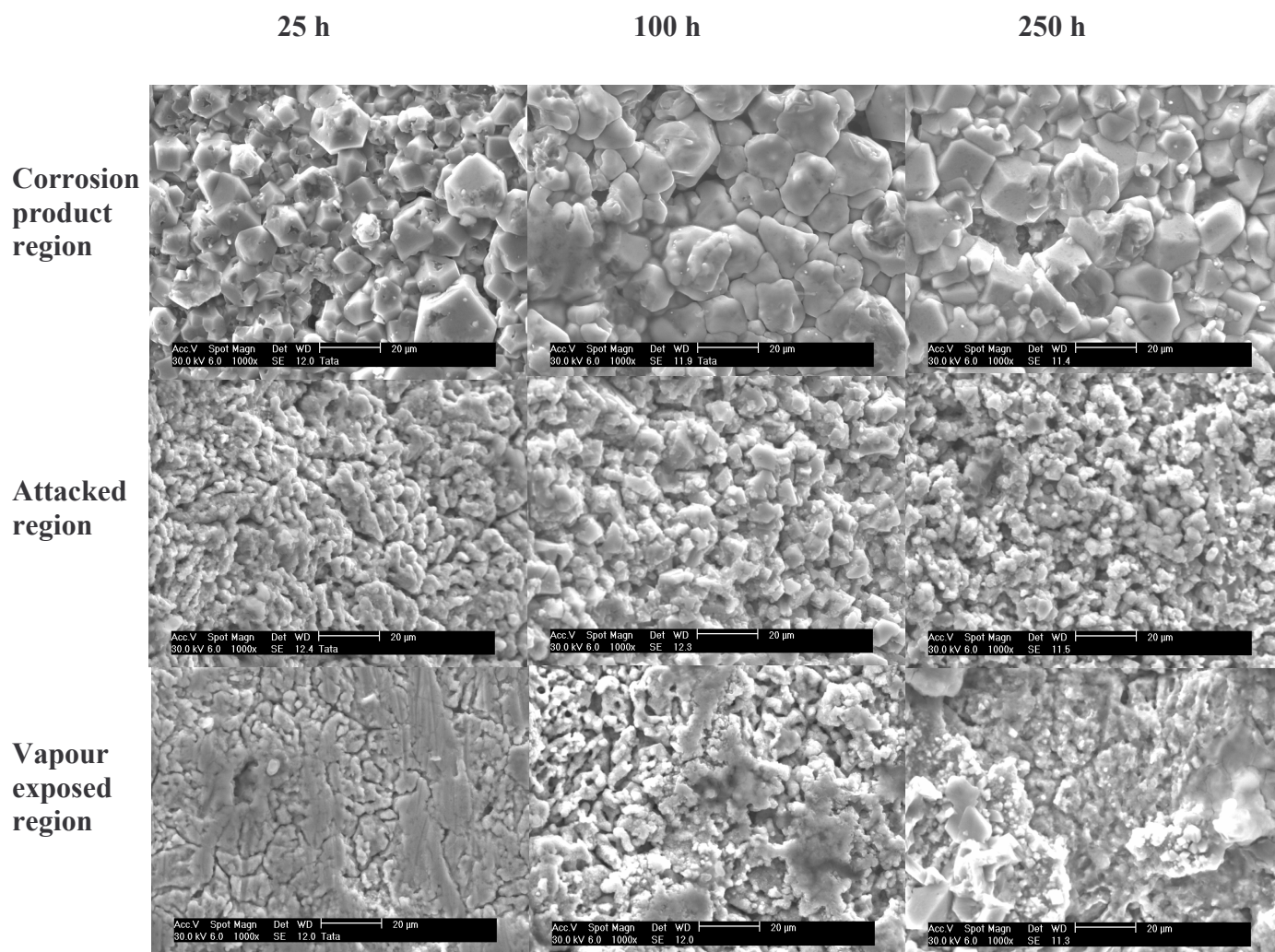
Figure 3.37. SEM micrographs from corrosion product region, attacked region and vapour exposed region of 2.25Cr-1Mo steel exposed to molten LiCl–KCl salt for 25, 100 and 250 h.

samples. Similarly the surface morphology of 25 h vapour exposed sample showed lesser attack and the attack was significant in the case of 100 h exposed sample and is severe in 250 h exposed sample. The porous morphology of attacked and vapour exposed region is attributed to the preferential leaching of elements from the surface and formation of corrosion products as can be seen clearly from the SEM micrographs. The chemical composition as analysed by EDX from 2.25Cr-1Mo exposed for 25 h are 95.28% Fe,

2.56% Cr and 2.16% Mo. Minor enrichment of Cr was observed after 250 h exposure as analysed by EDX. This indicates that in the attacked region Cr is preferentially leached by the corrosive molten salt and the corrosion product formed spalled out.

The SEM micrographs of 9Cr-1Mo steel exposed to molten LiCl–KCl salt at 600°C for 25 and 100 h from corrosion product region, attacked region and vapour exposed region are shown in Figue 3.38.

25 h   **100 h**
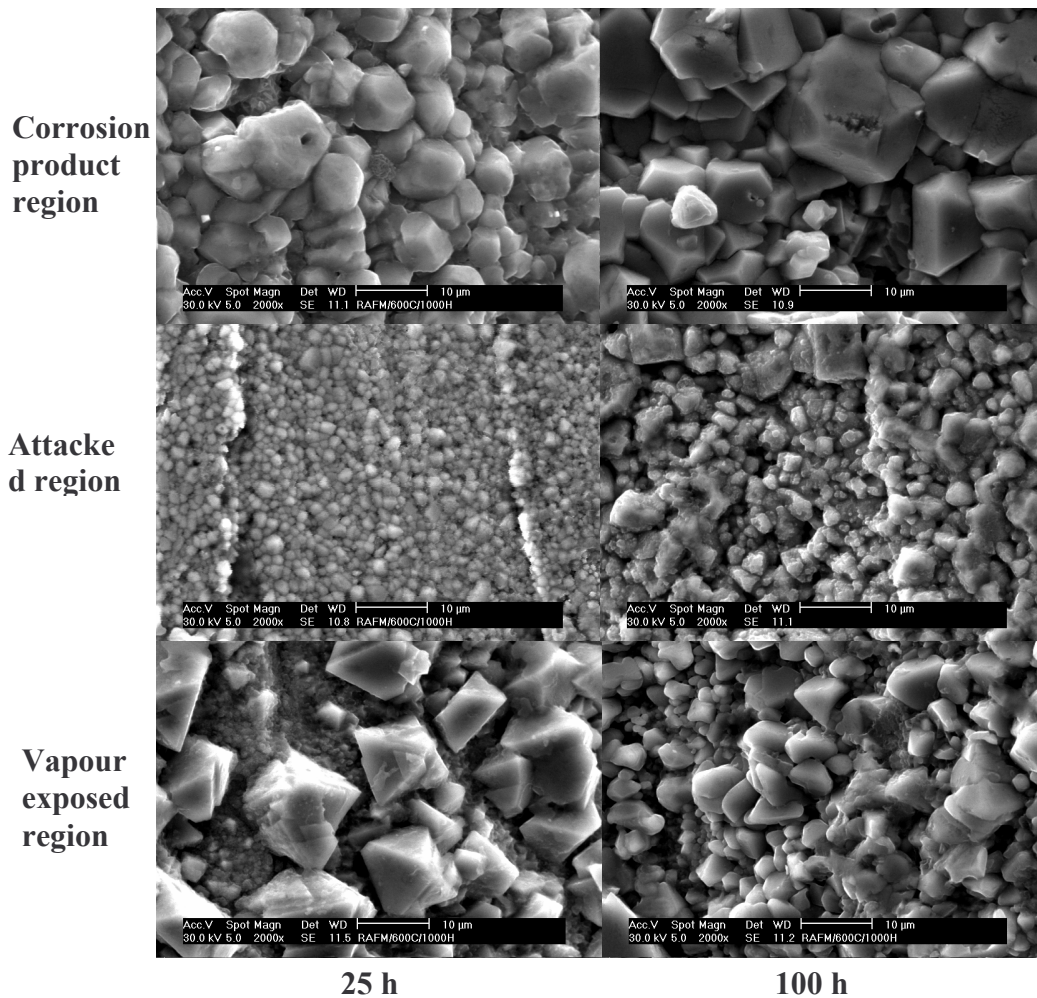
Figure 3.38. SEM micrographs from corrosion product region, attacked region and vapour exposed region of 9Cr-1Mo steel exposed to molten LiCl–KCl salt for 25 and 100 h.

The surface morphology of corrosion product region for the 9Cr-1Mo steel exposed samples is similar to that of 2.25Cr-1Mo steel sample, indicating uniform accelerated attack. EDX analysis of attacked region of 9Cr-1Mo steel sample also showed depletion of Cr compared to that of the base metal composition. This indicates that 9Cr-1Mo steel also corrode in molten salt by preferentially leaching of Cr and spallation of the corrosion product formed. The surface morphology of vapour exposed region of 9Cr-1Mo steel also exhibited isolated corrosion products on the surface as shown in Figure 3.38. Totemeier et al. [96] also reported that 2.25Cr-1Mo and 9Cr-1Mo-V steel severely oxidised in molten LiCl–3.5wt% Li_2O and 1 wt% Li_3N at 725°C and the mechanism of corrosion was attributed due to depletion of Cr.

3.3.1.3 Characterisation of exposed surfaces by GIXRD

GIXRD pattern of 2.25Cr-1Mo steel exposed for 250 h and 9Cr-1Mo steel exposed for 100 h is shown in Figure 3.39. Both the GIXRD pattern showed a peak at 44.6 indicating the presence of cubic Fe [06-0696]. The peaks in GIXRD pattern for 9Cr-1Mo matched to FeO [46-1312]. As the free energy of formation of $FeCl_2$ from FeO is more favourable in comparison with Ni, active oxidation is easy in Cr-Mo steels than in Ni base alloys.
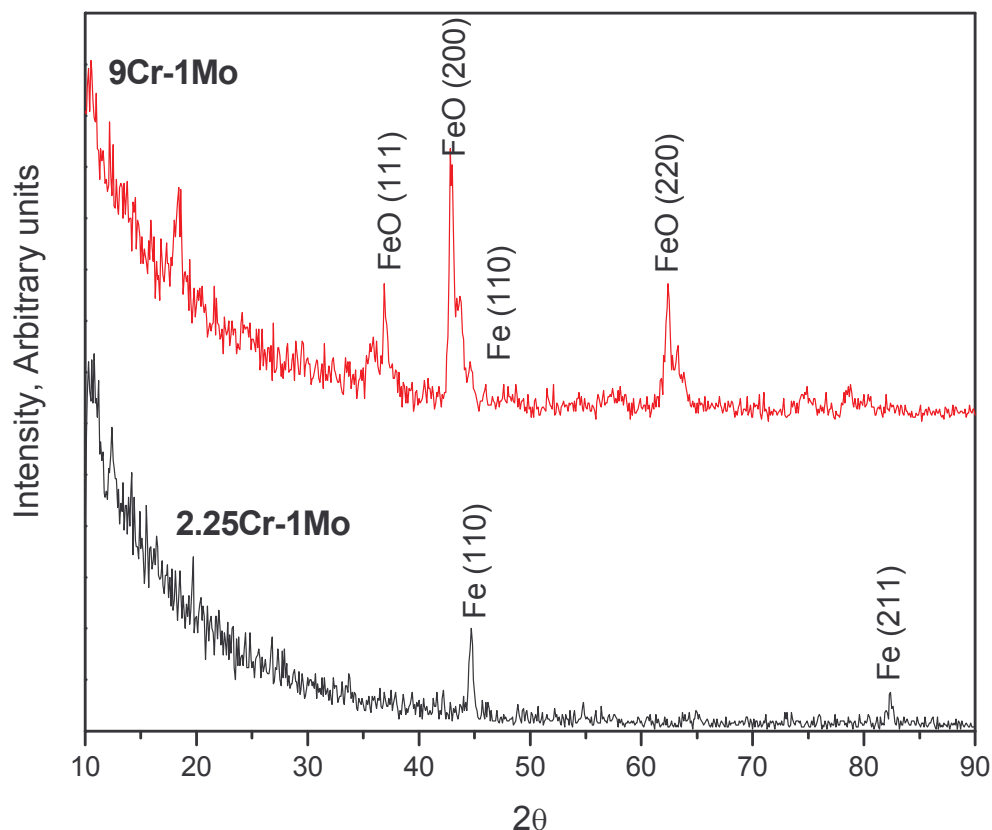
Figure 3.39. GIXRD pattern of 2.25Cr-1Mo steel surface exposed for 250 h and 9Cr-1Mo steel surface exposed for 100 h in molten LiCl–KCl salt at 600°C.

3.3.2 Corrosion of type 316LSS

The weight loss percentage of 316L SS samples exposed to molten LiCl-KCl eutectic salt at 600°C for 25, 100 and 250 h were 0.3, 0.45 and 2.83 respectively. The weight loss percentage of 316L SS samples increased with increasing duration of exposure. During exposure of sample for 250 h, the accidental ingression of moisture and O_2 in to the SS cell resulted in accelerated percentage weight loss. Material compatibility tests carried out by Totemeier et al. [96] on 2.25Cr-1Mo, 9Cr-1Mo-V, type 304, 316L and 347 in molten LiCl–3.5wt% Li_2O and 1 wt% Li_3N at 725°C upto 90 days showed that little corrosion was observed for type 347 SS and 2.25Cr-1Mo and highest corrosion was

observed for 316L SS and 9Cr-1Mo-V. It was also reported that the extent of corrosion observed were too erratic to formulate meaningful corrosion rates, and oxygen contamination was considered as a likely factor [96]. Therefore minor differences in oxygen contamination during the test, results in differences in corrosion behaviour. Hence, it is essential to precisely control the oxygen, moisture and nitrogen content during molten salt corrosion test. Therefore long term corrosion tests under precisely controlled argon atmosphere need to be carried out to make concrete conclusions and understand the nature of attack and reactions taking place.

The SEM micrograph showing the surface morphology of 316L SS samples exposed to LiCl–KCl eutectic salt at 600°C for 25 and 100 h are presented in Fig 3.40a and b, respectively. The surface morphology indicated two distinct regions. In Fig 3.40a and b, the black colour regions represent the corrosion product and white colour region represent the attacked surface. The surface morphology from the attacked region of 316L SS exposed for 25 and 100 h are shown in Fig 3.40c and d respectively. The figures clearly depict the porous nature of the surface and the pore size is getting enlarged with increasing duration of exposure as shown in the figure. The surface morphology of the corrosion product region exposed for 25 and 100 h are shown in Fig 3.40e and f, respectively. The morphology of corrosion product changed with increasing duration of exposure. In order to further understand the nature of corrosion product, EDX analysis was carried out on the attacked region and the corrosion product region of 316L SS exposed for 100 h.
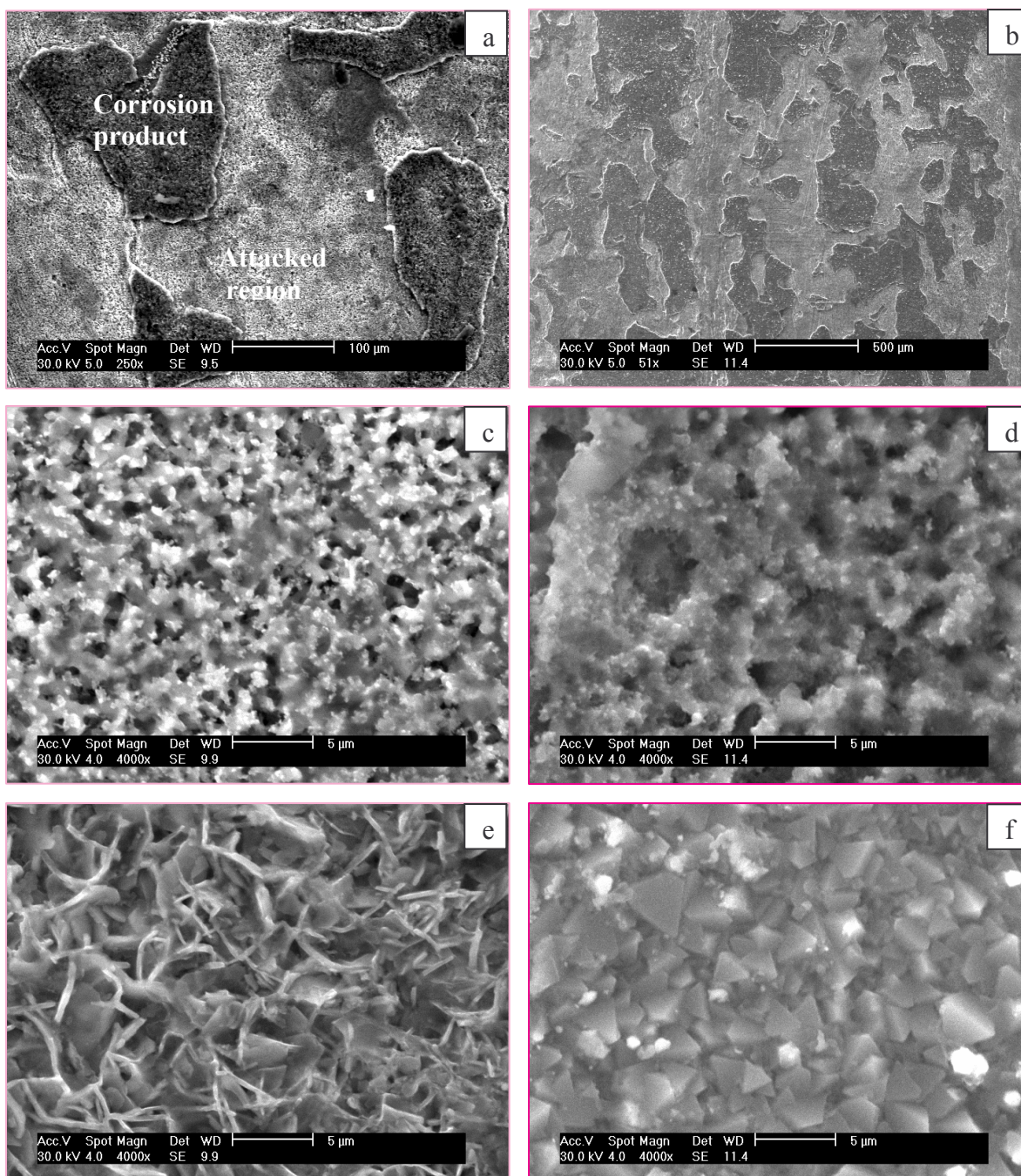
Figure 3.40. SEM micrographs of 316L SS exposed to molten LiCl–KCl eutectic salt for (a) 25 h (b) 100 h, (c) and (d) from attacked region for 25 h and 100 h, (e) and (f) from corrosion product region for 25 h and 100 h.

The EDX spectrum from the attacked region and corrosion product region are presented in Fig 3.41a and b, respectively. The EDX spectrum from the corrosion product region is rich in Cr, while those of attacked region shows Fe, Ni, and depletion of Cr. The composition in wt% of attacked region as determined by EDX is Fe - 69.69, Ni - 20.95, Cr - 6.54, S - 2.06, Cl - 0.75 and that from corrosion product is Cr - 78.45, Fe - 17.76, Ni - 3.05, Cl - 0.74. Thus the surface morphology of the corrosion product region is found to be rich in Cr, and the attacked region is depleted of Cr.

General or uniform, metal oxidation and dissolution is one of the common form of molten salt corrosion. Selective leaching is also very common mode of attack at high temperatures in molten salt corrosion [97]. The chromium depletion can occur by the formation of a chromium compound at the surface and by the subsequent removal of chromium from the matrix, leaving a depleted region forming voids [97]. Thus the mechanism of corrosion appears to be due to selective dissolution of Cr and formation of chromium rich compound at the surface as observed earlier in molten salt under air environment.
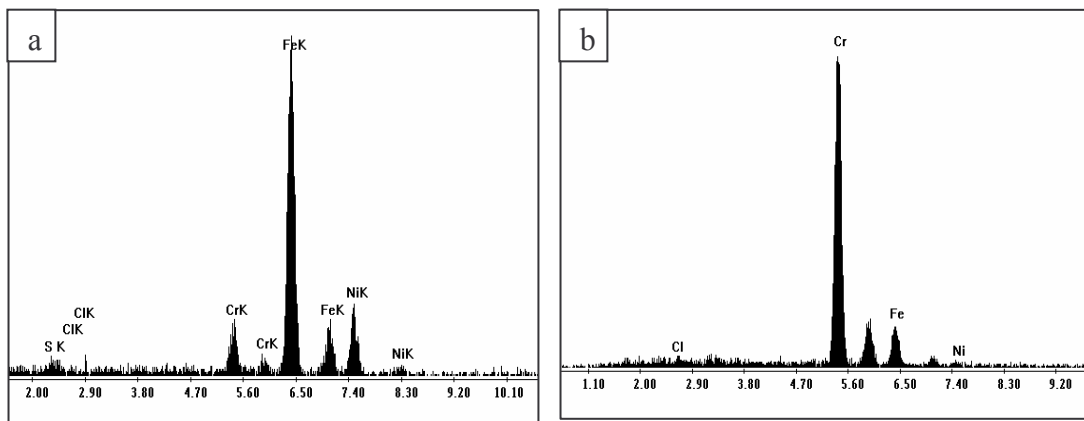
Figure 3.41. EDX spectra of 316L SS exposed to molten LiCl–KCl eutectic salt for 100 h (a) from the attacked region and (b) from the corrosion product region.

142

Cross section SEM micrographs of 316L SS exposed for 25, 100 and 250 h shown in Fig 3.42a, b and c, respectively, revealed the presence of voids. The thickness of the degraded layer containing voids increased with increasing duration of exposure and the spallation of chromium rich compound was also clearly revealed for the sample exposed for 250 h as shown in Fig 3.42c. X-ray elemental maps from cross section of 316L SS exposed for 250 h to molten LiCl–KCl eutectic salt for Cr, Ni, Fe and Si are shown in Fig 3.43b, c, d and e, respectively, taken from the region shown in Fig 3.43a. The SEM micrographs and cross section elemental maps clearly reveal a three layered structure. The layer A is a chromium rich compound, layer B containing voids is depleted of chromium and enriched with Ni, and, layer C is the substrate as shown in the figure. Fe has undergone dissolution in layer A, while the Si distribution was even in all the three layers.
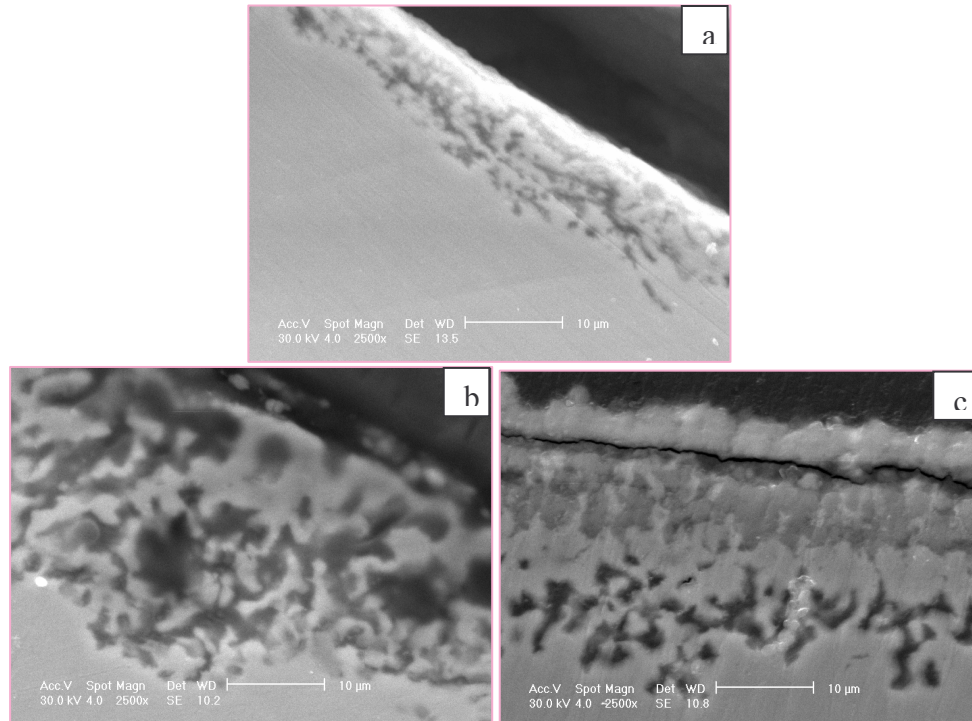
Figure 3.42. Cross section SEM micrographs of 316L SS exposed to molten LiCl– KCl eutectic salt for (a) 25 h (b) 100 h and (c) 250 h.

The enrichment of Cr towards the top surface and a Cr depleted layer below it with voids indicated that the mechanism of corrosion is by selective diffusion of Cr to the surface with the formation of voids below and formation of chromium rich compound at the surface and subsequent spallation. This mechanism of corrosion of corrosion of 316L SS in molten LiCl–KCl salt is similar to that under air environment as illustrated schematically in Fig 3.23. The formation of Cr rich and depleted layers with subsequent spallation is more clearly evident after exposure to molten LiCl–KCl salt under argon as shown in Fig 3.43.
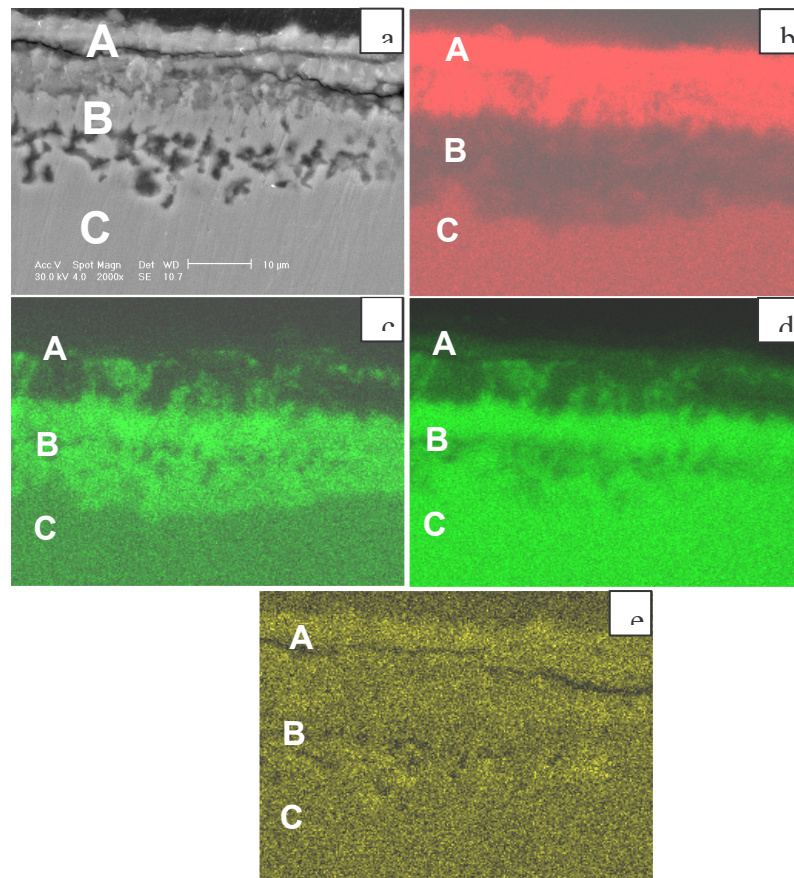
Figure 3.43. (a) Cross section SEM micrographs of 316L SS exposed to molten LiCl–KCl eutectic salt for 250 h from which X-ray elemental maps of (b) Cr (c) Ni (d) Fe and (e) Si are shown.

3.3.3 Corrosion of Inconel 600, 625 and 690 Alloys

3.3.3.1 Weight loss studies

Inconel 600, Inconel 625 and Inconel 690 samples exhibited a decreasing trend of weight loss with increasing time of exposure and weight gain was observed. Inconel 690 showed weight loss for the sample exposed for 25 h and 50 h, there after increase in weight gain with increase in time of exposure was observed. Similar trend was observed for Inconel 600 samples also. Inconel 625 samples exhibited only minor increase in weight gain with increase in time of exposure. The formation of adherent corrosion products on the surface of the sample would have contributed to the weight gain. This will be discussed in detail in next section. The weight loss of samples could be attributed to the loose oxide layer formed unevenly during short exposure period of 25 and 50 h which detached during cleaning process. It can be inferred from the weight loss measurements of Ni base alloys that Inconel 600, Inconel 625 and Inconel 690 suffers less corrosion attack when compared to Cr-Mo steels, stainless steel and graphite. The Gibbs free energy change of $FeCl_2$ formation is more negative than $NiCl_2$ formation which makes nickel base alloys more resistant than steels. The standard Gibb's free enrgy change for the formation of $FeCl_2$ and $NiCl_2$ is shown below.

$Fe + Cl_2(g) \rightarrow FeCl_2$ $\quad\quad\quad\quad\quad \Delta G° = -232.16$ kJ/mol (at $600°C$) ....Eq. (3.1)

$Ni + Cl_2(g) \rightarrow NiCl_2$ $\quad\quad\quad\quad\quad \Delta G° = -174.21$ kJ/mol (at $600°C$) .....Eq. (3.2)

$FeO + Cl_2(g) \rightarrow FeCl_2 + ½ O_2$ $\quad\quad \Delta G° = -24.36$ kJ/mol (at $600°C$) ....Eq. (3.3)

$NiO + Cl_2(g) \rightarrow NiCl_2 + ½ O_2$ $\quad\quad \Delta G° = -14.17$ kJ/mol (at $600°C$) ....Eq. (3.4)

As discussed earlier studies on Inconel 600, Inconel 625 and Inconel 690 in air and chlorine atmosphere has shown that Inconel 600 and 690 exhibited better corrosion resistance compared to Inconel 625. However such a comparison of corrosion resistance of Ni base alloys tested under ultra high purity argon gas environment could not be made as the results were found to be more or less similar. The increase in corrosion rate of Inconel 625 in comparison to Inconel 600 and Inconel 690 in molten LiCl–KCl salt under Cl_2 and air environment was attributed to the presence of Mo which could lead to the formation and breakaway of low melting MoO_3 film. As the oxide ion activity is very low for the tests carried out under ultra high purity argon gas environment, no such low melting Mo rich film could form and therefore Inconel 625 performed equally with Inconel 600 and Inconel 690. Ni base alloys has shown less corrosion in molten LiCl–KCl salt than high density graphite. Graphite is inert to molten salt, however, the degradation of graphite in molten LiCl–KCl salt is due to formation of intercalation compounds, surface porosity filling and diffusion of salt into graphite and thereby dislodge the atoms from its lattice [98]. Pyrolytic graphite on other hand exposed up to 2000 h revealed excellent corrosion resistance and showed negligible corrosion (4.28×10^{-4} %) [99] as shown in Figure 3.36. Thus the corrosion attack for the candidate materials is in the order of 2.25Cr-1Mo > 9Cr-1Mo > 316L SS > High density graphite > Inconel 625 ~ Inconel 690 ~ Inconel 600 > Pyrolytic graphite.

3.3.3.2 Surface morphology of exposed Inconel surfaces

Figure 3.44a and b shows the SEM micrograph and corresponding EDX spectrum from two different regions of 500 h exposed Inconel 625 sample. The SEM micrograph from region 1 and 2 consist of faceted grains (shown as (A) in Figure 3.44a and 3.44b)

146

over porous flaky corrosion product (shown as (B) in Figure 3.44a and 3.44b). The EDX spectrum of faceted grains shown in Figure 3.44c and 3.44d are similar except for the Cr content. The composition of grains as analysed by EDX is Ni-87.67, Fe-9.60, Cr-1.68 and Mo-1.04 in wt% from region 1, and from region 2 it is Ni-70.89, Fe-17.10, Cr-10.83 and Mo-1.18. There is an enrichment of Ni & Fe and depletion of Cr & Mo in the grains. The EDX spectrum from the flaky corrosion product region shown in Figure 3.44e and 3.44f are similar except for the Ni content. The composition of flaky region is Ni-52.11, Fe-10.12, Cr-36.09 and Mo-1.67 in wt% from region 1, and from region 2 it is Ni-8.20, Fe-34.17, Cr-56.42 and Mo-1.20. The flaky region showed a large enrichment of Cr and depletion of Ni. This indicates that the porous Cr enriched region is formed due to preferential leaching of Cr.

The SEM micrograph from matrix adjacent to corrosion product (attacked region) of Inconel 690 is shown in Figure 3.45a. The SEM micrograph clearly shows porous morphology. The area EDX from Figure 3.45a revealed Ni-80.50, Fe-15.15 and Cr-4.35 wt% indicating that the porous layer is depleted of Cr and enriched with Ni. The SEM micrograph from the corrosion product region shown in Figure 3.45b exhibited two distinct morphologies, flaky corrosion product (A) and faceted corrosion product (B). Figures 3.45b-d shows the SEM micrograph and corresponding EDX spectrum from two different corrosion products (A&B) of 500 h exposed Inconel 690 sample. The chemical composition from flaky corrosion product region (A) is Cr-57.37, Fe-39.34, Ni-3.29 wt% while from faceted corrosion product is Fe-93.72, Cr-4.74, Ni-1.55 wt%. The corrosion products showed enrichment of Cr and Fe and depletion of Ni as shown in Fig 3.45c and

147
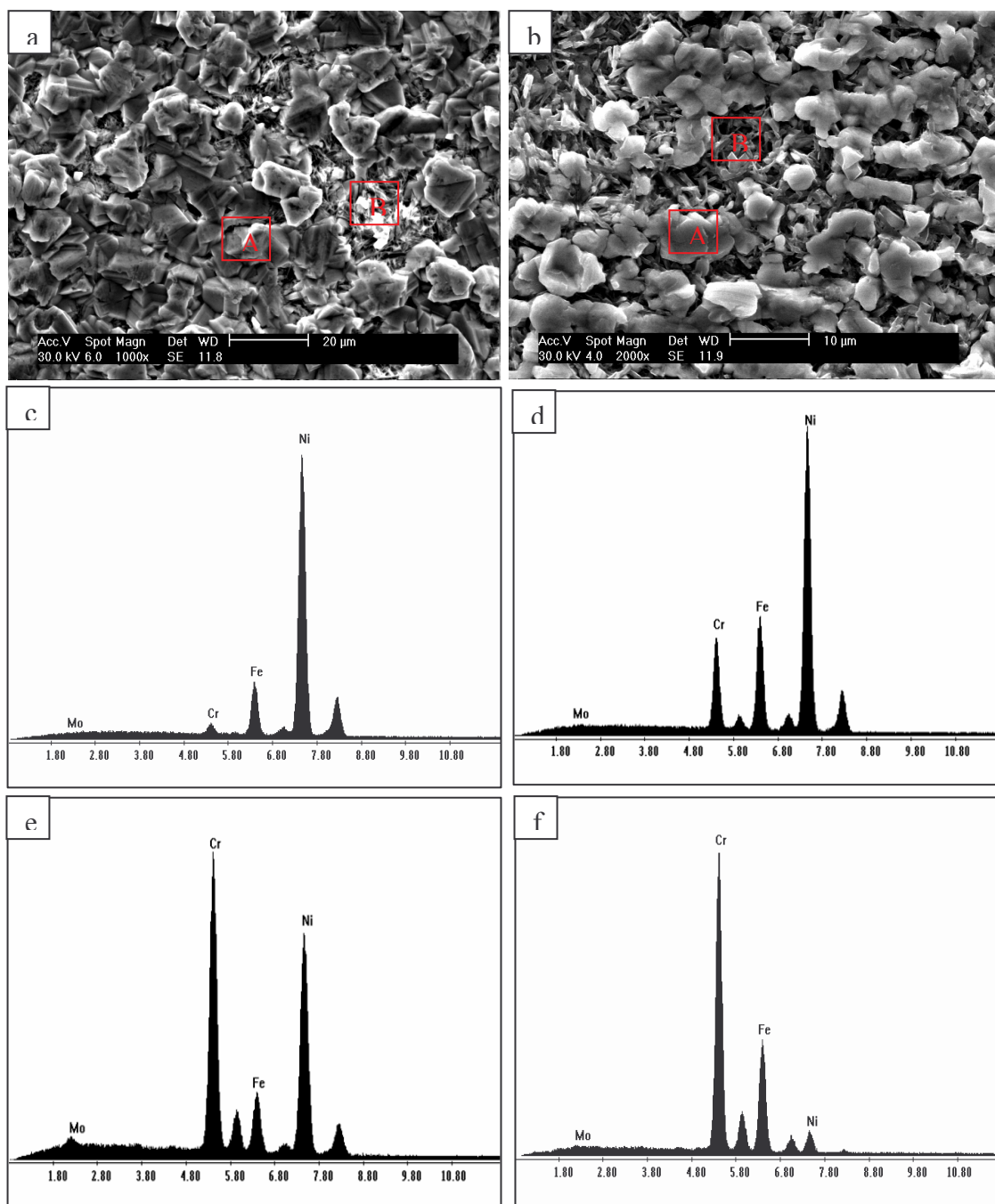
Figure 3.44. SEM micrograph of Inconel 625 (a) from region 1, (c & e) EDX spectra from A & B respectively (b) from region 2, (e & f) EDX spectra from A & B respectively.

Fig 3.45d. As shown in the SEM micrograph, there is huge difference, in morphology and composition, between corrosion product regions and matrix adjacent to corrosion product. The corrosion product region is rich in Cr and depleted in Ni while the porous matrix adjacent to corrosion product is rich in Ni and depleted in Cr. These differences are due to preferential leaching of Cr and formation of porous Ni rich layer. These results indicate that preferential leaching of Cr appears to be general phenomenon during molten LiCl–KCl salt corrosion.
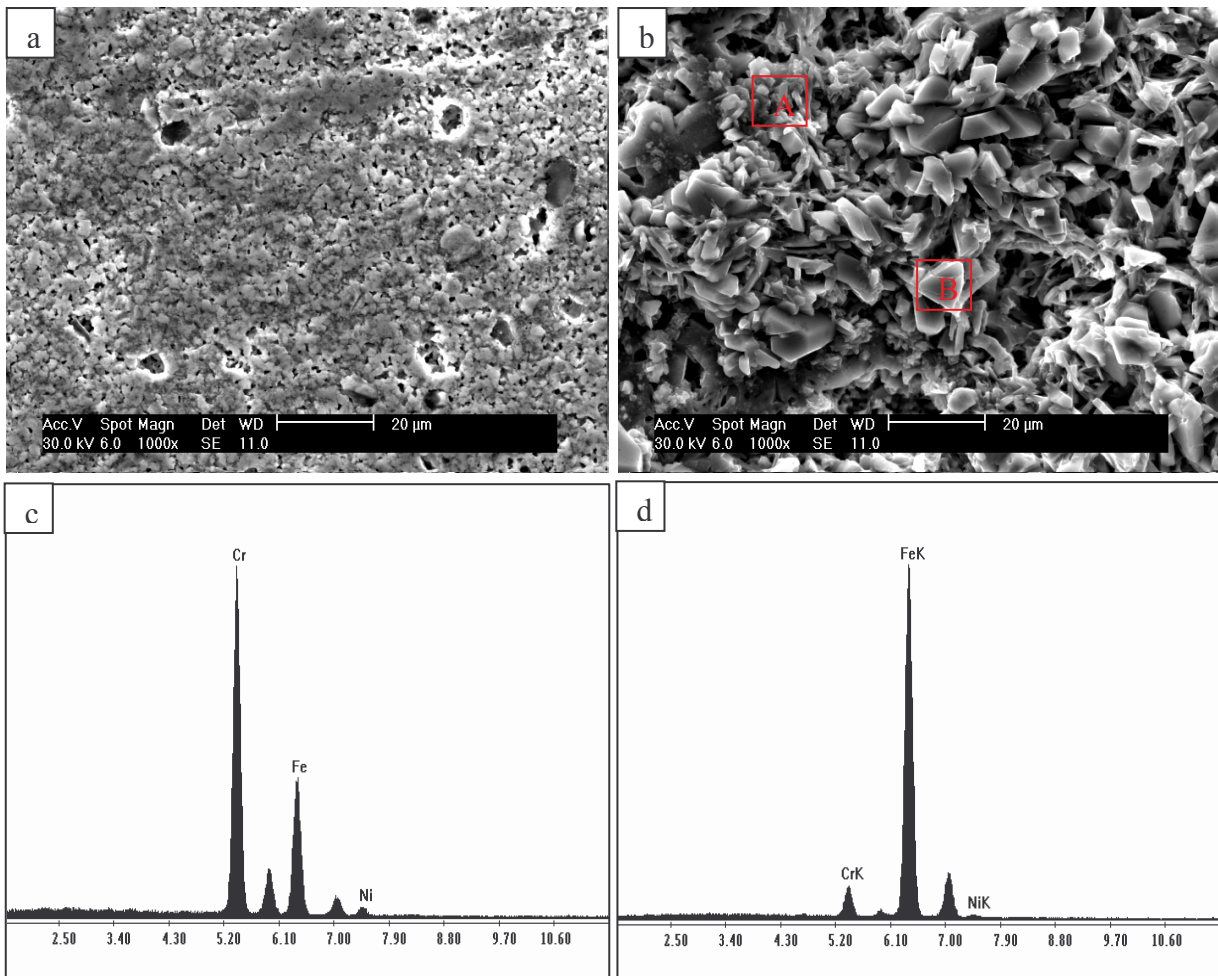
Figure 3.45. SEM micrographs of Inconel 690 (a) Attacked region, (b) Corrosion product region, (c & d) EDX spectra from region A and B respectively from Fig 3.45b.

Figure 3.46 shows the surface morphology of Inconel 600 sample after 500 h of exposure in molten LiCl–KCl salt. We can observe form the SEM micrograph that the surface is composed of a matrix on which corrosion product particles are present. The EDX spectrum from the matrix and from the corrosion product particle is shown in Figure 3.46b and 3.46c respectively. It is clear from the EDX spectrum that the composition from the matrix region (Ni-66.11, Fe-15.22, Cr-18.67) corresponds to the composition of Inconel 600 with minor depletion of Ni and enrichment of Cr & Fe. The EDX spectrum from the particle (Fe-75.25, Ni-22.19, Cr-2.55) clearly showed a huge enrichment of Fe (Figure 3.46c). The formation of these Fe rich particles on the surface could have contributed to the weight gain. In general when a temperature gradient exists on the alloy in contact with molten salt, dissolution at high temperature regions and deposition on low temperature regions occurs [38]. Thus the weight gain observed could be due to oxidation and also due to deposition as evident from the EDX results. EDX spectrum has not shown any presence of chloride on the surfaces indicating that the samples were cleaned thoroughly.

The SEM micrographs of the Ni base alloys tested for 30 min in molten LiCl–KCl salt at 600°C under Cl$_2$ bubbling exhibited severe intergranular attack and dissolution of precipitates. Various studies carried out by Cho et al. [56-59] on Ni base alloys in molten LiCl–Li$_2$O molten salt under an oxidising environment reported that Haynes HR 160 exhibited intergranular corrosion, Haynes 263 and Inconel 713LC exhibited localised corrosion, while Haynes 214, Haynes 75, Inconel MA 754, Inconel 718, Inconel X-750, Nimonic 80 A, and Nimonic 90 showed a uniform corrosion behaviour. In comparison to
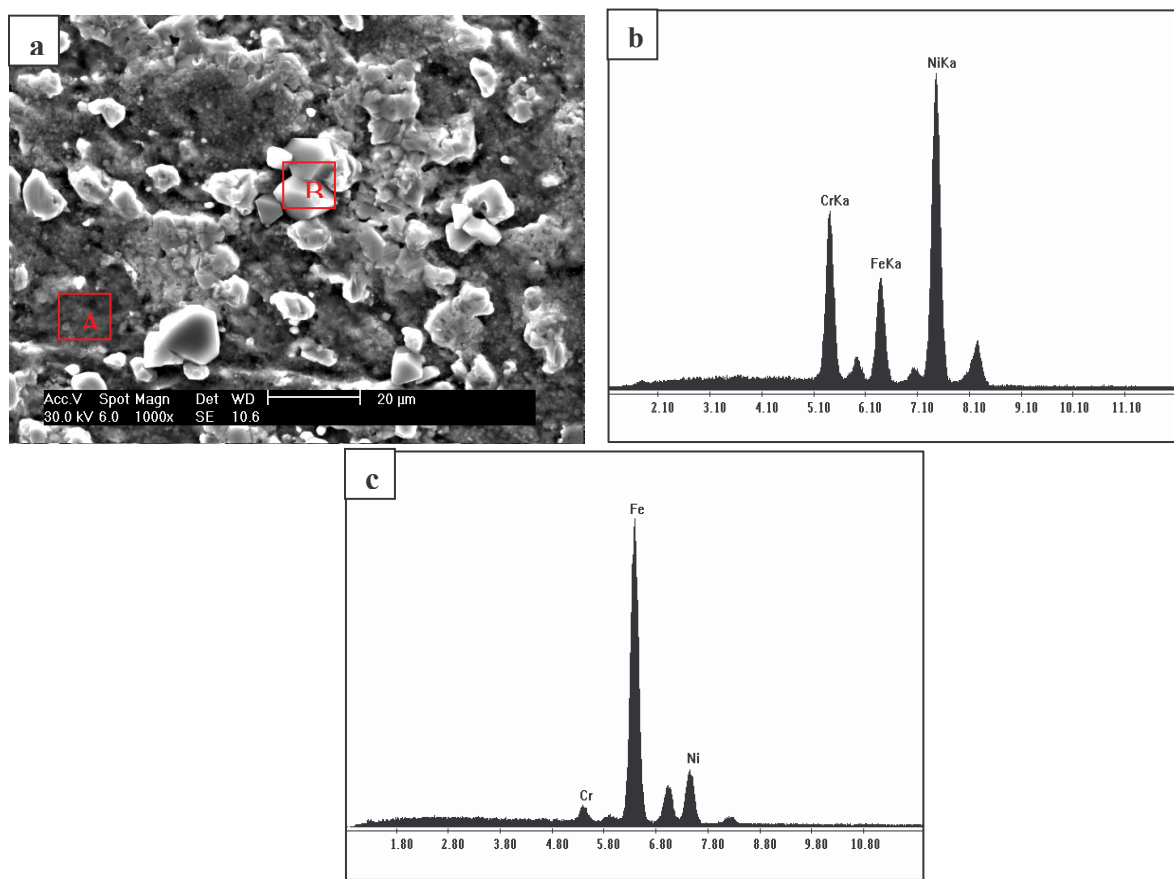
Figure 3.46. (a) SEM micrograph of Inconel 600 (b & c) EDX spectra from A & B respectively.

molten salt corrosion under oxidising and chlorine environment, Ni base alloys have undergone minor uniform corrosion under UHP argon environment tested up to 500 h.

3.3.3.3 Characterisation of exposed surfaces by GIXRD

GIXRD pattern of Inconel 600, 625 and 690 surfaces after 500 h corrosion test in molten LiCl–KCl salt is shown in Figure 3.47. GIXRD pattern from Inconel 600 and Inconel 625 matched with the peaks of standard FCC Ni [04-0850]. GIXRD pattern from Inconel 690 sample matched with standard FCC Ni [044-0850] and standard Rhomb-centered NiO [44-1159]. The presence of Ni peaks on the surface also indicates preferential outward diffusion of elements and enrichment of Ni on the surface and

subsequent oxidation of Ni to NiO. The improved corrosion resistance of Ni base alloys can be attributed to the adherent and protective NiO present on the surface. Thus the mechanism of corrosion of Ni base alloys exposed to molten LiCl–KCl salt under UHP argon is similar to that under air environment. The schematic illustration of the mechanism of Ni base alloys exposed to molten LiCl–KCl salt under air is shown in Fig 3.35. The corrosion rate for the Ni base alloys tested at 600°C for 2 h under air environment was as high as 100 to 250 mm/yr with thick scales of 100 to 300 μm containing Ni and Cr rich layers formed and detached leaving dealloyed Ni rich layer. These results clearly indicate that Ni base alloys corrode in molten salt by formation of Cr rich and Ni rich layers and subsequent spallation, however, the rate of formation and spallation of these layers greatly decreased under UHP Argon atmosphere.
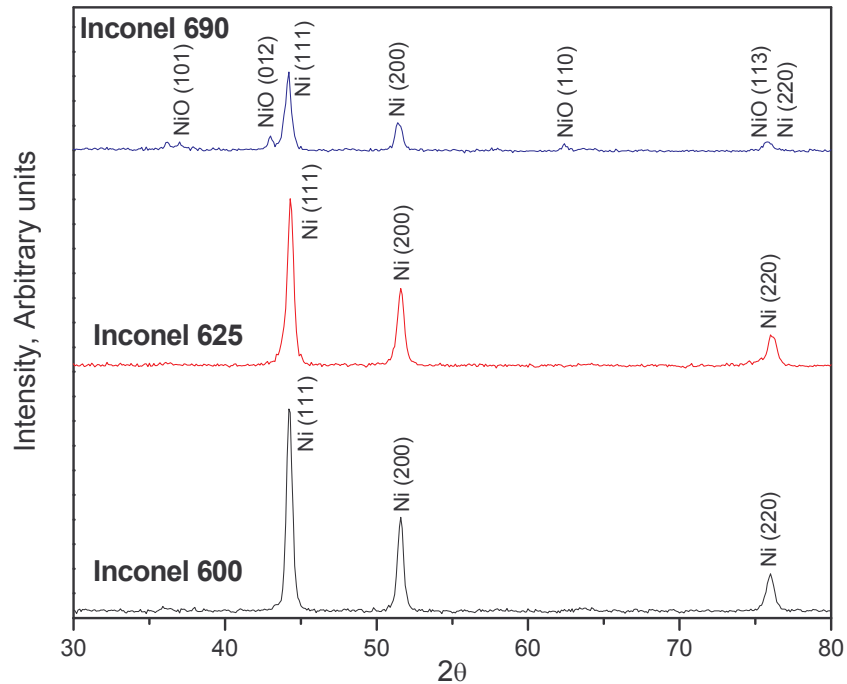
Figure 3.47. GIXRD pattern of Inconel 600, 625 and 690 surfaces exposed for 500 h in molten LiCl–KCl salt at 600°C.

3.3.4 Summary

1. Candidate materials for pyrochemical reprocessing applications such as 2.25Cr-1Mo, 9Cr-1Mo, 316L SS, Inconel 600, Inconel 625 and Inconel 690 samples was exposed to molten LiCl–KCl salt at 600°C under UHP Argon for various durations. The weight loss results indicated that the corrosion attack of the materials increased in the following order: 2.25Cr-1Mo > 9Cr-1Mo > 316L SS > High density graphite > Inconel 625 ~ Inconel 690 ~ Inconel 600 > Pyrolytic graphite.

2. The surface morphology of exposed 2.25Cr-1Mo and 9Cr-1Mo steels exhibited faceted grains and porous matrix adjacent to the corrosion product. The surface morphology of 316L SS exposed samples indicated two distinct regions; the corrosion product region rich in Cr, and the attacked region which is porous in nature and depleted of Cr.

3. Based on the cross section examination and elemental mapping, the mechanism of corrosion of 316L SS was found to be due to selective dissolution of Cr with eventual formation of voids and formation of chromium rich compound at the surface and subsequent spallation.

4. Ni base alloys also exhibited corrosion product regions rich in Cr & Fe and matrix adjacent to the corrosion product rich in Ni. Preferential leaching of Cr from the surface and formation of Cr rich corrosion product appeared to be the common phenomenon for all the alloys tested. Among the alloys studied Inconel 690 followed by Inconel 600 and Inconel 625 are recommended for salt purification and electrorefiner applications.

5. GIXRD analysis also revealed preferential leaching of elements and formation of Ni rich layer on Ni base alloys and Fe rich layer on Cr-Mo steels.

6. The study indicated the need for precisely controlling the argon, moisture and nitrogen content during molten salt corrosion test to avoid differences in the corrosion behaviour.

CHAPTER 4

PREPARATION AND CHARACTERISATION OF THERMAL BARRIER PSZ COATINGS (DUPLEX AND GRADED)

This chapter deals with the selection of coating, corrosion behaviour of coating in molten LiCl-KCl salt under UHP argon and optimization of coating for improving the durability.

4.1 Introduction

For undertaking various unit operations like salt preparation, electrorefining, cathode processing etc. components made of type 316L SS, Ni-base alloys, Cr-Mo steels and high density graphite will be utilized in the high temperature molten chloride salt environment. Since metallic materials undergo accelerated corrosion under molten chloride salt environment at high temperatures, the vessels and crucibles need to be coated with corrosion resistant ceramic material. Selection of material and coating technology is thus important, in manufacturing of reliable corrosion resistant engineering components.

4.2 Material Selection and Compatibility

As discussed earlier in section 1.3, thermodynamic evaluation of several materials by Takeuchi et al. [34] in $UO_2Cl_2 + Cl_2$ indicated better compatibility of ZrO_2 and $ZrSiO_4$. Based on literature, partially stabilized zirconia has been proposed for the first time as a candidate coating material for application in molten LiCl–KCl salt medium [100]. Apart from corrosion resistance, the ceramic coating material should possess

155

certain characteristics such as good mechanical strength, thermal shock resistance, wear and erosion resistance, phase stability, low thermal conductivity and thermal expansion coefficient similar to that of substrate [101-103]. Zirconia (ZrO_2) has high melting and boiling points, approximately 2690°C and 5000°C respectively, and the material is chemically inert at temperatures below 2600°C, has low vapor pressure, resistance to oxidation, low thermally conductivity and high coefficient of thermal expansion [102,104,105]. However, zirconia exhibits polymorphism with the three stable phases up to its melting point. From room temperature to 1170°C the crystal structure is monoclinic. At a temperature of 1170°C the material transforms from monoclinic to a tetragonal crystal structure. This transformations exhibit large thermal hysteresis, and at the temperature of 2370°C, the tetragonal phase is changed to cubic [102,106]. Zirconia ceramics undergo substantial contraction on heating and a corresponding expansion on cooling through the monoclinic-tetragonal transformation as shown in Fig 4.1. Although Zirconia possesses a low thermal conductivity and a suitable thermal expansion coefficient match with the substrate, the polymorphism of zirconia necessitates that it be alloyed with other oxides [101,105]. Stabilized ZrO_2 is outstanding in terms of low thermal conductivity, highest coefficient of thermal expansion (CTE) of about 11×10^{-6} °C^{-1} at 1000°C as compared to 17×10^{-6} °C^{-1} for Ni-base alloys. The effect of the yttria content on the thermal cycle life of ZrO_2–Y_2O_3 thermal barrier coatings is shown in Fig 4.2. The region of maximum lifetime was observed for ZrO_2–6 wt % to 8 wt % Y_2O_3 as shown in the figure. This correlates well with the presence of maximum amounts of non equilibrium, "non transformable" tetragonal phase which forms during quenching processes as indicated in the phase diagram of ZrO_2 – Y_2O_3 system shown in Fig. 4.3.
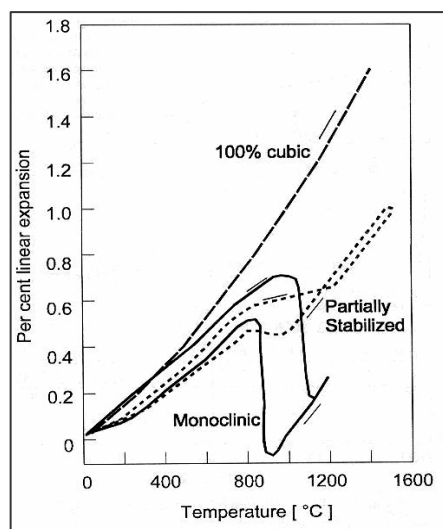
Figure 4.1. Linear thermal expansion of monoclinic, partially stabilized and fully stabilized zirconia [105].
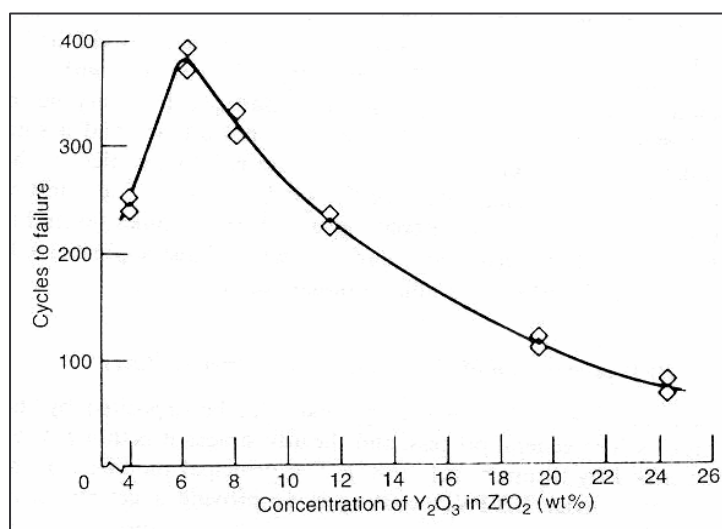
Figure 4.2. Effect of the yttria content on the thermal cycle life of ZrO_2–Y_2O_3 thermal barrier coatings [102].

Thus, coating of yttria (7-9 wt%) stabilized zirconia (PSZ) with an intermediate metallic bond coat on type 316L SS is considered as one of the options to manufacture the salt purification vessel and electrorefiner. Plasma spraying has been chosen for coating ceramic and metallic bond coat layers because this process is capable of

157

producing durable and reproducible coatings economically [100,107]. Apart from this, thick zirconia coatings can be easily produced. Plasma spray zirconia coatings on type 316L stainless steel, 9Cr-1Mo and Inconel 625 rod samples have been prepared in our present study for corrosion investigations in molten LiCl–KCl salt under UHP argon gas environment.
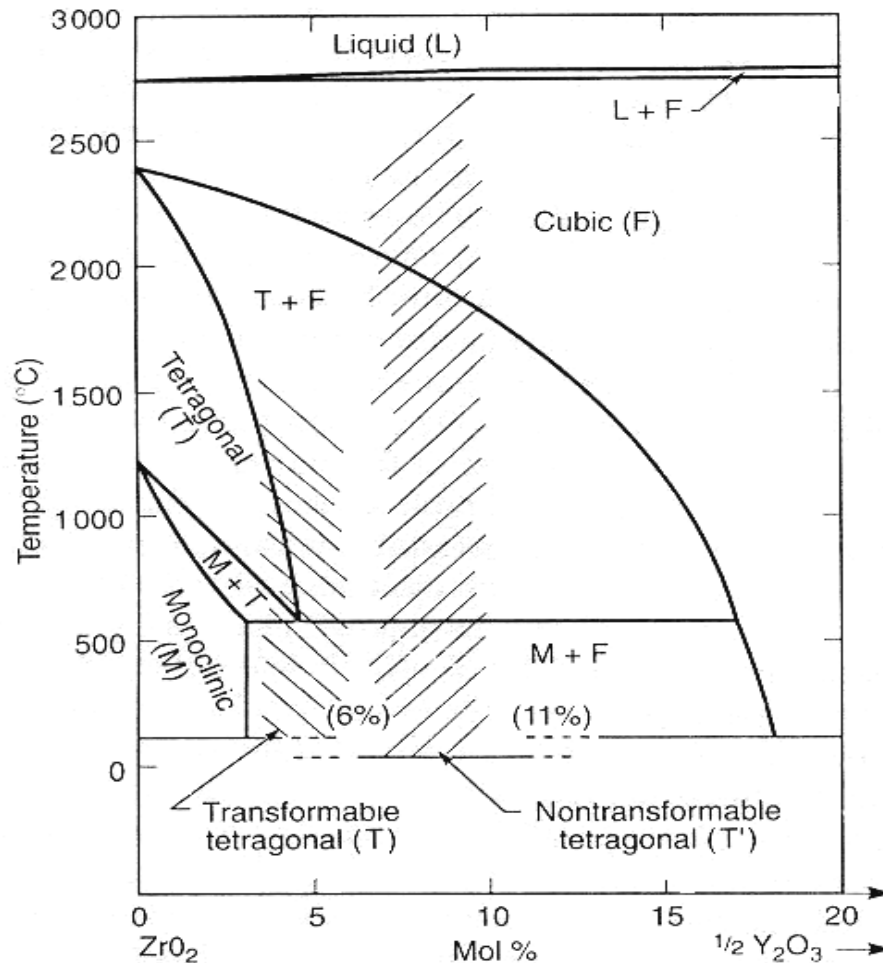
Figure 4.3. Phase diagram of the ZrO_2 – $YO_{1.5}$ system [104,106]. The shaded region indicates the non transformable tetragonal (T') phase (it is also Partially Stabilized Zirconia region); above 15 mol %, the cubic (F) phase is Fully Stabilized Zirconia.

4.3 Corrosion of PSZ Coating in Molten LiCl-KCl Salt

Figure 4.4 shows the percentage weight loss of PSZ coatings on candidate materials with intermediate NiCrAlY bond coat exposed to molten LiCl–KCl salt at 600°C. The percentage weight loss of uncoated 316L SS and PSZ coating over high density graphite were also included for comparison purpose. PSZ coating over 316L SS tested up to 1000 h exhibited excellent corrosion resistance in comparison to uncoated 316L SS as shown in Figure 4.4. No weight loss of the PSZ coated high density graphite [98] and PSZ coated 9Cr-1Mo samples was observed after exposure to molten salt for 2000 h. This clearly indicates that PSZ coating perform very well in molten LiCl–KCl salt at 600°C. However delamination of coating was observed on few of the exposed high density graphite samples coated with PSZ. This could be attributed to the poor adhesion of the coating on high density graphite substrates. PSZ coated 9Cr-1Mo samples tested in molten LiCl–KCl salt upto 2000 h showed minor increase in weight, but coating exhibited lot of cracks and buckling. PSZ coated on 304L SS samples exposed to molten LiCl–KCl salt upto 2000 h showed much higher weight loss with increase of exposure time as shown in Figure 4.4. Severe spallation of PSZ coating on 304L SS lead to the increased weight loss. The results of the present study indicate that premature spallation of PSZ coating on 9Cr-1Mo and 304L SS could have occurred due to differences in thermal expansion coefficient. The spallation of PSZ coatings could also be due to accidental ingression of oxygen and moisture. In another study by Quintana et al. [108] plasma sprayed PSZ coated specimens submerged for 72 h failed in molten LiCl–6wt% Li_2O at 650°C with Ar-10% O_2 gas bubbling. The presence of oxygen and moisture in molten salt will enhance the corrosion to a greater extent than in dried melts [38] It is

reported that moisture in the salt had a significant effect on the corrosion of 316L SS in molten LiCl–KCl eutectic salt [109]. Moisture-induced failure of PSZ top-coat was also reported after the sample is removed from the high temperature environment because of hydrogen embrittlement of PSZ [110].

The percentage weight loss of the uncoated 316L SS samples exposed for 250 h was about 2.83%, while the weight loss percentage of PSZ coated 316L SS was only 0.08 exposed for 1000 h, which clearly indicates that the corrosion attack is insignificant for PSZ coated 316L SS. Our studies on plasma sprayed partially stabilized zirconia (PSZ) coatings proposed and tested as one of the candidate materials in molten LiCl–KCl salt has shown excellent corrosion resistance. Recently plasma sprayed ZrO_2–Y_2O_3 and Al_2O_3–Cr_2O_3 coating on Inconel 713LC alloy tested in molten LiCl–LiO_2 salt for 216 h under Ar-10% O_2 atmosphere also exhibited excellent hot corrosion resistance to molten salt due to dense, continuous and protective top coat [111,112]. Pyrolytic graphite on other hand exposed up to 2000 h exhibited superior corrosion resistance (4.28×10^{-4} %) compared to PSZ coatings as shown in Figure 4.4 [99]. It is reported by Lee et al. [113] that the corrosion rate of Al_2O_3 coating in molten LiCl–Li_2O salt at 650°C under Ar-10% O_2 atmosphere up to 168 h was ~5.8×10^{-2} μm/h while for YSZ coating it was nearly zero. Therefore pyrolytic graphite and ceramic oxide coatings increase inertness, corrosion resistance and durability of substrate materials through barrier properties in aggressive molten chloride environment.
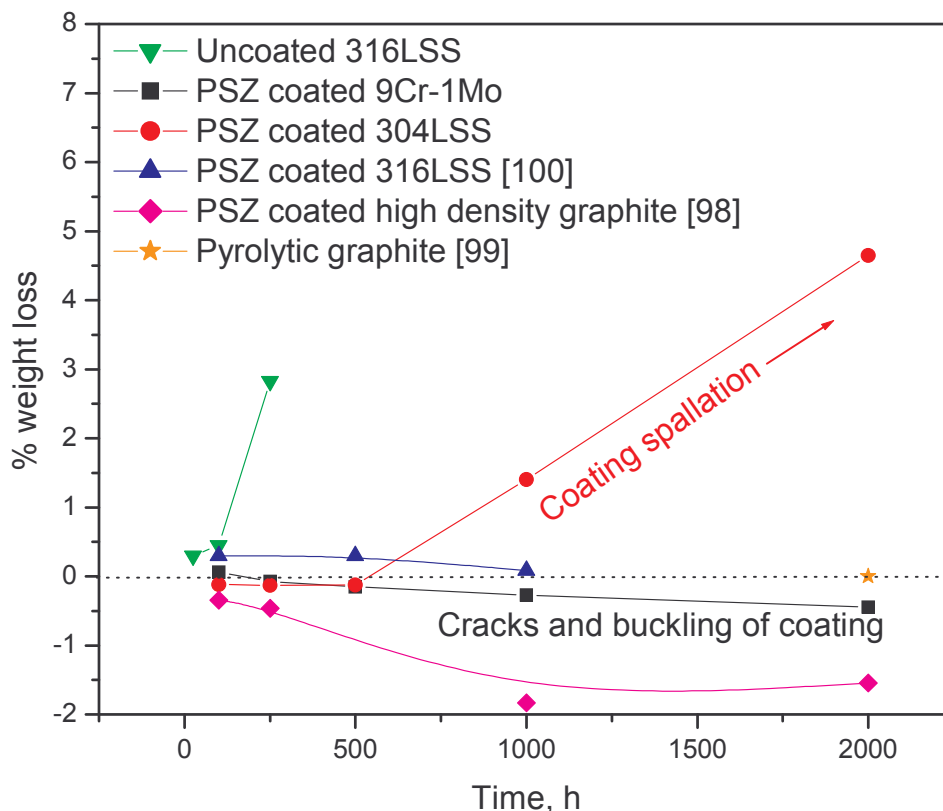
Figure 4.4. Percentage weight loss of uncoated 316L SS and PSZ coatings on candidate materials exposed to molten LiCl–KCl salt at 600°C.

Microstructural examination of the tested PSZ coated 316L stainless steel samples were carried out using optical microscopy and SEM. The surface morphology of the exposed (Fig 4.5a) and unexposed samples were similar. The surface morphology of 500 h exposed sample did not reveal significant degradation over the surface as shown in Fig 4.5b. The sample exposed for 1000 h exhibited salt deposits. The SEM micrograph of the 1000 h exposed sample (Fig. 4.5c) showed no degradation of the coating however, certain deposits rich in Fe are seen on the sample exposed for 1000 h. Figure 4.5d is the EDX spectrum taken from the exposed region. The composition determined by EDX from the deposits is Fe - 91.73 wt% and Zr - 8.27 wt%. The presence of such Fe rich particles

were observed on partially stabilized zirconia coated samples over high density graphite exposed for 2000 h in molten salt. The large enrichment of Fe which was also observed for Inconel 690 (Figure 3.45d) was discussed in section 3.3.3.2.

The cross section optical micrograph of PSZ coated 316L SS unexposed and exposed to molten LiCl–KCl eutectic salt for 1000 h, shown in Fig 4.6a and b, respectively, are similar and does not reveal any penetration of the salt across the coating. Figure 4.6c shows the cross section back scatter electron mode SEM micrograph of PSZ coating exposed for 1000 h.
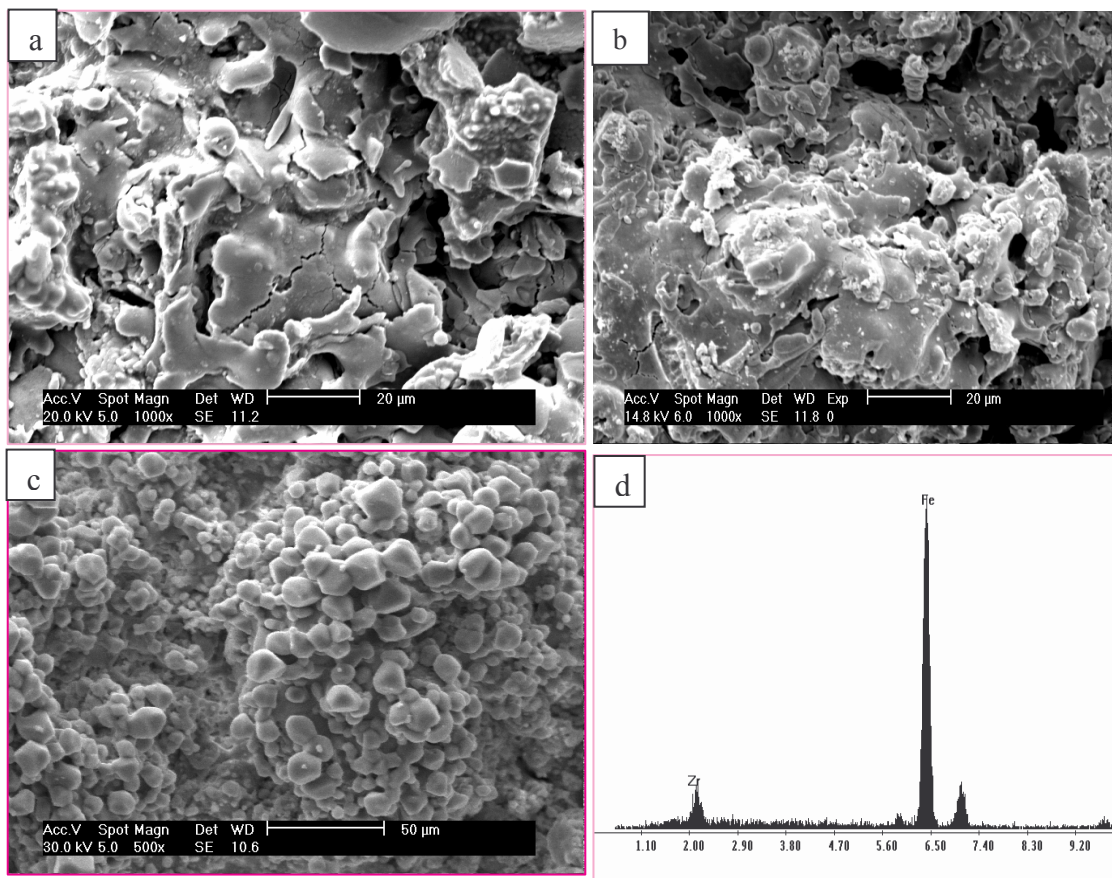
Figure 4.5. SEM micrographs of PSZ coated 316L SS (a) unexposed, (b) exposed for 500 h (c) exposed for 1000 h to molten LiCl–KCl eutectic salt, and (d) EDX from Fig 4.5c.

The cross section of SEM micrograph of PSZ coating exposed for 1000 h also did not reveal any selective diffusion of elements and degraded layer unlike uncoated 316L SS which showed selective leaching and enrichment of Cr on the surface, formation of voids and spallation of Cr rich layer. The cross section SEM micrograph also does not show any degraded layer unlike uncoated 316L SS. This indicates that the PSZ coating over 316L SS shows better corrosion resistance in the molten LiCl–KCl eutectic salt in comparison to the uncoated 316L SS.
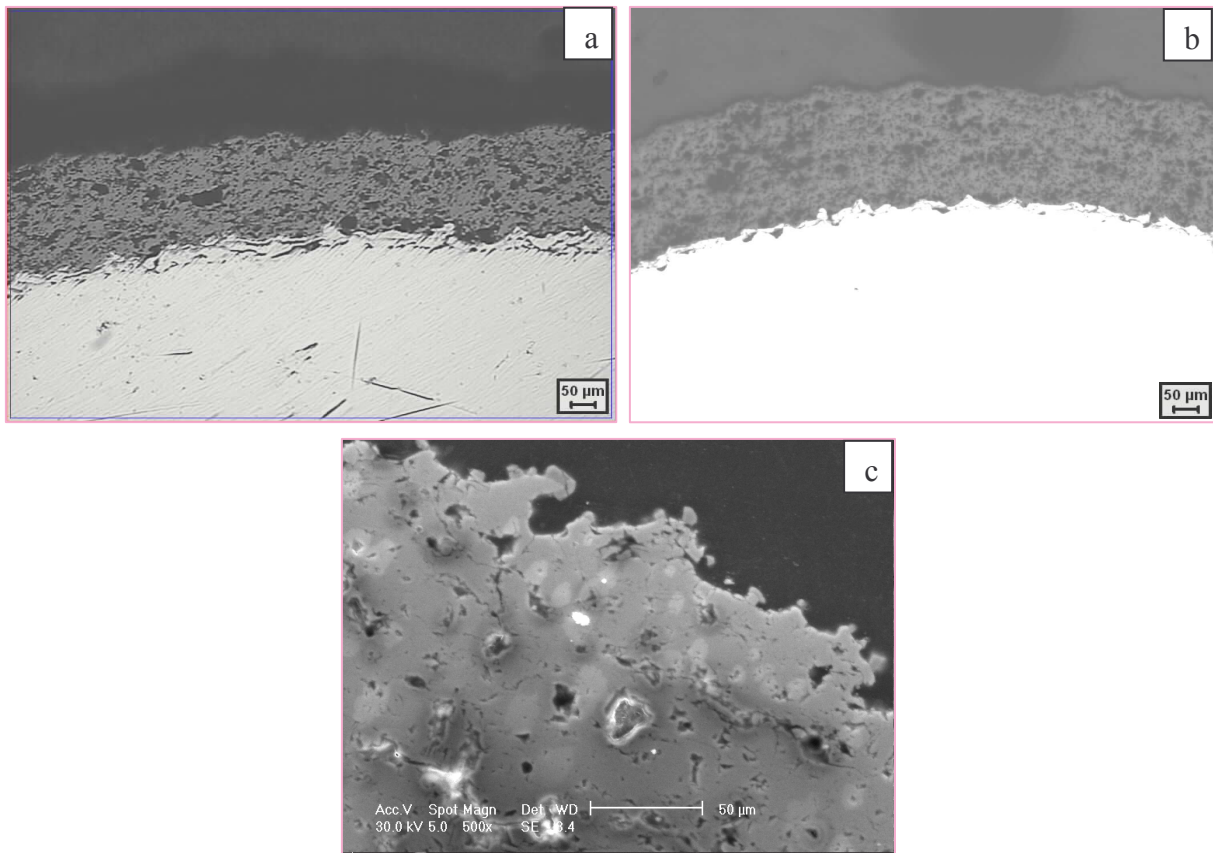
Figure 4.6. Cross section optical micrographs of PSZ coated 316L SS (a) unexposed (b) exposed to molten LiCl–KCl eutectic salt for 1000 h, and (c) SEM micrograph of exposed region.

4.4 Optimisation of Graded Coating

Plasma sprayed partially stabilized zirconia (PSZ) thermal barrier coatings (TBC's) on super alloys are widely used for protection against high temperature corrosion and abrasion in gas turbines of aerospace engines [114-116]. Conventional plasma sprayed TBC coatings (duplex coating) consist of two layers – the ceramic top coat and metallic bond coat. The failure of conventional plasma sprayed TBC coatings usually occur at the sharp interface between the ceramic top coat and metallic bond coat. The low durability of duplex coating is attributed to the thermal expansion mismatch stresses at the sharp interface between ceramic and bond coat, oxidation of bond coat and subsequent spallation of coating [116,117]. The thermal stresses generated due to thermal expansion mismatch between the ceramic coating and metallic bond coat results in premature spallation of the coating [118]. Oxidation of bond coat is also reported as another cause for the failure of coating [115,119]. These difficulties can be avoided by achieving graded coatings [118,120]. A two fold increase in bond strength of five layered functionally graded TBC coating has been reported by researchers in comparison to conventional duplex TBC [116,120-122]. A five fold increase in thermal cycling resistance of functionally graded coating has also been reported in comparison to duplex coating [117,121,122]. Functionally graded TBC also exhibited extended oxidation resistance compared to duplex TBC [117]. Thus it is clear that functionally graded coatings are more durable than duplex TBC and can also provide good corrosion resistance in molten salt for longer durations of service.

Many investigations have reported the preparation of partially stabilised zirconia (PSZ) functionally graded TBC through plasma spraying process [116,117,120-122] and

recently by slip casting [123,124], tape casting [125,126] and by airbrush spraying [127]. However plasma spraying is one of the well established and economical methods for deposition of thermal barrier coatings of thicknesses from 50 μm to 3000 μm [128]. Functionally graded thermal barrier coatings can be produced by plasma spray process, either by co-injection of metallic bond coat and ceramic powders using a single plasma torch or by using multiple-torches separately for metallic bond coat and ceramic powders [116]. In the present study spray parameters were optimized to produce a graded coating using premixed powders through a single plasma torch.

4.5 Microstructural Evolution and Characterization

In the present study, three different parameters (FGM1, FGM2 and FGM3) were employed to produce graded coating consisting of PSZ and bond coat laminates comprised of gradients. The plasma spray parameters employed for graded PSZ coating are tabulated in Table 2.2. In FGM1 coating, hydrogen flow rate was kept higher and spray distance was shorter, while FGM2 coating was produced with intermediate hydrogen flow rate and longer spray distance. FGM3 coating was produced with carefully controlled (optimized) hydrogen flow rate and spray distance to achieve graded coating. The duplex coating on the other hand was made as per the standard parameters.

4.5.1 Composite coating

Figure 4.7a shows the back scatter SEM image of cross section of FGM1 coating. The typical splat type laminar microstructure of plasma spray coating is clearly shown. No clear boundary delineating the bond coat and ceramic coat lamellae in the graded region was observed. The EDX spectrum obtained from region 1 and 2 of Fig. 4.7a is presented in Fig. 4.7b and c respectively. Region 1 in bright colour is the top ceramic coat which
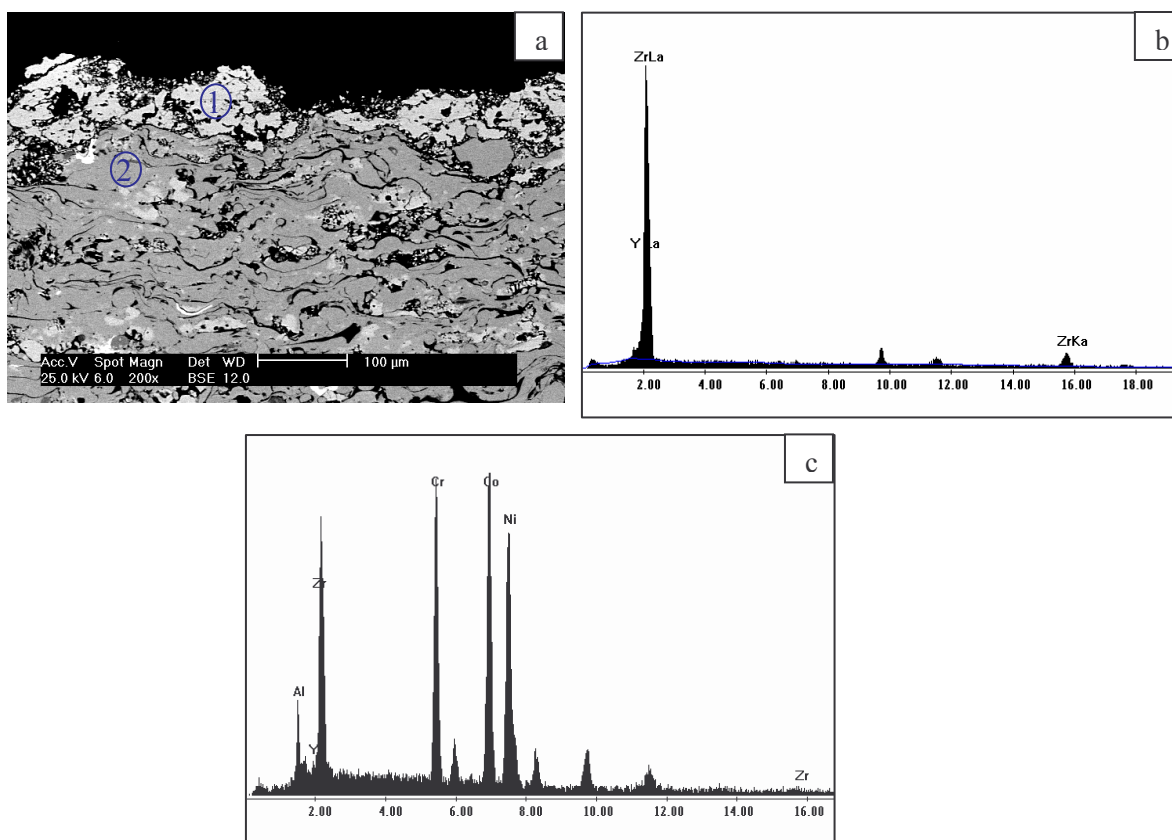
Figure 4.7. (a) Back scatter cross sectional SEM micrograph of FGM1 (b) and (c) EDX spectrum from region 1 and 2 respectively.

contained 90.04% Zr and 9.96% Y while the region 2 in grey colour near the top ceramic coat contained 31.35% Ni, 18.22% Cr, 34.70% Co, 6.66% Al, 8.44% Zr and 0.63% Y in wt%. This indicates that the bright colored region 1 is obviously PSZ top coat and is dispersed marginally in between bond coat and ceramic top coat. Composition from region 2 contained mostly of CoNiCrAlY with minor amount of PSZ which clearly indicates that the bond coat reacted with PSZ and a mixed reaction phase was formed.

Figure 4.8a and b shows the back scatter SEM micrograph of FGM1 coating from graded region. The micrograph in Fig. 4.8a shows a bright spherical particle at region 1 and grey colored spherical particle at region 2 in addition to laminar morphology. EDX measurements made from the regions indicated in the micrograph of Fig. 4.8a were tabulated in Table 4.1.
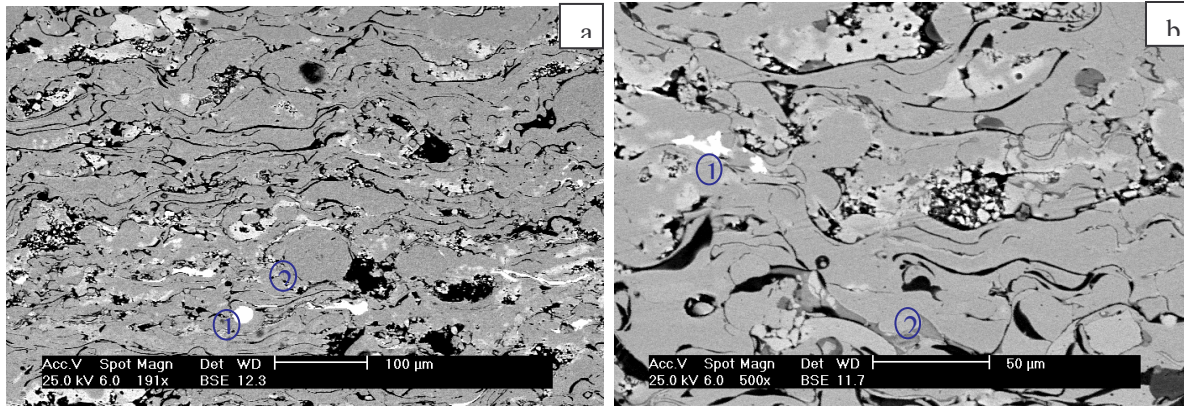
Figure 4.8. (a) and (b) Back scatter SEM micrograph of FGM1 coating with phases of different grey level.

Table 4.1 Chemical composition (in wt% by EDX) from regions shown in Fig 4.8a and b.

Position	Zr	Y	Ni	Co	Cr	Fe	Al
Fig. 4.8(a) Region 1	56.19	6.47	17.41	9.18	4.18	6.57	-
Fig. 4.8(a) Region 2	12.35	1.6	29.06	31.15	17.76	0.83	7.25
Fig. 4.8(b) Region 1	85.52	8.13	2.4	1.87	0.82	-	1.26
Fig. 4.8(b) Region 2	43.86	5.7	16.77	18.26	9.9	0.76	4.74

The EDX analysis carried out from region 1 of Fig. 4.8a indicates that the bright spherical particle contains mostly of PSZ with minor amount of bond coat, while the grey colored spherical particle (region 2) contained bond coat with minor amount of PSZ. The reason for the presence of spherical particles of different contrast is explained as follows.

Plasma sprayed TBC usually contains unmelted or partially melted particles, fully melted particles, deformed splats, metastable phases and oxidized bond coat depending on the parameters employed. Due to high operating temperature in the plasma spray gun, the bond coat and PSZ particles are melted and reacted during their course of flight. The

high velocity achieved during plasma spraying causes this spherical molten droplet to flatten on hitting the substrate and solidify instantaneously resulting in the splat type of microstructure. The reacted molten droplets solidified quickly before it impinged on the substrate and the solidified spherical particle thus gets locked in the lamellae. Hence from the microstructure it is clear that the bright and grey colour spherical particles are a mixture of PSZ and bond coat. The unmelted or partially melted particles present in the coating are not desirable because these particles affect uniform deposition of splats and results in pores or voids. The microstructure in Fig. 4.8b consists of regions of different grey levels with molten droplets deposited as splat type of morphology. This indicates complete melting and hitting of the particles on the substrate in molten condition and depositing as typical splats in plasma sprayed coatings. EDX analysis carried out from region 1 in white colour and region 2 in grey colour of Fig. 4.8b were tabulated in Table 4.1. The results clearly indicate that the molten droplets of bond coat reacted with PSZ resulting in a composite structure. The presence of regions of different grey levels in back scatter SEM micrograph thus indicates a composite structure with mixture of PSZ and bond coat of varying compositions. In FGM1 coating the higher operating temperature caused melting and subsequent reaction; while the lower spray distance resulted predominantly splat type morphology. In FGM2 coating the intermediate operating temperature and higher spray distance resulted in formation of spherical particles.

Figure 4.9a–d shows the optical micrograph of FGM2 coating consisting of spherical particle, partially deformed particle and, partially deformed particle surrounded by oxidized bond coat. These micrographs also suggest that such particles can be easily identified from optical microstructure as well. Thus a composite microstructure with

varying morphologies and compositions are produced. Such composite layers with reaction phases consisting regions of oxides of ZrO_2 and Al_2O_3 appearing as grey, Al_2O_3 appearing as dark and ZrO_2 as bright were reported in FGM TBC coatings [116,121,122]. FGM TBC coating, with the composite structure as reported above, also showed a two fold increase in bond strength and five fold increase in thermal cycling resistance [116,121,122]. This improvement in bond strength was attributed to the oxide complexes formed in the composite layers [121] and the improvement in thermal cycling resistance was attributed to the reduction in thermal mismatch stresses and improvement in cohesive strength [117].
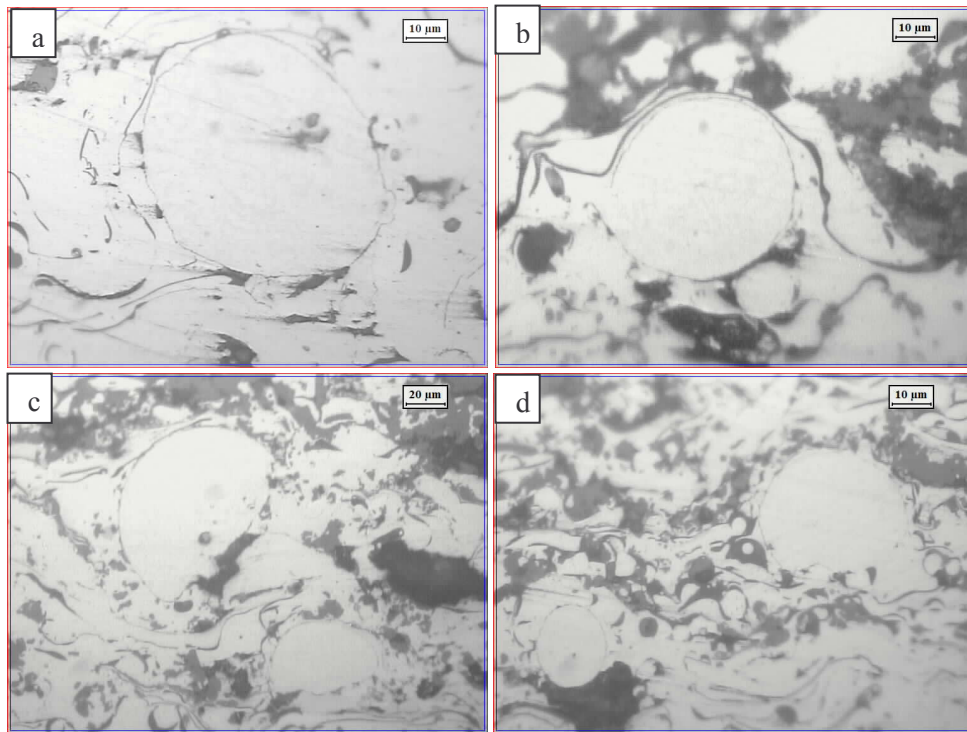
Figure 4.9. Optical micrographs of FGM2 coating (a) and (b) spherical particle (c) partially deformed particle and (d) partially deformed particle surrounded by oxidized bond coat.

4.5.2 Oxidized bond coat

Figure 4.10a–d shows the optical micrographs of FGM2 coating consisting of spherical oxidized bond coat, oxidized bond coat with irregular shape, inter splat oxidized bond coat, and partially oxidized spherical bond coat. Figure 4.11c shows the back scatter SEM micrograph of FGM2 coating consisting of black lamellae as observed in optical microstructure of Fig. 4.10c. EDX spectrum from black lamellae of Fig. 4.11a is shown in Fig. 4.11b which contains 37.78% Al, 13.14% Cr, 16.37% Co, 14.54% Ni, 10.97% Zr, 0.63% Fe, and 6.58% Y. Similarly, EDX spectrum from black lamellae of irregular morphology taken from Fig. 4.11c is shown in Fig. 4.11d which contains 60.48% Al, 9.98% Ni, 9.2% Cr, 10.14% Co, and 10.2% Y. EDX analysis clearly indicates that the oxidized bond coat is mainly composed of aluminium. Since Al is having higher affinity to oxygen, Al gets easily oxidized compared to other elements. The selective oxidation of aluminium to Al_2O_3 was reported by Dong et al. [116], by XRD of stripped coating layer which indicated that aluminium preferentially got oxidized in comparison to other elements in CoNiCrAlY. Microhardness measurements were made on the substrate, bond coat, oxidized bond coat and PSZ top coat. The ceramic top coat (HV 1097) and oxidized bond coat (HV 824) exhibited higher hardness values compared to the bond coat (HV 441) and substrate (HV 332). The colour, composition and higher hardness of dark colored bond coat of various morphologies suggest that the bond coat is oxidized. Khor et al. [121] indicated that the selective oxidation of aluminium in the NiAl-YSZ coating promoted the formation of fine structures in the composite layers and thus increased the mechanical properties. However, one of the main reasons for the failure of TBC coating is the oxidation of bond coat [115,119]. The increased oxidation and continuous oxide

network formation can lead to spallation of coating [116,121]. It is reported that even though minor oxide formation improved the microstructure of metallic + zirconia composite, oxidation during plasma spraying process should be controlled [121,129]. Khor et al. [121] suggested that oxidation of metallic elements present in the bond coat must be controlled as excessive oxidation will result in the formation of detrimental oxide inclusions which degrade the mechanical properties. Researchers suggested low pressure plasma spraying or Argon protection during deposition of FGM coating to avoid selective oxidation [116,121]. Therefore, it is important to precisely control processing parameters such that selective oxidation and morphology can be controlled to acceptable limits.
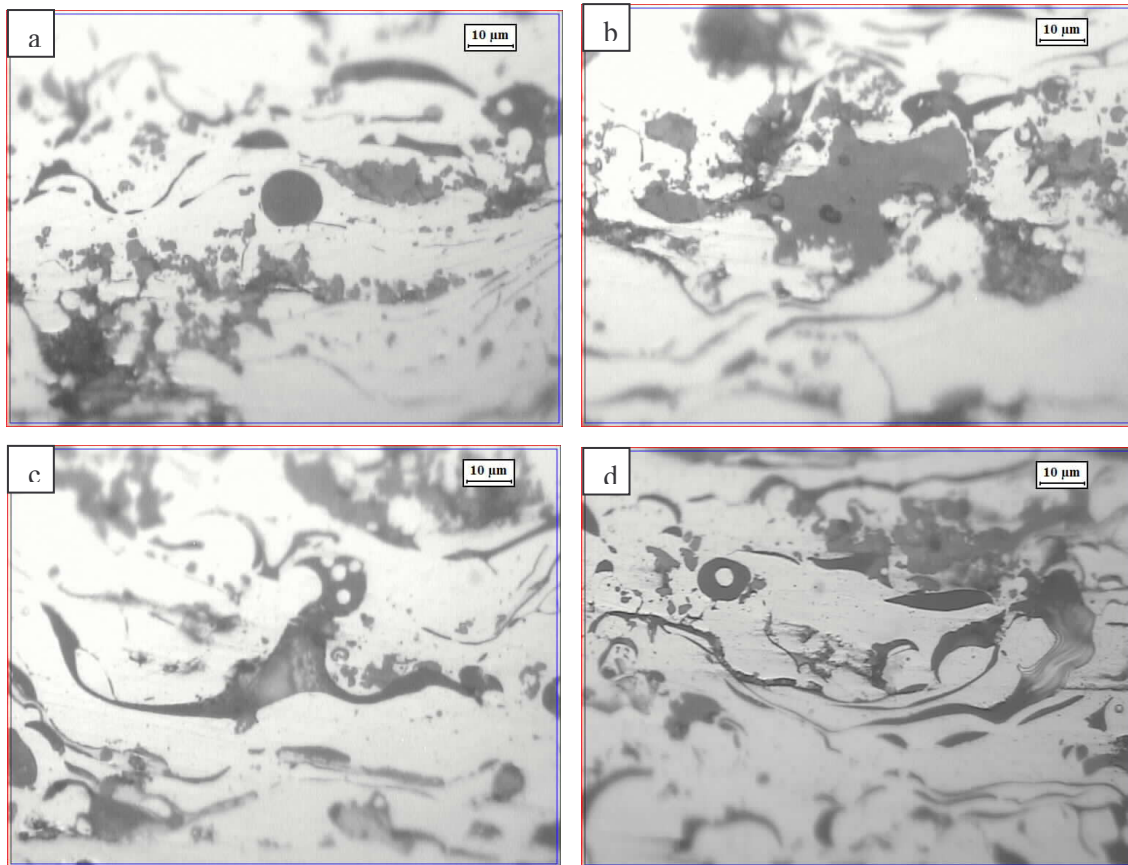
Figure 4.10. Optical micrographs of FGM2 coating (a) spherical oxidized bond coat (b) oxidized bond coat with irregular shape (c) inter splat oxidized bond coat (d) partially oxidized spherical bond coat.
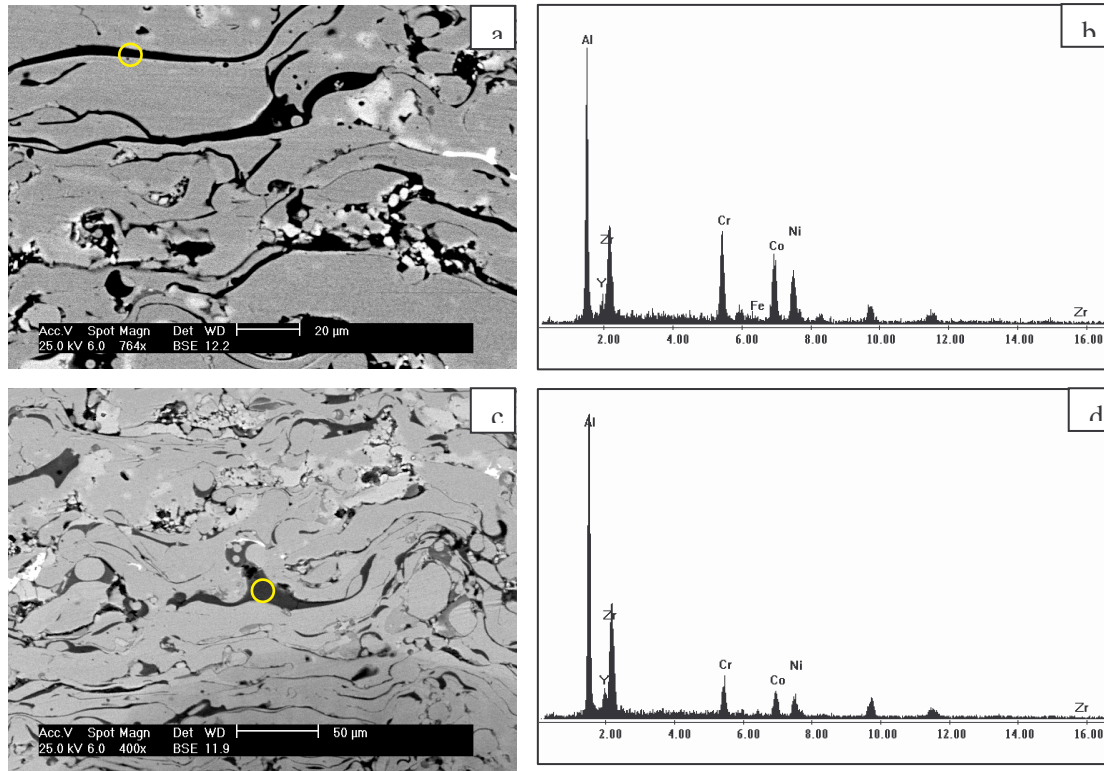
Figure 4.11. (a) and (c) Back scatter cross sectional SEM microstructure of FGM2 coating (b) and (d) corresponding EDX spectrum of the encircled region from Fig 4.11(a) and (c) respectively.

The large difference in physical characteristics of the ceramic and metallic bond coat powders results in different deposition characteristics [130], therefore, it is likely that some ceramic particles remain unmelted, while bond coat particles get oxidized and mixed phases of bond coat and ceramic particles form as observed in the microstructures. The control of spray parameters to deposit a graded layer using premixed powders through a single plasma torch becomes even more difficult to obtain graded coating layers. This is essentially due to the differences in properties of metallic bond coat and ceramic powders such as melting point, density, morphology and size of powders [116,122]. At such high plasma temperatures, it is essential to avoid the reaction between molten bond coat particles and ceramic particles passing through single plasma torch. In

172

addition it is also essential to avoid oxidation of bond coat (NiCrAlY) while both molten premixed powders are passing through single torch. Therefore the parameters have to be chosen such that individual lamellae comprising of gradients without any reaction and selective oxidation are obtained. Though functionally graded materials should exhibit continuously varying compositions on a microscopic scale, the gradation can be as laminates comprised of variation in composition [130].

4.5.3 Graded coating

Figure 4.12a and c shows the backscatter SEM cross sectional micrograph of duplex and optimized (FGM3) coating respectively. As expected duplex coating microstructure shows bond coat and uniform lamellae with sharp interface, while FGM3 coating shows graded region. Unlike the microstructure (FGM1 and FGM2) consisting of regions of different grey levels, FGM3 coating showed only bond coat dispersed as typical splat type laminar microstructure. This indicated that no reaction between the bond coat and ceramic powders occurred and the individual powders remained molten prior to impact on substrate resulting in laminar microstructure. Figure 4.12b and d shows the corresponding EDX line profile taken from duplex and FGM3 coating respectively as shown in Fig. 4.12a and c. The EDX line profile taken from the duplex coating indicates PSZ top coat, bond coat (BC) and Inconel 625 substrate region. The absence of Ni, Cr and Al peaks in top coat and the presence of Ni, Cr and Al peaks in bond coat obviously indicated the top coat and bond coat regions. The EDX line profile of Al is important as aluminium easily undergoes selective oxidation and shows a sharp increase in intensity if selective oxidation takes place or if mixed reaction phases are formed. The intensity of Al peak clearly delineates top ceramic coat and Inconel 625 substrate regions as indicated in
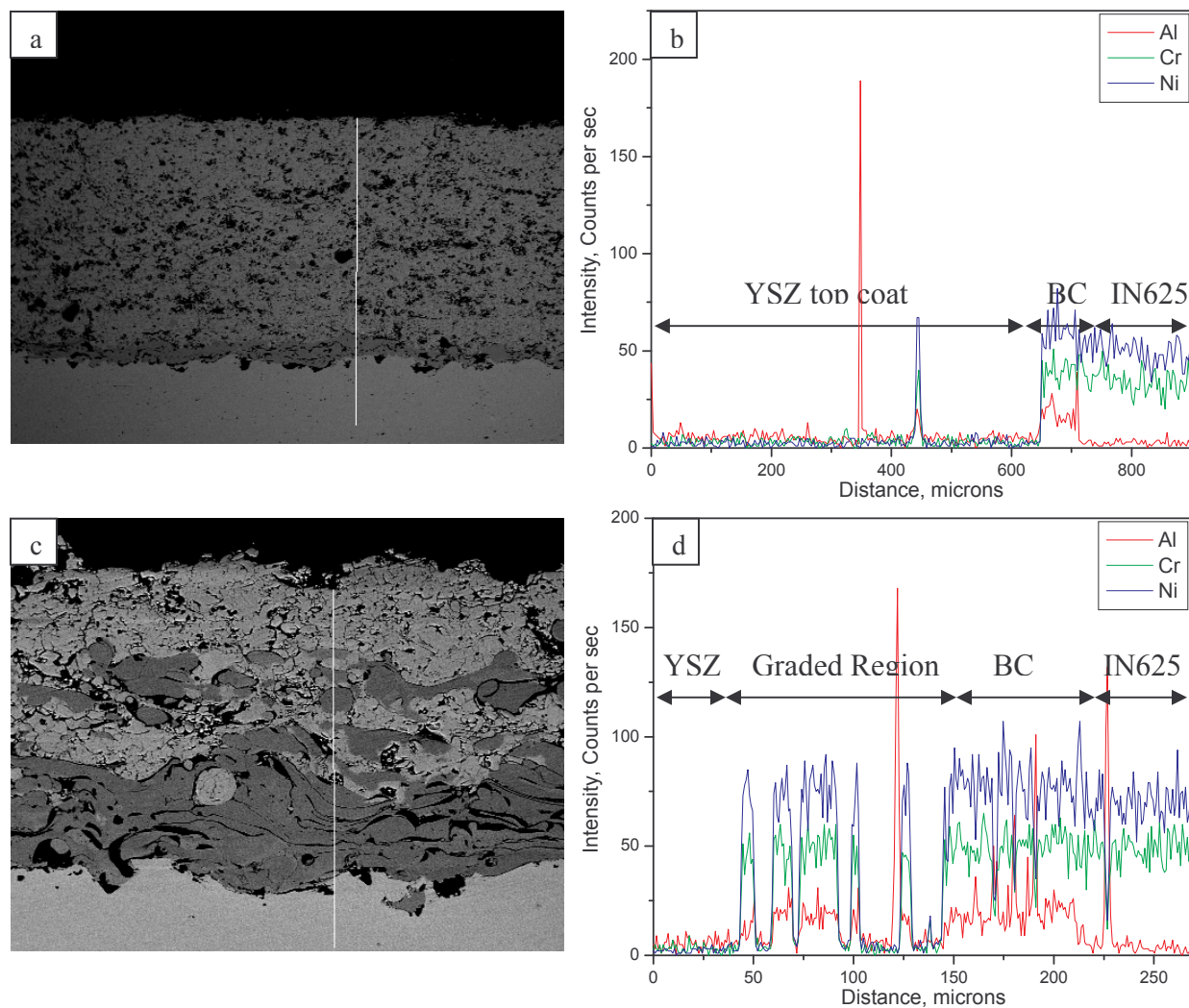
Figure 4.12. Back scatter SEM micrograph and corresponding EDX line profile (a) and (b) from duplex coating and (c) and (d) from FGM3 coating on Inconel 625.

the figure. The EDX line profile from FGM3 coating indicated the top coat, the graded region, the bond coat and the substrate regions. In the graded region the alternate presence and absence of Ni, Cr and Al peaks on the alternate bond coat and ceramic lamellae is clearly evident. The Ni, Cr and Al peaks fell almost to zero on ceramic lamellae and raises on the bond coat lamellae in the graded region. The backscatter SEM

micrograph and EDX line profile indicates that there are no mixed reaction phases or oxidized bond coat in the graded coating. In order to further confirm that the graded coating was free from mixed reaction phases and oxidized bond coat, elemental X-ray maps of the graded coating was obtained from high magnification SEM micrograph. Figure 4.13 shows the SEM micrograph and corresponding elemental X-ray maps of FGM3 coating on Inconel 625 sample. The elemental x-ray maps indicating the absence of Ni, Cr and Al in the ceramic layers suggested no reaction between PSZ and NiCrAlY, and graded layers (lamellae's) were formed.

The X-ray diffraction patterns showed the presence of beneficial non-transformable tetragonal phase in top ceramic coat in duplex and graded coating. Figure 4.14 shows the percentage weight loss of duplex and graded partially stabilised zirconia coating exposed to molten LiCl–KCl salt at 600°C up to 2000 h. Initially graded coating exhibited higher percentage weight loss compared to duplex coating; however 1000 h and 2000 h tested samples showed lower percentage weight loss for graded coating compared to duplex coating. No spallation of the coating was observed for duplex as well as graded coating.

Figure 4.15a and b shows the SEM micrograph of duplex and graded PSZ coating respectively exposed to molten LiCl–KCl salt for 2000 h. The surface morphology of duplex and graded PSZ coating exhibited flaky and needle like corrosion product on the surface. No marked difference in surface morphology was observed for duplex and graded PSZ coating as the top surface is 100% PSZ coating for both samples.
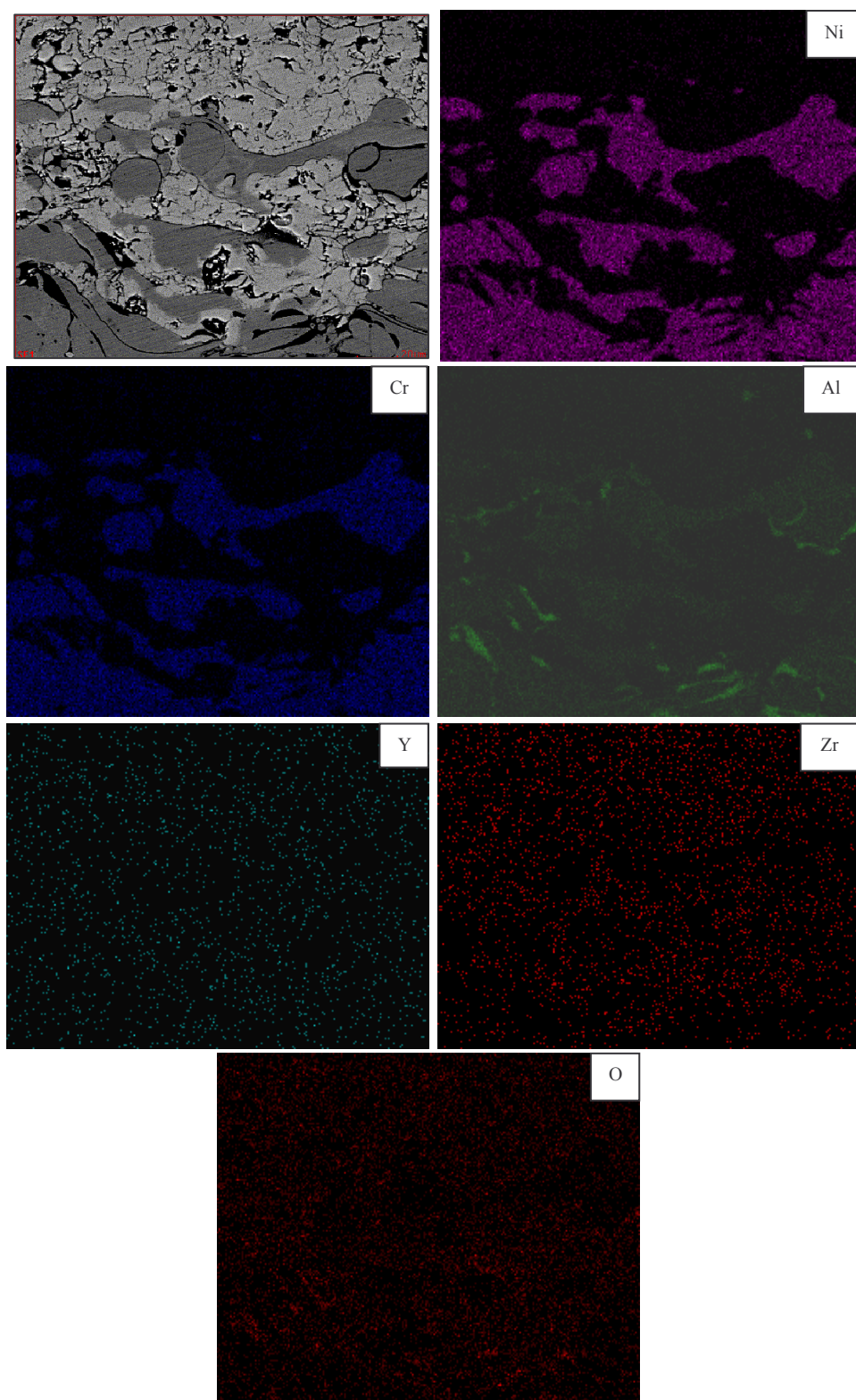
Figure 4.13. SEM micrograph and corresponding elemental X-ray maps of FGM3 coating on Inconel 625 sample.
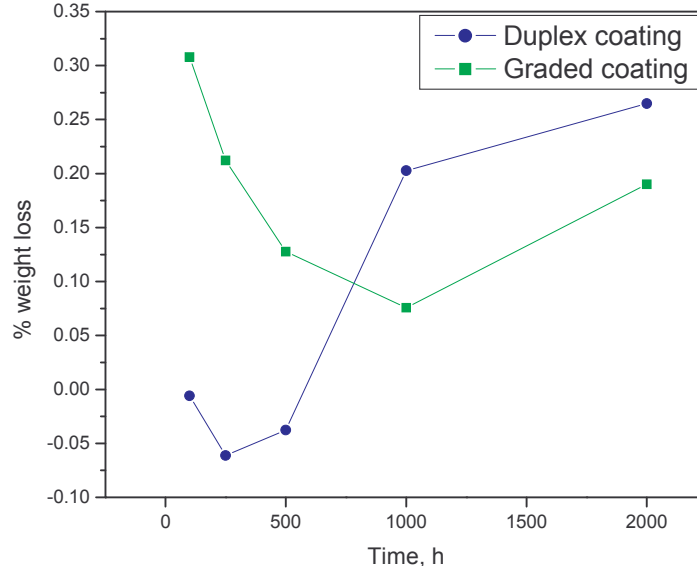
Figure 4.14. Percentage weight loss of duplex and graded partially stabilised zirconia coating exposed to molten LiCl–KCl salt at 600°C.
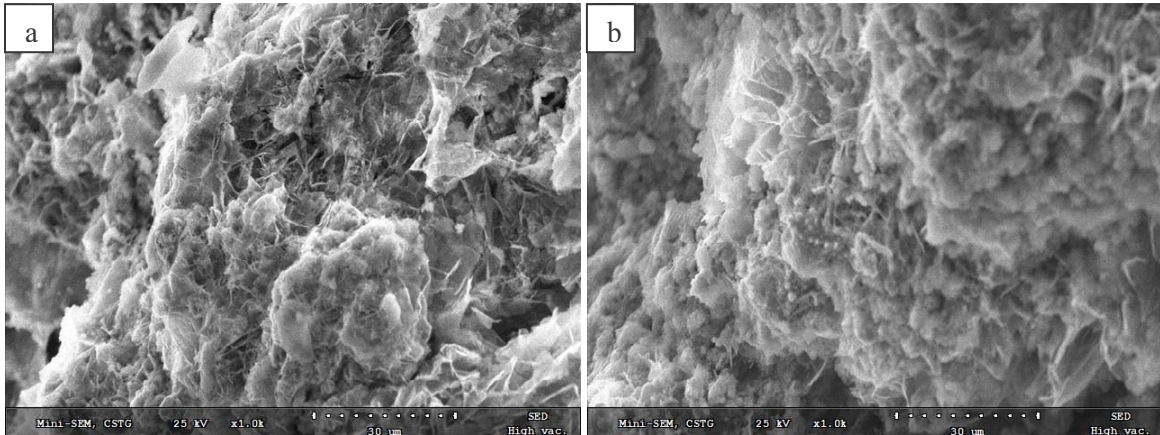
Figure 4.15. SEM micrograph of (a) duplex and (b) graded PSZ coating exposed to molten LiCl–KCl salt for 2000 h.

Figure 4.16 shows the adhesion strength of duplex and graded (FGM3) partially stabilized zirconia coating. The adhesion strength results indicated average adhesive strength of 7.6 ± 2.3 MPa and 9.6 ± 2.3 MPa for duplex and graded coating respectively. This shows that the adhesion strength of the graded coating increased marginally in comparison to duplex coated sample.

177
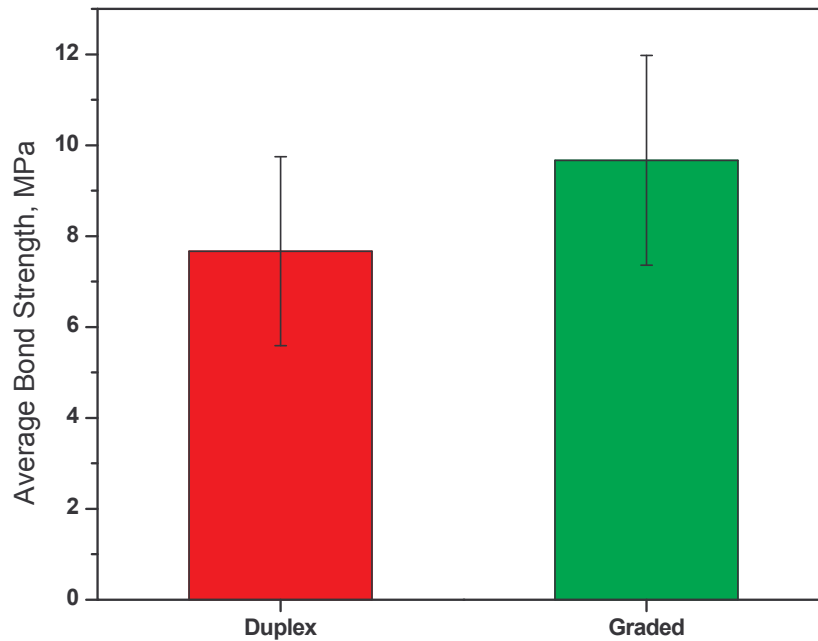
Figure 4.16. Adhesion strength of duplex and graded partially stabilized zirconia coating.

Figure 4.17 shows the thermal cycling behaviour of duplex and graded (FGM3) PSZ coating. No spallation or delamination of the coating from the substrates was observed and duplex and graded PSZ coating showed minor weight change. Graded coating showed marginally higher percentage weight gain compared to duplex coating tested up to 250 cycles. The higher percentage weight gain of the graded coating could be attributed to the higher fraction of bond coat present. However, unlike duplex coating, it would take longer time for the graded coating to form a continuous oxide network.

The plasma spray parameters were extensively optimized by Sampath et al. [130] using inflight diagnostics in such a way that the metallic bond coat and ceramic particles were molten just before impacting the surface and with multi institutional and
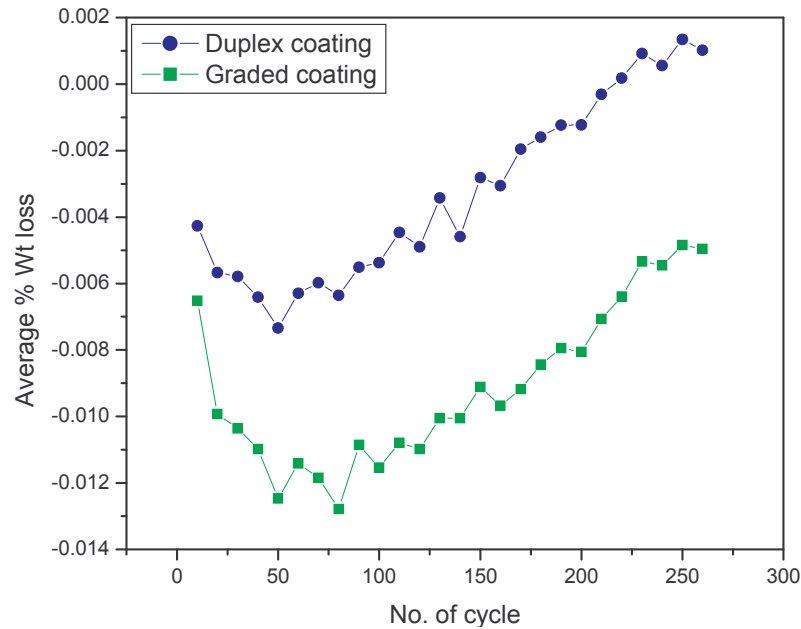
Figure 4.17. Thermal cycling behaviour of duplex and graded partially stabilized zirconia coating.

interdisciplinary efforts, a 20 step linear and parabolically graded FGMs were produced [130]. Inflight diagnostics, modelling strategies and response surface methodology are essential in design and development of functionally graded TBC, because many variables are involved that effect the functionally graded microstructures.

4.6 Summary

1. The weight loss and surface morphology results of PSZ coating over 316L SS exposed for 1000 h to molten LiCl–KCl eutectic salt at 600°C exhibited superior corrosion resistance compared to uncoated 316L SS, however accidental ingression of oxygen and moisture could result in premature spallation of the coating.

2. The cross section examination of exposed PSZ coated 316L SS did not reveal significant attack and selective diffusion of elements unlike uncoated 316L SS even after 1000 h exposure.

3. Functionally graded coating prepared initially exhibited a composite structure consisting of PSZ, reaction phase of bond coat and PSZ, and oxidized bond coat. The reaction phase of bond coat and PSZ mixture of various grey levels consisting of varying compositions and morphologies were observed.

4. Oxidized bond coat of lamellar, spherical and irregular morphologies observed in SEM and optical microscope consisted predominantly of aluminium indicating that the oxidized bond coat mainly composed of alumina.

5. Optimization of parameters led to the formation of graded region without significant reaction of bond coat with PSZ and selective oxidation of bond coat. This was confirmed from the back scatter SEM micrograph, EDX line profile and X-ray elemental mapping.

6. Graded coating exhibited marginally lower percentage weight loss in comparison to duplex coating exposed to molten LiCl–KCl eutectic salt at 600°C for 2000 h under UHP argon.

7. The average adhesion strength and percentage weight gain of the graded coated sample increased marginally in comparison to duplex coated sample. Presence of beneficial non-transformable tetragonal phase in top ceramic coat of duplex and graded coating was confirmed by X-ray diffraction studies.

CHAPTER 5

LASER REMELTING OF PLASMA SPRAYED PSZ COATINGS

5.1 Introduction

Plasma-sprayed thermal barrier coatings usually contain up to 10% porosity, microcracks, partially melted particles and unmelted particles due to splat type of melting and solidification [131]. The presence of porosity and micro-cracks in the coated specimen would cause the penetration of salt and subsequent corrosion of the substrate over long periods of service. The cross-section of the molten-salt exposed PSZ coated 316L SS samples in the present study did not reveal the penetration of molten salts through the pores and subsequent corrosion of the substrate up to the exposure period of 1000 h. However, in order to eliminate the porosity and micro-cracks, and to produce a smooth dense surface, different post coating treatments like, annealing, laser melting and laser shock processing was proposed.

Lasers are used to close the pores and densify on the surface of refractory bricks and to densify the surface of plasma sprayed zirconia coatings in order to improve their mechanical and chemical properties. Laser processing has been attempted as a promising technique for surface modification of partially stabilized zirconia (PSZ) coatings to improve the wear resistance, thermal-shock resistance [132], corrosion resistance [132,133], and life of the coating [134]. Numerous studies on laser surface treatment of zirconia were performed to eliminate cracks and porosity using CW and multimode, CO_2 laser, high power diode laser, Nd: YAG laser, etc. [132,135-138]. The work conducted by

Batista et al. [136] showed that by laser glazing a fully dense and pore-free external layer with a polyfaceted columnar microstructure highly adherent to the plasma sprayed coating, with significant decrease in surface roughness was obtained.

Our earlier studies, [139] on laser surface modification with varying laser powers of 50, 75 and 100 W indicated that a lower laser power of 50 W was beneficial against higher laser powers as they lead to delamination at the bond coat/ceramic coat interface. In the present study the laser power of 50 W was fixed and scan speed was varied with and without sealant and laser re-melted in order to decrease the segmented crack density.

5.2 Effect of Scan Speed

5.2.1 Surface and cross sectional coating characterisation

Optical microstructure of laser re-melted PSZ coating treated at 50 W and 1 mm/s scan speed is shown in Fig 5.1. After laser re-melting the coatings with rough surface changed to a smooth glassy transparent surface. Microstructural inhomogeneities, such as unmelted/partially melted powder particles, pores and cavities, common to plasma-sprayed coatings, were eliminated as reported by Barista et al. [140]. Figure 5.1a, shows the segmented crack morphology consisting of laser tracks with fine grains on the laser track and coarse grains at the interface of laser tracks.

The surface morphology of laser re-melted samples as observed in SEM, also exhibited segmented cracks for all scan speeds. The segmented crack network formed during laser re-melting was formed due to shrinkage and relaxation of residual stresses developed during cooling down of molten zirconia to room temperature [140]. It is reported that when the laser scanning speed is increased, the thermal gradient is higher and consequently the solidification is faster, resulting in higher thermal stresses and thus

higher crack initiation [140]. However in the present study the segmented cracks were found to be more or less equal for all scan speeds. Figure 5.1b, shows the interface separating coarse and fine grain structure. This was also observed for the laser re-melted samples at different scan speeds of 2.5 and 5 mm/s. Khor et al. [141] reported that the size of the grains varied depending on the location within the laser treated surface. The large grains are found mostly at the points where the ripples coalescened during laser processing where additional heat entrapment in these areas possibly causing grain growth [141]. Thus the formation of sharp interface with development of coarse grains was attributed to the (additional heat entrapment) reheating of the solidified material where the ripples coalesce, during rastering of the laser beam with a shift. The entrapped heat causes extensive grain growth leading to the formation of fine and course grain structure. The combination of coarse and fine grain structure offers optimum properties. The fine grain structure obtained due to fast cooling (Fig 5.1c) was also observed with other scan speeds. This polygonal fine grain structure is also beneficial as it improves the hardness and thereby improves the wear resistance of the surface.

The cross sectional micrographs in Fig. 5.2a, b and c show the laser re-melted PSZ coated samples at scan speeds of 1, 2.5 and 5 mm/s, respectively. The cross section microstructure of the laser re-melted region also showed significant decrease in the porosity. Delamination was not observed in the PSZ coatings after laser re-melting at 50 W and at scan speeds of 1, 2.5 and 5 mm/sec. The microcracks are oriented vertically in the coating as seen in Fig 5.2.
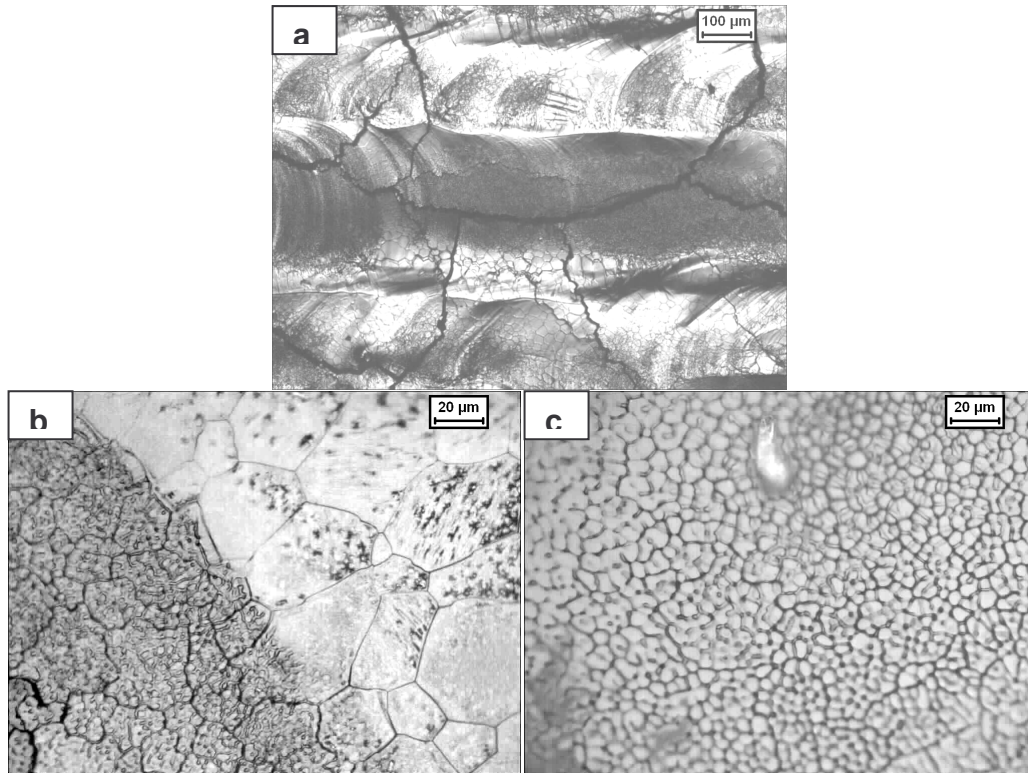
Figure. 5.1. Optical microstructure of laser re-melted PSZ coatings at 50 W and 1 mm/s showing (a) segmented cracked morphology (b) interface separating coarse and fine grains and (c) fine grain structure.

The cross sectional micrographs in Fig. 5.2a, b and c show the laser re-melted PSZ coated samples at scan speeds of 1, 2.5 and 5 mm/s, respectively. The cross section microstructure of the laser re-melted region also showed significant decrease in the porosity. Delamination was not observed in the PSZ coatings after laser re-melting at 50 W and at scan speeds of 1, 2.5 and 5 mm/sec. The microcracks are oriented vertically in the coating as seen in Fig 5.2. These cracks run all the way through the top layer and do not reach the substrate. There was branching in the cracks and some cracks could lead to delamination of the coating near the bond coat layer. However, for the samples laser treated at 1, 2.5 and 5 mm/s, no delamination at the bond coat was observed. The
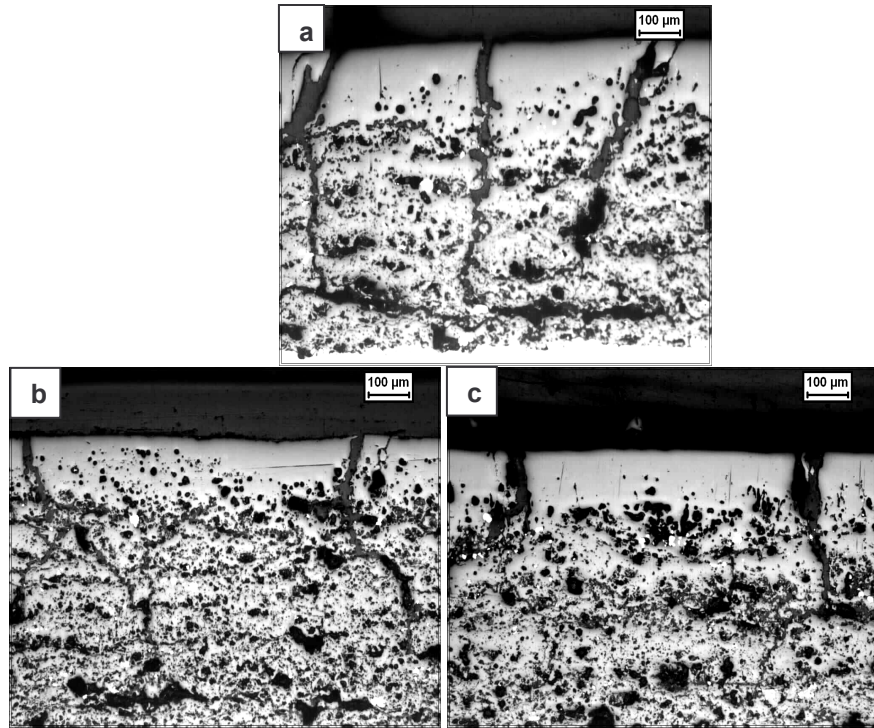
Figure. 5.2. Cross-sectional microstructure of laser re-melted PSZ coatings with varying scan speed of (a) 1mm/s, (b) 2.5 mm/s, and (c) 5 mm/s at 50W power.

presence of these vertical cracks are less harmful than horizontal cracks as they lead to delamination [135]. The segmented cracks, perpendicular to the surface along the densified layer induced by laser treatment improved the thermal shock resistance by improving the strain accommodation [140]. However these vertical cracks are not preferable for corrosion resistance as they provide easy path for molten salt to penetrate and attack the substrate.

5.2.2 *XRD analysis*

The XRD spectra for the as-sprayed and laser re-melted PSZ at scan speeds of 1, 2.5 and 5 mm/s are shown in Fig 5.3. The XRD spectra covered the 2θ range where the characteristic peaks of tetragonal, cubic and minor monoclinic zirconia could be found.

185

The monoclinic phase was present in the as-sprayed sample, while in laser re-melted sample the monoclinic phase disappeared, and tetragonal and cubic phase were only observed. Due to the rapid cooling, the phase change from the cubic phase, comprising the whole yttria content, transforms to the non transformable tetragonal phase with the same composition by a displacive and diffusionless mechanism, which is accompanied by a lattice distortion [138]. The deleterious monoclinic phase present in the as-sprayed coating disappeared and beneficial nontransformable t' phase appeared after laser remelting as determined by XRD analysis.
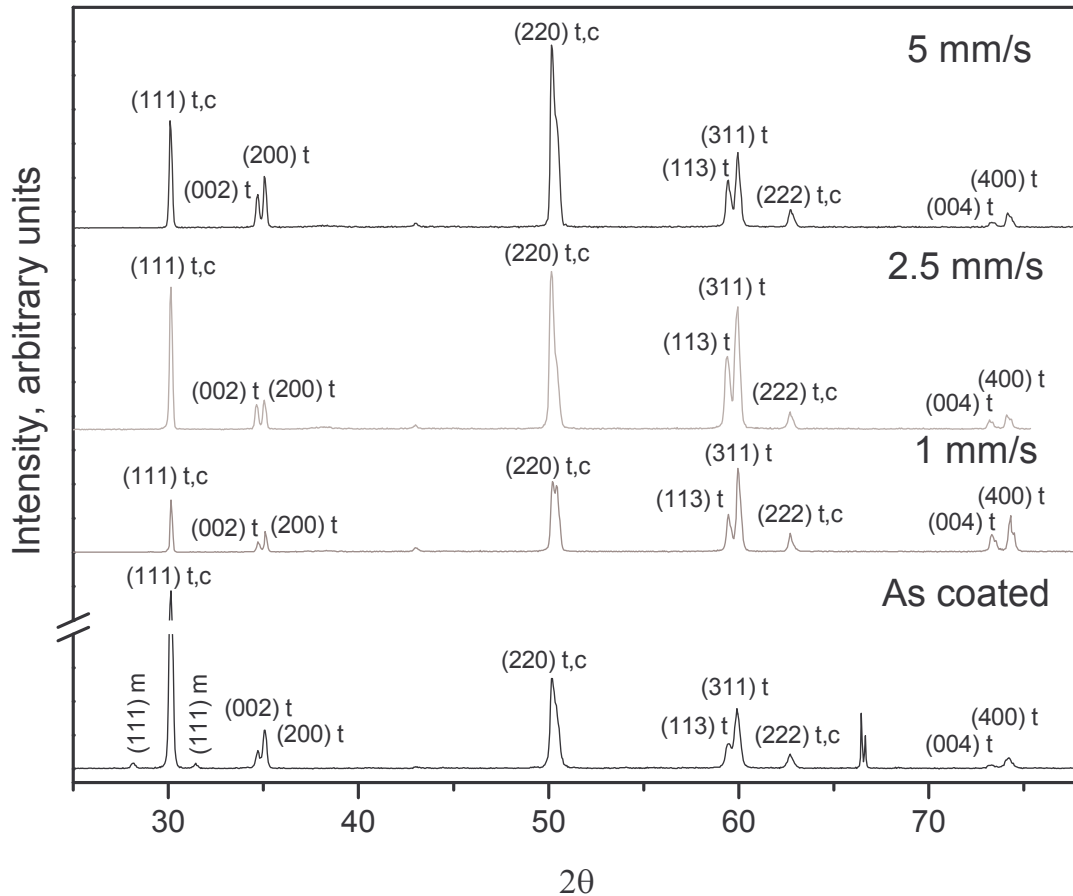
Figure. 5.3. XRD spectra for as-coated and laser re-melted PSZ at 50W at varying scan speeds of 1, 2.5 and 5 mm/s.

5.2.3 Micro-hardness

The micro-hardness measurement showed that the hardness in the laser re-melted surface increased significantly. The average hardness value was 598 VHN in as-sprayed plasma coated ceramic region, 262 VHN in the bond coat, and 177 VHN in the stainless steel substrate. The micro-hardness values in coarse and fine grain structured regions (Fig 5.1b) was 1265 and 1338 VHN respectively, for laser re-melted sample for scan speed of 1 mm/s and 1256 and 1313 VHN for 2.5 mm/s and 1338 and 1382 VHN for 5 mm/s respectively. As expected the hardness in the fine grain structured region was high. The hardness of a two phase coating depends on the microstructure, phase distribution, phase composition and residual stresses in the coating [138]. The significant increase in the hardness value in the laser re-melted region was probably due to microstructure, significant decrease in the porosity and the presence of non-transformable tetragonal phase.

5.3 Sealing

The investigation of hot corrosion of as-sprayed and laser glazed thermal barrier coatings in molten salts by Batista et al. [133] showed that the laser glazed specimens were not efficient in avoiding the molten salt penetration along the thickness direction due to the presence of cracks on the glazed layer. However due to reduced specific surface area of the dense glazed layer, the corrosion reaction of the molten salts with the PSZ has been lower than in coatings in the as-sprayed condition [133]. Segmented cracks during laser remelting are formed due to shrinkage and relief of thermal stresses [132,136] and attempts are being made by numerous researchers to achieve a dense, pore and crack-less surface. Lee et al. [142] have reported the formation of smooth, pore free

surface, eliminating thermally induced cracks by pre-heating of alumina ceramics prior to CO_2 laser treatment. The combined laser beam processing technique carried out on 85% alumina ceramic by Triantafyllidis et al. [143] also resulted in a crack free surface. The formation of thermally induced micro cracks during laser treatment on alumina ceramics, was also avoided by modifying the heat transfer conditions on the surface, resulting in slower surface cooling rates [144]. Chen et al. [145] reported that a dense and crack-less thin layer can be achieved on the surface of 3 wt% SiO_2-doped ZrO_2 coating by applying laser re-melting. Hence SiO_2 was selected along with ZrO_2 as a sealant in the present study in order to produce a crack-less surface. In another study segmentation-cracked coatings produced during laser glazing process were impregnated with aluminium phosphate-based sealant or with sol-gel based sealant to obtain a crack free surface [146].

The optical microstructure of laser re-melted PSZ coated 316L SS surface is shown in Fig 5.4a. Figure 5.4b, is the optical microstructure of as-sprayed PSZ after giving an overlay of ZrO_2 sealant and laser re-melting, while Fig 5.4c is after giving an overlay of $ZrO_2 + SiO_2$ sealant and then laser re-melting. The purpose of the sealant is to alter the surface composition and thereby decrease the segmented cracks. As shown in Fig 5.4b and 5.4c, there was decrease in the segmented cracks for the sealed and laser re-melted samples. The surface morphology of these sealed and laser re-melted samples as observed in SEM also exhibited lesser segmented cracks with large cell size. However, the cross section optical micrograph clearly indicated complete delamination of the laser re-melted ZrO_2 sealant layer and partial delamination of the $ZrO_2 + SiO_2$ sealant layer. This delamination is primarily due to the differences in thermal expansion co-efficient and phase transformation of the sealant used, and the PSZ coating, during heating and
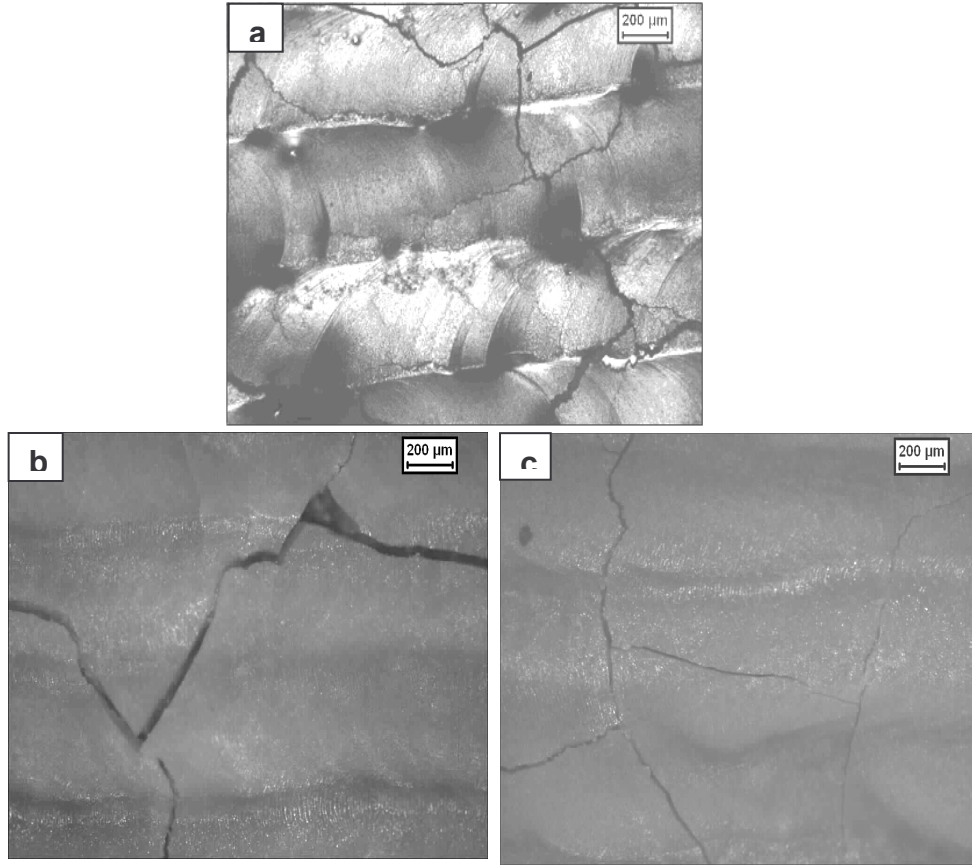
Figure. 5.4. Optical microstructure of laser treated (a) PSZ coating, (b) ZrO₂ sealed coating and (c) ZrO₂ + SiO₂ sealed coating, laser treated at 5 mm/s scan speed at 50W power.

cooling. It was reported that when the amount of SiO_2 additive exceeded the optimal value of 3 wt%, not only the remelted layer cracked but also extremely large pores remained in the coating after laser remelting which deteriorates the adhesive strength of the coating [145]. So the composition of sealant, particularly SiO_2 is crucial in order to achieve crack-less surface after laser remelting.

Although the segmented cracks on the surface of sealed and laser re-melted samples decreased, the presence of segmented cracks appear to be unavoidable. So an attempt was made to seal the segmented cracks formed after laser re-melting with ZrO_2 sealant through heat treatment. The SEM micrograph of PSZ laser re-melted, ZrO_2 sealed and heat treated is shown in Fig. 5.5. The typical segmented crack morphology of the laser re-melted surface with the sealant powder filling the cracks is clearly visible as white colour network in Fig 5.5 a. At high magnification the sealant powder that filled the cracks, was not sintered properly due to lower sintering temperature, as shown in Fig. 5.5 b. However, the cracks were reasonably sealed with zirconia as shown in the Fig 5.5 a and b to offer protection against penetration of corrosive molten salts. Further optimization of parameters are required to achieve, a homogeneous, uniform and pore-less and crack-less surface.
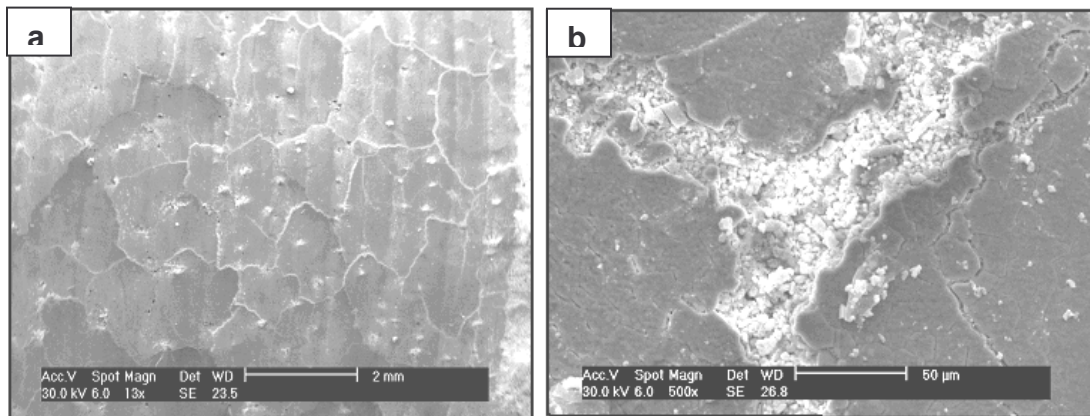
Figure. 5.5 (a) SEM micrograph of PSZ laser treated, ZrO_2 sealed and heat treated (b) at high magnification.

190

5..4 Silica Deposition

The surface morphology of silica deposited over PSZ coated sample is shown in Fig 5.6. Plasma sprayed coating exhibit typical splat type of morphology with pores and microcracks (Fig 4.5a). From Fig 5.6a, we can see that silica deposited sample exhibited dense spherical morphology. The spherical particles are then getting agglomerated into clusters. Figure 5.6b is the high resolution SEM image which clearly shows clusters of agglomerated spherical particles. This kind of dense surface morphology is desirable for better protection against corrosion. The EDX spectrum obtained from SEM micrograph shown in Fig 5.6a is shown in Fig 5.6c. The composition of the surface is Si-41.38, O-35.84, Zr-20.97 and Y-1.81 in weight percentage. Similar EDX analysis carried out on another sample showed Si-31.74, O-33.27, Zr-30.70 and Y-4.30 wt%. The values were more or less same and indicates that significant amount of silica is present on the top surface.

The XRD spectra of as-sprayed PSZ coating and silica deposited PSZ coating is shown in Fig 5.7. Minor peak corresponding to monoclinic phase (m) was also observed as shown in Fig. 5.7. The monoclinic phase could have formed due to slow cooling rates during plasma spray process. The monoclinic phase is undesirable as the phase transformations with accompanying volume changes would result in coating spallation. The XRD pattern from as-sprayed PSZ coated surface and silica deposited surface exhibited similar phases. This suggests that silica is present in amorphous form or in solid solution. The presence of glassy silica is also beneficial as SiO_2 is compatible in molten salt under O_2 and Cl_2 gas environment [52].

5.5 Microstructure

The cross section SEM micrographs of plasma sprayed PSZ, sealed with ZrO_2 and laser re-melted region is shown in Fig 5.8. The typical solidification structure consisting of dendrites of zirconia is clearly seen in Fig 5.8a. The columnar grains underneath the dendritic structure on the surface are shown in Fig 5.8b. As the solidification was directional and vertically from the substrate to the re-melted area, formation of columnar dendritic structure takes place. This unidirectional solidification where the thermal gradient was perpendicular to the substrate, should have grain growth primarily perpendicular to the surface [138].
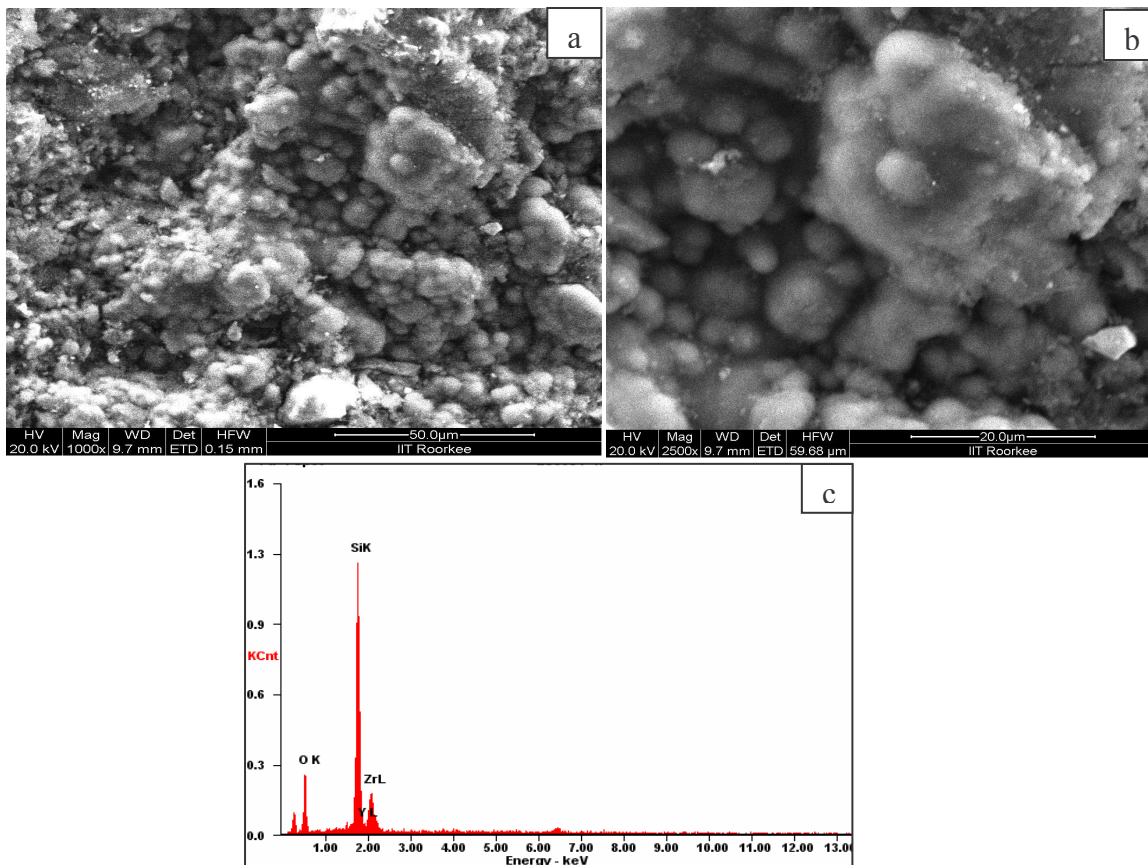
Figure 5.6. SEM micrograph of silica deposited PSZ (a) 1000x magnification (b) 2500x magnification (c) EDX spectrum.
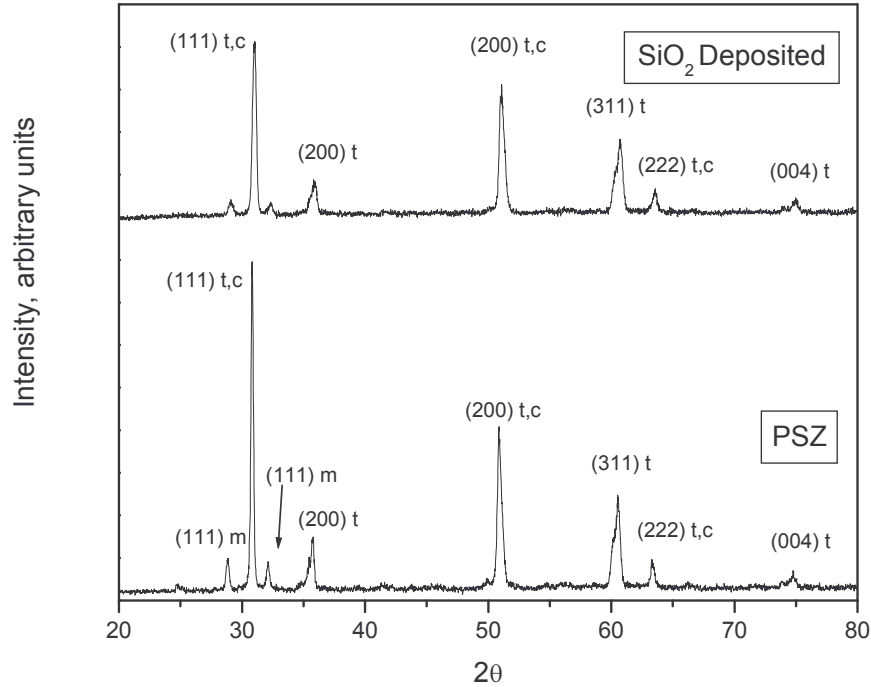
Figure 5.7. XRD spectra of as-sprayed PSZ coating and SiO$_2$ deposited PSZ coating.

The microstructure with cellular morphology with a dendritic structure near the surface of the coating was observed by Wang et al. [138]. The interface separating the dendritic structure and columnar structure is also shown in the figure. In comparison to the lamellar structure resulting from thermal spraying, the columnar structure may provide better thermo-mechanical properties [135]. The surface microstructure of the laser treated coating is characterized by a crack network, depressions or craters and fine grain structures, [141]. As reported by Khor et al. [141] the probable mechanism for the formation of depression involves the bubbles formed from entrapped gas during plasma spraying, being released or floated to the surface during laser processing and rupturing the surface. Although the molten pool has solidified rapidly as the laser beam moved away, there was enough time for pores existing in the as-sprayed coating, to coalescene and rise to the surface [136].
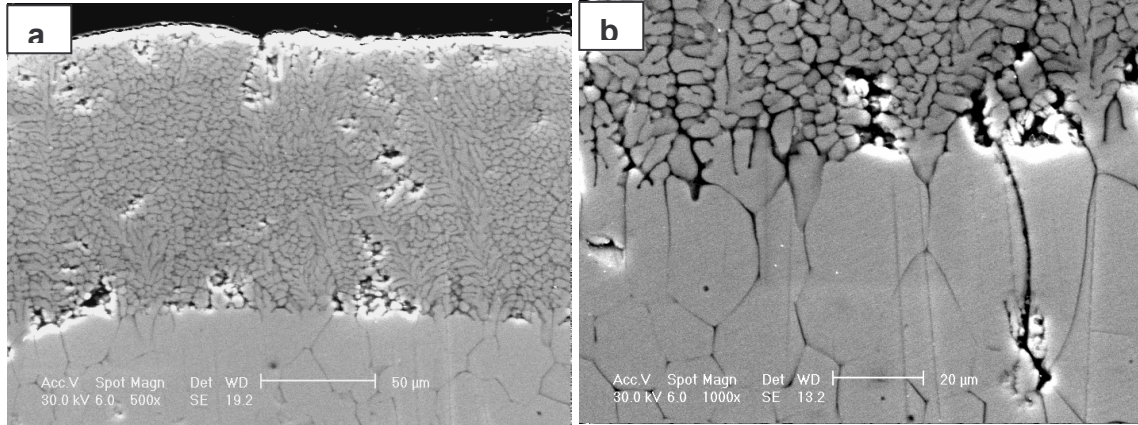
Figure. 5.8. (a) Cross section SEM micrographs of laser treated PSZ over 316L SS sealed with ZrO₂ (b) interface at high magnification.

The SEM micrograph in Fig. 5.9a shows the pores raised to the top surface on part of the grain and does not get eliminated, while in the other part of the grain, pores get completely eliminated. The temperature fluctuations during laser re-melting might have led to this type of microstructure indicating that the pores indeed raise to the top surface and get eliminated. If the intersplat porosity is large, they coalescene in to a large bubble and raise to the top surface and bursts, leading to the formation of depressions.

The micrograph shown in Fig 5.9a with large grains containing smaller grains on the laser remelted top surface was also observed by Antou et al. [147]. They reported that the smaller grains are formed by the division of single columnar grain in to smaller columns which is also seen in the fractographs, and the phenomenon was explained by the decrease of the solid/liquid interfacial energy near the surface (free energy of formation of nucleus). The smaller columnar grains were absent in the adjacent grains as shown in Fig 5.9a. Tsai et al. [148] referred that the commonly observed defect in the laser glazing of thermal barrier coatings include surface nucleation. Since the top surface undergoes faster cooling rate than the inside layers, nucleation would be more in the top region than growth processes. These small grains formed by surface nucleation would

grow in to large grains on reheating (entrapped heat) of the adjacent material during laser beam rastering. If this reheating was not sufficient enough to cause complete grain growth, then remnants of growing grains would be seen as shown in the figure.

The characteristic bands observed in our earlier work, [132] and also shown in Fig 5.9b is explained as follows. The small grains less than six sides on a two dimensional cut become smaller and large grains more than six sides on a two dimensional cut become larger as a result of curvature induced growth according to Gibbs-Thomson equation [149].
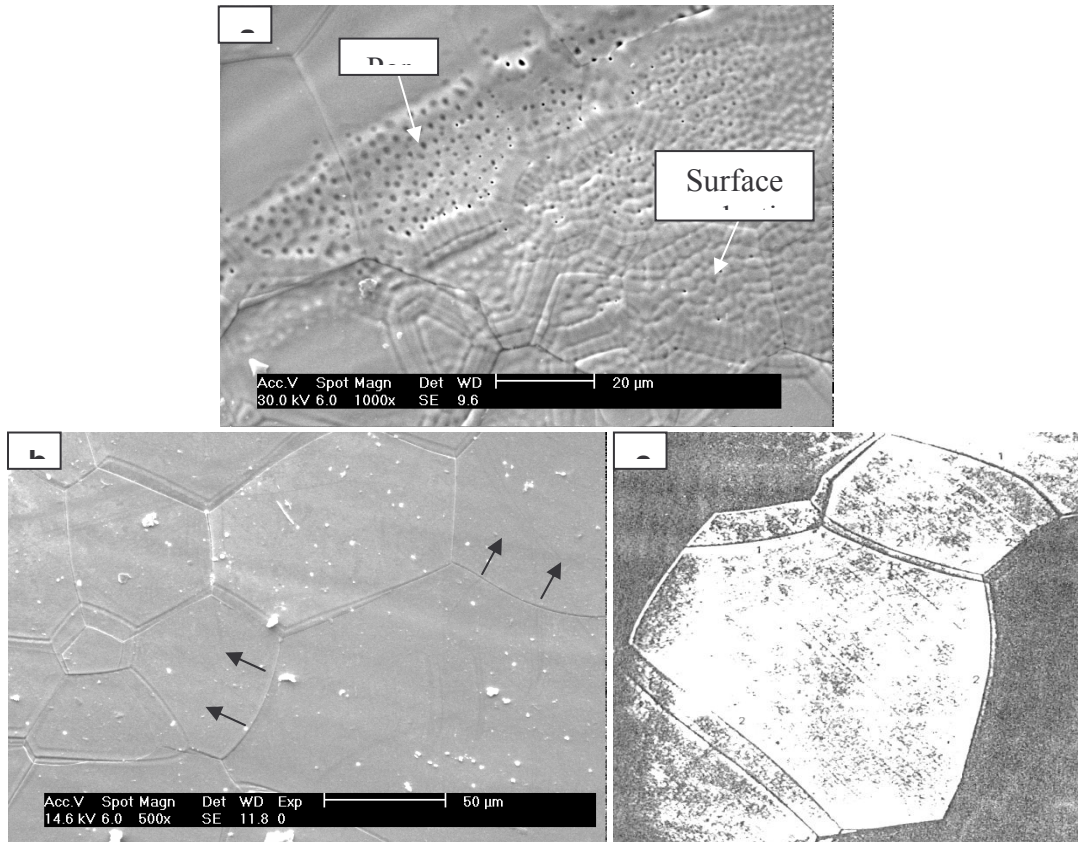
Figure. 5.9. SEM micrograph of surface of laser re-melted PSZ coating (a) depicting grain growth and pores raised to the top surface (b) depicting curvature induced grain growth and (c) grain growth in aluminium [149].

The chemical potential difference will cause atoms to move toward the convex side and under this, curvature induced growth, the boundary moves toward the concave side [149]. This curvature induced grain growth is observed in Fig 5.9b, which is much similar to Fig 5.9c for grain growth in aluminium where the boundaries have moved during heat treatment. Thus lasers producing intense localised heating on the surface also produces novel microstructures due to rapid cooling, which could aid in improving the performance [150].

5.6 Summary

1. Laser re-melting of PSZ coating eliminated pores and cavities present in the rough as-sprayed coating and a smooth glassy transparent surface was produced.

2. The optical microstructure of laser re-melted surface exhibited a sharp interface with coarse and fine grains which was attributed to the reheating effect.

3. The hardness of as-sprayed coating (598 VHN) increased after laser re-melting and the fine grain structure in laser remelted sample showed high hardness of 1300 VHN.

4. The cross- section micrograph of laser re-melted region revealed vertical cracks, and microstructure exhibited dendritic structure at the top and columnar grains below.

5. The segmented cracks on the surface of sealed and laser re-melted sample decreased, however delamination was observed for ZrO_2 sealant. An attempt was made to seal the segmented cracks formed by applying ZrO_2 sealant and heat treating. Silica was deposited by laser deposition to obtain dense surface on plasma sprayed PSZ coating.

6. SEM examination of the laser re-melted PSZ coating revealed the pores being raised to the top surface and getting eliminated. The coarsening of the grains in the laser re-melted region was found to be curvature induced growth.

CHAPTER 6

SUMMARY AND SCOPE FOR FUTURE WORK

Metallic fuelled fast breeder reactors with co-located pyrochemical reprocessing plants has been proposed as the best option to increase the breeding gain, reduce the doubling time and reprocess short cooled and high burnup fuel. The major part in implementation of the pyrochemical reprocessing technology involves identification, development, testing and qualification of reliable corrosion resistant materials/coatings for service in corrosive molten LiCl–KCl salt environment operating at 600°C-1200°C for various unit operations. Limited literature exists on the materials used under molten LiCl–KCl salt environment. Corrosion studies on candidate materials like 2.25Cr-1Mo, 9Cr-1Mo, 316L SS, Ni base alloys and partially stabilised zirconia were carried out in molten LiCl–KCl salt medium. Corrosion studies were carried out on candidate materials in molten LiCl–KCl salt under air, Cl_2 and ultra high purity argon environments typically encountered in pyrochemical reprocessing plant. The results indicated that Inconel 600 and Inconel 690 offer better corrosion resistance compared to Inconel 625 in air and chlorine environment. The higher corrosion of Inconel 625 in molten LiCl–KCl salt under air and chlorine environment was attributed to the higher Mo content. Ni base alloys exhibited better corrosion resistance than Cr-Mo steels and 316L SS in molten LiCl–KCl salt under UHP Ar environment. Corrosion studies under UHP argon environment indicated that the corrosion attack of the materials increased in the following order: 2.25Cr-1Mo > 9Cr-1Mo > 316L SS > High density graphite > Inconel 600 ~ Inconel 690 ~ Inconel 625 > Pyrolytic graphite. Inconel 600 and Inconel 625 base metal exposed to molten LiCl–KCl

197

salt under Cl_2 atmosphere clearly revealed intergranular corrosion, corrosion along twin boundaries and preferential dissolution of precipitates within the grain, while weldment revealed interdendritic dissolution and cell boundary dissolution in the weld region. Based on the surface morphology of corrosion product, X-ray diffraction and energy dispersive analysis of X-rays, the mechanism of corrosion of Cr-Mo steels, 316L SS and Ni base alloys (Inconel 600, Inconel 690, Inconel 625) has been attributed to the selective dissolution of Cr with eventual formation of voids/cracks and subsequent spallation of chromium rich compound at the surface. The tungsten rich film formed over EF Ni-W offered better corrosion resistance compared to EF Ni where unprotective porous and brittle NiO salt film formed. Partially stabilized zirconia coating on type 316L SS showed superior corrosion resistance in molten LiCl–KCl salt. Careful control of oxygen and moisture during corrosion tests are of paramount importance in order to avoid accelerated corrosion.

Functionally graded coatings offer good adhesion and thermal cycle life compared to conventional duplex partially stabilized zirconia coating. Optimization of parameters was carried to achieve graded layer without any reaction between ceramic coat and bond coat and also without oxidation of bond coat. The control of spray parameters to deposit a graded layer using premixed metallic and ceramic powders through a single plasma torch is challenging due to large difference in physical characteristics of the ceramic and metallic powders which results in different deposition characteristics. By controlling the hydrogen flow rate and spray distance a graded coating was achieved without oxidation of bond coat (NiCrAlY) and reaction of bond coat and ceramic coat (PSZ) during deposition. The graded coating exhibited marginally higher adhesion strength and

percentage weight gain in comparison to duplex coating. Surface modification techniques like laser remelting was envisaged to densify the surface of ceramic coatings. Consolidation of plasma sprayed partially stabilised zirconia coatings by laser remelting improved microstructure, density, surface roughness, hardness and homogeneity. An attempt was made to seal the segmented cracks formed by applying SiO_2 and ZrO_2 sealant. The surface of sealed and laser re-melted sample decreased, however delamination was observed. Silica deposition by laser cladding over as-sprayed PSZ coating appears to be promising technique. Densification of laser remelted surface by pores being raised to the top surface and curvature induced grain growth was observed.

Scope for future work:

The following are the scope of future work towards testing and development of materials and coatings for pyrochemical reprocessing applications.

➢ Electrochemical polarisation and impedance studies in molten LiCl–KCl salt.

As discussed in section 1.2.4 limited literature exists on the electrochemical studies of structural materials in molten LiCl–KCl salt. In order to understand the characteristics of salt films formed it is essential to conduct electrochemical polarisation and impedance studies in molten LiCl–KCl salt.

➢ Molten salt corrosion studies under varying concentrations of oxygen.

From earlier studies and the present investigation it is clear that corrosion of structural materials in molten LiCl–KCl salt is sensitive to oxygen. In order to understand the extent of corrosion due to trace amounts of oxygen it is essential to carryout molten salt corrosion studies by varying the concentrations of oxygen from 10 to 1000 ppm.

➢ Thermogravimetry studies of candidate materials in molten LiCl–KCl salt.

Thermogravimetry studies allow precise measurement of weight changes as a function of temperature and time by controlling the atmosphere. Thermogravimetry studies are quite useful in understanding the mechanism of degradation of materials and reaction kinetics.

➢ Optimising the parameters for achieving graded coating.

Durability of coating is important for practical application of ceramic coated materials for fabrication of critical components. Therefore it is essential to achieve graded coating with smooth gradation and enhance the thermal cycle life and adhesion strength of the coating.

➢ Laser surface modification of ceramic coatings to achieve crack free dense surface.

Laser surface treatments with simultaneous melting and additives (laser cladding) could result in corrosion resistant, crack free, dense surfaces. Therefore optimisation of laser cladding parameters is essential to achieve dense coatings to provide better corrosion protection than coatings with pores and micro cracks.

➢ Molten salt corrosion and thermal cycling studies of laser surface modified ceramic coatings.

For practical application laser surface modified ceramic coatings should exhibit better corrosion resistance and thermal cycle life. Therefore it is essential to carryout molten salt corrosion and thermal cycling studies of laser surface treated coatings after achieving crack free dense surfaces.

REFERENCES

[1] Baldev Raj, H.S. Kamath, R. Natarajan, P.R. Vasudeva Rao, Prog. Nucl. Energy., 47 (2005) 369-379.

[2] K. Nagarajan, T. Subramanian, B. Prabhakara Reddy, P.R. Vasudeva Rao, Baldev Raj, Nucl. Technol., 162 (2008) 259-263.

[3] U. Kamachi Mudali, A. Ravi Shankar, S. Ningshen, Girija Suresh, Ravikumar Sole, K. Thyagarajan, Energy Procedia., 7 (2011) 468-473.

[4] Baldev Raj, U. Kamachi Mudali, Materials challenges at the back end of the fuel cycle, Twelfth annual conference (INSAC-2001), Indore, Vol.2, 10-12 Oct 2001, pp.117-126.

[5] B.Prabhakara Reddy, K. Nagarajan, P.R. Vasudeva Rao, Pyrochemical Reprocessing of Metallic Fuels- An overview, Presented at Fourth ISEAC International Discussion Meet on Electrochemistry and its Applications, at Thiruvananthapuram, Kerala, India, 7-10 Feb 2011, pp.101-105.

[6] K. Nagarajan, INCAS Bulletin, 14 (1998) 40-43.

[7] B.Prabhakara Reddy, S.P. Ruhela, G. Ravisankar, K. Nagarajan, P.R. Vasudeva Rao, Current status of Pyroprocess Development activities at IGCAR, Kalpakkam, India, International workshop on Nuclear Pyroprocessing (NUPYRO-2012) was held at Daejeon, Korea, 16-18 Dec 2012, Plenary Session 1.

[8] C.E. Till, Y.I. Chang, Plentiful Energy: The Story of the Integral Fast Reactor, 2011.

[9]   L.C. Walters, J. Nucl. Mater., 270 (1999) 39-48.

[10] C.E. Till, Y.I. Chang, The Integral Fast Reactor, Advances in Nuclear Science and Technology, Plenum Publishing Corp., New York, 20 (1988) 127-154.

[11] J.P. Ackerman, T.R. Johnson, L.S.H. Chow, E.L. Carls, W.H. Hannum, J.J. Laidler, Prog. Nucl. Energy., 31 (1997) 141-154.

[12] T. Koyama, M. Iizuka, Y. Shoji, R. Fujita, H. Tanaka, T. Kobayashi, M. Tokiwai, J. Nucl. Sci. Technol., 34 (1997) 384-393.

[13] J.L. Willit, W.E. Miller, J.E.Battles, J. Nucl. Mater., 195 (1992) 229-249.

[14] M.V. Kormilitsyn, A.V. Bychkov, V.S. Ishunin, Pyroelectrochemical reprocessing of irradiated fuel of fast reactors. VI. Generalization of experience on BOR-60 spent nuclear fuel reprocessing using approaches "$UO_2 \rightarrow UO_2$" "MOX$\rightarrow PuO_2$" and

"MOX→MOX", Proc of Global 2003, New Orleans, November 16-20 (2003) 782-783.

[15] T. Inoue, L. Koch, Nucl. Eng. Technol., 40 (2008) 183-190.

[16] H.F. Mcfarlane, M.J. Lineberry, Prog. Nucl. Energy., 31 (1997) 155-173.

[17] L. Burris, Chem. Eng. Prog., Feb, 1986, pp.35-39.

[18] J.J. Laidler, J.E. Battles, W.E. Miller, J.P. Ackerman, E.L. Carls, Prog. Nucl. Energy., 31, No. l/2, (1997) 131-140.

[19] J.P. Ackerman, Ind. Eng. Chem. Res., 30 (1991) 141-145.

[20] L. Burris, R.K. Steunenberg, W.E. Miller, The application of electrorefining for recovery and purification of fuel discharged from the integral fast reactor, AlChE Symp. Ser., (1987), 83, no.254, 135-142.

[21] J.E. Herceg, K.J. Belcher, L. Bova, H.J. Haupt, S.A. Kamal, J.G. Saiveau, "Engineering and Acquisition of Equipment for Electrometallurgical Treatment of Spent Nuclear Fuel", Proceedings of Eighth International Conference on Nuclear Engineering, held April 2-6, 2000 (Baltimore, USA), p.1.

[22] A.R. Brunsvold, P.D. Roach, B.R. Westphal, Design and Development of a Cathode Processor for Electrometallurgical Treatment of Spent Nuclear Fuel, Proceedings of Eighth International Conference on Nuclear Engineering, held April 2-6, 2000 (Baltimore, USA), p.1.

[23] B.R. Westphal, K.C. Marsden, J.C. Price, D.V. Laug, Nucl. Eng. Technol., 40 (2008) 163-174.

[24] B.R. Westphal, J.C. Price, D. Vaden, R.W. Benedict, J. Alloys Compd., 444–445 (2007) 561–564.

[25] B.R. Westphal, K.C. Marsden, J.C. Price, Metall. Mater. Trans. A., 40A (2009) 2861-2866.

[26] J.W. Koger, C.E. Holcombe, J.G. Banker, Thin Solid Films., 39 (1976) 297-303.

[27] G.de Vasconcelos, L.C.O. Dacal, M.E. Sbampato, N.A.S. Rodrigues, J.R. Martinelli, Phys. Status Solidi A., 201 (2004) 2351–2355.

[28] A. Ravi Shankar, B. Prabhakara Reddy, Vipin Chawla, M. Jeya Preyanga, Ramesh Chandra, U. Kamachi Mudali, Surf. Coat. Technol., 204 (2010) 3214-3221.

[29] A. Ravi Shankar, U. Kamachi Mudali, Vipin Chawla, Ramesh Chandra, Ceram. Int., 39 (2013) 5175–5184.

[30] C.E. Stevenson, The EBR-II fuel cycle story, Production of pins, American Nuclear Society, Illinois, USA, (1987) pp.123-126.

[31] P.S. Chen, W.C. Stevens, C.L. Trybus, Reusable Molds for Casting U-Zr Alloys, ANL Report:ANL/FE/CP-75641, September 1992; Paper submitted to the Sixth International Conference on Surface Modification Technology, Chicago, Illinois, November 1-5, 1992.

[32] Nagaraj Alangi, Jaya Mukherjee, P. Anupama, M.K. Verma, Y. Chakravarthy, P.V.A. Padmanabhan, A.K. Das, L.M. Gantayet, J. Nucl. Mater., 410 (2011) 39–45.

[33] Choon-ho Cho, Yun-sang Lee, Eung-soo Kim, Jeong-guk Kim, Han-soo Lee, J Radioanal Nucl Chem., 287 (2011) 485-490.

[34] C.A.C. Sequeria, Molten Salt Forum., 7 (2003) 3-40.

[35] J.E. Indacochea, J.L. Smith, K.R. Litko, and E.J. Karell, J. Mater. Res., 14 (1999) 1990-1995.

[36] A. Nishikata, H. Numata, T. Tsuru, Mater. Sci. Eng., A, 146 (1991) 15-31.

[37] R.D. Kane, Molten salt corrosion in: ASM hand book, Vol.13A, Corrosion: Fundamentals, testing and protection, ASM International, Materials Park Ohio pp.216-219.

[38] L.L. Shreir, Corrosion: Metal/Environment reactions, second edition, Newnes Butterworths Publication, London, 1 (1977) 2.110-2.119.

[39] M.A. Uusitalo, P.M.J. Vuoristo, T.A. Mantyla, Corros. Sci., 46 (2004) 1311-1331.

[40] A. Ruh, M. Spiegel, Corros. Sci., 48 (2006) 679-695.

[41] G.Y. Lai, Molten salt corrosion in: High temperature corrosion of engineering alloys, ASM International, pp.169-183.

[42] C.Edeleanu, J.G. Gibson, J. Inst. Met., 88 (1960) p.321.

[43] H. Kinoshita, C.A. Sharrad, I. May, R.G. Lewin, Behaviour of moisture in LiCl-KCl eutectic for pyrochemical process, Proceedings of Global 2005, Oct 9-13, 2005, Tsukuba, Japan, paper No.191.

[44] A. Nishikata, Y. Shimatani, S. Haruyama, J. Jpn. Inst. Met., 48 (1984) 705-712.

[45]   X.K. Feng, C.A. Melendres, J. Electrochem. Soc., 129 (1982) 1245-1249.

[46]   F. Colom, A. Bodalo, Corros. Sci., 12 (1972) 731-738.

[47]   D.O. Raleigh, J.T. White, C.A. Ogden, J. Electrochem. Soc., 126 (1979) 1093-1099.

[48]   M. Tada, Y. Ito, Mater. Sci. Forum., 185-188 (1995) 917-924.

[49]   F. Colom, A. de la Plaza, J. Electroanal. Chem., 290 (1990) 105-118.

[50]   C. Junming, X. Songbo, J. Chin. Soc. Corrosion Protect., 15 (1995) 167-172.

[51]   W.H. Smyrl, M.J. Blackburn, Corrosion., 31 (1975) 370-375.

[52]   M. Asou, S. Tamura, T. Namba, H. Kamoshida, Y. Shoji, K.Mizuguchi, T. Kobayashi, in: Proceedings of Global 1999, Jackson Hole, Wyoming, Aug 29–Sep 3, 1999.

[53]   M. Takeuchi, T. Kato, K. Hanada, T. Koizumi, S. Aose, J. Phy. Chem. Solids., 66 (2005) 521–525.

[54]   J.E. Indacochea, J.L. Smith, K.R. Litko, E.J. Karell, A.G. Raraz, Oxid. Met., 55 (2001) 1-16.

[55]   Y. Hosoya, T. Terai, T. Yoneoka, S. Tanaka, J. Nucl. Mater., 248 (1997) 348-353.

[56]   S.H. Cho, J.M. Hur, C.S. Seo, S.W. Park, J. Alloys Compd., 452 (2008) 11–15.

[57]   S.H. Cho, J.M. Hur, C.S. Seo, J.S. Yoon, S.W. Park, J. Alloys Compd., 468 (2009) 263–269.

[58]   S.H. Cho, C.S. Seo, J.S. Yoon, H.S. Park, S.W. Park, J. Ind. Eng. Chem., 13 (2007) 729-734.

[59]   S.H. Cho, I.J. Cho, G.S. You, J.S. Yoon, S.W. Park, Met. Mater. Int., 13 (2007) 303-309.

[60]   S.H. Cho, J.S. Zhang, Y.J. Shin, S.W. Park, H.S. Park, J. Nucl. Mater., 325 (2004) 13-17.

[61]   R.Y. Liu, X. Wang, J.S. Zhang, X.M. Wang, J. Nucl. Mater., 327 (2004) 194-201.

[62]   R.Y. Liu, Y. Sun, J.S. Zhang, J.T. Guo, M.L. Zhu, Mater. Lett., 57 (2003) 4433-4438.

[63]   P. Periasamy, M.F. Hurley, B.M. Marx, M.F. Simpson, D.P. Butt, J. Nucl. Mater., 405 (2010) 266–273.

[64] S. Sampath, U. Schulz, M.O. Jarligo, S. Kuroda, MRS Bulletin, 37 (2012) 903-910.

[65] W.Y. Lee, D.P. Stinton, C.C. Berndt, F. Erdogan, Y.D. Lee, Z. Mutasim, J. Am. Ceram. Soc., 79 (1996) 3003-3012.

[66] N. Reddy, A.S. Gandhi, J. Am. Ceram. Soc., 33 (2013) 1867–1874.

[67] N. Eliaz, G. Shemesh, R.M. Latanision, Eng. Fail. Anal., 9 (2002) 31-43.

[68] D.R. Clarke, M. Oechsner, N.P. Padture, MRS Bulletin, 37 (2012) 891-898.

[69] C.G. Levi, J.W. Hutchinson, M.H. Vidal-Sétif, C.A. Johnson, MRS Bulletin, 37 (2012) 932-941.

[70] ASTM Standard G28-02, "Standard Test Methods of Detecting Susceptibility to Intergranular Corrosion in Wrought, Nickel-Rich, Chromium-Bearing Alloys" (USA: ASTM International, 2002) p. 1.

[71]   Powder Diffraction File-2 (PDF-2) JCPDS-ICDD, PCPDFWIN Version 2.02, May 1999.

[72]   ASTM standard: E 1920-03, Standard Guide for Metallographic Preparation of Thermal Sprayed Coatings, ASTM International, West Conshohocken, PA, USA, 2003, 1-5.

[73]   ASTM standard: C 633 – 01, Standard Test Method for Adhesion or Cohesion Strength of Thermal Spray Coatings, ASTM International, West Conshohocken, PA, USA, 2001, 1-7.

[74] Y.S. Li, M. Spiegel, S. Shimada, Mater. Chem. Phys., 93 (2005) 217-223.

[75] N. Birks, G.H. Meier, F.S. Pettit, Introduction to the High Temperature Oxidation of Metals, 2nd ed., UK: Cambridge University Press, (2006), p. 126,149.

[76] K.R. Peters, D.P. Whittle, J. Stringer, Corros. Sci., 16 (1976) 791-796.

[77] ASM Handbook: Corrosion: Fundamentals; Testing and Protection, Metals Park, OH: ASM International, 13A (2003) p. 216.

[78] R. Bender, M. Schütze, Mater. Corros., 54 (2003) 567–586.

[79] R. Bender, M. Schütze, Mater. Corros., 54 (2003) 652-686.

[80] Di Zhu, Bin Wei: Proc. of 1st Int. Symposium on Electrochemical Microfabrication, 92 (1992) 333-339.

[81] T. Hart, A. Watson, Met. Finish., 99 (2001) 387-398.

[82] W.Z. Friend: in Corrosion of Nickel and Nickel base alloys, John Wiley-Interscience Publication, New york, 1980, p.12.

[83] T. Tzvetkoff, A. Girginov, M. Bojinov, J. Mater. Sci., 30 (1995) 5561-5575.

[84] R.M. Arons, C.M. Edstrom, Thin Solid Films., 73 (1980) 53-58.

[85] N. Eliaz, T.M. Sridhar, E. Gileadi, Electrochim. Acta., 50 (2005) 2893–2904.

[86] F.Colom, A. Bodalo, Corros. Sci., 12 (1972) 731-738.

[87] K. Sriraman, S. Ganesh Sundara Raman, S.K. Seshadri, Mater. Sci. Eng., A., 460-461 (2007) 39-45.

[88] C.F. Windisch Jr., C.H. Henager Jr., M.H. Engelhard, W.D. Bennett, J. Nucl. Mater., 383 (2009) 237–243.

[89] S.H. Cho, S.B. Park, D.S. Kang, M.S. Jeong, H. Park, J. M. Hur, H.S. Lee, J. Nucl. Mater., 399 (2010) 212-218.

[90] J.H. DeVan, "Catastrophic Oxidation of High-Temperature Alloys", Oak Ridge National Laboratory Report, Report No: ORNL-TM-51, 1961.

[91] Y.S. Li, M. Spiegel, Corros. Sci., 46 (2004) 2009-2023.

[92] E.H. Kim, J.H. Lee, S.H. Cho, J.K. Oh, H.S. Lee, S.W. Park, "Development of a corrosion resistant structural material in an electroreducer", Proceedings of International Pyroprocessing Research Conference, held Aug 24-27, 2008, Republic of Korea.

[93] S.H. Cho, S.B. Park, J.H. Lee, J.M. Hur, H.S. Lee, J. Nucl. Mater., 412 (2011) 157-164.

[94] Y.J. Park, H.R Pyo, D.Y. Kim, K.Y. Jee, W.H. Kim, J. Korean Nucl. Soc., 32 (2000) 514-520.

[95] M.J. Lineberry, R.D. Phipps, R.H. Rigg, R.W. Benedict, M.D. Carnes, C.E. Herceg, R.E. Holtz, "IFR Fuel cycle demonstration in the EBR-II Fuel cycle facility", Argonne National Laboratory Report , Report No: ANL/CP—73973.

[96] T.C. Totemeier, S.D. Herrmann, "Materials compatibility testing for a pilot-scale oxide reduction system", Argonne National Laboratory Report, Report No: ANL/ED/CP-101337.

[97] J.R. Davis, Davis & Associates, ASM Speciality Hand Book on Stainless Steels, ASM International, Materials Park, Ohio, (1994) p.220.

[98] Jagadeesh Sure, A. Ravi Shankar, S. Ramya, U. Kamachi Mudali, Ceram. Int., 38 (2012) 2803-2812.

[99] Jagadeesh Sure, A. Ravi Shankar, U. Kamachi Mudali, A. Nowicki and Baldev Raj, Surf. Eng., 29 (2013) 28-33(6).

[100] A. Ravi Shankar, U. Kamachi Mudali, Ravikumar Sole, H.S. Khatak, Baldev Raj, J. Nucl. Mater., 372 (2008) 226-232.

[101] R. Taylor, J.R. Brandon, P. Morrell, Surf. Coat. Technol., 50 (1992) 141-149.

[102] R.L. Jones, Thermal barrier coatings, (eds) Kurt H Stern, "Metallurgical and ceramic protective coatings", Chapman and Hall, 1996, pp 194-235.

[103] K.A. Khor, S. Jana, J. Mater. Process. Technol., 66 (1997) 4-8.

[104] J.R. Brandon, R. Taylor, Surf. Coat. Technol., 39/40 (1989) 143-151.

[105] E. Lugscheider, I. Kvernes, Thermal Barrier Coatings: Powder spray process and coating technology, (Eds) Narendra. B. Dahotre and T. S. Sudarshan, "Intermetallic and Ceramic Coatings" 1999.

[106] T.N. Rhys-Jones, F.C. Toriz, High Temp. Technol., 7 (1989) 73–81.

[107] R.A. Miller, Surf. Coat. Technol., 30 (1987) 1-11.

[108] O.A. Quintana, J.E. Indacochea, M. Williamson, C. Snyder, "High-Temperature Corrosion of YSZ Plasma-Sprayed on Nickel-Alloys in Molten Chloride Salts", TMS 2010 Annual Meeting & Exhibition, held February 14-18, 2010 (Seattle, WA, USA).

[109] H. Kinoshita, C.A. Sharrad, I. May, R.G. Lewin, "Effect of Uranium on corrosion of stainless steel in High temperature molten salt in the presence of moisture", Proceedings of the Eighth Actinides Conference 2005, held July 4-8, 2005 (Manchester, UK).

[110] M. Rudolphi, D. Renusch, M. Schu̇tze, Scr. Mater., 59 (2008) 255–257.

[111] S.H. Cho, S.B. Park, D.S. Kang, M.S. Jeong, H. Park, J.M. Hur, H.S. Lee, J. Nucl. Mater., 399 (2010) 212-218.

[112] S.H. Cho, B.H. Park, J.M. Hur, H.S. Lee, K.C. Song, J.H. Lee, Corros. Sci., 52 (2010) 2353-2364.

[113] H.Y. Lee, K.H. Baik, Met. Mater. Int., 15 (2009) 783-787.

[114] M. Bartsch, B. Baufeld, S. Dalkilic, L. Mircea, Mater. Sci. Forum., 492-493 (2005) 3-8.

[115] O. Trunova, T. Beck, R. Herzog, R.W. Steinbrech, L. Singheiser, Surf. Coat. Technol., 202 (2008) 5027-5032.

[116] Z.L. Dong, K.A. Khor and Y.W. Gu, Surf. Coat. Technol., 114 (1999) 181-186.

[117] K.A. Khor, Y.W. Gu, Thin Solid Films., 372 (2000) 104-113.

[118] A.M. Khoddami, A. Sabour, S.M.M. Hadavi, Surf. Coat. Technol., 201 (2007) 6019 – 6024.

[119] C.C. Ge, W.B. Cao, Z.J. Zhou, Z.H. Chen, Mater. Sci. Forum., 492-493 (2005) 15-20.

[120] Y.W. Gu, K.A. Khor, Y.Q. Fu, Y. Wang, Surf. Coat. Technol., 96 (1997) 305 – 312.

[121] K.A. Khor, Z.L. Dong, Y.W. Gu, Thin Solid Films., 368 (2000) 86 – 92.

[122] K.A. Khor, Z.L. Dong, Y.W. Gu, Mater. Lett., 38 (1999) 437 – 444.

[123] Y.G. Jung, S.C. Choi, Mater. Lett., 37 (1998) 312–319.

[124] S. Lo´pez-Esteban, J.F. Bartolome´, C. Pecharroma´n, J.S. Moya, J. Eur. Ceram. Soc., 22 (2002) 2799–2804.

[125] J.G. Yeo, Y.G. Jung, S.C. Choi, J. Eur. Ceram. Soc., 18 (1998) 1281-1285.

[126] Y.G. Jung, C.G. Ha, J.H. Shin, S.K. Hur, U. Paik, Mater. Sci. Eng., A., 323 (2002) 110–118.

[127] R. Polanco, P. Miranzo, M.I. Osendi, Acta Mater., 54 (2006) 2215–2222.

[128] J. Musil, M. Alaya, R. Oberacker, J. Therm. Spray Technol., 6 (1997) 449-455.

[129] M. Gasik, A. Kawasaki, Y.S Kang, Mater. Sci. Forum., 492-493 (2005) 9-14.

[130] S. Sampath, W.C. Smith, T.J. Jewett, H. Kim, Mater. Sci. Forum., 308-311 (1999) 383-388.

[131] J.R. Davis, Davis & Associates: in 'ASM handbook', Microstructural Characterization of Thermal Spray Coatings, 9 (2004) 1038.

[132] A. petitbon, L. Boquet, D. Delsart, Surf. Coat. Technol., 49 (1991) 57-61.

[133] C. Batista, A. Portinha, R.M. Ribeiro, V. Teixeira, C.R. Oliveira, Surf. Coat. Technol., 200 (2006) 6783-6791.

[134] P. C. Tsai, C. S. Hsu, Surf. Coat. Technol., 183 (2004) 29-34.

[135] G. Antou, G. Montavon, F. Hlawka, A. Cornet, C. Coddet, F. Machi, Surf. Coat. Technol., 172 (2003) 279-290.

[136] C. Batista, A. Portinha, R.M. Ribeiro, V. Teixeira, M.F. Costa, C.R. Oliveira, Surf. Coat. Technol., 200 (2006) 2929-2937.

[137] S.O. Chwa, A. Ohmori, Surf. Coat. Technol., 148 (2001) 88-95.

[138] X. Wang, P. Xiao, M. Schmidt, L. Li, Surf. Coat. Technol., 187 (2004) 370-376.

[139] A. Ravi Shankar, B. Jagdeesh Babu, Ravikumar Sole, U. Kamachi Mudali, H.S. Khatak, Surf. Eng., 23 (2007) 147-154.

[140] C. Batista, A. Portinha, R.M. Ribeiro, V. Teixeira, M.F. Costa, C.R. Oliveira, Appl. Surf. Sci., 247 (2005) 313-319.

[141] K.A. Khor, S. Jana, J. Mater. Process. Technol., 66 (1997) 4-8.

[142] S.Z. Lee, K.H. ZumGahr, Matwiss. u. Werkstofftech., 23 (1992) 117-123.

[143] D. Triantafyllidis, L. Li, F.H. Stott, Appl. Surf. Sci., 186 (2002) 140-144.

[144] D. Triantafyllidis, L. Li, F.H. Stott, Surf. Coat. Technol., 201 (2006) 3163–3173.

[145] H.C. Chen, E. Pfender, J. Heberlein, Thin Solid Films., 315 (1998) 159-169.

[146] S. Ahmaniemi, P. Vuoristo, T. Mantyla, C. Gualco, A. Bonadei, R.D. Maggio, Surf. Coat. Technol., 190 (2005) 378-387.

[147] G. Antou, G. Montavon, F. Hlawka, A. Cornet, C. Coddet, Ceram. Int., 31 (2005) 611-619.

[148] P.C. Tsai, H. L. Tsai, David C. Tu, Mater. Sci. Eng., A, 165 (1993) 167-173.

[149] J.D. Verhoeven, Interfaces, Fundamentals of Physical Metallurgy, John Wiley and Sons, New York, (1975) 169-215.

[150] J. Dutta Majumdar, I. Manna, Int. Mater. Rev., 56 (2011) 341-388.